Extracellular Vesicle Profiling Towards Disease Detection by Using Micro/Nano-fluidic Devices

By Zheng Zhao

B.S., Kansas State University, Manhattan, 2015

Submitted to the graduate degree program in Bioengineering and the Graduate Faculty of the University of Kansas in partial fulfillment of the requirements for the degree of Doctor of Philosophy.

Chair: Steven A. Soper

Brandon J. Dekosky

Andrew K. Godwin

Jenny Robinson

Liang Xu

Date Defended: 12 November, 2020

The dissertation committee for Zheng Zhao certifies that this is the approved version of the following dissertation:

Extracellular Vesicle Profiling Towards Disease Detection by Using Micro/Nano-fluidic Devices

Chair: Steven A. Soper

Date Approved: 06 April, 2021

Abstract

Based on the American Cancer Society, in 2020 there will be an estimated 1.8 million new cancer cases diagnosed and about 0.6 million cancer patients will die because of cancer. Meanwhile, millions of people in the United State do not have proper treatment regimens, early diagnosis opportunities, and continuously monitoring recurrence. Point-of-care testing (POCT) is one possible solution to reduce the cost while maintaining disease management capabilities. To achieve the potential of POCT, extracellular vesicles (EVs) have garnered much attention because of the ability to secure these biomarkers in a minimially invasive manner and also, the wealth of information they contain to realize full management of disease for cancer patients. To facilitiate the realization of POCT for cancer diseases, microfluidic and nanofluidic technologies have been recognized as possessing high efficiency, throughput, accuracy, and low-cost to replace conventional benchtop experiments and realized POCT for oncology.

We successfully developed a microfluidic system, ExoSearch chip, for cancer diagnosis with on-chip EV isolation using immune-magnetic beads. The ExoSearch chip also included features of continuous flow and customizable capture antibodies, which makes the ExoSearch chip able to target different types of cancer by targeting the appropriate antigen. Three ovarian cancer-related biomarkers, CA-125, EpCAM, and CD24, which reside on the surface of EVs, were analyzed to provide accurate results ($p = 0.0001$, 0.0009, 0.003, respectively). Furthermore, 3-dimensional (3D) printing technology was used for microfluidic fabrication to boost prototyping capabilities. The EVs were also able to be collected, engineered, and released for immunotherapy. The EVs were modified by cancer-related peptides and were able to trigger an immune response and activate the cytotoxic T cell (CTL) to target tumor cells. Both *in vitro* and *ex-vivo* experiments were performed to evaluate the engineered EVs for immunotherapy.

Our lab also developed an EV-MAP chip made from thermoplastic materials, which lifted the possibility of chip mass production for clinical applications that require one-time use devices, more binding sites, and faster sample processing rate, which increased the binding capacity and also the sampling efficiency. The EV-MAP chip was used for ovarian cancer plasma sample characterization and for radiation injury diagnosis. The EV related miRNA, miR-92a-3p, and miR-204-5p were also targeted as biomarkers for exposure to ionizing radiation. The combination of total protein expression and miRNA expression indicated that the CD8 expressing EV subpopulation showed upregulated numbers of CD8 expressing EVs without significant changes in protein expression and the CD8 subpopulation did not show major expression of miR-92a-3p or miR-204-5p.

Current enumeration platforms for EVs consist of nanoparticle tracking analysis (NTA), electron microscopy (EM), high-resolution flow cytometry (hFC) and are used for both EV size distribution and concentration analysis. However, disadvantages of these technologies include large sample volume requirements, vibration-free operation, temperature consistency, and extensive software analysis, which have reduced the EV translation capacity. We have developed an in-plane nano-Coulter counter (nCC) device for enumerating EVs rapidly. With the concept of resistive pulse sensing (RPS), an electrical signal is generated for each EV when the EV travels through the nanopore. By understanding the electrical signals' frequency and amplitude, both the concentration and size distribution profiles can be collected for each EV sample quickly and efficiently. The nCC chip can also be used for EV enumeration for SARS-CoV-2 viral particle counting to determine viral load of SARS-CoV-2 viral particles enriched from biological samples to screen the infectious status of patients suspected of possessing COVID-19.

Acknowledgments

There is so much gratitude that I would like to nominate during my period of Ph.D. program study. First of all, I would like to express my sincere gratitude to Dr. Steven Soper for his support and kindness guidance. Dr. Soper accepted me to join the group in 2018 fall and provide an excellent research environment and potential projects. I would not have the success and been this far without his help and the whole research group's support.

Then I would like to thank the rest of my program committee members, including Dr. Brandon J. Dekosky, Dr. Andrew Godwin, Dr. Jenny Robinson, and Liang Xu. All of your guidance have been supporting me to keep the right track of my study.

Also, I would like to thank Dr. Maggie Witek and Dr. Matt Jackson. Both of them gave me lab orientations and hands-on experiences to become a valid researcher. Dr. Matt Hupert and Dr. Mengjia Hu provided a lot of support for the automatic robot system and device fabrication. All the supports have boosted my knowledge, gaining progress and experiment efficiency.

I would also like to thank all of the collaborators of the projects I involved, including Dr. Harsh Pathak with the Tina's wish project for the plasma sample collection and experiments proceed; Dr. Subhrajit Saha's lab for the offering of radiation mice models; Dr. Collin McKenney and Dr. Matthew David Verber for the training of nanochannel amplifier system and electrical signal analysis.

I also want to express my gratitude to the Bioengineering program head Dr. Fischer and coordinator Denise, for their kind help and keeping me on the right track of graduate-level study. I will not be in the current status without their help and suggestion. I would also like to thank Dr. Lisa Friss for the guidance and help during the period of being a teaching assistant for her class. I

want to thank Dr. Mei He and Dr. Yong Zeng for their previous support and training to be a valid researcher, especially during my first two years at Kansas State University.

I also want to thank our lab members: Swarna, for all the simulation and discussion with the nanodevice and all the hard-working; Ian, for the kindness offering of the cell culture media; Uldita, for all the nanodevice fabrication that boosted our experiment progress; Sachindra, for the help and discussion of the real-time PCR instrument; and all the other lab members including Dr. Lulu Zhang, Dr. Anishkumar Manoharan, Charuni, Thilanga, Chathurika, Katie, Ziyu, Lindsey.

I would also like to thank my parents: Mr. Huaihai Zhao and Ms. Xuqin Qin, for their supports and guidance for my living, and also thanks to Lanjing Wei for all the support in both research study and life.

Table of Contents

List of Figures

List of Tables

List of Equations

Chapter 1: Isolation and Analysis Methods of Extracellular Vesicles (EVs)

EVs have been recognized as an evolving biomarker within the liquid biopsy family. While carrying both host cell proteins and different types of RNAs, EVs are also present in sufficient quantities in biological samples to be tested using many molecular analysis platforms to interrogate their content. However, because EVs in biological samples are comprised of both disease and non-diseased related EVs, enrichment is often required to remove potential interferences from the downstream molecular assay.

Most benchtop isolation/enrichment methods require milliliter levels of sample and can cause varying degrees of damage to the EVs. Simultaneously, the detection of the overall concentration, size distribution, and morphology of EVs is highly dependent on established techniques such as electron microscopy or Nanoparticle Tracking Analysis (NTA), which can include unexpected variations and biases. This review discusses why EVs are an important biomarker secured from a liquid biopsy sample and cover some of the traditional and non-traditional, including microfluidics and resistive pulse sensing (RPS) technologies, for EV isolation and detection.

1.1. Introduction

Biomarkers secured from a liquid biopsy sample are generating significant interest in the research and medical communities due to the minimally invasive nature of acquiring them and the fact that they can enable precision medicine that seeks to manage a variety of diseases, including oncology and non-oncology-related diseases using molecular signatures unique to the patient.[1, 2] One of the major biomarkers this chapter will discuss are EVs, which is one of many of the liquid biopsy related markers that can be secured from a clinical sample, such as whole blood.

Biological cells release vesicles of varying sizes through both the endosomal pathway or budding/blebbing from the plasma membrane. These vesicles are known by different names, including microvesicles (MVs), exosomes, apoptotic bodies, and are collectively called EVs (Figure 1.1a).[3] The particular subtype classification of EVs is based on their cellular origin and biogenesis.[4] Each vesicle has unique characteristics that can provide complementary information to manage a variety of cellular states. MVs are heterogeneous, membrane-bound vesicles generated by budding/blebbing from the plasma membrane,[5] and can range from 100 nm to 1 μm in size. On the other hand, exosomes are the smallest category in the EV family with sizes ranging from 30 – 150 nm and are released into the extracellular environment after the fusion of late endosomes/multivesicular bodies (MVB) with the plasma membrane. Finally, apoptotic bodies, are generated due to programmed cell death called apoptosis, and range from 1 – 5 μm in size. Figure 1.1b shows the size variations of the different types of EVs.[6]

EVs contain variable components including lipids, carbohydrates, cytokines, proteins, and RNAs.[7] Both the surface and intra-vesicle material of EVs originate from their host cells, making the EVs suitable biomarkers for disease management, such as diagnosis, monitoring response to therapy, and determining disease recurrence.[6] However, before analyzing any of the aforementioned biomarkers, they must typically be “enriched” from the clinical sample because they are typically a vast minority in a mixed population.

The research field has now discovered that exosomes, a subtype of the EV family, plays a critical role in the transmission, delivery, and mediation of intercellular communication without the necessity of cell-to-cell contact.[8-11] Published research has shown that EVs can bind to cell membranes, the extracellular matrix, or enter extracellular fluid such as blood plasma or cerebrospinal fluid.[9, 12] Secreted EVs can bring cellular content of their hosts to the target location

through the extracellular fluid and circulatory system. In addition, markers on the surface of EVs can act as targeting subunits, allowing them to bind to specific cell types to mediate the exchange of genetic information and signal transduction.

There is now a pressing need to "enumerate" EV biomarkers and analyze their molecular contents to provide relevant information for disease detection and management. The challenge with liquid biopsy markers is the mass limits they imposed on the molecular assay. Even though EVs are high in numbers (10^6 – 10^{13} EVs per mL of plasma), their small size limits the molecular content within a single EV. For example, a 150 nm (diameter) EV may contain approximately 10 nucleotides of nucleic acids. In addition, components present in a sample may interfere with the molecular processing, and enrichment can obviate this issue.

Enrichment and detection techniques can take advantage of either the physical properties of the EVs (size, density, electrical properties, morphology) or their biological properties (antigen expression). The next few sections of this chapter will focus on reviewing EVs' physical properties, intra-vesicle contents, diagnostic and therapeutic applications, isolation methods, and direct detection methods.

1.2. Types of EVs

Cells release vesicles of varying sizes through both the endosomal pathway and by budding from the plasma membrane, namely exosomes, microvesicles, respectively, and apoptotic bodies. These vesicles are collectively termed EVs. The subtypes of EVs are based on their biogenesis and cellular origins (Figure 1.1).[13, 14] EVs can be found in various biological fluids including saliva, urine, blood, ascites, breast milk, and cerebrospinal fluid. Blood is an excellent source of EVs, and serum is estimated to contain approximately 3×10^6 exosomes per microliter.[14]

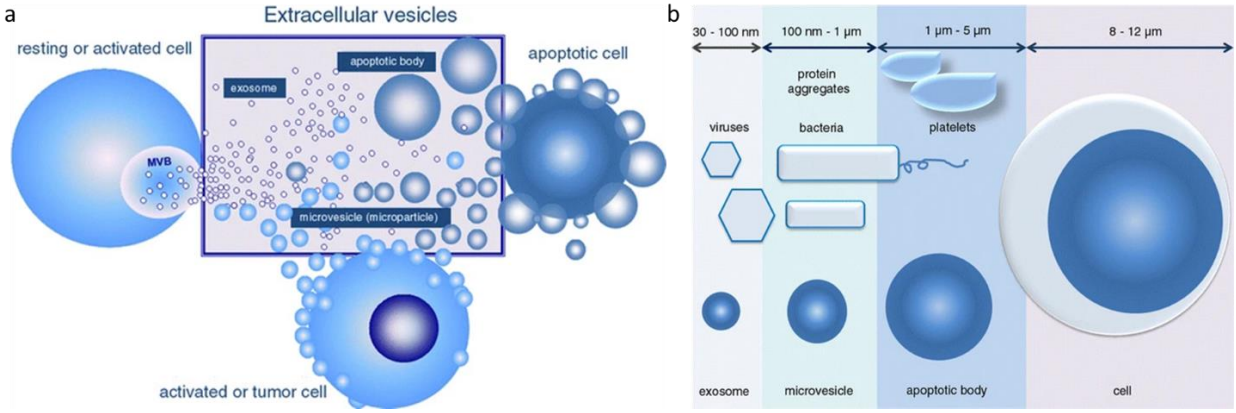

Figure 1.1. a) Sub-types of extracellular vesicles, including microvesicles, exosomes, and apoptotic bodies. **b)** Size ranges of the three sub-types of extracellular vesicles, that exosome is the smallest with a range from 30 to 150 nm; microvesicles are range from 100 to 1000 nm, and the size is from 100 to 400 nm when present in the circulating system; apoptotic bodies are range from 1 µm and up to 5 µm (Reproduced from reference 13).

1.2.1. Microvesicles

Microvesicles (MVs) are heterogeneous, membrane-bound vesicles that are 100 nm to 1 µm in size and are released from the surface of many cell types, including embryonic stem cells, neurons, and astrocytes, under both physiological and disease conditions.[14] MV biogenesis takes place through direct outward blebbing and pinching of the plasma membrane.[14] The platelets, red blood cells, and endothelial cells have been verified as a significant source of MV secretion, and tumor cells also constantly release MVs.[13, 15] MVs are important in altering the extracellular environment, intracellular signaling, and facilitating cell invasion through cell-independent matrix proteolysis.[16] MVs can also contribute to the pro-invasive character of tumors and also can increase the oncogenic intercellular transformation.[17, 18] Differential centrifugation and flow cytometry are the commonly used isolation and detection, respectively, methods for MVs.[13, 19]

1.2.2. Exosomes

Exosomes were first discovered by the Stahl and Johnstone groups in 1983.[20, 21] Exosomes are small EVs with a size from 30 – 150 nm and can be produced by a majority of living cells.[22, 23] Exosomes are secreted by exocytosis of multivesicular bodies and released into the intercellular environment.[24] As Figure 1.2 shows, the hallmarks of exosomes includes the tetraspanins (CD9, CD81, and CD63), ALG-2-interacting protein X (ALIX), and tumor susceptibility gene 101 protein (TSG101).[25] The tetraspanins can serve as surface markers for exosome immuno-affinity isolation, and the ALIS and TSG101 are commonly intravesicle biomarkers of exosomes.[26, 27] In addition, exosomes are involved in many cellular functions such as metabolism and receptor transportation,[25, 28] horizontal transfer of mRNA and miRNA,[29] and also as a vector for oncogenic transfer.[13] Studies focused on exosomes include isolation and purification,[30-33] surface and intra-vesicle protein marker analysis,[34-37] cargo mRNA and miRNA analysis,[6, 38, 39] secretion and uptake pathways,[40-42] surface and cargo modification,[43-46] drug delivery,[47-49] and disease diagnosis and management.[50-52]

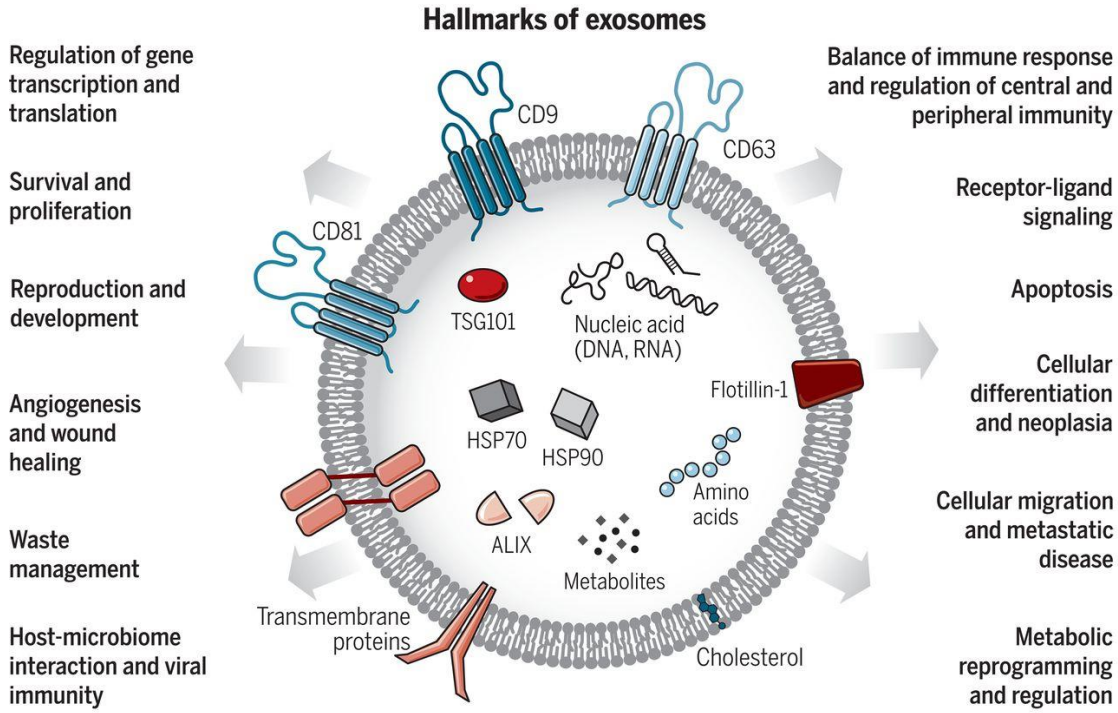

Figure 1.2. Exosomes are small EVs that size range from 30 to 150 nm. Exosomes carry various types of molecules originating from the host cell, including proteins, nucleic acids, lipids, and metabolites. Exosomes also play essential roles in cellular communication and regulation (Reproduced from reference 25).

1.2.3. Apoptotic bodies

Apoptotic bodies are from programed cell death and are primarily produced by cells undergoing apoptosis. Apoptosis occurs during cell-damaging or aging with the purpose of homeostasis. Cells can also show characteristic morphologies, including cell blebbing and shrinkage, nuclear fragmentation, condensation, and fragmentation of genetic materials, and formation of small vesicles known as apoptotic bodies.[53-55] As Figure 1.3 shows, one of the most distinguished morphologies of apoptosis is membrane blebbing. While the cell's hydrostatic pressure increases, other morphologies such as microtubule spike, beaded apoptopodia, and apoptopodia can also be present.[55] Apoptotic bodies that are 500-1000 nm in size are released as a product of apoptotic cell disassembly.[14] Like other types of EVs, apoptotic bodies contain protein,

RNA, DNA, and other cellular fragments.[53, 55-57] However, the only marker to recognize apoptotic bodies is phosphatidylserine (PS).[58] Apoptotic bodies coordinate many cellular membrane molecular patterns, including high-mobility group box 1 (HMGB1), heat shock protein 90 (HSP90), and interleukin-33 (IL-33) to facilitate cell blebbing.[59] Also, the caspase-mediated activation of pannexin 1 (PANX1) signal pathway serves as a "find-me" signal phagocytosis and further apoptotic cell removal.[59] Currently, the research field consistently concludes that apoptotic bodies are the result of highly regulated cell programmed death. The receptor locating (PANX1,[60] CX_3C-chemokine ligand 1 (CX_3CL1)),[61] and uptaking (phosphatidylserine (PtdSer),[62] calreticulin (CRT)[63]) signaling pathway are well studied, but the detailed pathway on how the cells are divided into small apoptotic bodies remains unraveled.[53, 55, 59]

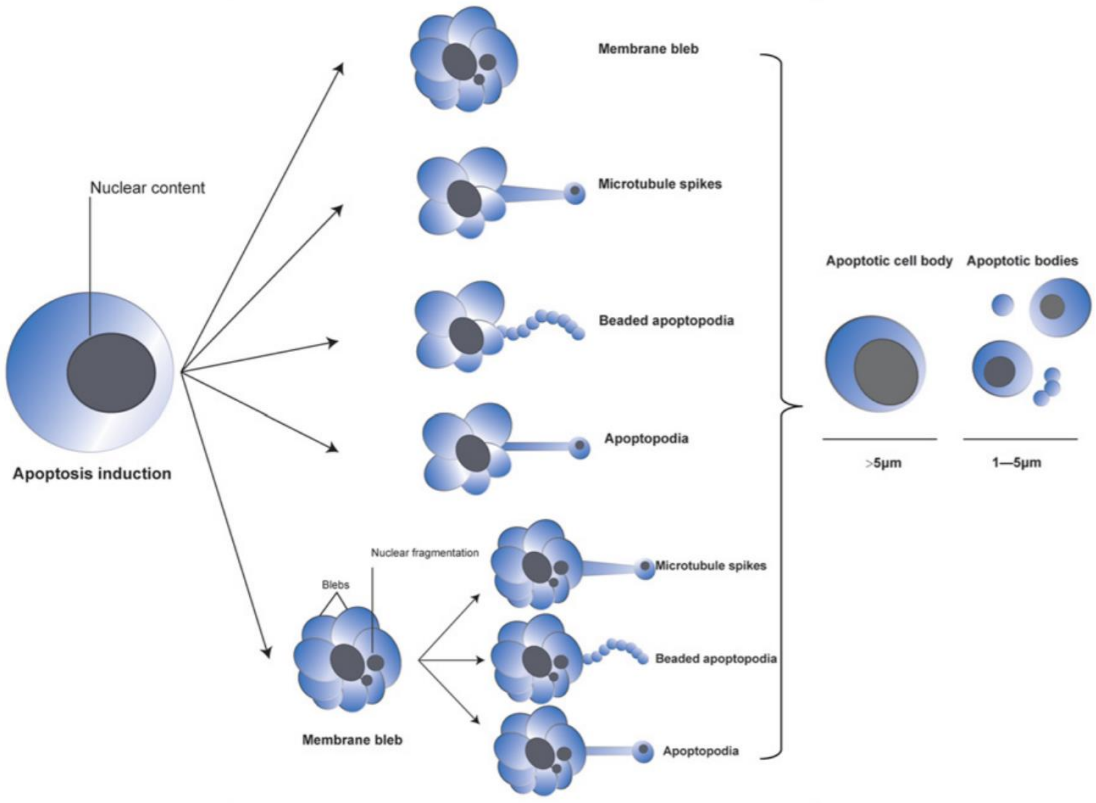

Figure 1.3. Different ways of cell disassembly into apoptotic bodies patterns of apoptotic breakage into apoptotic bodies are illustrated in this Figure. The apoptotic bodies can carry part of the nucleus, including DNA and RNA, and part of the cellular contents (Reproduced from reference 55).

1.3. The molecular composition of EVs

EV cargo mainly consists of various types of proteins and RNA. Commonly found proteins in EVs are cytoskeletal, cytosolic, plasma membrane, and proteins that show post-translational modifications.[64] In addition, the tetraspanins, such as CD9, CD63, CD81, and CD82, have been found to be present in exosome and serve as surface expression markers.[64] These transmembrane proteins are usually found on the surface of small EVs and can be used as targets for both small EV isolation and detection. However, recent studies have found that the tetraspanins can also be expressed on the surface of large EVs, including MVs and apoptotic bodies, making the immuno-affinity isolation contain unexpected EV subtypes.[65, 66] As a result, further studies of small EV-specific surface markers for their specific isolation is necessary. EVs can be secreted by most living cells, particularly in tumor cells, because of the continuous release and transfer of oncogenic information within the vesicles.[22, 23] With the feature of containing host cells' hallmark proteins, the tumor-related markers can be expressed on both EV surfaces and within the vesicle.[67-69]

The EV membrane also contains different types of receptors or ligands to trigger intracellular signaling pathways via a simple interaction in order to initiate the uptaking process to deliver the enclosed information into the target cells. The well-studied receptors and ligands for EVs uptake include the pairs of C-type and P-selectin glycoprotein ligand-1 (PSGL-1),[40, 70] Galectins and Glycans,[71, 72] mucins to galectin-3,[72, 73] PANX1 to purinergic receptor ($P2Y_{2}$).[59, 61]

RNA is also an important biomarker for disease detection because of the function RNAs play in genetic regulation. Due to developed technology in recent years, the RNA contents of EVs have been studied using such techniques as next generation RNA sequencing and RT-qPCR.[74] Many different types of RNAs have been found in EVs, which includes mRNA, non-coding RNA, miRNA, and tRNA.[64] mRNA is one of the widely studied RNA types found in EVs. Although

cellular mRNA has about 400 – 12,000 nucleotides, EV mRNA typically has <700 nucleotides.[75, 76] The mRNA is loaded in EVs and sent to recipient cells. Some publications have shown that some group of the mRNAs will only express inside of the transportation EV, but not expressed in the parental cells, which makes EVs trending more as valuable biomarker.[29, 77, 78]

miRNAs are small non-coding RNAs of about 22 nt in length. miRNAs are best known as gene silencing agents of complementary mRNAs, and serve to regulate the gene expression.[79, 80] Because miRNA is at the frontier of gene expression regulation, upregulated mRNA may not be translated into the expected protein due to miRNA interference.[81] The situation makes miRNA an essential biomarker for understanding different cellular conditions. miRNA has been found in body fluids with complementary RNA-binding proteins to avoid enzymatic degradation.[82-84] With the same purpose as carrying mRNA, EVs also serve as vectors to transport miRNA to recipient cells.[74] EV-related miRNAs have been studied for cancer, such as miR-21 and miR-210,[85-87] post-radiotherapy related miRNA such as miR-130a-3pand miR-92a-3p.[39, 88] Understanding the RNA composition of EVs has become a critical endeavor for disease diagnosis and management.

1.4. Diagnostic potential of EVs

Due to the valuable cargo of EVs, they have been widely studied as potential biomarkers for different diseases.[89-91] However, processes such as anticoagulation and endotoxin tube contamination can affect EV concentration in blood, which complicates enumeration data.[92-94] One advantage of EVs as a biomarker over many other soluble molecules in the blood like hormones and cytokines, is the inherent protection of the EV cargo from degradation, thus keeping the cargo intact and functional. Hence, EVs can be transported from any location to the bloodstream making them easily accessible for liquid biopsies.

Additionally, the literature has shown that the EV quantity, phenotype, or cargo content can change during various disease states.[95-98] In many cases, tumor cells constantly release EVs, which makes tumor-related EVs present in the plasma at higher concentrations compared to normals.[95, 99] Many published works have indicated that EVs secreted by tumor cells can carry the same molecular markers found in the host cells, and understanding the tumor-related EV molecular profiles can help provide a fingerprint for disease diagnosis and management.

EVs have also been studied as biomarkers for many non-cancer diseases, including diseases of the central nervous system,[100] liver (liver damage in viral hepatitis, hepatocyte injury in alcoholic, drug-induced, and inflammatory liver diseases),[101] kidney (intrinsic kidney disease),[102] brain (stroke),[103] lung (Asthma),[104] arteries (atherosclerosis)[105] and radiation injury.[39]

1.5. Therapeutic potential of EVs

A large amount of EVs present in circulation can serve for communication and regulation purposes, and also can be secreted and uptaken by cells, which indicates that EVs could be utilized as drug delivery vehicles. EVs are primarily up taken by cells using three mechanisms: endocytotic, membrane fusion, and receptor interactions with cells.[3, 8, 23, 106] As a transportation vector, EVs can also be used as a drug delivery capsule for target and precision medicine. EV drug delivery capsules have multiples features, which are summarized in Figure 1.4.[3, 7, 19] First of all, as natural secreted vesicles, EVs can possess a high degree of biocompatibility, especially when the EVs are isolated from and applied to the same biological unit.[106, 107] In addition, EVs can travel in circulation far distant due to their long self-life and ethidium penetration properties.[93] EV vectors can solve the challenges of drug effective dose reduction by biological barriers.[23] EVs carry cell/tissue-specific markers and contain receptors and ligands that can direct them to the target

recipient cells, which can be applied for targeting therapy and minimize unnecessary presence in the circulating system.[108, 109] Another important features of EV drug delivery vectors is the compartmentalization of internal drug components. The EV's lipid layer can serve as a shutter to protect the drug molecule from enzymatic degradation or complementary binding. In addition, the drug molecule can also be kept inside the EV until they reach the expected location to protect the non-related cell/tissue from the drug molecule and minimizing size-effects.[8, 106]

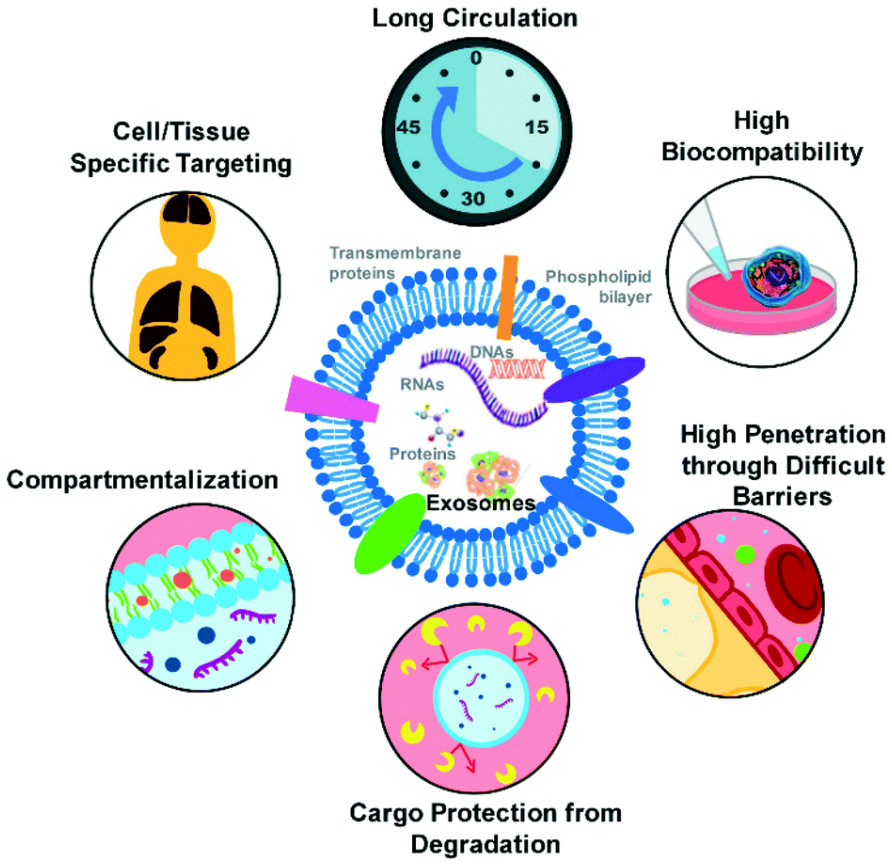

Figure 1.4. Advantages of small EVs as drug delivery vectors include carrying cell/tissue-specific markers, stable structure for a longer time of circulation, high biocompatibility, higher penetration through barriers, the cargo protection from degradation, and compartmentalization of the drugs from non-target tissues, that are naturally designed as vectors (Reproduced from reference 23).

1.6. Conventional methods of EV isolation

In order to analyze EVs' cargo, EVs of interest must be isolated in high purity and high yields from body fluids because non-diseased EVs also generate EVs that can mask subtle molecular signatures of the disease. With increasing research studies conducted on EVs, many techniques have been developed to isolate EVs. Some of these isolation techniques isolate the entire EV types irrespective of the cells of origin and others can specific so as to isolate on the disease-related EVs. In the next few sections, different isolation strategies will be discussed.

1.6.1. Ultracentrifugation

Ultracentrifugation (UC) is a classical method used for EV isolation and is based on the separation of particles according to their buoyant density. Particles with a high buoyant density like cells, cell debris, apoptotic bodies, and aggregates sediment more easily (*i.e.*, low spin speeds) compared to smaller particles, for example exosomes and MVs. To decrease the level of contamination, this step is divided into sub-steps: Centrifugation at 300-400g for 10 min to sediment cells; 2,000g to sediment cell debris; and then centrifugation at 10,000g to remove aggregates of biopolymers, apoptotic bodies. The resulting supernatant with EVs is ultracentrifuged at >100,000g for 2 h, which will yield a pellet of small particles.[110, 111]

Density gradient UC is a technique that uses two methods for the formation of a gradient, which can consist of a continuous density gradient or a stepwise gradient based on sucrose. High spin speeds for extended periods of spin times result in the concentration of exosome-like vesicles in a band with somewhat similar densities (approximately 1.1-1.9 g/mL). Because different EV subtypes have similar densities, the isolation of EVs by density gradient does not provide a pure fraction of exosomes.[112, 113] In some cases, isolated EVs are further purified using filtration (0.1,0.22 or 0.45 µm filters) or subsequent washing steps. Although these additional steps increase

the purity of isolated EV subtypes, it also decreases the quantity of EVs in the isolate.[112, 114] It should be noted that whatever type of UC is undertaken, UC does not have the ability to isolate only disease-associated EVs; the entire subtype of EVs are in the isolate following UC.

While UC can take from 140 – 600 min for the isolation, isolation of EVs from larger volumes of sample with no additional chemicals can be undertaken. Some drawbacks of this method include non-exosomal impurities, low reproducibility, and the efficiency affected by the type of rotor, force, and sample velocity.[110, 114, 115] Also, only six samples can be concurrently processed when using a cone ultracentrifuge. Density gradient UC includes sucrose or iodixanol density gradient, and differential centrifugation can take from 250 min to 2 days. However, it yields more pure fractions of EVs after iodixanol centrifugation. Loss of sample, and the inability to separate large vesicles with similar sedimentation rates are some of the significant disadvantages.[30, 116] UC methods, including iodixanol density gradient UC, and sucrose density gradient UC can yield low EV quantities compared to other methods, such as precipitation with polymers using commercial kits (ExoQuick, TEI, Norgen).[112] Using different methods for urinary exosome isolation, Alvarez *et al.* reported that UC and sucrose density gradient UC yielded the highest purity followed by ExoQuick kit and EVs isolated from ultrafiltration showed the lowest purity.[117]

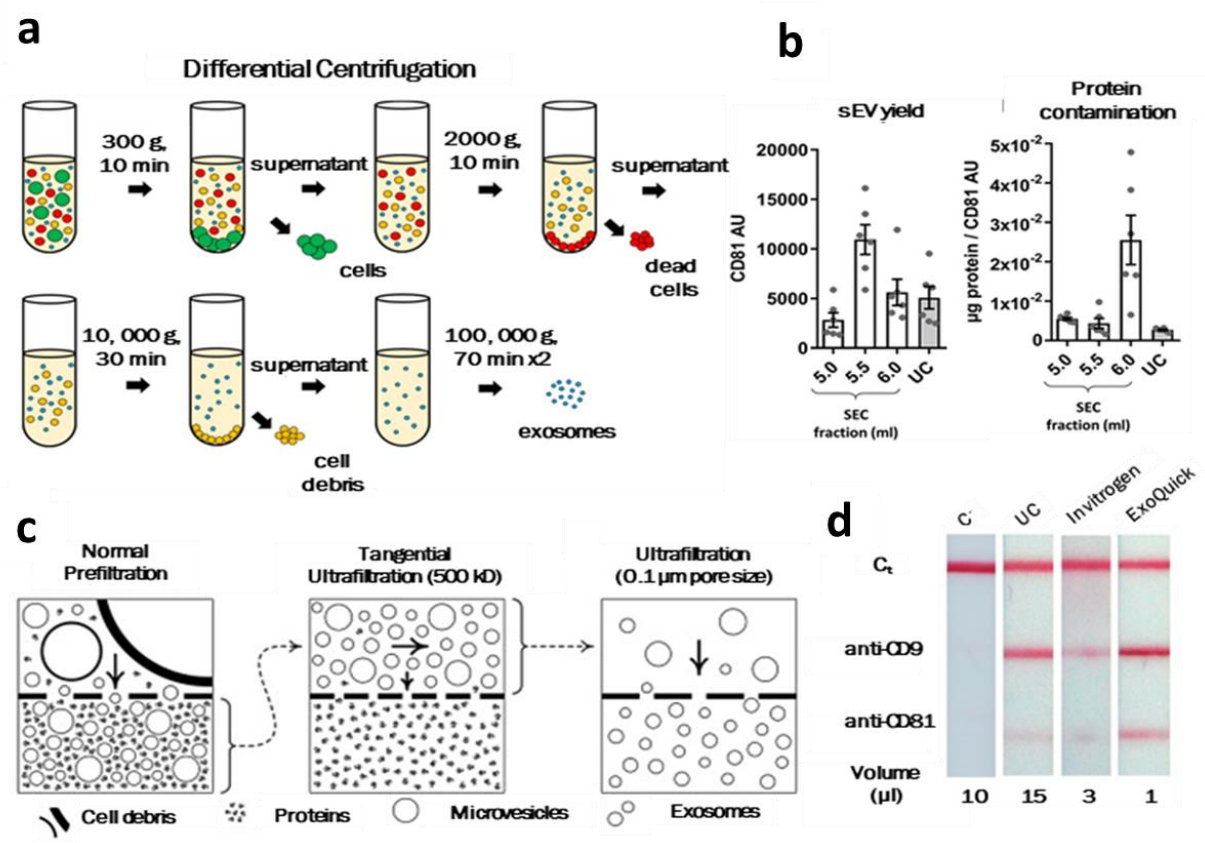

Figure 1.5. a) Differential ultracentrifugation for exosome isolation (Reproduced from reference 113). **b)** Summary of yield and purity of EVs isolated by SEC or UC. The normalization of APOB signal to CD81 content, as an estimate of sEV purity from lipoproteins, also demonstrated almost 60 times higher APOB/CD81 ratio in the peak sEV fraction of SEC (5.5 ml) compared to the UC samples. SEC resulted in a higher yield of EVs but with marked contamination by soluble protein and lipoproteins (Reproduced from reference 118). **c)** Filtration and ultrafiltration for EV isolation: normal prefiltration can collect small EVs and particles into the bottom layer of the culture dish. The bottom layer solution will need to be processed through tangential ultrafiltration, and the retentate will be collected. Further ultrafiltration with expected pore size will be processed, and the EVs with a size smaller than the pore will present in the permeate (Reproduced from reference 33). **d)** Detection of the EV isolated by lateral flow immunoassay (LFIA), using anti-CD9 and anti-CD81 as capture antibodies, and reflectance measurements of AuNPs on each test line (estimated as the peak area of the signal in mV × mm). EV-depleted plasma was used as a negative control (C−). Unbound antiCD63-AuNP captured with anti-IgG were used as system functional verification (Ct) (Reproduced from reference 130).

EV fractions of the size range 20 – 250 nm can be isolated from UC, and these isolated EVs display markers including CD9, CD63, CD81, TSG101, Alix, Flotillin-1, AQP2, and FLT1

and are appropriate for assaying RNA and microRNA.[112] UC and size-exclusion chromatography have been systematically compared for isolating EVs (EVs) in rat plasma, and results (Figure 1.5) revealed that SEC-EVs had higher particle numbers, protein content, particle/protein ratios, and sEV marker signal than UC-EVs. However, SEC-EVs also contained significant amounts of $APOB^+$ lipoproteins and large quantities of non-sEV protein, bringing unexpected interference to the downstream molecular analyses.[118]

1.6.2. Filtration

Filtration has been used as an isolation method for small particles based on size. With the use of a nanomembrane, filtration can isolate EVs for diagnostic applications.[33, 119] Because filtration will not affect the structure or function of proteins or RNAs within the EVs, a sequential filtration and UC is commonly used to provide clinical-grade exosomes (Figure 1.5c). An expected pore size modified polyethersulfone (mPES) is one of the established membranes for the pre-filtration of cell culture media. With separate layers of the culture, EV, protein, and other types of microvesicles can pass through the membrane to reach the bottom layer. Then, a tangential flow filtration (TTF) with a 500 kDa molecular weight cut off (MWCO) hollow fiber filter was used to filter out proteins. By applying the TTF, clogging is not an issue for the continuous operational process. A final step with a low-pressure filtration can only make the desired size (smaller than pore size) of particles present in the retentate. The sequential filtration can maintain a throughput limit of 0.96 mL/hour, and the size distribution of isolated EVs can be controlled firmly. However, clogging problems and high shear stress applied to the particle can damage it or reduce the number of EVs in the isolate.[116, 120] On the other hand, ultrafiltration can only be applied to low viscosity fluids, making the operation for plasma samples difficult.

1.6.3. Precipitation reagents

Precipitation of EVs uses hydrophilic polymers, such as polyethylene glycol, that reduce the solubility of small particles by lowering their hydration, which leads to precipitation.[112] For example PEG 6000, which is included in the ExoQuick (System Biosciences), Total Exosome Isolation Reagent (Invitrogen), ExoPrep (HansaBioMed), Exosome Purification Kit (Norgen Biotek), and miRCURY Exosome Isolation Kit (Exiqon), is generally used for EV isolation. Precipitation techniques can isolate EVs using lower spin speeds with higher yields compared to UC. However, upon addition of the precipitation reagents, the solubility of proteins also decrease.[121] Some of the advantages of the precipitation techniques include preserving EV integrity, no need for additional equipment, pH close to the physiological range, and the possibility to concurrently process a large number of samples. These advantages make precipitation methods attractive for clinical use.[122] However, poor reproducibility, impurities, and retention of the polymer are a few drawbacks.[123-125] In addition, precipitation isolates all EVs irrespective of cell origin, which means that diseased and non-diseased EVs are isolated.

When five different commercial EV isolation kits were compared, the total number of particles isolated from serum was the highest for miRCURY (precipitation), followed by Exo-spin (size-exclusion chromatography), qEV (size-exclusion chromatography), UC, and exoRNeasy (membrane affinity). Also, SEC-based isolation yielded EVs with significantly higher particle-to-protein ratios than the other methods, indicating less co-isolation of soluble protein. Isolates derived from precipitation and UC, on the other hand, displayed the lowest ratios due to increased protein contamination.[126]

When all four of the aforementioned methods were carried out side-by-side, different performances were observed. The size distribution of the isolated particles was 40–150 nm, and

ExoQuick™ Exosome Precipitation Solution (EXQ) generated a relatively high yield of exosomes. However, albumin impurity was abundant for all these methods, and TEI yielded a relatively pure isolate. There was a significant correlation of the exosomal miRNA profile and specific miRNAs between kits, but with differences. ExoRNeasy Serum/Plasma Midi Kit (EXR) and EXQ performed better in specific exosomal miRNA recovery.[127]

1.6.4. Affinity selection

As discussed above, EVs can contain protein makers that can represent the host cells and cell conditions from which the EVs originated. Tumor-derived EVs can express essential tumor-related proteins used for cancer disease diagnosis or progress monitoring.[64, 128] By targeting specific proteins on the surface of EVs using immunoaffinity-based approaches, a specific sub-type of EV can be collected. A variety of proteins can be targeted as biomarkers for EV isolation; those include the tetraspanins such as CD9, CD81, CD63, and cancer-related markers such as EpCAM, CD24, and CA125. Antibodies can be immobilized on a substrate such as the surface of a microplate or beads, and bind the EVs onto their surfaces only if they express an antigen specific to the capture antibody. Using immunoaffinity, the isolation can result in high specificity and purity for a particular EV subtype.[129, 130] However, due to the high cost of affinity-based assays, the isolation can only be applied with a small volume of sample, and EV-related proteins or RNA yields can be limited.[129, 131]

The primary advantage of affinity isolation of EVs is that if the correct targeting surface antigen is used, the isolated EVs can be associated predominately of those that are disease-associated as opposed to the aforementioned techniques that can be advantageous for the

downstream molecular analysis. However, if the affinity isolation uses the tetraspanins, all EVs, in particular the exosomes and MVs, will be contained in the isolate.

1.7. Novel approaches for EV enrichment

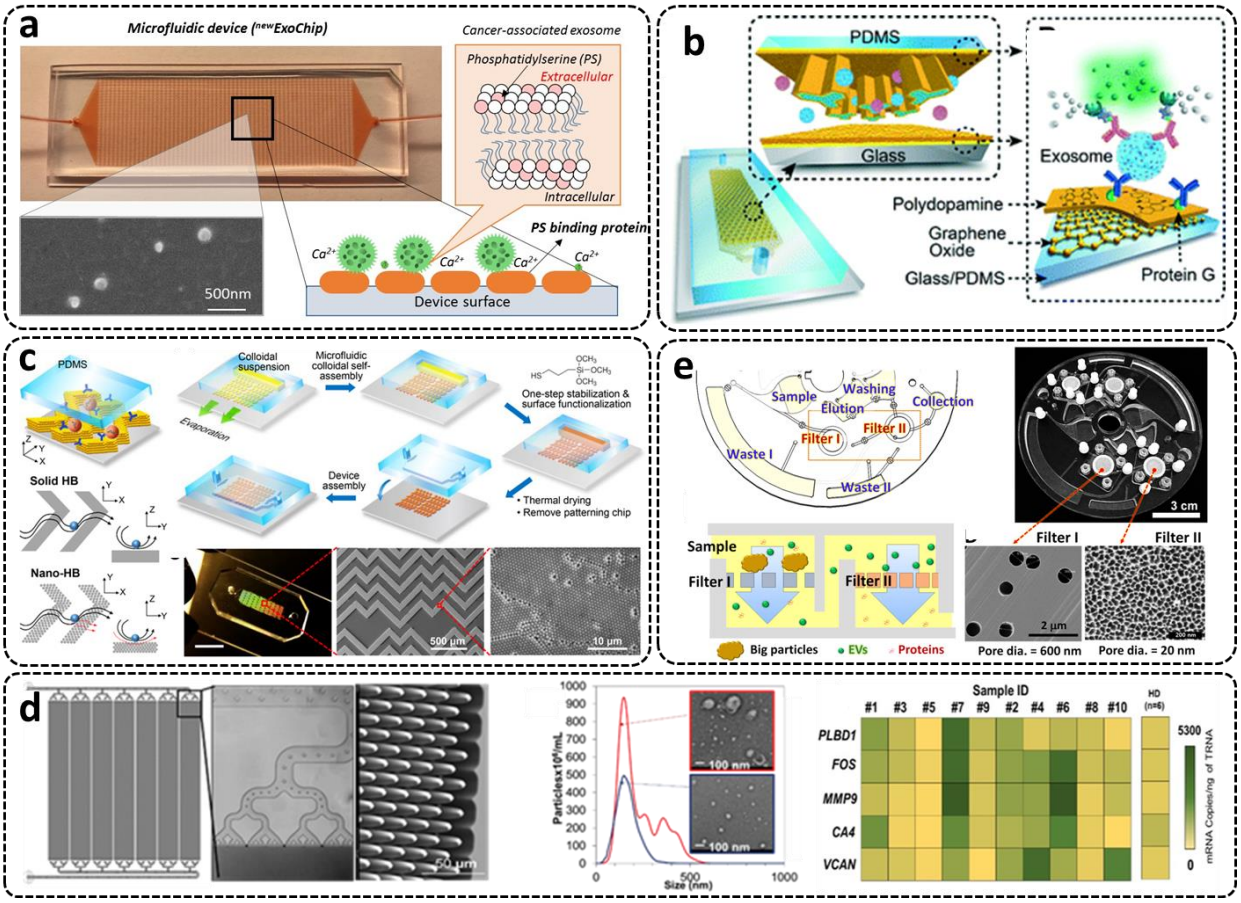

Figure 1.6. **a**) [new]ExoChip design, which features 30 × 60 circular patterns with a diameter of 500 µm in standard slide glass size. The mechanism of the capture and release of cancer-associated exosomes using Ca2+-dependent binding between PS and annexin V and ethylenediaminetetraacetic acid (EDTA)-based Ca2+ chelation, respectively. The micrograph shows capture and released exosomes (Reproduced from reference 141). **b**) The nano-interfaced microfluidic exosome platform (nano-IMEX). Schematic of a single-channel PDMS/glass device with expanded-view highlighting the coated PDMS chip containing an array of Y-shaped microposts. The surface of the channel and microposts coated with graphene oxide (GO) and polydopamine (PDA) as a nanostructured interface for the sandwich ELISA with fluorescence signal amplification (Reproduced from reference 133). **c)** 3D herringbone nanopatterns are designed on a microfluidic device with the ability to detect tumor-associated EVs in plasma with a minimum of 200 vesicles per 20 µL. The nano-structures were used to increase the surface area,

content mass transfer, EV capturing speed, and reduce the hydrodynamic resistance (Reproduced from reference 139). **d**) The microfluidic device made from COC allows for high-rate production at a low cost to accommodate diagnostic applications. CAD drawing of a 7-bed EV Microfluidic Affinity Purification (EV-MAP) showing the distribution channels and the diamond-shaped micropillars of the device. NTA and TEM images of EVs isolated from a clinical sample by PEG precipitation and affinity were selected with anti-CD8 mAb using the EV-MAP device. Heat map analysis of clinical samples (marked with numbers) and healthy donor for 5 genes whose upregulation is associated with acute ischemic stroke (Reproduced from reference 148). **e)** An ExoDisc integrated system that is combining a sequential filtration and centrifugation used for low viscosity fluidc. The EVs will be collected between the filter I and filter II, and the filters can be replaced with different pore-size for different expected size range of selection (Reproduced from reference 38).

Many of the recently reported platforms for the isolation of EVs have been based on the use of microfluidics for a variety of reasons, including their ability to be integrated to post-enrichment processing steps such as enumeration and/or molecular profiling of the EV cargo. The enriched EVs can be enumerated,[132-137] surface and cargo proteins analyzed,[34, 132, 133, 138-140] RNA profiled,[38, 134, 137] and diagnostics or therapeutics performed.[117, 141, 142] By including the appropriate micro- or nanoscale structures within the chip, approaches including affinity selection, filtration, centrifugation, viscoelasticity, and acoustic waves can be used for EV isolation using a microfluidic.

1.7.1. Affinity enrichment

Affinity enrichment can enrich primarily disease-associated EVs, improving the quality of the molecular data secured from the isolate.[143] The ExoChip is an early example of a microfluidic used for affinity enriching EVs.[133] The ExoChip was fabricated using soft lithography with polydimethylsiloxane (PDMS) with surface-attached antibodies targeting CD63. Clinical serum samples were analyzed with immune-electron-microscopy and Western blotting used to confirm isolation of the disease-associated EVs.

Many microfluidic devices used EV-specific markers for affinity enrichment, such as the tetraspanins, because in some cases, disease-specific markers may not provide viable molecular processing information. For example, in the later stages of cancer progression, cancer-related markers can be down-regulated. The new version of the ExoChip (^{new}ExoChip) used a phosphatidylserine (PS) strategy (Figure 1.6a).[140] PS is usually expressed in the lipid bilayer of EVs and has been shown to be expressed on the outer surface of cancer-related EVs. The ^{new}ExoChip achieved 90% capture efficiency of cancer-related EVs with the affinity-captured EVs released by Ca^{2+} chelation.

A graphene oxide/polydopamine (GO/PDA) nano-interface was used to increase the EV capturing surface area (Figure 1.6b).[132] Similar to sandwich ELISAs, the capture antibody targeting CD81 and detection antibodies targeting CD81, CD63, and EpCAM were used to characterize the EVs and remove interferences in the plasma sample. The GO-induced PDA formed a 3D nano-matrix environment. The assay provided a detection limit of 10^6 particles/mL. Compared to the direct surface modification of GO or PDA only, the GO/PDA nano-matrix increased antibody capture efficiency of EVs by ~2-fold.

An approach was reported using multiscale integration by designed self-assembly (MINDS) 3D nanostructures as the capture surface for EVs (Figure 1.6c).[138] With MINDS, flow streams can pass through a bumper structure, and a nanostructured herringbone (nano-HB) results in less hydrodynamic resistance and enhanced contact time of the EVs with the capture surface. This strategy offered a limit-of-detection of 10 EVs/μL and a total minimum detectable particle number of 200 per assay. The microfluidic also used affinity selection with EpCAM, CD24, and FRα as the capture targets. For verification of the platform, 20 ovarian cancer patients and 10 non-cancer control plasma samples were processed, and differences were achieved between the two groups in

terms of the number of enriched EVs. The assay also successfully achieved early detection of disease stages by targeting the subpopulation of FRα expressing EVs.

It is difficult to mass-produce PDMS-based microfluidic devices.[144] As an alternative, thermoplastics are attractive because of their ability to be mass-produced and the simple modification protocols that can be employed to change their surface chemistry.[36, 145, 146] A cyclic olefin copolymer (COC) ^{EV}HB-chip was manufactured with micro-injection molding and was designed to isolate tumor-specific EV-RNAs within 3 h.[134] The herringbone structure was compared to a flat channel surface, and the results indicated that the herringbone device captured ~60% more EVs. The device could process a wide range of sample volumes (100 µL to 5 mL) with a limit-of-detection of 100 EVs/µL.

Another group developed a microfluidic device using thermoplastics made via micro-injection molding.[147] A 7-bed EV Microfluidic Affinity Purification (EV-MAP) device contained diamond-shape pillars (Figure 1.6d) with a 10 µm diameter and 10 µm spacing to allow for high throughput processing for enriching EVs via affinity selection (1.5 million pillars per chip). The device was used for diagnosing ischemic stroke patients using mRNA. mRNA expression of CD8+ EVs indicated that for genes upregulated during an ischemic stroke event, the EV-MAP device was successful in enriching EVs from clinical plasma samples, and gene profiling the EVs via droplet digital PCR for identifying stroke patients with a total processing assay time of 220 min. When the EVs were isolated using PEG precipitation, which isolates the entire EV population, mRNA expression differences for stroke patients were not observed.

1.7.2. Filtration and centrifugal enrichment

With the design flexibility of microfluidic devices, filtration can also be used as an EV isolation method. An Exodisc was reported using a combination of centrifugal forces and nano-filtration (Figure 1.6e).[38] With a centrifugal force limit of 500g, EV sizes of 20 – 600 nm could be collected between two nano-filters. Filter I (600 nm pore size) was used to remove large particles, and Filter II (20 nm pore size) was used to enrich the EVs and exclude free proteins. The entire EV population was collected in 30 min, with a recovery of 95%. Another platform with a combination of centrifugal force and filters was reported for inline EV detection by flow cytometry.[135] The EVs were isolated by anti-CD81 antibodies, and with affinity microbead incubation, the enriched EVs could be concentrated and reconstituted and stained with a fluorescent dye. A 532 nm laser was used to detect the fluorescent signal to provide event frequency to profile the EVs' concentration.

1.7.3. Contactless and label-free EV enrichment methods

Researchers have also focused on contactless methods for EV enrichment, which consists of using either fluid dynamics in a microchannel and/or microstructures in the channel to affect the EV enrichment process. A microfluidic viscoelastic flow was developed for size-dependent and label-free isolation of EVs.[136] Poly(oxyethylene), PEO, was added into a sheath fluid at a concentration of 0.1%, which maintained the feed solution at a particular viscosity. The particles were driven by an elastic force that situated particles in certain flow lines based on the size of the particle; larger particles traveled more towards the center of the channel. With the application of viscoelastic isolation, the platform could handle samples as small as 100 μL. The authors were able to demonstrate small EV recovery of ~80%, and a purity >90%.

The microfluidic viscoelastic flow was also developed using an acousto-fluidic device for label-free and contactless EV isolation.[137] The platform included two unique surface acoustic wave (SWA) modules that were operated at 19.6 MHz for cell isolation and 39.4 MHz for EV isolation. The acoustic isolation was based on size because of the deflection caused by the acoustic pressure, and the drag force proportional to the size of the particles. The cell removal rate by the first module was >99.999%, which resulted in 75% to 90% reduction of red blood cells. Using the modules in series, the isolation of 110 nm particles from whole blood yielded >99% recovery, and the purity of the small EVs reached ~98.4%.

1.8. Methods for EV detection

Following isolation/enrichment of EVs, the EVs must be enumerated and/or their molecular content analyzed. Currently, most analytical methods rely on protein or nucleic acid analysis of EVs, such as western blotting, ELISA, RT-qPCR and so on. However, these methods rely on the disassembly of the EV to detect the presence of EVs using their intra-vesicular content. This means that EVs need to be extracted from biological samples first and have a relatively high level of purity. The properties and parameters of the EV sample must be known in advance before performing any of these molecular analysis methods. For example, to perform mRNA analysis, in spite of the exponential amplification of the cDNA following reverse transcription, a certain mass must be secured to see a detectable signal. This is complicated by the fact that most EVs do not contain full-length transcripts, and as such, the polyadenylated tail used for priming for the reverse transcription step may not be present and the yield of cDNA is low. Therefore, it is necessary to conduct steps to understand the population properties of the enriched EV fractions.

A challenge with EV direct analysis includes the diverse size range of the vesicles (30 – 1000 nm), their low mass loads (for a 150 nm diameter vesicle, may contain ~10,000 nucleotides of nucleic acids, and 10 – 100 single protein molecules), and their relatively high particle numbers. As opposed to biological cells, which are 1-100 μm in diameter, special types of techniques must be used to characterize and count the vesicles due to their small size. For example, while conventional flow cytometry can be used for biological cells, variants of flow cytometry must be used for enumerating EVs. In addition, while conventional Coulter counters can be used to enumerate biological cells, nano-Coulter counters must be used to enumerate EVs.

Current methods that can directly analyze EVs from a physical perspective includes: (1) size and concentration analysis (Nanoparticle tracking analysis (NTA), resistive pulse sensing (RPS), which can provide information on the size distribution of EVs and estimate concentrations; (2) surface protein expression analysis of EVs, which can determine the type and amount of protein expression by labeling with specific antibodies and fluorescent reporters that can permit the use of nano-flow cytometry; and (3) electron imaging of EVs. Direct imaging techniques include Transmission electron microscopy (TEM), Scanning electron microscopy (SEM), and atomic force microscopy (AFM), are used to visualize the overall structure of EVs as well as their size. In the sections that follow, a discussion of NTA, electron microscopy, nano-flow cytometry, and RPS will be provided.

1.8.1. Nanoparticle tracking analysis

NTA is a commonly used method for size determinations and concentration analysis of EVs.[148-150] Both dynamic light scattering and Brownian motion are the essential processes that are used to analyze the size and concentration of particles using NTA. Figure 1.7 shows the principle

of the NTA measurement.[151] A laser beam illuminates through the sample cell and the scattered laser beam can travel through the objective of the microscope and analyzed by a CCD camera. The Brownian motion of each particle can be recorded and analyzed by the Stokes-Einstein equation Figure 1.7a, where Dt is the diffusion coefficient and calculated by the mean-squared of particle movement path , K_B is the Boltzmann's constant, T is the temperature, η is the solvent viscosity, and d_h is the particle diameter. From this equation, the particle diameter d_h can be calculated if the solvent viscosity and temperature are known. In addition, by analyzing the particle presenting frequency in each of the CCD image frames, the concentration information can also be collected.

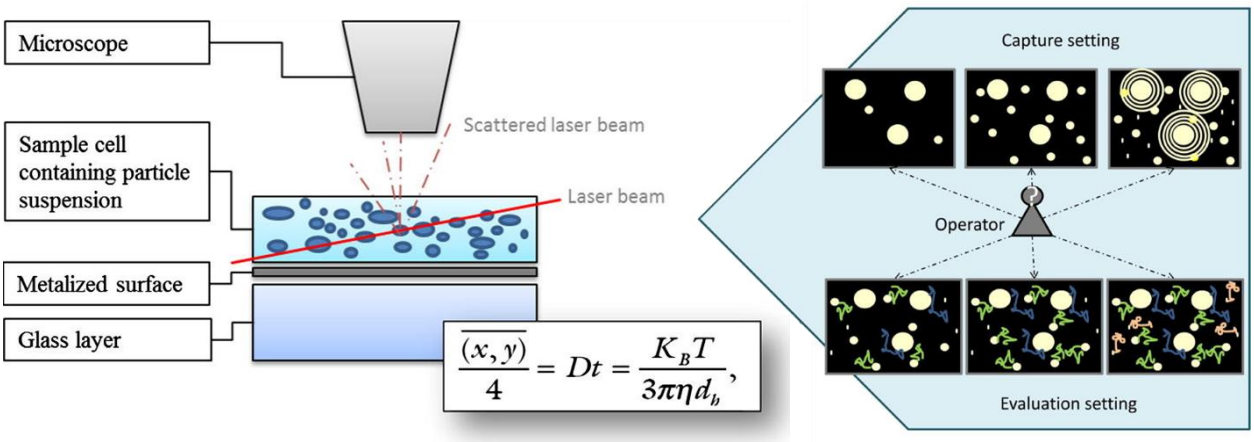

Figure 1.7. The principle of NTA measurement and the Stokes-Einstein equation for the analysis of particle size (Reproduced from reference 152).

Considering the calculation is based on particle diffusion, NTA is typically used to analyze small particles with a size between 10 and 1000 nm in diameter. NTA performance for monodispersed and polydispersed homogeneous particles has been confirmed in previously published research, while the performance for non-homogeneous particles, such as EVs or biological vesicles, is still under development.[152]

In past studies, researchers have found that the introduction of a variety of parameters can increase the variability of results by up to 50%, including the threshold setting of the camera, the source of the EV sample, small vibrations, and even the method of operation.[149, 150, 153] Some researchers state that sample dilution, camera grade, version of the analysis software, and the sample's size distribution should also be considered for an accurate EV size and concentration determination, and all the parameters listed above should be reported.[149, 151, 152] A study encompasses the detection and analysis of EV samples, microvesicle samples, artificial vesicle samples, polystyrene latex beads, and silica microspheres with NTA (Figure 1.8).[149] Because NTA has shown accurate analysis for homogeneous particles, for the artificial vesicles and polystyrene beads the size variation and concentration is no more than 3% and 9%, respectively. However, it was demonstrated that for the same assay, the differences in size of the EVs in the sample ranged from 1% to 6%, and the difference in concentration varied from 5% to 18%. NTA also has some other drawbacks, such as a large sample size requirement (>250 µL), limited dynamic range (10^6 -10^9 particles/mL), only low viscosity samples can be analyzed, and a vibration-free environment.

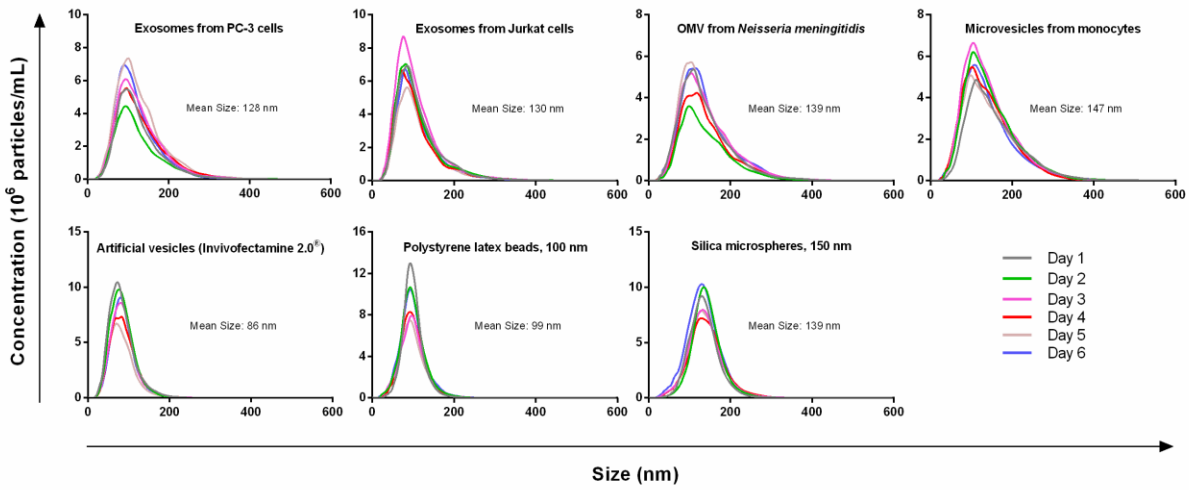

Figure 1.8. Concentration variations for different types of samples, including small EVs from PC-3 cell culture media, EVs from Jurkat cell culture media, Outer membrane vesicle from *Neisseria meningitidis*, microvesicles from monocytes, article vesicles, polystyrene latex beads (100nm),

and silica microspheres (150 nm). The samples were tested on 6 different days, and the variation is from 1% to 18% (Reproduced from reference 150).

1.8.2. Electron and Atomic force microscopies

Electron microscopy is used to image nanoscale samples, including EVs. In some cases, a perception bias may be introduced with imaging location selection, and it is also challenging to get an overall population estimation when the imaging areas are manually selected. However, electron microscopy, which includes TEM and SEM, is still a primary option when the morphology of EVs need to be determined. Both electron microscopies use a beam of electrons to impact the sample, while the TEM produces images using electrons transmitted through the sample, while SEM analyzes scattered electrons. The TEM is most often used to collect information from the internal structure of the EV, while SEM can be used to interrogate surface structure. The resolution of both TEM and SEM can be as small as 1 nm while imaging a biological sample.[154] However, while imaging EVs, the high-resolution advantage of TEM can be circumvented by sample preparation. The EV sample needs to be fixed and dehydrate before imaging. Unlike the cells with the cytoskeleton, EVs do not have an internal supporting structure. When the EV samples is dehydrated, the vesicle can form a cup-shape with lose of original morphology (Figure 1.9a, c).[52, 138, 155, 156] Several studies have shown that EVs have a sphere-shaped morphology (Figure 1.9b).[157] Other papers have reported that EVs in SEM still show a cup-shaped morphology because the EV samples also undergo the same fixation and dehydration process (Figure 1.9c). To overcome the sample deformation, cryo-TEM is included in EV imaging. Since the sample can be enclosed in vitreous ice at the temperature of liquid nitrogen, the sample fixing and dehydration is not necessary anymore. Instead, a small drop (~3 μL) of the sample needs to be frozen in liquid ethane to -180°C rapidly in order to avoid the formation of ice crystals.[158, 159]

Atomic force microscopy (AFM) can record surface structure using a probe and laser reflection. A cantilever (*i.e.*, the probe) can deform while it interacts with the surface of the sample, and the deformation can be recorded by the laser reflection with position-sensitive detectors. The AFM can obtain a true 3-D image of the surface structure and is commonly used for surface topology determinations of nanostructures (Figure 1.9d).[160] The AFM requires the sample to attach to a flat surface before imaging. However, because EVs do not have an internal supporting structure, the vesicles tend to deform during sample preparation and imaging due to direct forces. Therefore, for EV samples, probe scans and monoclonal antibody immobilization are usually combined for better imaging quality.[161, 162] The captured EVs can also provide quantitative information of the sample, and it is possible to obtain better resolution than TEM or SEM.[163]

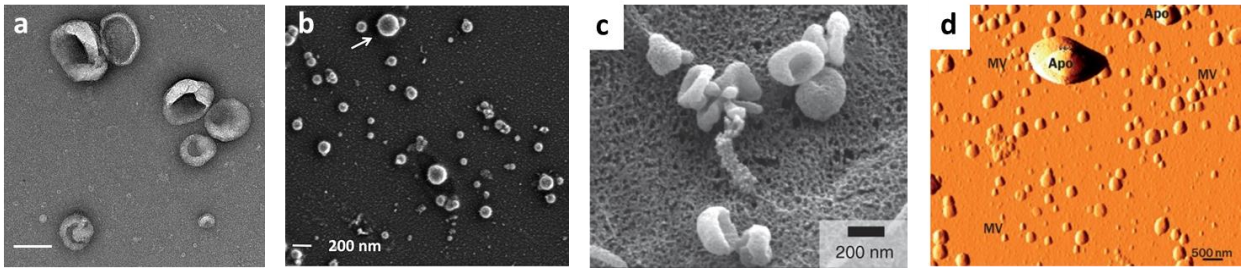

Figure 1.9. a) Transmission electron microscopy image for EVs (scale bar 100 nm). **b)** Scanning electron microscope image for EVs with reports of circle shape of EVs (Reproduced from reference 158). **c)** Scanning electron microscope image for EVs with reports of cup-shape of EVs (Reproduced from reference 157). **d)** Atomic force microscope image for EVs (Reproduced from reference 161).

1.8.3. High-resolution flow cytometry

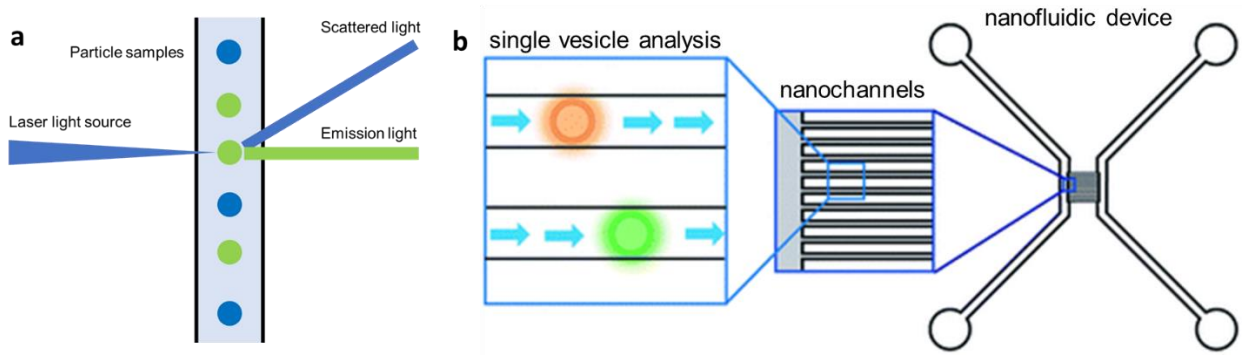

Figure 1.10. a) The principle of flow cytometry. **b)** A flow cytometry platform designed by Friedrich *et al*. The nanofluidic device contains about 100 nanochannels with a width of 300 nm, and the dye-labeled EV can be sensed and recorded by the fluorescent microscope (Reproduced from reference 172).

Flow cytometry (FC) is frequently used for cell analysis, providing the quantity of markers on the surface and internally to the cells. Typically, FC is used to analyze particles with a size >300 nm. As Figure 1.10 shows, FC uses a laser beam with a specific wavelength, which impinges on a sample stream consisting of single particles arranged in a single file line generated by sheath flow. The particles in the stream can scatter light from which critical information can be secured. For example, the scattered light can be analyzed for particle size. Another functional mode of FC is fluorescent readout, which is typically produced by labeling certain cellular organelles or molecules with fluorescent labels. While the specific biomarker is dye-labeled, FC is able to collect information that includes the expression level of the marker. For example, FC can be used to analyze the cytotoxic T-lymphocyte (CTL) related immune response by labeling CD8 expressing cells.

In recent years, FC has also been applied for quantitative analysis of EVs. However, FC has a sensitivity limitation when it is applied to particles with a size smaller than 200 nm.[164-166] To overcome this drawback, the EV membrane is usually over labeled with a lipophilic dye, such as

PKH26 or PKH74 to increase signal intensity.[167, 168] The EV can also be analyzed indirectly when an adapter is applied.[169, 170] The adapter typically carries a sufficient amount of fluorescent molecules to enable detection. Instead of directly sensing the EV, the well-calibrated adapter can provide higher intensity readouts by the FC. Friedrich *et al.* developed a nanofluidic device to analyze EVs using FC (Figure 1.10b).[171] In this case, the sensing component consisted of a fluorescence microscope, and a nanofluidic channel was used as the flow tube. The device contained ~100 nanochannels with a size of 300 nm (W) × 300 nm (D) . Each of the nanochannels served as an individual FC sheath flow sampling unit and only 20 μL of sample was necessary for a typical measurement. The dynamic range of the nanofluidic device was from 10^{10} particles/mL to 10^{14} particles/mL. However, with this FC principle, only concentration information of the EV sample was provided and will need highly specific pre-isolation before sample readout.[166, 172]

1.8.4. Resistive pulse sensing (RPS).

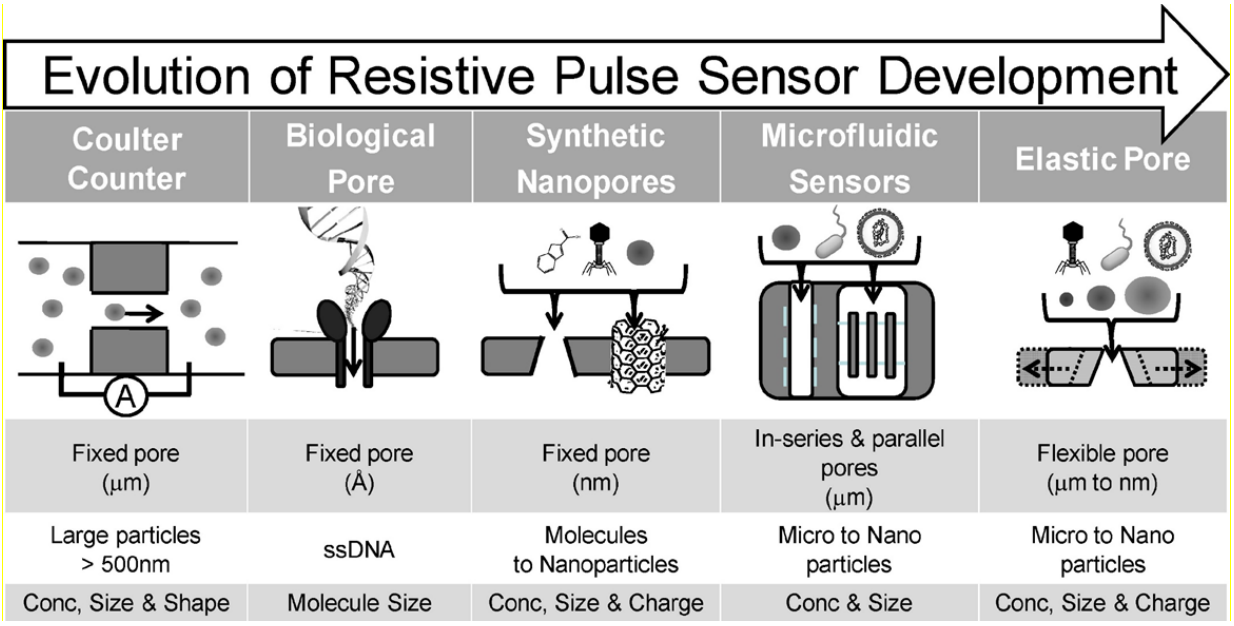

Figure 1.11. The evolution of resistive pulse sensor (RPS), from fixed pore with micro-scale to flexible pore with micro to nano-scale. For now, RPS is also applicable as a coulter counter for EV analysis (Reproduced from reference 181).

RPS was first developed in 1976 for viral particle detection and characterization.[173, 174] In 1996, Kasianowicz *et al.* utilized the biological nanopore as a Coulter counter of single-stranded DNA,[175] and soon the RPS principle was applied to DNA sequencing due to different signal shapes of the four canonical DNA bases.[176, 177] In recent years, due to the development of material science, the RPS with flexible pore size and shape was established, which stretched in size from nm to μm, and the pore has been used for EV concentration determinations and size variation analysis as well (Figure 1.11).[153, 178]

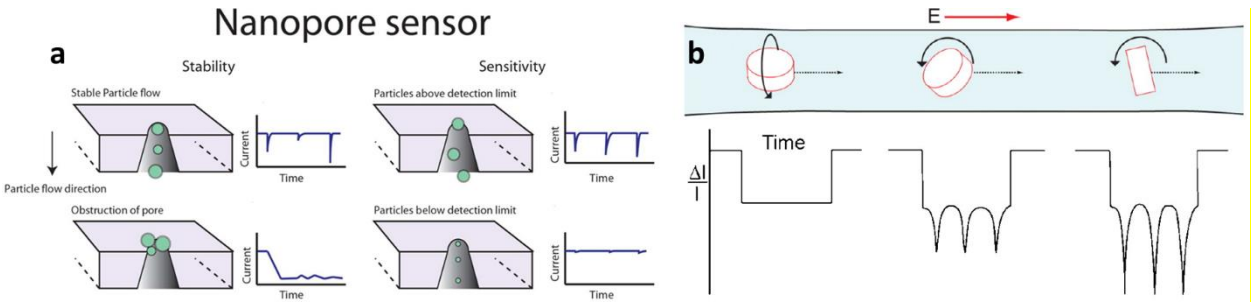

Figure 1.12. a) The principle of the RPS, that a constant potential or current clamping across the nanopore. The amplitude profile is showing a relationship with the particle sizes. The particle size distribution and concentration information can be collected by analyzing the amplitude, and the events show up frequency can be analyzed for concentration information (Reproduced from reference 180). **b)** The RPS is also used to study the particle shape, movement, and interaction with the solvent. The event can express the particle shape and also the rotation level and axis (Reproduced from reference 193).

Equation 1.1. $$\Delta E = \frac{E d^3 \left[1 - 0.8(d/D)^3\right]^{-1}}{LD^2(1 + 4\rho/D\rho_s)(1 + \alpha)} \longrightarrow \Delta E = \frac{d^3}{\left[1 - 0.8(d/D)^3\right]} \cdot Constant$$

The RPS principles requires an output, which can either be a change in potential or current measured across the nanopore structure. Whenever a particle moves through the nanopore, a proportion of the carrier electrolytes is replaced, which creates a change in the resistivity across the pore (Figure 1.12a).[179] The change in voltage across the pore can be described using Equation 1.1, where ΔE is the voltage change between the occupied and unoccupied pore, E is the applied

potential, ρ_s is the pore surface resistivity, α is the pore resistance to load resistance, L is the effective length of the nanopore, d is the particle diameter, D is the pore diameter, and ρ is the fluid resistivity.[173, 174] For most of the cases, the majority of the parameters remain constant when a rigid pore and homogeneous electrolytes are considered, and the only variables left are the particle diameter and amplitude. Thus, the size profiles of the particles in the sample can be understood by analyzing the amplitude of the electrical event. In addition, with a known flow rate and event number, the concentration of the particles in the sample can be obtained as well. Equation 1.1 is primarily applicable to non-conductive particles because additional parameters must be considered for conductive particles, including surface charge, particle charge density, and permeability coefficient.[174, 180] In addition, for permeable biological vesicles, the particle resistivity may be lower than the carrier electrolyte due to the internal composition of the particle. As a result, some particles can produce the opposite polarity of the signal compared to non-conductive particles.[180-182]

Most synthetic RPS are fabricated in micro/nanofluidic devices, which generate the possibility of unique measurement opportunities compared to naturally occurring (*i.e.*, biological) nanopores, such as nanopore shape and nanopores in-series or in parallel. The nanopore in-series can provide additional information about particle movement and generate the zeta potential of the particle. When the nanopore in-series is used for monodispersed samples, the system can provide precise flow rate feedback, which can help to control the stream flow in real-time.[183] When the nanopore in-series is used for polydisperse samples with a known flow rate, particles with different charge densities can provide different event duration. The pore in-series can also be applied to DNA sequencing because each of the nucleotides shows a characteristic time-of-flight (ToF).[184, 185] Nanopore in-parallel is another design strategy for RPS to increase sampling efficiency and

throughput. Typically, the nanopores will be set up in parallel with individual electrodes, and each nanopore will provide information simultaneously from the output circuit.[186-188] It is also feasible to couple the RPS with an EV isolation microfluidic chip that can be used to analyze the EV sample on-chip negating the need for off-loading the enriched EVs for analysis by NTA for example. With real-time electrical signal readout, RPS can provide EV sample information during the isolation/elution phases of the assay.[179, 182]

Compared to optical sensing methods for EV quantification, such as NTA or flow cytometry, RPS can overcome some of their inherent drawbacks. For example, RPS can provide a faster sampling rate, up to 1000× higher.[149, 179, 189] For optical sensing, the exposure time has to be optimized to the millisecond or second scale, which can make the sampling frequency reach to 1000 per second. Based on the equation showed in Figure 1.7, the higher frames rate can provide a better estimate of diffusion coefficient for size analysis, but for NTA, while achieving enough intensity for imaging, the limitation of frames rate can reduce the instrument's reliability.[149, 151] However, the electrical signal recording for RPS can typically be set to 500 kHz.[190] The high sampling frequency can gather more information about particle movement, which can be used for precision flow control and high-resolution signal output. In addition, the broad range of sampling frequencies can used for a broad range of sample concentrations, from 10^5 to 10^{14} particles/mL.[180, 190, 191] RPS is also used to collect information about particle shape and movement profile. Figure 1.12b shows a particle shape and movement signal trace demonstration that includes a disc-shaped particle translocation with different levels and axis of rotation.[180, 192] The size, movability, and interaction between particle and electrolyte can be understood with the analysis of the events.

RPS also has limitations for the detection of nano-scale particles. First of all, because of the nanostructure, the sampling efficiency and detection speed can be confined, and the majority

of RPS platforms can process samples only in the nanoliter to picolitre-scale.[180, 193] The nanopore in-parallel does make it possible to overcome this limitation, which can linearly increase the processed sample volume based on the number of pores in parallel.[180, 194] On the other hand, increasing the translocation speed or decreasing the sampling frequency and bandwidth can decrease the measurement sensitivity. Uram *et al.* used submicrometer pores and nanopore to test the bandwidth and claimed that, by reducing the sampling frequency from 40 kHz to 1 kHz, the current amplitude was reduced by 50% (Figure 1.13a).[195] However, it does not mean that a higher bandwidth is always better. Parkin *et al.* in 2018 noted that part of the noise is from thermal current noise and high-frequency capacitive noise, and increasing the bandwidth will increase the noise level but has no effect on signal amplitudes (Figure 1.13b).[196] In addition, Rosenstein *et al.* tested the signal-to-noise ratio (SNR) with a complementary metal-oxide semiconductor (CMOS)-integrated nanopore (Figure 1.13c-e).[190] The results indicated that increasing the bandwidth can increase the peak-to-peak noise and further reduce the SNR for the measurement.

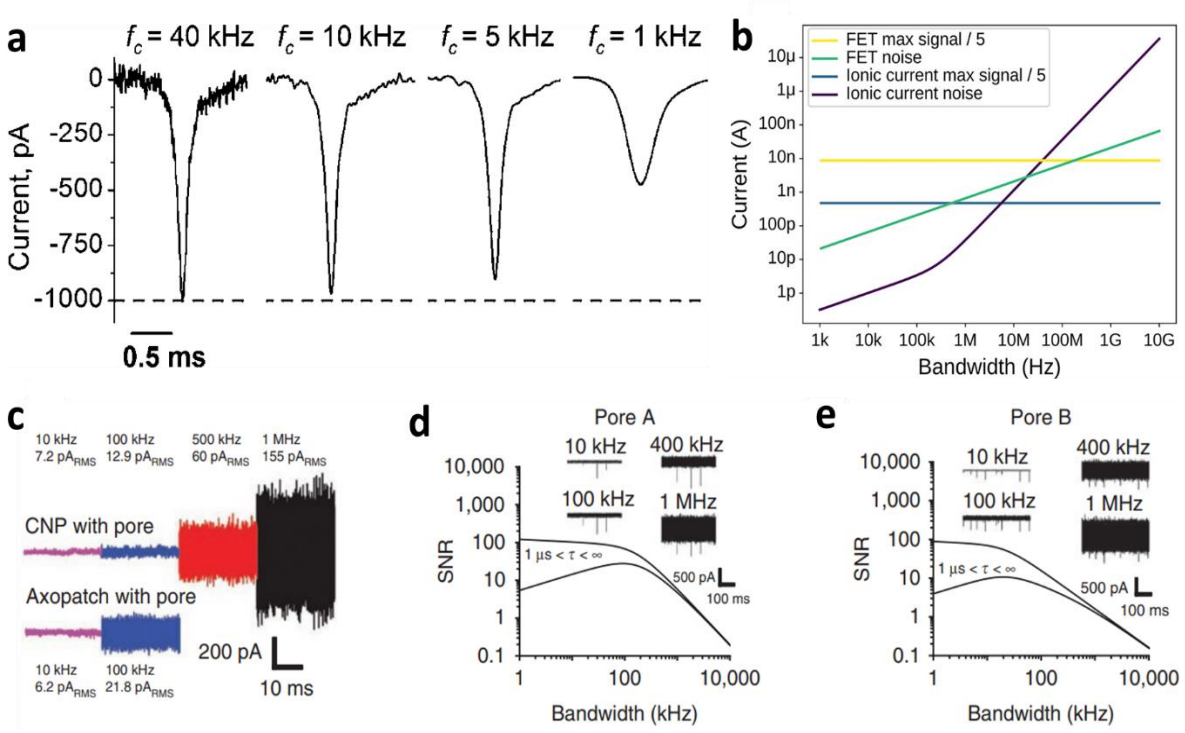

Figure 1.13. a) The amplitude was reduced to about 50% while the sampling frequency reduced from 40 kHz to 1 kHz (Reproduced from reference 196). **b)** Signal-to-noise ratio was studied with the field-effect transistor (FET-nanopore). When the thermal noise and high frequency capacitive noise dominate the noise level, increasing the bandwidth could increase the noise level as well while the signal level unaffected (Reproduced from reference 197). **c-e)** With the study of CMOS-integrated nanopore platform (CNP) and Axopatch platform, both of the systems showed a higher noise level with the increasing of bandwidth while the signal level unaffected (Reproduced from reference 191).

1.9. Conclusions

As liquid biopsies have become one of the primary methods for disease detection, EVs have undoubtedly become an important target due to the biological and physical properties.[197-200] EVs are rich in proteins, RNAs that are associated with host cells, and these markers have been shown to be useful for screening patients and as well as better management of disease progression.[35, 201, 202] On the other hand, as biomaterials and particles secreted by the host cells, EVs have an excellent biocompatibility level and can easily pass through a series of biological barriers and travel through the circulating system to their intended location.[23, 117, 203, 204] This property allows EVs to be used as vehicles for drug delivery. EVs have also been studied as biomarkers for many non-cancer diseases, including the central nervous system,[100] liver (liver damage in-viral hepatitis, hepatocyte injury in alcoholic, drug-induced, and inflammatory liver diseases),[101] kidney (intrinsic kidney disease),[102] brain (stroke),[103] lung (asthma),[104] arteries (atherosclerosis),[105] and radiation injury.[39] In any case, EV isolation/enrichment and quantification have become an important topic for both disease diagnosis and therapeutic purposes.

However, the challenge is that EVs must be enriched or isolated from a clinical sample prior to analysis of their molecular content and current methods for EV isolation are sometime inefficient, because they require a large volume of sample (UC) or alter the overall structure of the EV (filtration or precipitation).[112, 114, 123, 129] In addition, most traditional methods of EV isolation

enrich the entire EV population consisting of both diseased and non-diseased EVs that can complicate the molecular analysis phase of the assay.

In some protein or nucleic acid assays for EVs (e.g., ELISA, PCR), high purity of the downstream sample is often required.[205-207] By applying micro/nanofluidic technology, the high throughput and precision control with immunoassay can secure a higher purity comparing to conventional method, but most of the platform is only capable of μL-scale of sample feed. Some microfluidic platforms using label-free or contactless technologies can compensate for this shortfall of total process volume but at the expense of sample purity.[136, 137, 208]

On the other hand, the analysis of the entire EV population, including concentration, size distribution, and morphology, is still based on electron microscopy, AFM, FC or NTA.[32, 149] Recently, RPS has also been used for EV detection by the ability of size and concentration analysis for nanoparticles.[164, 209] The RPS model for nonconductive particles was well-established, and it is developing fast for EV enumeration with the involvement of the surface charged and conductive intra-vesicle content.[180] Thus, most of the microfluidic platforms are more suitable for the detection and monitoring of clinical samples in small scales. However, with more and more investment in microfluidics research, large-scale production and sample processing capacity are foreseeable.

1.10. References

(1). Macias, M.; Alegre, E.; Diaz-Lagares, A.; Patino, A.; Perez-Gracia, J. L.; Sanmamed, M.; Lopez-Lopez, R.; Varo, N.; Gonzalez, A., Liquid Biopsy: From Basic Research to Clinical Practice. *Adv Clin Chem* **2018,** *83*, 73-119.

(2). Jeffrey, S. S.; Toner, M., Liquid biopsy: a perspective for probing blood for cancer. *Lab Chip* **2019,** *19* (4), 548-549.

(3). Tkach, M.; Thery, C., Communication by Extracellular Vesicles: Where We Are and Where We Need to Go. *Cell* **2016,** *164* (6), 1226-1232.

(4). Zaborowski, M. P.; Balaj, L.; Breakefield, X. O.; Lai, C. P., Extracellular Vesicles: Composition, Biological Relevance, and Methods of Study. *Bioscience* **2015,** *65* (8), 783-797.

(5). Raposo, G.; Stoorvogel, W., Extracellular vesicles: exosomes, microvesicles, and friends. *J Cell Biol* **2013,** *200* (4), 373-83.

(6). Wei, Z.; Batagov, A. O.; Schinelli, S.; Wang, J.; Wang, Y.; El Fatimy, R.; Rabinovsky, R.; Balaj, L.; Chen, C. C.; Hochberg, F.; Carter, B.; Breakefield, X. O.; Krichevsky, A. M., Coding and noncoding landscape of extracellular RNA released by human glioma stem cells. *Nat Commun* **2017,** *8* (1), 1145.

(7). He, M.; Zeng, Y., Microfluidic Exosome Analysis toward Liquid Biopsy for Cancer. *J Lab Autom* **2016,** *21* (4), 599-608.

(8). Barile, L.; Vassalli, G., Exosomes: Therapy delivery tools and biomarkers of diseases. *Pharmacol Ther* **2017,** *174*, 63-78.

(9). Robbins, P. D.; Morelli, A. E., Regulation of immune responses by extracellular vesicles. *Nat Rev Immunol* **2014,** *14* (3), 195-208.

(10). Fuhrmann, G.; Herrmann, I. K.; Stevens, M. M., Cell-derived vesicles for drug therapy and diagnostics: opportunities and challenges. *Nano Today* **2015,** *10* (3), 397-409.

(11). Gehrmann, U.; Naslund, T. I.; Hiltbrunner, S.; Larssen, P.; Gabrielsson, S., Harnessing the exosome-induced immune response for cancer immunotherapy. *Semin Cancer Biol* **2014,** *28*, 58-67.

(12). Tang, X. J.; Sun, X. Y.; Huang, K. M.; Zhang, L.; Yang, Z. S.; Zou, D. D.; Wang, B.; Warnock, G. L.; Dai, L. J.; Luo, J., Therapeutic potential of CAR-T cell-derived exosomes: a cell-free modality for targeted cancer therapy. *Oncotarget* **2015,** *6* (42), 44179-90.

(13). Gyorgy, B.; Szabo, T. G.; Pasztoi, M.; Pal, Z.; Misjak, P.; Aradi, B.; Laszlo, V.; Pallinger, E.; Pap, E.; Kittel, A.; Nagy, G.; Falus, A.; Buzas, E. I., Membrane vesicles, current state-of-the-art: emerging role of extracellular vesicles. *Cell Mol Life Sci* **2011,** *68* (16), 2667-88.

(14). Revenfeld, A. L.; Baek, R.; Nielsen, M. H.; Stensballe, A.; Varming, K.; Jorgensen, M., Diagnostic and prognostic potential of extracellular vesicles in peripheral blood. *Clin Ther* **2014,** *36* (6), 830-46.

(15). Smalley, D. M.; Sheman, N. E.; Nelson, K.; Theodorescu, D., Isolation and identification of potential urinary microparticle biomarkers of bladder cancer. *J Proteome Res* **2008,** *7* (5), 2088-96.

(16). Raposo, G.; Stoorvogel, W., Extracellular vesicles: Exosomes, microvesicles, and friends. *J Cell Biol* **2013,** *200* (4), 373-383.

(17). Giusti, I.; D'Ascenzo, S.; Millimaggi, D.; Taraboletti, G.; Carta, G.; Franceschini, N.; Pavan, A.; Dolo, V., Cathepsin B mediates the pH-dependent proinvasive activity of tumor-shed microvesicles. *Neoplasia* **2008,** *10* (5), 481-8.

(18). Antonyak, M. A.; Li, B.; Boroughs, L. K.; Johnson, J. L.; Druso, J. E.; Bryant, K. L.; Holowka, D. A.; Cerione, R. A., Cancer cell-derived microvesicles induce transformation by transferring tissue transglutaminase and fibronectin to recipient cells. *Proc Natl Acad Sci U S A* **2011,** *108* (12), 4852-7.

(19). Momen-Heravi, F.; Balaj, L.; Alian, S.; Mantel, P. Y.; Halleck, A. E.; Trachtenberg, A. J.; Soria, C. E.; Oquin, S.; Bonebreak, C. M.; Saracoglu, E.; Skog, J.; Kuo, W. P., Current methods for the isolation of extracellular vesicles. *Biol Chem* **2013,** *394* (10), 1253-1262.

(20). Harding, C.; Stahl, P., Transferrin recycling in reticulocytes: pH and iron are important determinants of ligand binding and processing. *Biochem Biophys Res Commun* **1983,** *113* (2), 650-8.

(21). Pan, B. T.; Johnstone, R. M., Fate of the transferrin receptor during maturation of sheep reticulocytes in vitro: selective externalization of the receptor. *Cell* **1983,** *33* (3), 967-78.

(22). Stickney, Z.; Losacco, J.; McDevitt, S.; Zhang, Z.; Lu, B., Development of exosome surface display technology in living human cells. *Biochem Biophys Res Commun* **2016,** *472* (1), 53-9.

(23). Zhu, Q.; Heon, M.; Zhao, Z.; He, M., Microfluidic engineering of exosomes: editing cellular messages for precision therapeutics. *Lab Chip* **2018,** *18* (12), 1690-1703.

(24). Thery, C.; Zitvogel, L.; Amigorena, S., Exosomes: composition, biogenesis and function. *Nat Rev Immunol* **2002,** *2* (8), 569-79.

(25). Kalluri, R.; LeBleu, V. S., The biology, function, and biomedical applications of exosomes. *Science* **2020,** *367* (6478).

(26). Willms, E.; Johansson, H. J.; Mager, I.; Lee, Y.; Blomberg, K. E.; Sadik, M.; Alaarg, A.; Smith, C. I.; Lehtio, J.; El Andaloussi, S.; Wood, M. J.; Vader, P., Cells release subpopulations of exosomes with distinct molecular and biological properties. *Sci Rep* **2016,** *6*, 22519.

(27). Aliotta, J. M., Tumor exosomes: a novel biomarker? *J Gastrointest Oncol* **2011,** *2* (4), 203-5.

(28). Al-Nedawi, K.; Meehan, B.; Micallef, J.; Lhotak, V.; May, L.; Guha, A.; Rak, J., Intercellular transfer of the oncogenic receptor EGFRvIII by microvesicles derived from tumour cells. *Nat Cell Biol* **2008,** *10* (5), 619-24.

(29). Valadi, H.; Ekstrom, K.; Bossios, A.; Sjostrand, M.; Lee, J. J.; Lotvall, J. O., Exosome-mediated transfer of mRNAs and microRNAs is a novel mechanism of genetic exchange between cells. *Nat Cell Biol* **2007,** *9* (6), 654-9.

(30). Greening, D. W.; Xu, R.; Ji, H.; Tauro, B. J.; Simpson, R. J., A protocol for exosome isolation and characterization: evaluation of ultracentrifugation, density-gradient separation, and immunoaffinity capture methods. *Methods Mol Biol* **2015,** *1295*, 179-209.

(31). Street, J. M.; Koritzinsky, E. H.; Glispie, D. M.; Yuen, P. S. T., Urine Exosome Isolation and Characterization. *Methods Mol Biol* **2017,** *1641*, 413-423.

(32). Helwa, I.; Cai, J.; Drewry, M. D.; Zimmerman, A.; Dinkins, M. B.; Khaled, M. L.; Seremwe, M.; Dismuke, W. M.; Bieberich, E.; Stamer, W. D.; Hamrick, M. W.; Liu, Y., A Comparative Study of Serum Exosome Isolation Using Differential Ultracentrifugation and Three Commercial Reagents. *Plos One* **2017,** *12* (1), e0170628.

(33). Heinemann, M. L.; Ilmer, M.; Silva, L. P.; Hawke, D. H.; Recio, A.; Vorontsova, M. A.; Alt, E.; Vykoukal, J., Benchtop isolation and characterization of functional exosomes by sequential filtration. *J Chromatogr A* **2014,** *1371*, 125-35.

(34). Zhao, Z.; Yang, Y.; Zeng, Y.; He, M., A microfluidic ExoSearch chip for multiplexed exosome detection towards blood-based ovarian cancer diagnosis. *Lab Chip* **2016,** *16* (3), 489-96.

(35). Li, W.; Li, C.; Zhou, T.; Liu, X.; Liu, X.; Li, X.; Chen, D., Role of exosomal proteins in cancer diagnosis. *Mol Cancer* **2017,** *16* (1), 145.

(36). Jackson, J. M.; Witek, M. A.; Hupert, M. L.; Brady, C.; Pullagurla, S.; Kamande, J.; Aufforth, R. D.; Tignanelli, C. J.; Torphy, R. J.; Yeh, J. J.; Soper, S. A., UV activation of polymeric high aspect ratio microstructures: ramifications in antibody surface loading for circulating tumor cell selection. *Lab on a Chip* **2014,** *14* (1), 106-117.

(37). Harshani Wijerathne, M. A. W., Mateusz L. Hupert, Joshua M. Jackson, Steven A. Soper, Microfluidic Device for EV and T-cell Isolation. **2019**.

(38). Woo, H. K.; Sunkara, V.; Park, J.; Kim, T. H.; Han, J. R.; Kim, C. J.; Choi, H. I.; Kim, Y. K.; Cho, Y. K., Exodisc for Rapid, Size-Selective, and Efficient Isolation and Analysis of Nanoscale Extracellular Vesicles from Biological Samples. *ACS Nano* **2017,** *11* (2), 1360-1370.

(39). Yentrapalli, R.; Merl-Pham, J.; Azimzadeh, O.; Mutschelknaus, L.; Peters, C.; Hauck, S. M.; Atkinson, M. J.; Tapio, S.; Moertl, S., Quantitative changes in the protein and miRNA cargo of plasma exosome-like vesicles after exposure to ionizing radiation. *Int J Radiat Biol* **2017,** *93* (6), 569-580.

(40). Tian, T.; Zhu, Y. L.; Zhou, Y. Y.; Liang, G. F.; Wang, Y. Y.; Hu, F. H.; Xiao, Z. D., Exosome uptake through clathrin-mediated endocytosis and macropinocytosis and mediating miR-21 delivery. *J Biol Chem* **2014,** *289* (32), 22258-67.

(41). Fares, J.; Kashyap, R.; Zimmermann, P., Syntenin: Key player in cancer exosome biogenesis and uptake? *Cell Adh Migr* **2017,** *11* (2), 124-126.

(42). Hessvik, N. P.; Llorente, A., Current knowledge on exosome biogenesis and release. *Cell Mol Life Sci* **2018,** *75* (2), 193-208.

(43). Tian, Y.; Li, S.; Song, J.; Ji, T.; Zhu, M.; Anderson, G. J.; Wei, J.; Nie, G., A doxorubicin delivery platform using engineered natural membrane vesicle exosomes for targeted tumor therapy. *Biomaterials* **2014,** *35* (7), 2383-90.

(44). Nakase, I.; Futaki, S., Combined treatment with a pH-sensitive fusogenic peptide and cationic lipids achieves enhanced cytosolic delivery of exosomes. *Sci Rep* **2015,** *5*, 10112.

(45). Hu, L.; Wickline, S. A.; Hood, J. L., Magnetic resonance imaging of melanoma exosomes in lymph nodes. *Magn Reson Med* **2015,** *74* (1), 266-271.

(46). Wang, J.; Li, W.; Zhang, L.; Ban, L.; Chen, P.; Du, W.; Feng, X.; Liu, B. F., Chemically Edited Exosomes with Dual Ligand Purified by Microfluidic Device for Active Targeted Drug Delivery to Tumor Cells. *ACS Appl Mater Interfaces* **2017,** *9* (33), 27441-27452.

(47). Hood, J. L.; Scott, M. J.; Wickline, S. A., Maximizing exosome colloidal stability following electroporation. *Anal Biochem* **2014,** *448*, 41-9.

(48). Shtam, T. A.; Kovalev, R. A.; Varfolomeeva, E. Y.; Makarov, E. M.; Kil, Y. V.; Filatov, M. V., Exosomes are natural carriers of exogenous siRNA to human cells in vitro. *Cell Commun Signal* **2013,** *11*, 88.

(49). Wahlgren, J.; De, L. K. T.; Brisslert, M.; Vaziri Sani, F.; Telemo, E.; Sunnerhagen, P.; Valadi, H., Plasma exosomes can deliver exogenous short interfering RNA to monocytes and lymphocytes. *Nucleic Acids Res* **2012,** *40* (17), e130.

(50). Besse, B.; Charrier, M.; Lapierre, V.; Dansin, E.; Lantz, O.; Planchard, D.; Le Chevalier, T.; Livartoski, A.; Barlesi, F.; Laplanche, A.; Ploix, S.; Vimond, N.; Peguillet, I.; Thery, C.; Lacroix, L.; Zoernig, I.; Dhodapkar, K.; Dhodapkar, M.; Viaud, S.; Soria, J. C.; Reiners, K. S.; Pogge von Strandmann, E.; Vely, F.; Rusakiewicz, S.; Eggermont, A.; Pitt, J. M.; Zitvogel, L.; Chaput, N., Dendritic cell-derived exosomes as maintenance immunotherapy after first line chemotherapy in NSCLC. *Oncoimmunology* **2016,** *5* (4), e1071008.

(51). Viaud, S.; Ploix, S.; Lapierre, V.; Thery, C.; Commere, P. H.; Tramalloni, D.; Gorrichon, K.; Virault-Rocroy, P.; Tursz, T.; Lantz, O.; Zitvogel, L.; Chaput, N., Updated technology to produce highly immunogenic dendritic cell-derived exosomes of clinical grade: a critical role of interferon-gamma. *J Immunother* **2011,** *34* (1), 65-75.

(52). Zhao, Z.; McGill, J.; Gamero-Kubota, P.; He, M., Microfluidic on-demand engineering of exosomes towards cancer immunotherapy. *Lab Chip* **2019,** *19* (10), 1877-1886.

(53). Hauser, P.; Wang, S.; Didenko, V. V., Apoptotic Bodies: Selective Detection in Extracellular Vesicles. *Methods Mol Biol* **2017,** *1554*, 193-200.

(54). Becker, A.; Thakur, B. K.; Weiss, J. M.; Kim, H. S.; Peinado, H.; Lyden, D., Extracellular Vesicles in Cancer: Cell-to-Cell Mediators of Metastasis. *Cancer Cell* **2016,** *30* (6), 836-848.

(55). Xu, X.; Lai, Y.; Hua, Z. C., Apoptosis and apoptotic body: disease message and therapeutic target potentials. *Biosci Rep* **2019,** *39* (1).

(56). Elmore, S., Apoptosis: a review of programmed cell death. *Toxicol Pathol* **2007,** *35* (4), 495-516.

(57). Fleisher, T. A., Apoptosis. *Ann Allergy Asthma Immunol* **1997,** *78* (3), 245-9; quiz 249-50.

(58). Atkin-Smith, G. K.; Tixeira, R.; Paone, S.; Mathivanan, S.; Collins, C.; Liem, M.; Goodall, K. J.; Ravichandran, K. S.; Hulett, M. D.; Poon, I. K., A novel mechanism of generating extracellular vesicles during apoptosis via a beads-on-a-string membrane structure. *Nat Commun* **2015,** *6*, 7439.

(59). Poon, I. K.; Lucas, C. D.; Rossi, A. G.; Ravichandran, K. S., Apoptotic cell clearance: basic biology and therapeutic potential. *Nat Rev Immunol* **2014,** *14* (3), 166-80.

(60). Elliott, M. R.; Chekeni, F. B.; Trampont, P. C.; Lazarowski, E. R.; Kadl, A.; Walk, S. F.; Park, D.; Woodson, R. I.; Ostankovich, M.; Sharma, P.; Lysiak, J. J.; Harden, T. K.; Leitinger, N.; Ravichandran, K. S., Nucleotides released by apoptotic cells act as a find-me signal to promote phagocytic clearance. *Nature* **2009,** *461* (7261), 282-6.

(61). Truman, L. A.; Ford, C. A.; Pasikowska, M.; Pound, J. D.; Wilkinson, S. J.; Dumitriu, I. E.; Melville, L.; Melrose, L. A.; Ogden, C. A.; Nibbs, R.; Graham, G.; Combadiere, C.; Gregory, C. D., CX3CL1/fractalkine is released from apoptotic lymphocytes to stimulate macrophage chemotaxis. *Blood* **2008,** *112* (13), 5026-36.

(62). Hanayama, R.; Tanaka, M.; Miwa, K.; Shinohara, A.; Iwamatsu, A.; Nagata, S., Identification of a factor that links apoptotic cells to phagocytes. *Nature* **2002,** *417* (6885), 182-7.

(63). Gardai, S. J.; McPhillips, K. A.; Frasch, S. C.; Janssen, W. J.; Starefeldt, A.; Murphy-Ullrich, J. E.; Bratton, D. L.; Oldenborg, P. A.; Michalak, M.; Henson, P. M., Cell-surface calreticulin initiates clearance of viable or apoptotic cells through trans-activation of LRP on the phagocyte. *Cell* **2005,** *123* (2), 321-34.

(64). Witwer, K. W.; Buzas, E. I.; Bemis, L. T.; Bora, A.; Lasser, C.; Lotvall, J.; Nolte-'t Hoen, E. N.; Piper, M. G.; Sivaraman, S.; Skog, J.; Thery, C.; Wauben, M. H.; Hochberg, F., Standardization of sample collection, isolation and analysis methods in extracellular vesicle research. *J Extracell Vesicles* **2013,** *2*.

(65). Tauro, B. J.; Greening, D. W.; Mathias, R. A.; Mathivanan, S.; Ji, H.; Simpson, R. J., Two distinct populations of exosomes are released from LIM1863 colon carcinoma cell-derived organoids. *Mol Cell Proteomics* **2013,** *12* (3), 587-98.

(66). Crescitelli, R.; Lasser, C.; Szabo, T. G.; Kittel, A.; Eldh, M.; Dianzani, I.; Buzas, E. I.; Lotvall, J., Distinct RNA profiles in subpopulations of extracellular vesicles: apoptotic bodies, microvesicles and exosomes. *J Extracell Vesicles* **2013,** *2*.

(67). Dorsam, B.; Reiners, K. S.; von Strandmann, E. P., Cancer-derived extracellular vesicles: friend and foe of tumour immunosurveillance. *Philos Trans R Soc Lond B Biol Sci* **2018,** *373* (1737).

(68). Sehrawat, T. S.; Arab, J. P.; Liu, M.; Amrollahi, P.; Wan, M.; Fan, J.; Nakao, Y.; Pose, E.; Navarro-Corcuera, A.; Dasgupta, D.; Liao, C. Y.; He, L.; Mauer, A. S.; Avitabile, E.; Ventura-Cots, M.; Bataller, R. A.; Sanyal, A. J.; Chalasani, N. P.; Heimbach, J. K.; Watt, K. D.; Gores, G. J.; Gines, P.; Kamath, P. S.; Simonetto, D. A.; Hu, T. Y.; Shah, V. H.; Malhi, H., Circulating extracellular vesicles carrying sphingolipid cargo for the diagnosis and dynamic risk profiling of alcoholic hepatitis. *Hepatology* **2020**.

(69). Choi, D. S.; Lee, J.; Go, G.; Kim, Y. K.; Gho, Y. S., Circulating extracellular vesicles in cancer diagnosis and monitoring: an appraisal of clinical potential. *Mol Diagn Ther* **2013,** *17* (5), 265-71.

(70). Yuan, D.; Zhao, Y.; Banks, W. A.; Bullock, K. M.; Haney, M.; Batrakova, E.; Kabanov, A. V., Macrophage exosomes as natural nanocarriers for protein delivery to inflamed brain. *Biomaterials* **2017,** *142*, 1-12.

(71). Barres, C.; Blanc, L.; Bette-Bobillo, P.; Andre, S.; Mamoun, R.; Gabius, H. J.; Vidal, M., Galectin-5 is bound onto the surface of rat reticulocyte exosomes and modulates vesicle uptake by macrophages. *Blood* **2010,** *115* (3), 696-705.

(72). Lakshminarayan, R.; Wunder, C.; Becken, U.; Howes, M. T.; Benzing, C.; Arumugam, S.; Sales, S.; Ariotti, N.; Chambon, V.; Lamaze, C.; Loew, D.; Shevchenko, A.; Gaus, K.; Parton, R. G.; Johannes, L., Galectin-3 drives glycosphingolipid-dependent biogenesis of clathrin-independent carriers. *Nat Cell Biol* **2014,** *16* (6), 595-606.

(73). Merlin, J.; Stechly, L.; de Beauce, S.; Monte, D.; Leteurtre, E.; van Seuningen, I.; Huet, G.; Pigny, P., Galectin-3 regulates MUC1 and EGFR cellular distribution and EGFR downstream pathways in pancreatic cancer cells. *Oncogene* **2011,** *30* (22), 2514-25.

(74). Kim, K. M.; Abdelmohsen, K.; Mustapic, M.; Kapogiannis, D.; Gorospe, M., RNA in extracellular vesicles. *Wiley Interdiscip Rev RNA* **2017,** *8* (4).

(75). Batagov, A. O.; Kurochkin, I. V., Exosomes secreted by human cells transport largely mRNA fragments that are enriched in the 3'-untranslated regions. *Biol Direct* **2013,** *8*, 12.

(76). Chen, Y. Y.; Lee, M. B.; Chang, C. M.; Liao, S. C., Methods of suicide in different psychiatric diagnostic groups. *J Affect Disord* **2009,** *118* (1-3), 196-200.

(77). Mitsuhashi, M.; Taub, D. D.; Kapogiannis, D.; Eitan, E.; Zukley, L.; Mattson, M. P.; Ferrucci, L.; Schwartz, J. B.; Goetzl, E. J., Aging enhances release of exosomal cytokine mRNAs by Abeta1-42-stimulated macrophages. *FASEB J* **2013,** *27* (12), 5141-50.

(78). Tannous, B. A.; Kim, D. E.; Fernandez, J. L.; Weissleder, R.; Breakefield, X. O., Codon-optimized Gaussia luciferase cDNA for mammalian gene expression in culture and in vivo. *Mol Ther* **2005,** *11* (3), 435-43.

(79). Martellucci, S.; Orefice, N. S.; Angelucci, A.; Luce, A.; Caraglia, M.; Zappavigna, S., Extracellular Vesicles: New Endogenous Shuttles for miRNAs in Cancer Diagnosis and Therapy? *Int J Mol Sci* **2020,** *21* (18).

(80). Vlaeminck-Guillem, V., Extracellular Vesicles in Prostate Cancer Carcinogenesis, Diagnosis, and Management. *Front Oncol* **2018,** *8*, 222.

(81). Huntzinger, E.; Izaurralde, E., Gene silencing by microRNAs: contributions of translational repression and mRNA decay. *Nat Rev Genet* **2011,** *12* (2), 99-110.

(82). Nishida-Aoki, N.; Ochiya, T., Interactions between cancer cells and normal cells via miRNAs in extracellular vesicles. *Cell Mol Life Sci* **2015,** *72* (10), 1849-61.

(83). Mitchell, P. S.; Parkin, R. K.; Kroh, E. M.; Fritz, B. R.; Wyman, S. K.; Pogosova-Agadjanyan, E. L.; Peterson, A.; Noteboom, J.; O'Briant, K. C.; Allen, A.; Lin, D. W.; Urban, N.; Drescher, C. W.; Knudsen, B. S.; Stirewalt, D. L.; Gentleman, R.; Vessella, R. L.; Nelson, P. S.; Martin, D. B.; Tewari, M., Circulating microRNAs as stable blood-based markers for cancer detection. *Proc Natl Acad Sci U S A* **2008,** *105* (30), 10513-8.

(84). Weber, J. A.; Baxter, D. H.; Zhang, S.; Huang, D. Y.; Huang, K. H.; Lee, M. J.; Galas, D. J.; Wang, K., The microRNA spectrum in 12 body fluids. *Clin Chem* **2010,** *56* (11), 1733-41.

(85). Taylor, D. D.; Gercel-Taylor, C., MicroRNA signatures of tumor-derived exosomes as diagnostic biomarkers of ovarian cancer. *Gynecol Oncol* **2008,** *110* (1), 13-21.

(86). Langhe, R.; Norris, L.; Saadeh, F. A.; Blackshields, G.; Varley, R.; Harrison, A.; Gleeson, N.; Spillane, C.; Martin, C.; O'Donnell, D. M.; D'Arcy, T.; O'Leary, J.; O'Toole, S., A novel serum microRNA panel to discriminate benign from malignant ovarian disease. *Cancer Lett* **2015,** *356* (2 Pt B), 628-36.

(87). Jeppesen, D. K.; Hvam, M. L.; Primdahl-Bengtson, B.; Boysen, A. T.; Whitehead, B.; Dyrskjot, L.; Orntoft, T. F.; Howard, K. A.; Ostenfeld, M. S., Comparative analysis of discrete exosome fractions obtained by differential centrifugation. *J Extracell Vesicles* **2014,** *3*, 25011.

(88). Acharya, S. S.; Fendler, W.; Watson, J.; Hamilton, A.; Pan, Y.; Gaudiano, E.; Moskwa, P.; Bhanja, P.; Saha, S.; Guha, C.; Parmar, K.; Chowdhury, D., Serum microRNAs are early indicators of survival after radiation-induced hematopoietic injury. *Sci Transl Med* **2015,** *7* (287), 287ra69.

(89). Tian, J.; Casella, G.; Zhang, Y.; Rostami, A.; Li, X., Potential roles of extracellular vesicles in the pathophysiology, diagnosis, and treatment of autoimmune diseases. *Int J Biol Sci* **2020,** *16* (4), 620-632.

(90). Jiang, W. Y.; Xun, Y. H., [Value of detection of extracellular vesicles in the diagnosis of nonalcoholic fatty liver disease]. *Zhonghua Gan Zang Bing Za Zhi* **2020,** *28* (1), 92-96.

(91). Shaimardanova, A. A.; Solovyeva, V. V.; Chulpanova, D. S.; James, V.; Kitaeva, K. V.; Rizvanov, A. A., Extracellular vesicles in the diagnosis and treatment of central nervous system diseases. *Neural Regen Res* **2020,** *15* (4), 586-596.

(92). Skog, J.; Wurdinger, T.; van Rijn, S.; Meijer, D. H.; Gainche, L.; Sena-Esteves, M.; Curry, W. T., Jr.; Carter, B. S.; Krichevsky, A. M.; Breakefield, X. O., Glioblastoma microvesicles transport RNA and proteins that promote tumour growth and provide diagnostic biomarkers. *Nat Cell Biol* **2008,** *10* (12), 1470-6.

(93). Vlassov, A. V.; Magdaleno, S.; Setterquist, R.; Conrad, R., Exosomes: current knowledge of their composition, biological functions, and diagnostic and therapeutic potentials. *Biochim Biophys Acta* **2012,** *1820* (7), 940-8.

(94). Aziz, N.; Detels, R.; Quint, J. J.; Li, Q.; Gjertson, D.; Butch, A. W., Stability of cytokines, chemokines and soluble activation markers in unprocessed blood stored under different conditions. *Cytokine* **2016,** *84*, 17-24.

(95). Johnsen, K. B.; Gudbergsson, J. M.; Andresen, T. L.; Simonsen, J. B., What is the blood concentration of extracellular vesicles? Implications for the use of extracellular vesicles as blood-borne biomarkers of cancer. *Biochim Biophys Acta Rev Cancer* **2019,** *1871* (1), 109-116.

(96). Ruhen, O.; Meehan, K., Tumor-Derived Extracellular Vesicles as a Novel Source of Protein Biomarkers for Cancer Diagnosis and Monitoring. *Proteomics* **2019,** *19* (1-2), e1800155.

(97). Brenner, A. W.; Su, G. H.; Momen-Heravi, F., Isolation of Extracellular Vesicles for Cancer Diagnosis and Functional Studies. *Methods Mol Biol* **2019,** *1882*, 229-237.

(98). Zhang, Q.; Bansal, A., Role of Extracellular Vesicles in the Diagnosis and Pathogenesis of Barrett's Esophagus: A Mini-Review. *Dig Dis Sci* **2020**.

(99). Rahbarghazi, R.; Jabbari, N.; Sani, N. A.; Asghari, R.; Salimi, L.; Kalashani, S. A.; Feghhi, M.; Etemadi, T.; Akbariazar, E.; Mahmoudi, M.; Rezaie, J., Tumor-derived extracellular

vesicles: reliable tools for Cancer diagnosis and clinical applications. *Cell Commun Signal* **2019,** *17* (1), 73.

(100). Kawikova, I.; Askenase, P. W., Diagnostic and therapeutic potentials of exosomes in CNS diseases. *Brain Res* **2015,** *1617*, 63-71.

(101). Masyuk, A. I.; Masyuk, T. V.; Larusso, N. F., Exosomes in the pathogenesis, diagnostics and therapeutics of liver diseases. *J Hepatol* **2013,** *59* (3), 621-5.

(102). Spanu, S.; van Roeyen, C. R.; Denecke, B.; Floege, J.; Muhlfeld, A. S., Urinary exosomes: a novel means to non-invasively assess changes in renal gene and protein expression. *Plos One* **2014,** *9* (10), e109631.

(103). Couch, Y.; Akbar, N.; Davis, S.; Fischer, R.; Dickens, A. M.; Neuhaus, A. A.; Burgess, A. I.; Rothwell, P. M.; Buchan, A. M., Inflammatory Stroke Extracellular Vesicles Induce Macrophage Activation. *Stroke* **2017,** *48* (8), 2292-2296.

(104). Levanen, B.; Bhakta, N. R.; Torregrosa Paredes, P.; Barbeau, R.; Hiltbrunner, S.; Pollack, J. L.; Skold, C. M.; Svartengren, M.; Grunewald, J.; Gabrielsson, S.; Eklund, A.; Larsson, B. M.; Woodruff, P. G.; Erle, D. J.; Wheelock, A. M., Altered microRNA profiles in bronchoalveolar lavage fluid exosomes in asthmatic patients. *J Allergy Clin Immunol* **2013,** *131* (3), 894-903.

(105). Hoefer, I. E.; Steffens, S.; Ala-Korpela, M.; Back, M.; Badimon, L.; Bochaton-Piallat, M. L.; Boulanger, C. M.; Caligiuri, G.; Dimmeler, S.; Egido, J.; Evans, P. C.; Guzik, T.; Kwak, B. R.; Landmesser, U.; Mayr, M.; Monaco, C.; Pasterkamp, G.; Tunon, J.; Weber, C.; Atherosclerosis, E. S. C. W. G.; Vascular, B., Novel methodologies for biomarker discovery in atherosclerosis. *Eur Heart J* **2015,** *36* (39), 2635-42.

(106). Ren, J.; He, W.; Zheng, L.; Duan, H., From structures to functions: insights into exosomes as promising drug delivery vehicles. *Biomater Sci* **2016,** *4* (6), 910-21.

(107). Tan, A.; De La Pena, H.; Seifalian, A. M., The application of exosomes as a nanoscale cancer vaccine. *Int J Nanomedicine* **2010,** *5*, 889-900.

(108). Das, C. K.; Jena, B. C.; Banerjee, I.; Das, S.; Parekh, A.; Bhutia, S. K.; Mandal, M., Exosome as a Novel Shuttle for Delivery of Therapeutics across Biological Barriers. *Mol Pharm* **2019,** *16* (1), 24-40.

(109). Yamashita, T.; Takahashi, Y.; Takakura, Y., Possibility of Exosome-Based Therapeutics and Challenges in Production of Exosomes Eligible for Therapeutic Application. *Biol Pharm Bull* **2018,** *41* (6), 835-842.

(110). Thery, C.; Amigorena, S.; Raposo, G.; Clayton, A., Isolation and characterization of exosomes from cell culture supernatants and biological fluids. *Curr Protoc Cell Biol* **2006,** *Chapter 3*, Unit 3 22.

(111). Sunkara, V.; Woo, H. K.; Cho, Y. K., Emerging techniques in the isolation and characterization of extracellular vesicles and their roles in cancer diagnostics and prognostics. *Analyst* **2016,** *141* (2), 371-81.

(112). Konoshenko, M. Y.; Lekchnov, E. A.; Vlassov, A. V.; Laktionov, P. P., Isolation of Extracellular Vesicles: General Methodologies and Latest Trends. *Biomed Res Int* **2018,** *2018*, 8545347.

(113). Yoo, Y. K.; Lee, J.; Kim, H.; Hwang, K. S.; Yoon, D. S.; Lee, J. H., Toward Exosome-Based Neuronal Diagnostic Devices. *Micromachines (Basel)* **2018,** *9* (12).

(114). Livshits, M. A.; Khomyakova, E.; Evtushenko, E. G.; Lazarev, V. N.; Kulemin, N. A.; Semina, S. E.; Generozov, E. V.; Govorun, V. M., Isolation of exosomes by differential centrifugation: Theoretical analysis of a commonly used protocol. *Sci Rep* **2015,** *5*, 17319.

(115). Abramowicz, A.; Widlak, P.; Pietrowska, M., Proteomic analysis of exosomal cargo: the challenge of high purity vesicle isolation. *Mol Biosyst* **2016,** *12* (5), 1407-19.

(116). Tauro, B. J.; Greening, D. W.; Mathias, R. A.; Ji, H.; Mathivanan, S.; Scott, A. M.; Simpson, R. J., Comparison of ultracentrifugation, density gradient separation, and immunoaffinity capture methods for isolating human colon cancer cell line LIM1863-derived exosomes. *Methods* **2012,** *56* (2), 293-304.

(117). El-Andaloussi, S.; Lee, Y.; Lakhal-Littleton, S.; Li, J.; Seow, Y.; Gardiner, C.; Alvarez-Erviti, L.; Sargent, I. L.; Wood, M. J., Exosome-mediated delivery of siRNA in vitro and in vivo. *Nat Protoc* **2012,** *7* (12), 2112-26.

(118). Takov, K.; Yellon, D. M.; Davidson, S. M., Comparison of small extracellular vesicles isolated from plasma by ultracentrifugation or size-exclusion chromatography: yield, purity and functional potential. *J Extracell Vesicles* **2019,** *8* (1), 1560809.

(119). Lamparski, H. G.; Metha-Damani, A.; Yao, J. Y.; Patel, S.; Hsu, D. H.; Ruegg, C.; Le Pecq, J. B., Production and characterization of clinical grade exosomes derived from dendritic cells. *J Immunol Methods* **2002,** *270* (2), 211-26.

(120). Li, X.; Corbett, A. L.; Taatizadeh, E.; Tasnim, N.; Little, J. P.; Garnis, C.; Daugaard, M.; Guns, E.; Hoorfar, M.; Li, I. T. S., Challenges and opportunities in exosome research-Perspectives from biology, engineering, and cancer therapy. *APL Bioeng* **2019,** *3* (1), 011503.

(121). Atha, D. H.; Ingham, K. C., Mechanism of precipitation of proteins by polyethylene glycols. Analysis in terms of excluded volume. *J Biol Chem* **1981,** *256* (23), 12108-17.

(122). Andreu, Z.; Rivas, E.; Sanguino-Pascual, A.; Lamana, A.; Marazuela, M.; Gonzalez-Alvaro, I.; Sanchez-Madrid, F.; de la Fuente, H.; Yanez-Mo, M., Comparative analysis of EV isolation procedures for miRNAs detection in serum samples. *J Extracell Vesicles* **2016,** *5*, 31655.

(123). Li, P.; Kaslan, M.; Lee, S. H.; Yao, J.; Gao, Z., Progress in Exosome Isolation Techniques. *Theranostics* **2017,** *7* (3), 789-804.

(124). Salih, M.; Zietse, R.; Hoorn, E. J., Urinary extracellular vesicles and the kidney: biomarkers and beyond. *Am J Physiol Renal Physiol* **2014,** *306* (11), F1251-9.

(125). Taylor, D. D.; Zacharias, W.; Gercel-Taylor, C., Exosome isolation for proteomic analyses and RNA profiling. *Methods Mol Biol* **2011,** *728*, 235-46.

(126). Buschmann, D.; Kirchner, B.; Hermann, S.; Marte, M.; Wurmser, C.; Brandes, F.; Kotschote, S.; Bonin, M.; Steinlein, O. K.; Pfaffl, M. W.; Schelling, G.; Reithmair, M., Evaluation of serum extracellular vesicle isolation methods for profiling miRNAs by next-generation sequencing. *J Extracell Vesicles* **2018,** *7* (1), 1481321.

(127). Ding, M.; Wang, C.; Lu, X.; Zhang, C.; Zhou, Z.; Chen, X.; Zhang, C. Y.; Zen, K.; Zhang, C., Comparison of commercial exosome isolation kits for circulating exosomal microRNA profiling. *Anal Bioanal Chem* **2018,** *410* (16), 3805-3814.

(128). Whiteside, T. L., Tumor-Derived Exosomes and Their Role in Tumor-Induced Immune Suppression. *Vaccines (Basel)* **2016,** *4* (4).

(129). Ayala-Mar, S.; Donoso-Quezada, J.; Gallo-Villanueva, R. C.; Perez-Gonzalez, V. H.; Gonzalez-Valdez, J., Recent advances and challenges in the recovery and purification of cellular exosomes. *Electrophoresis* **2019,** *40* (23-24), 3036-3049.

(130). Serrano-Pertierra, E.; Oliveira-Rodriguez, M.; Rivas, M.; Oliva, P.; Villafani, J.; Navarro, A.; Blanco-Lopez, M. C.; Cernuda-Morollon, E., Characterization of Plasma-Derived Extracellular Vesicles Isolated by Different Methods: A Comparison Study. *Bioengineering (Basel)* **2019,** *6* (1).

(131). Cvjetkovic, A.; Lotvall, J.; Lasser, C., The influence of rotor type and centrifugation time on the yield and purity of extracellular vesicles. *J Extracell Vesicles* **2014,** *3*.

(132). Zhang, P.; He, M.; Zeng, Y., Ultrasensitive microfluidic analysis of circulating exosomes using a nanostructured graphene oxide/polydopamine coating. *Lab Chip* **2016,** *16* (16), 3033-42.

(133). Kanwar, S. S.; Dunlay, C. J.; Simeone, D. M.; Nagrath, S., Microfluidic device (ExoChip) for on-chip isolation, quantification and characterization of circulating exosomes. *Lab Chip* **2014,** *14* (11), 1891-900.

(134). Reátegui, E.; van der Vos, K. E.; Lai, C. P.; Zeinali, M.; Atai, N. A.; Aldikacti, B.; Floyd, F. P., Jr.; A, H. K.; Thapar, V.; Hochberg, F. H.; Sequist, L. V.; Nahed, B. V.; B, S. C.; Toner, M.; Balaj, L.; D, T. T.; Breakefield, X. O.; Stott, S. L., Engineered nanointerfaces for microfluidic isolation and molecular profiling of tumor-specific extracellular vesicles. *Nat Commun* **2018,** *9* (1), 175.

(135). Dudani, J. S.; Gossett, D. R.; Tse, H. T.; Lamm, R. J.; Kulkarni, R. P.; Carlo, D. D., Rapid inertial solution exchange for enrichment and flow cytometric detection of microvesicles. *Biomicrofluidics* **2015,** *9* (1), 014112.

(136). Liu, C.; Guo, J.; Tian, F.; Yang, N.; Yan, F.; Ding, Y.; Wei, J.; Hu, G.; Nie, G.; Sun, J., Field-Free Isolation of Exosomes from Extracellular Vesicles by Microfluidic Viscoelastic Flows. *ACS Nano* **2017,** *11* (7), 6968-6976.

(137). Wu, M.; Ouyang, Y.; Wang, Z.; Zhang, R.; Huang, P. H.; Chen, C.; Li, H.; Li, P.; Quinn, D.; Dao, M.; Suresh, S.; Sadovsky, Y.; Huang, T. J., Isolation of exosomes from whole blood by integrating acoustics and microfluidics. *Proc Natl Acad Sci U S A* **2017,** *114* (40), 10584-10589.

(138). Zhang, P.; Zhou, X.; He, M.; Shang, Y.; Tetlow, A. L.; Godwin, A. K.; Zeng, Y., Ultrasensitive detection of circulating exosomes with a 3D-nanopatterned microfluidic chip. *Nat Biomed Eng* **2019,** *3* (6), 438-451.

(139). He, M.; Crow, J.; Roth, M.; Zeng, Y.; Godwin, A. K., Integrated immunoisolation and protein analysis of circulating exosomes using microfluidic technology. *Lab on a Chip* **2014,** *14* (19), 3773-3780.

(140). Kang, Y. T.; Purcell, E.; Palacios-Rolston, C.; Lo, T. W.; Ramnath, N.; Jolly, S.; Nagrath, S., Isolation and Profiling of Circulating Tumor-Associated Exosomes Using Extracellular Vesicular Lipid-Protein Binding Affinity Based Microfluidic Device. *Small* **2019,** *15* (47), e1903600.

(141). Zhang, J.; Huang, H.; Xue, L.; Zhong, L.; Ge, W.; Song, X.; Zhao, Y.; Wang, W.; Dong, X., On-demand drug release nanoplatform based on fluorinated aza-BODIPY for imaging-guided chemo-phototherapy. *Biomaterials* **2020,** *256*, 120211.

(142). Haney, M. J.; Klyachko, N. L.; Zhao, Y.; Gupta, R.; Plotnikova, E. G.; He, Z.; Patel, T.; Piroyan, A.; Sokolsky, M.; Kabanov, A. V.; Batrakova, E. V., Exosomes as drug delivery vehicles for Parkinson's disease therapy. *J Control Release* **2015,** *207*, 18-30.

(143). Ko, J.; Carpenter, E.; Issadore, D., Detection and isolation of circulating exosomes and microvesicles for cancer monitoring and diagnostics using micro-/nano-based devices. *Analyst* **2016,** *141* (2), 450-460.

(144). Becker, H., It's the economy... *Lab Chip* **2009,** *9*, 2759 - 2762.

(145). O'Neil, C. E.; Jackson, J. M.; Shim, S. H.; Soper, S. A., Characterizing Surface Functional Group Density for O2 Plasma and UV/O3 Activated Thermoplastics using Superresolution Microscopy. *Analytical Chemistry* **2016,** *88*, 3686-3696.

(146). O'Neil, C. E.; Taylor, S.; Ratnayake, K.; Pullagurla, S.; Singh, V.; Soper, S. A., Characterization of activated cyclic olefin copolymer: effects of ethylene/norbornene content on the physiochemical properties. *Analyst* **2016,** *141* (24), 6521-6532.

(147). Wijerathne, H.; Witek, M. A.; Jackson, J. M.; Brown, V.; Hupert, M. L.; Herrera, K.; Kramer, C.; Davidow, A. E.; Li, Y.; Baird, A. E.; Murphy, M. C.; Soper, S. A., Affinity enrichment of extracellular vesicles from plasma reveals mRNA changes associated with acute ischemic stroke. *Commun Biol* **2020,** *3* (1), 613.

(148). Soo, C. Y.; Song, Y.; Zheng, Y.; Campbell, E. C.; Riches, A. C.; Gunn-Moore, F.; Powis, S. J., Nanoparticle tracking analysis monitors microvesicle and exosome secretion from immune cells. *Immunology* **2012,** *136* (2), 192-7.

(149). Vestad, B.; Llorente, A.; Neurauter, A.; Phuyal, S.; Kierulf, B.; Kierulf, P.; Skotland, T.; Sandvig, K.; Haug, K. B. F.; Ovstebo, R., Size and concentration analyses of extracellular vesicles by nanoparticle tracking analysis: a variation study. *J Extracell Vesicles* **2017,** *6* (1), 1344087.

(150). Gardiner, C.; Ferreira, Y. J.; Dragovic, R. A.; Redman, C. W.; Sargent, I. L., Extracellular vesicle sizing and enumeration by nanoparticle tracking analysis. *J Extracell Vesicles* **2013,** *2*.

(151). Gross, J.; Sayle, S.; Karow, A. R.; Bakowsky, U.; Garidel, P., Nanoparticle tracking analysis of particle size and concentration detection in suspensions of polymer and protein samples: Influence of experimental and data evaluation parameters. *Eur J Pharm Biopharm* **2016,** *104*, 30-41.

(152). Filipe, V.; Hawe, A.; Jiskoot, W., Critical evaluation of Nanoparticle Tracking Analysis (NTA) by NanoSight for the measurement of nanoparticles and protein aggregates. *Pharm Res* **2010,** *27* (5), 796-810.

(153). Maas, S. L.; de Vrij, J.; van der Vlist, E. J.; Geragousian, B.; van Bloois, L.; Mastrobattista, E.; Schiffelers, R. M.; Wauben, M. H.; Broekman, M. L.; Nolte-'t Hoen, E. N., Possibilities and limitations of current technologies for quantification of biological extracellular vesicles and synthetic mimics. *J Control Release* **2015,** *200*, 87-96.

(154). Ludwig Reimer, H. K., *Transmission Electron Microscopy: Physics of Image Formation*. Springer: 2008; p 487.

(155). Peak, T. C.; Praharaj, P. P.; Panigrahi, G. K.; Doyle, M.; Su, Y.; Schlaepfer, I. R.; Singh, R.; Vander Griend, D. J.; Alickson, J.; Hemal, A.; Atala, A.; Deep, G., Exosomes secreted by placental stem cells selectively inhibit growth of aggressive prostate cancer cells. *Biochem Biophys Res Commun* **2018,** *499* (4), 1004-1010.

(156). Shao, H.; Chung, J.; Balaj, L.; Charest, A.; Bigner, D. D.; Carter, B. S.; Hochberg, F. H.; Breakefield, X. O.; Weissleder, R.; Lee, H., Protein typing of circulating microvesicles allows real-time monitoring of glioblastoma therapy. *Nat Med* **2012,** *18* (12), 1835-40.

(157). Enderle, D.; Spiel, A.; Coticchia, C. M.; Berghoff, E.; Mueller, R.; Schlumpberger, M.; Sprenger-Haussels, M.; Shaffer, J. M.; Lader, E.; Skog, J.; Noerholm, M., Characterization of RNA from Exosomes and Other Extracellular Vesicles Isolated by a Novel Spin Column-Based Method. *PLoS One* **2015,** *10* (8), e0136133.

(158). Koifman, N.; Biran, I.; Aharon, A.; Brenner, B.; Talmon, Y., A direct-imaging cryo-EM study of shedding extracellular vesicles from leukemic monocytes. *J Struct Biol* **2017,** *198* (3), 177-185.

(159). Cizmar, P.; Yuana, Y., Detection and Characterization of Extracellular Vesicles by Transmission and Cryo-Transmission Electron Microscopy. *Methods Mol Biol* **2017,** *1660*, 221-232.

(160). Buzas, E. I.; Gyorgy, B.; Nagy, G.; Falus, A.; Gay, S., Emerging role of extracellular vesicles in inflammatory diseases. *Nat Rev Rheumatol* **2014,** *10* (6), 356-64.

(161). Sharma, S.; Gillespie, B. M.; Palanisamy, V.; Gimzewski, J. K., Quantitative nanostructural and single-molecule force spectroscopy biomolecular analysis of human-saliva-derived exosomes. *Langmuir* **2011,** *27* (23), 14394-400.

(162). Yuana, Y.; Oosterkamp, T. H.; Bahatyrova, S.; Ashcroft, B.; Garcia Rodriguez, P.; Bertina, R. M.; Osanto, S., Atomic force microscopy: a novel approach to the detection of nanosized blood microparticles. *J Thromb Haemost* **2010,** *8* (2), 315-23.

(163). Creasey, R.; Sharma, S.; Gibson, C. T.; Craig, J. E.; Ebner, A.; Becker, T.; Hinterdorfer, P.; Voelcker, N. H., Atomic force microscopy-based antibody recognition imaging of proteins in the pathological deposits in pseudoexfoliation syndrome. *Ultramicroscopy* **2011,** *111* (8), 1055-61.

(164). van der Pol, E.; Coumans, F. A.; Grootemaat, A. E.; Gardiner, C.; Sargent, I. L.; Harrison, P.; Sturk, A.; van Leeuwen, T. G.; Nieuwland, R., Particle size distribution of exosomes and microvesicles determined by transmission electron microscopy, flow cytometry, nanoparticle tracking analysis, and resistive pulse sensing. *J Thromb Haemost* **2014,** *12* (7), 1182-92.

(165). Nolan, J. P.; Jones, J. C., Detection of platelet vesicles by flow cytometry. *Platelets* **2017,** *28* (3), 256-262.

(166). Szatanek, R.; Baj-Krzyworzeka, M.; Zimoch, J.; Lekka, M.; Siedlar, M.; Baran, J., The Methods of Choice for Extracellular Vesicles (EVs) Characterization. *Int J Mol Sci* **2017,** *18* (6).

(167). Baj-Krzyworzeka, M.; Szatanek, R.; Weglarczyk, K.; Baran, J.; Urbanowicz, B.; Branski, P.; Ratajczak, M. Z.; Zembala, M., Tumour-derived microvesicles carry several surface determinants and mRNA of tumour cells and transfer some of these determinants to monocytes. *Cancer Immunol Immunother* **2006,** *55* (7), 808-18.

(168). Zhang, J.; Li, S.; Li, L.; Li, M.; Guo, C.; Yao, J.; Mi, S., Exosome and exosomal microRNA: trafficking, sorting, and function. *Genomics Proteomics Bioinformatics* **2015,** *13* (1), 17-24.

(169). Morales-Kastresana, A.; Jones, J. C., Flow Cytometric Analysis of Extracellular Vesicles. *Methods Mol Biol* **2017,** *1545*, 215-225.

(170). Suarez, H.; Gamez-Valero, A.; Reyes, R.; Lopez-Martin, S.; Rodriguez, M. J.; Carrascosa, J. L.; Cabanas, C.; Borras, F. E.; Yanez-Mo, M., A bead-assisted flow cytometry method for the semi-quantitative analysis of Extracellular Vesicles. *Sci Rep* **2017,** *7* (1), 11271.

(171). Friedrich, R.; Block, S.; Alizadehheidari, M.; Heider, S.; Fritzsche, J.; Esbjorner, E. K.; Westerlund, F.; Bally, M., A nano flow cytometer for single lipid vesicle analysis. *Lab Chip* **2017,** *17* (5), 830-841.

(172). Koritzinsky, E. H.; Street, J. M.; Star, R. A.; Yuen, P. S., Quantification of Exosomes. *J Cell Physiol* **2017,** *232* (7), 1587-1590.

(173). DeBlois, R. W.; Wesley, R. K., Sizes and concentrations of several type C oncornaviruses and bacteriophage T2 by the resistive-pulse technique. *J Virol* **1977,** *23* (2), 227-33.

(174). DeBlois, R. W.; Uzgiris, E. E.; Cluxton, D. H.; Mazzone, H. M., Comparative measurements of size and polydispersity of several insect viruses. *Anal Biochem* **1978,** *90* (1), 273-88.

(175). Kasianowicz, J. J.; Brandin, E.; Branton, D.; Deamer, D. W., Characterization of individual polynucleotide molecules using a membrane channel. *Proc Natl Acad Sci U S A* **1996,** *93* (24), 13770-3.

(176). Astier, Y.; Braha, O.; Bayley, H., Toward single molecule DNA sequencing: direct identification of ribonucleoside and deoxyribonucleoside 5'-monophosphates by using an engineered protein nanopore equipped with a molecular adapter. *J Am Chem Soc* **2006,** *128* (5), 1705-10.

(177). Deamer, D. W.; Akeson, M., Nanopores and nucleic acids: prospects for ultrarapid sequencing. *Trends Biotechnol* **2000,** *18* (4), 147-51.

(178). Lobb, R. J.; Becker, M.; Wen, S. W.; Wong, C. S.; Wiegmans, A. P.; Leimgruber, A.; Moller, A., Optimized exosome isolation protocol for cell culture supernatant and human plasma. *J Extracell Vesicles* **2015,** *4*, 27031.

(179). Anderson, W.; Lane, R.; Korbie, D.; Trau, M., Observations of Tunable Resistive Pulse Sensing for Exosome Analysis: Improving System Sensitivity and Stability. *Langmuir* **2015,** *31* (23), 6577-87.

(180). Kozak, D.; Anderson, W.; Vogel, R.; Trau, M., Advances in Resistive Pulse Sensors: Devices bridging the void between molecular and microscopic detection. *Nano Today* **2011,** *6* (5), 531-545.

(181). Wen-Jie Lan, C. K., Jie-Wen Xiong, Andreas Bund, and Henry S. White, Effect of Surface Charge on the Resistive Pulse Waveshape during Particle Translocation through Glass Nanopores. *The Journal of Physical Chemistry C* **2014,** *118* (5), 2726-2734.

(182). Pan, R.; Hu, K.; Jiang, D.; Samuni, U.; Mirkin, M. V., Electrochemical Resistive-Pulse Sensing. *J Am Chem Soc* **2019,** *141* (50), 19555-19559.

(183). Y Wu, J. D. B., J K Critser, M Almasri, MEMS-based Coulter counter for cell counting and sizing using multiple electrodes. *J Micromech Microeng* **2010,** *20* (8).

(184). Clarke, J.; Wu, H. C.; Jayasinghe, L.; Patel, A.; Reid, S.; Bayley, H., Continuous base identification for single-molecule nanopore DNA sequencing. *Nat Nanotechnol* **2009,** *4* (4), 265-70.

(185). Harms, Z. D.; Mogensen, K. B.; Nunes, P. S.; Zhou, K. M.; Hildenbrand, B. W.; Mitra, I.; Tan, Z. N.; Zlotnick, A.; Kutter, J. P.; Jacobson, S. C., Nanofluidic Devices with Two Pores in Series for Resistive-Pulse Sensing of Single Virus Capsids. *Anal Chem* **2011,** *83* (24), 9573-9578.

(186). Ashish V Jagtiani, J. Z., Jun Hu, Joan Carletta, Detection and counting of micro-scale particles and pollen using a multi-aperture Coulter counter. *Measurement Science and Technology* **2006,** *17* (7).

(187). Jiang Zhe, A. J., Prashanta Dutta, Jun Hu, Joan Carletta4, A micromachined high throughput Coulter counter for bioparticle detection and counting. *J Micromech Microeng* **2007,** *17* (3).

(188). Ashish V Jagtiani, J. C., Jiang Zhe, An impedimetric approach for accurate particle sizing using a microfluidic Coulter counter. *J Micromech Microeng* **2011,** *21* (4).

(189). Lannigan, J.; Erdbruegger, U., Imaging flow cytometry for the characterization of extracellular vesicles. *Methods* **2017,** *112*, 55-67.

(190). Rosenstein, J. K.; Wanunu, M.; Merchant, C. A.; Drndic, M.; Shepard, K. L., Integrated nanopore sensing platform with sub-microsecond temporal resolution. *Nat Methods* **2012,** *9* (5), 487-92.

(191). Li, J.; Stein, D.; McMullan, C.; Branton, D.; Aziz, M. J.; Golovchenko, J. A., Ion-beam sculpting at nanometre length scales. *Nature* **2001,** *412* (6843), 166-9.

(192). N.G. Stanley-Wood, R. W. L., *Particle Size Analysis*. The Royal Society of Chemistry: 1992.

(193). Song, Y.; Zhang, J.; Li, D., Microfluidic and Nanofluidic Resistive Pulse Sensing: A Review. *Micromachines (Basel)* **2017,** *8* (7).

(194). Vaclavek, T.; Prikryl, J.; Foret, F., Resistive pulse sensing as particle counting and sizing method in microfluidic systems: Designs and applications review. *J Sep Sci* **2019,** *42* (1), 445-457.

(195). Uram, J. D.; Ke, K.; Mayer, M., Noise and bandwidth of current recordings from submicrometer pores and nanopores. *ACS Nano* **2008,** *2* (5), 857-72.

(196). Parkin, W. M.; Drndic, M., Signal and Noise in FET-Nanopore Devices. *ACS Sens* **2018,** *3* (2), 313-319.

(197). Cui, S.; Cheng, Z.; Qin, W.; Jiang, L., Exosomes as a liquid biopsy for lung cancer. *Lung Cancer* **2018,** *116*, 46-54.

(198). Mader, S.; Pantel, K., Liquid Biopsy: Current Status and Future Perspectives. *Oncol Res Treat* **2017,** *40* (7-8), 404-408.

(199). Poulet, G.; Massias, J.; Taly, V., Liquid Biopsy: General Concepts. *Acta Cytol* **2019,** *63* (6), 449-455.

(200). Chen, M.; Zhao, H., Next-generation sequencing in liquid biopsy: cancer screening and early detection. *Hum Genomics* **2019,** *13* (1), 34.

(201). Manna, I.; Iaccino, E.; Dattilo, V.; Barone, S.; Vecchio, E.; Mimmi, S.; Filippelli, E.; Demonte, G.; Polidoro, S.; Granata, A.; Scannapieco, S.; Quinto, I.; Valentino, P.; Quattrone, A., Exosome-associated miRNA profile as a prognostic tool for therapy response monitoring in multiple sclerosis patients. *FASEB J* **2018,** *32* (8), 4241-4246.

(202). Alimirzaie, S.; Bagherzadeh, M.; Akbari, M. R., Liquid biopsy in breast cancer: A comprehensive review. *Clin Genet* **2019,** *95* (6), 643-660.

(203). Vader, P.; Mol, E. A.; Pasterkamp, G.; Schiffelers, R. M., Extracellular vesicles for drug delivery. *Adv Drug Deliv Rev* **2016,** *106* (Pt A), 148-156.

(204). Batrakova, E. V.; Kim, M. S., Using exosomes, naturally-equipped nanocarriers, for drug delivery. *J Control Release* **2015,** *219*, 396-405.

(205). Tang, Y. T.; Huang, Y. Y.; Zheng, L.; Qin, S. H.; Xu, X. P.; An, T. X.; Xu, Y.; Wu, Y. S.; Hu, X. M.; Ping, B. H.; Wang, Q., Comparison of isolation methods of exosomes and exosomal RNA from cell culture medium and serum. *Int J Mol Med* **2017,** *40* (3), 834-844.

(206). Chen, B. Y.; Sung, C. W.; Chen, C.; Cheng, C. M.; Lin, D. P.; Huang, C. T.; Hsu, M. Y., Advances in exosomes technology. *Clin Chim Acta* **2019,** *493*, 14-19.

(207). Nath Neerukonda, S.; Egan, N. A.; Patria, J.; Assakhi, I.; Tavlarides-Hontz, P.; Modla, S.; Munoz, E. R.; Hudson, M. B.; Parcells, M. S., Comparison of exosomes purified via ultracentrifugation (UC) and Total Exosome Isolation (TEI) reagent from the serum of Marek's disease virus (MDV)-vaccinated and tumor-bearing chickens. *J Virol Methods* **2019,** *263*, 1-9.

(208). Lee, K.; Shao, H.; Weissleder, R.; Lee, H., Acoustic purification of extracellular microvesicles. *ACS Nano* **2015,** *9* (3), 2321-7.

(209). Franz, C.; Boing, A. N.; Montag, M.; Strowitzki, T.; Markert, U. R.; Mastenbroek, S.; Nieuwland, R.; Toth, B., Extracellular vesicles in human follicular fluid do not promote coagulation. *Reprod Biomed Online* **2016,** *33* (5), 652-655.

Chapter 2: A Microfluidic ExoSearch Chip for Multiplexed Exosome Detection Towards Blood-based Ovarian Cancer Diagnosis

Tumor-derived circulating exosomes, enriched with a group of tumor antigens, have been recognized as a promising biomarker source for cancer diagnosis via less invasive procedure. Quantitatively pinpointing exosome tumor markers is appealing, yet challenging. In this study, we developed a simple microfluidic approach (ExoSearch) which provides enriched preparation of blood plasma exosomes for in-situ, multiplexed detection using immunomagnetic beads. The ExosSearch chip offers robust, continuous-flow design for quantitative isolation and release of blood plasma exosomes in a wide range of preparation volumes (10 μL to 10 mL). We employed the ExoSearch chip for blood-based diagnosis of ovarian cancer by multiplexed measurement of three exosomal tumor markers (CA-125, EpCAM, CD24) using a training set of ovarian cancer patient plasma, which showed significant diagnostic power (a.u.c. = 1.0, p = 0.001) and was comparable with standard Bradford assay. This work provides an essentially needed platform for utilization of exosomes in clinical cancer diagnosis, as well as fundamental exosome research.

2.1. Introduction

Extracellular vesicles, particularly exosomes, have become essential for intercellular communications involved in many pathophysiological conditions, such as cancer progression and metastasis.[1-6] Exosomes are a distinct population of small microvesicles (50 ~ 150 nm) that are released from multivesicular bodies (MVBs) through an endolysosomal pathway, as opposed to other subcellular membrane derived vesicles.[2, 7] Studies have shown that exosomes are abundant in cancer patient blood.[8-10] Probing of tumor-derived circulating exosomes has been emerging to better serve non-invasive cancer diagnosis and monitoring of treatment response.[11] However,

exosome biogenesis at the molecular level is still not well understood, and clinical utilization of exosomes lags, due to current technical challenges in rapid isolation and molecular identification of exosomes.[7, 12]

The most common procedure for purifying exosomes involves a series of high-speed ultracentrifugation steps in order to remove cell debris and pellet exosomes. However, this procedure does not discriminate exosomes from other vesicular structures or large protein aggregates.[13-15] Moreover, the isolation protocols are extremely tedious, time-consuming (> 10 h), and inefficient especially for blood samples, making clinical application difficult.[16-19] Although physical size is employed to define exosomes, this property has not completely distinguished exosomes as a specific population apart from other vesicles that originate from different cellular locations, such as apoptotic vesicles, exosome-like vesicles, membrane particles, and ectosomes[5]. Exosomes carry a group of specific proteins, RNAs, and mitochondrial DNA, that represents their cells of origin.[20, 21] The molecular signature of exosomes is essential for defining exosome populations and origins.[22, 23] However, conventional flow cytometry for molecular marker identification is limited by detectable size (> 200 nm), thereby excluding the majority of exosomes.[24] Standard benchtop ultracentrifugation, western blotting and enzyme-linked immunosorbent assay (ELISA) require lengthy processes, and large amounts of purified, concentrated exosomes from blood (~ 2 mL) or cell culture media (~ 300 mL).[14, 25]

Herein, we developed a simple and robust microfluidic continuous-flow platform (ExoSearch chip) for rapid exosome isolation streamlined with in-situ, multiplexed detection of exosomes. Several microfluidic approaches have been previously developed for exosome study,[26, 27] such as isolation,[28, 29] quantification,[30, 31] and molecular profiling.[32-34] However, these platforms require either complicated fabrication or sophisticated sensing methods. We previously developed

a microfluidic system for integrated exosome lysis and detection of intravesicular protein markers that exosomes carry.[27] However, on-chip isolation and enrichment of exosomes streamlined with multiplexed detection of marker combinations have not been established yet. In addition, previous approach involves off-chip exosome capture using a small amount of magnetic beads and thus lacks the ability to prepare large-scale enriched exosomes for variable downstream molecular characterizations. Therefore, we developed the ExoSearch chip which combines on-chip continuous-flow mixing and immunomagnetic isolation with an in-situ, multiplexed exosome immunoassay. Compared to other existing microfluidic methods, the ExoSearch chip possesses distinct features: first, continuous-flow operation affords dynamic scalability in processing sample volumes from microliter for on-chip analysis to millilitre preparation for variable downstream measurements; second, it enables multiplexed quantification of marker combinations in one sample with much improved speed (~40 mins); lastly, because of simplicity, cost-effectiveness and robustness, the ExoSearch chip holds the potential to be developed into a viable technology in point-of-care and clinical settings. The one-step exosome assay enabled by the ExoSearch chip has been applied for ovarian cancer diagnosis via quantifying a panel of tumor markers from exosomes in a small-volume of blood plasma (20 μL), which showed significant diagnostic accuracy and was comparable with standard Bradford assay.

2.2. Experimental

2.2.1. ExoSearch chip fabrication and operation

The microfluidic chip was fabricated using a 10:1 mixture of PDMS base with curing agent over a master wafer, and then bound with a microscope glass slide. The master was the pattern of SU8 photoresist on a 4-inch silicon wafer and was silanized to facilitate generation of many

replicas as needed. A 2-mm magnet disk was molded into a PDMS layer during the curing process at desired location and magnet is removable for switching off magnet force. A surface treatment for PDMS chip was applied for avoiding non-specific adsorption and any bubbles generated in microchannel, using blocking buffer (2.5 w/w% BSA and 0.01 w/w% Tween-20 in 1X PBS) with 30-min flushing at flow rate of 1 μL/min. A programmable syringe pump (picolitter precision) with two 20-μL micro-syringes were used to provide optimized flow rate for continuous, on-line mixing of plasma sample and immunomagnetic beads. The magnetic beads (2.8 μm, 0.1 mg/mL) were conjugated with capture antibodies for isolating intact plasma exosomes. Washing buffer (1 w/w% BSA in 1X PBS) was applied for 5 mins after exosome capturing. A mixture of three probing antibodies (anti CA-125/A488, anti EpCAM/A550, anti CD24/A633) labeled in distinct fluorescence was introduced afterwards for 10-min incubation at slow flow rate of 100 nL/min, then followed with 5-min washing. The non-specific adsorption, specificity of probing antibodies, and incubation, were well characterized.

For comparison with standard benchtop approaches, differential centrifugations were carried out on the collected fresh frozen blood plasma (2 mL) to obtain exosomes. The amount of protein recovered from pellets was measured by Bradford assay (BioRad). The exosome vesicles were conserved at −80 °C until use. Nanoparticle tracking analysis (NTA) was performed using NanoSight V2.3 following the standard protocols. By monitoring the trajectory of microvesicles movement, the particle numbers within the size range of 0–500 nm were estimated in serial dilutions. The concentrations were calibrated back to the human plasma concentration. For consistent reading, the measurement settings were optimized and five replicas were performed to obtain the average measurements. Transmission electron microscopy and image analysis were performed for characterizing exosomes morphology and size captured on beads surface. The agar

and resin embedding protocols were employed to ensure that exosome morphology was maximally maintained under TEM imaging. Ultra-thin sections (80 nm) were cut on Leica Ultracut-S Ultramicrotome and viewed after counterstaining in a JEOL JEM-1400 Transmission Electron Microscope operating at 80 kV. Micrographs were prepared to a known scale, and exosome sizes were measured and calculated using TEM imaging software with ruler function at 20 K magnification and normalized to the scale bar.

2.2.2. Data collection and analysis

Fluorescence Images were collected by an inverted epifluorescence microscope with a 20x (N.A. = 0.35) Zeiss objective and a scientific CMOS camera (OptiMOS, QImaging). The camera exposure time was set to 2000 ms with a 10 MHz frequency controlled by an open source software Micro-Manager 1.4. The filter sets of FITC, Rhodamine and Cy-5 were used for multiplexed three-color fluorescence detection with LED light source for excitation. Fluorescence image analysis was performed using ImageJ with an in-house written Macro to determine 1000 points randomly across consistent regions of bead aggregates for obtaining averaged fluorescence intensity. Two fluorescence images were collected right before and after antibody detection in three fluorescence channels respectively, for calculating the difference of fluorescence signals. The measured fluorescence signal was then normalized to background.

2.3. Results & discussion

2.3.1. Working principle of the ExoSearch chip

Exosomes contain a variety of surface markers originated from their host cells.[35, 36] Selective isolation and specific analysis of disease-responsive exosome subpopulations is essential

to evaluate clinical relevance of circulating exosomes.[24, 37-39] To this end, the ExoSearch chip is designed to specifically isolate exosome subpopulations and simultaneously measures a panel of tumor markers for better defining disease, compared to single-marker detection. As shown in Figure 2.2a, the ExoSearch chip consists of a Y-shaped injector, a serpentine fluidic mixer for bead-based exosome capture (~25.5 cm in length), and a microchamber (4-mm in diameter) with a replaceable magnet for collection and detection of exosomes. The microchannel is 300 μm wide and 50 μm deep. Such microfluidic geometry was adapted from our previous studies on on-chip mixing and magnetic bead capture.[27] The operation was simply driven by a programmable microsyringe pump with picoliter resolution. Briefly, a plasma sample and immunomagnetic beads were introduced at the same flow rate from the injection channels (Figure 2.2b) through the long serpentine channel where they are uniformly mixed to facilitate exosomes binding with the beads (Figure 2.2c). No significant aggregation of beads by interactions with exosomes or other plasma components was observed during flow mixing at the bead concentrations and flow rates used here (Figure 2.2b & c). Magnetic beads with bound exosomes can be retained as a tight aggregate in the downstream microchamber by magnetic force (Figure 2.2d). The amount of beads retained in chamber was found to be proportional to the injection volume, allowing for quantitative isolation and detection of exosomes.[27] A mixture of antibodies labeled with unique fluorescence dyes was injected into the chamber to stain the exosomes for multi-color fluorescence imaging. Total analysis is completed with as low as 20 μL plasma samples in ~40 mins. Alternative, the beads can be released by removing the magnet and collected off chip to yield purified and enriched exosome samples for variable benchtop measurements, such as morphological studies by transmission electron microscopy (TEM, Figure 2.2e and Figure 2.1).

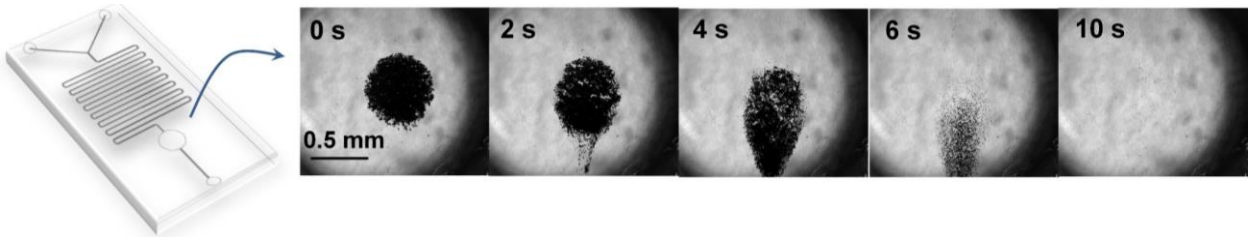

Figure 2.1. The sequential snapshots showing the release process of bead aggreagates after switching off the magnetic field during continuous flow in ExoSearch chip.

While a 20 μL sample volume was used throughout this study, the smallest sample volume that can be reliably handled was estimated to be 10 μL, given the dead volume of the system (i.e., syringes, tubing and the chip). Our previous results showed that the magnetic bead aggregate formed in the chamber increased linearly in size by a factor of 8 with a 50-fold increase in the total injected bead number.[27] and that ~10^6 beads formed an aggregate of ~1 mm in size. Based on this observation, the chamber size (4 mm in diameter), and the bead concentration used (~10^6/mL), it is reasonable to estimate that this device can readily process 10 mL plasma in a single continuous run. The processing capacity can be increased by operating in a repetitive capture-and-release manner (Figure 2.1). The single-channel device is readily scaled up to multi-channel systems for high-throughput exosome immuno-isolation and analysis.

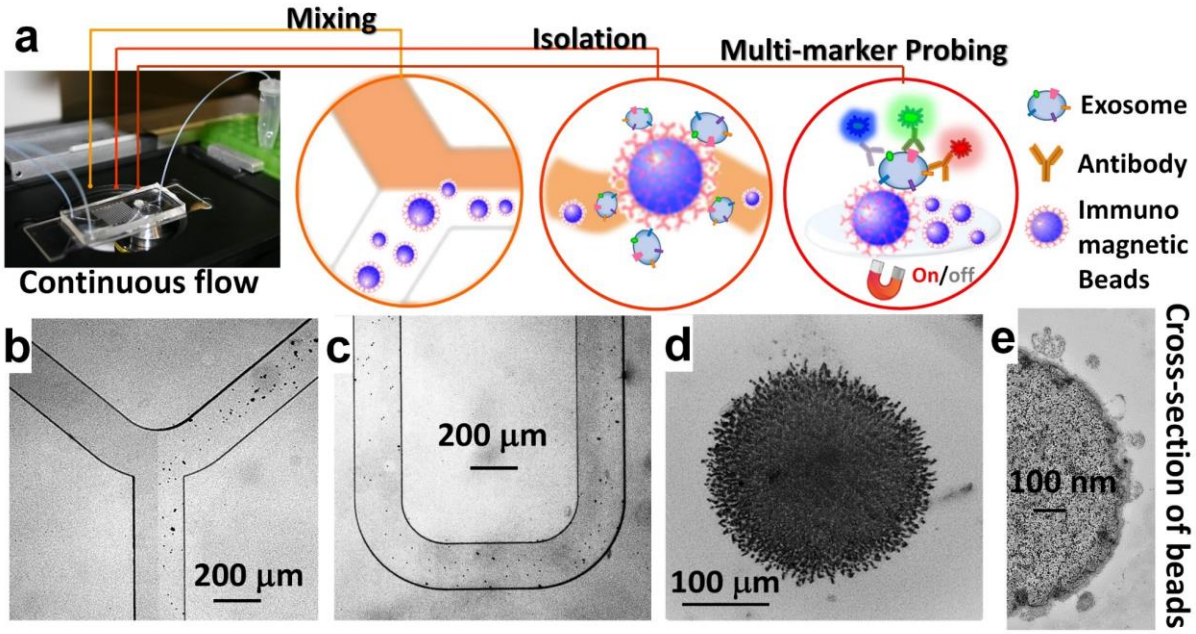

Figure 2.2. a) Workflow of the ExoSearch chip for continuous mixing, isolation and in-situ, multiplexed detection of circulating exosomes. **b&c)** Bright-field microscope images of immunomagnetic beads manipulated in microfluidic channel for mixing and isolation of exosomes. **d)** Exosome-bound immunomagnetic beads aggregated in a microchamber with on/off switchable magnet for continuous collection and release of exosomes. **e)** TEM image of exosome-bound immunomagnetic bead in a cross-sectional view.

2.3.2. Characterization of microfluidic continuous-flow mixing for exosome isolation

We systematically characterized on-chip mixing behaviour of particles in various sizes for efficient exosome isolation. First, fluorescently labeled nanoparticles (50 nm) and micro-sized magnetic beads (2.8 μm) were flowed through the ExoSearch chip, respectively, in order to mimic the mixing process for exosome isolation (Figure 2.3a). In both cases, two streams were well mixed passively by the serpentine channel, showing uniform distribution of particles across the channel width. Mixing of fluorescently labelled exosomes with antibody-conjugated microbeads was then studied. We observed uniform distributions of both exosome stream and the microbeads that emitted bright fluorescence due to the binding of exosomes on bead surface (Figure 2.3a). The

microbeads are dominated for effective mixing which provide much faster mixing. The minimum flow travel distance required for complete mixing in the microchannel was measured for each case, which exhibited a linear semi-log response to the flow rates applied (50 to 10^4 nL/min) (Figure 2.3b). Higher mixing efficiency was observed at relative lower flow rates for all three cases. Low-Reynolds-number conditions allow the exosomes and magnetic-bead suspension to flow side by side. Thus, complete mixing is critical and determines the effective residence time (incubation time), and in-turn determines the effective capture. In the serpentine microchannel, mixing is promoted by the Dean flow and inertial lift.[40] For larger particles, the lift force increases rapidly and positions particles across the channel.[41] Therefore, the micro-sized magnetic beads showed faster mixing, compared to the smaller exosomes and nanoparticles (Figure 2.3a & b). In addition, in such mixing system, the shear stress is low and particularly suitable for isolating and collecting intact exosomes.[40, 41] For all flow rates we studied (50 to 10^4 nL/min), effective mixing was completely achieved, which can significantly reduce the incubation time for efficient immunomagnetic capture of exosomes.[42] We also investigated exosome capture efficiency by comparing fluorescence intensity of flows at the inlet and outlet of capture chamber. The capture efficiency of 42%–97.3% was achieved at flow rates from 50 to 10^4 nL/min (Figure 2.3c). Subsequent studies were performed at the flow rate of 1 μL/min which results in a fairly good capture efficiency of 72%. This flow speed allows exosome isolation from a 20-μL plasma sample in 20 mins. For preparing enriched exosomes from large-volume samples, the throughput can be increased by using a relatively faster flow rate or expanding the single-channel device to a multi-channel system. For instance, a 2 mL of blood plasma can be processed within 3 hours (10 μL/min) without the need of manual intervention, which is at least 3 times faster than standard

ultracentrifugation for processing the same amount of plasma with only 25% exosome recovery rate.[43]

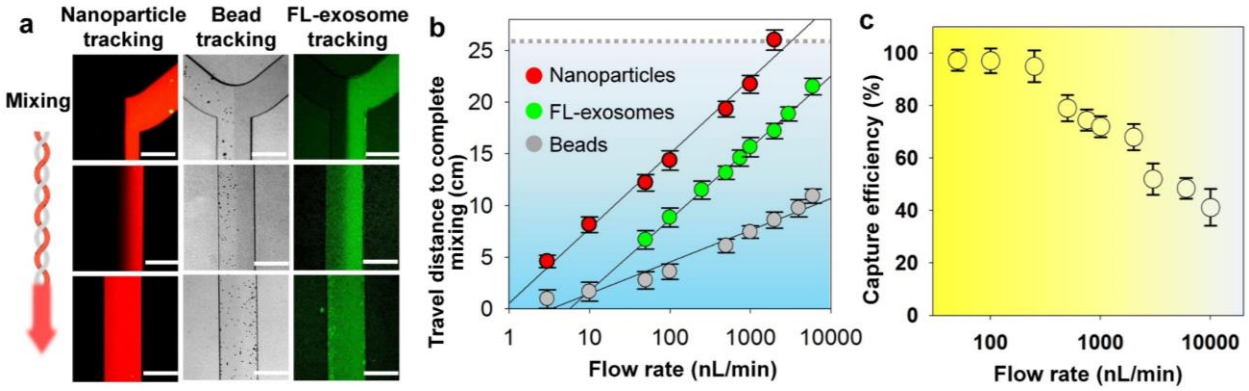

Figure 2.3. Microfluidic continuous-flow mixing for efficient exosome isolation. **a)** Two-stream particle mixing in the microchannel. Left: Fluorescence CCD images of mixing process for a stream of Texas Red labeled nanoparticles (50 nm) co-flowed with a bead solution. Middle: Immuno-magnetic beads (2.8 μm) tracked under bright field for mixing with human blood plasma. Right: Mixing of fluorescently labeled exosomes with antibody beads. Exosomes were purified from ovarian cancer patient plasma by ultracentrifugation. Scale bars: 300 μm. **b)** Plots of minimum travel length required for uniform mixing over a flow rate range. Grey dashed line indicates mixing channel length in the ExoSearch chip. **c)** Exosome capture efficiency as a function of mixing flow rate measured using purified, fluorescently labeled exosomes and capture beads.

2.3.3. Specificity for isolating tumor-derived exosomes

Recent studies have suggested that both tumor cells and normal cells secrete exosomes, although significantly higher amounts of exosomes have been observed from tumor cells.[44] Therefore, specifically isolating, purifying and characterizing tumor cell derived exosomes is essential.[45] We characterized specificity for on-chip immunomagnetic isolation of exosomes from ovarian cancer patient blood plasma. On-chip isolation of variable exosome subpopulations was conducted by targeting both ovarian tumor-associated markers (EpCAM and CA-125) and common exosomal markers (CD9, CD81, and CD63). EpCAM is a cargo protein in exosomes and is highly overexpressed in multiple types of carcinomas, including ovarian tumor. CA-125 antigen is the most commonly measured biomarker for epithelial ovarian tumors, which accounts for 85–

90% of ovarian cancer. The exosome-bound beads were washed on the chip and then released and concentrated for morphology evaluation and counting of intact exosomes using TEM, as presented in Figure 2.4a. Significantly higher amounts of round membrane vesicles (smaller than 150 nm) were observed for EpCAM+, CA-125+, and CD9+ subpopulations from ovarian cancer plasma, compared to healthy controls. Negative control beads with IgG conjugation showed negative capture of vesicles, demonstrating a good specificity of immunomagnetic isolation. The relative expression levels of five surface markers were measured by counting the number of intact exosomes bound to beads (n = 25). The results showed a ~3–5 fold increase in expression levels of five markers from ovarian cancer patient, compared to the healthy control (Figure 2.4b, p = 0.001).

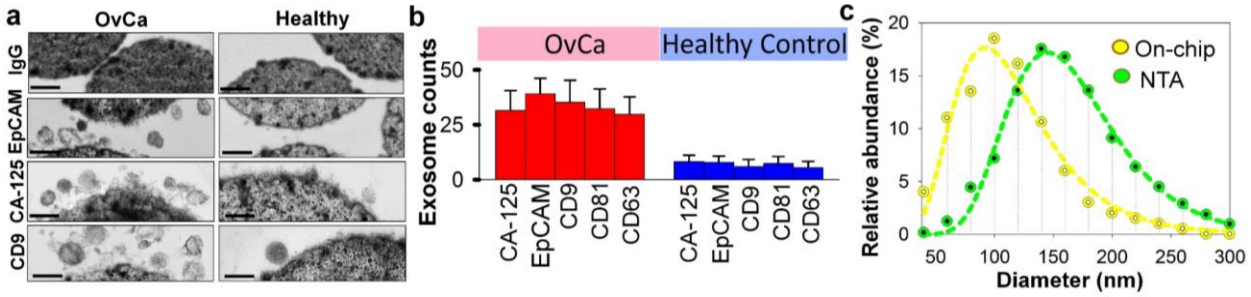

Figure 2.4. Microfluidic ExoSearch chip for specific isolation of ovarian cancer plasma derived exosomes. **a)** TEM images of on-chip immunomagnetically isolated exosomes from ovarian cancer plasma, compared to healthy control. Scale bar is 100 nm. IgG-conjugated immunomagnetic beads were negative control beads. **b)** Exosome counts analyzed from surfaces of variable capture beads (EpCAM+, CA-125+, CD9+, CD81+, CD63+) using TEM particle analysis (n = 25, CV = 2.8%–10%). Single bead diameter was 2.8 μm and sliced bead layer was 80-nm thick. **c)** Size distribution of on-chip isolated exosomes (CD9+) using TEM particle analysis, compared to standard NTA analysis of ultracentrifugation-purified exosomes. Dashed lines were log-normal fit ($R^2 > 0.98$).

To verify the results of on-chip isolation, we conducted nanoparticle tracking analysis (NTA) of ultracentrifugation-isolated exosomes to measure their size distribution and concentrations. In Figure 2.4c, on-chip isolated exosomes (CD9+) exhibited notably narrower

range with the Log-normal fitted size distribution ($R^2 > 0.98$). The smaller size than 150 nm is a commonly used criterion to differentiate exosomes from larger microvesicles.[5] Compared to ultracentrifugation approaches, microfluidic immunoaffinity isolation yields a higher percentage of vesicles smaller than 150 nm (~79.7% vs. 60.7%), suggesting that the developed ExoSearch chip offers high specificity in isolation of circulating exosomes.

2.3.4. Quantitative and multiplexed exosomal marker detection

We first characterized the ExoSearch chip for quantitative isolation and detection of exosomes. Figure 2.5a shows the fluorescence images of exosomes isolated from serial dilutions of purified, fluorescently labeled plasma exosomes. The concentrations of purified plasma exosomes were determined by NTA measurements. Employing the same mixing and isolating conditions, increased fluorescence signals (ΔFL) were observed and proportional to exosome concentrations. Using fluorescently labeled anti-EpCAM as the detection antibody, exosome titration curves were obtained for a healthy plasma sample and an ovarian cancer plasma, which exhibited good linear response as seen in Figure 2.5b (R^2 >0.98, CV = ~5%). The small variation of measurements indicates the good robustness of the method. Moreover, much higher ΔFL signal (~30-fold increase) was observed for the ovarian cancer sample, compared to the healthy control under the same concentration. These results demonstrated the ability of the ExoSeach chip in quantitative measurement of exosome surface markers for differentiating changes associated with disease. The results were in consistent with other recent reports that EpCAM is highly overexpressed in ovarian tumor exosomes.[46] The quantitative detection of intact exosomes was achieved with a limit of detection of 7.5×10^5 particles/mL (LOD, S/N = 3), which is 1000-fold sensitive than Western blotting.[33] While such sensitivity is comparable with that of previously

reported microfluidic method,[33] our method features simple fabrication, easy operation and low cost.

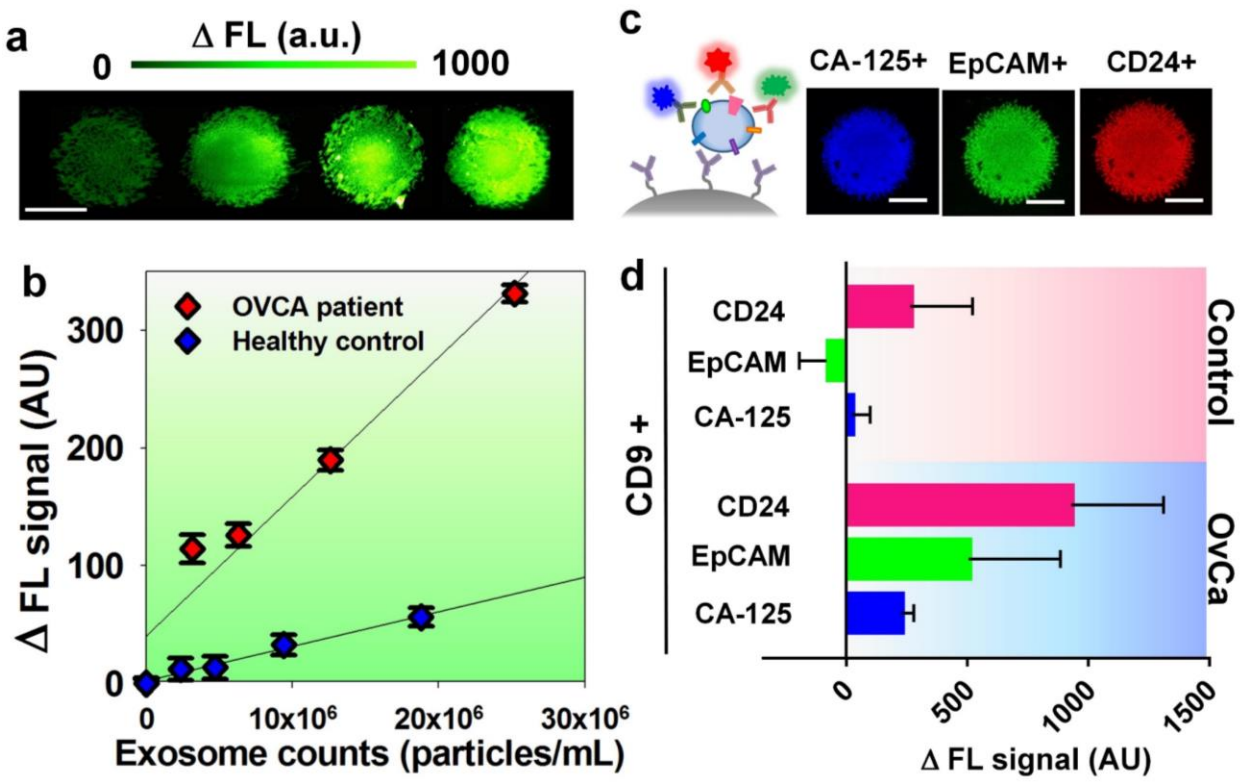

Figure 2.5. a) CCD images of bead aggregates in ExoSearch chip captured with fluorescence-labeled plasma exosomes in serial dilutions (from left to right: 5×10^5, 1×10^6, 5×10^6, 1×10^7 particles/mL). Scale bar was 100 μm. **b)** Calibration curves for quantitative detection of intact exosomes (R^2 >0.98, CV = ~5%). Exosomes were purified from one healthy control plasma and one ovarian cancer patient plasma using ultracentrifugation. Concentrations were measured by NTA. **c)** CCD images of multiplexed three-color fluorescence detection of tumor markers (CA-125, EpCAM, CD24) from captured exosome subpopulation (CD9+). Scale bar was 50 μm, indicating bead aggregate size. **d)** Average expression levels of three ovarian tumor markers measured by ExoSearch chip from 20 human subjects (n_{OvCa} = 15, $n_{healthy}$ = 5). Error bars indicate standard deviations.

In-situ, multiplexed biomarker detection was then developed for rapid and quantitative microfluidic analysis of ovarian tumor derived plasma exosomes. We chose common exosome marker CD9 as the capture antibody for selective isolation of exosomes, because of the consistently high expression of CD9 we observed from human plasma derived exosomes (Figure 2.7). In

addition to the established ovarian cancer biomarker CA-125, human epididymis protein 4 (HE4) has been recognized for improving diagnostic specificity of CA-125 in pathological tests. We did not observe substantial expression of HE4 from the exosome samples (Figure 2.8), which could be due to the different secretion pathway of HE4.[21] This observation was consistent with other recent reports.[33, 47] Previous observations have indicated that CD24 could be a significant marker in ovarian tumor prognosis and diagnosis.[48] Therefore, we developed a multiplexed sandwich immunofluorescence assay to quantify isolated exosomes by targeting three markers, CA-125, EpCAM, and CD24 from the same population of exosomes, as exemplified in Figure 2.4c. Quantitative tests of raw human plasma collected from 20 subjects (n_{OvCa} = 15, $n_{healthy}$ = 5) were conducted for three-marker classification of ovarian tumor derived exosomes, and a distinctive three-marker expression pattern was observed for ovarian cancer patients (Figure 2.5d). The average expression level of individual exosomal marker from ovarian cancer patients was statistically higher as compared to healthy controls (CD24: 3-fold increase, $p = 0.003$; EpCAM: 6.5-fold increase, $p = 0.0009$; CA-125: 12.4-fold increase, $p < 0.0001$).

2.3.5. Characterization of non-specific adsorption and cross-reactivity for on-chip immunomagnetic assay

In order to characterize the non-specific adsorption and cross-reactivity of antibodies used in this study, the negative and positive control experiments were designed and conducted in parallel. The fluorescence background of magnetic beads themselves was measured, compared with fluorescence intensity after detection antibody probing and washing, without introducing plasma exosome samples. The slight auto-fluorescence of capture beads and negligible non-specific adsorption fluorescence were observed. There is no cross-reaction between antibodies we

used in this study. The positive control (ovarian cancer patient plasma exosomes) showed strong fluorescence signals after antibodies probing (CA-125, EpCAM, and CD24). However, we did not observe acceptable positive response from HE4 antibody probing. In order to achieve the accurate fluorescence readout, we set the same image threshold (0-255 grey scale). Meanwhile, for each sample analysis, we collected one image of PDMS microchamber as the background, one image of beads aggregate right before antibody probing step, and one image of beads aggregate after antibody probing and washing step. The difference of fluorescence signals before and after antibody probing was calculated, and then normalized to background. We designed a macro function of ImageJ for randomly picking up 1000 points in the consistent area of sample signals and measuring the average of mean gray value of fluorescence intensity.

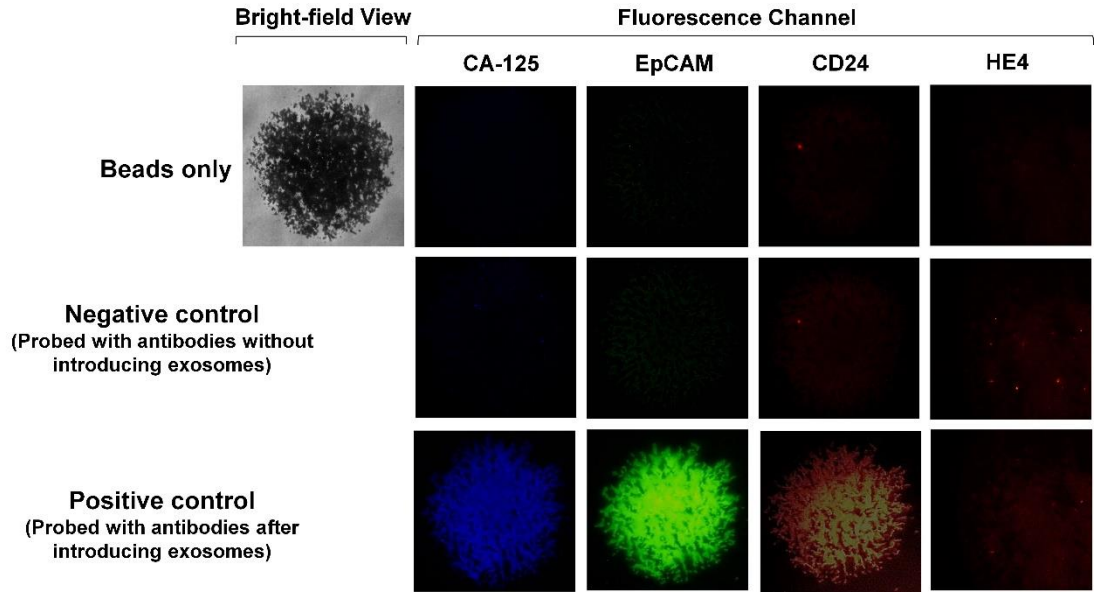

Figure 2.6. CCD captured microscopic images of bead aggregates under negative and positive control experimental conditions. Image size is 200 μm × 200 μm.

Non-specific adsorption of exosomes and antibody cross-reactivity were characterized in Figure 2.6. The negative and positive control experiments were designed and conducted in parallel

for testing four antibodies we used in this study (CA-125, EpCAM, CD24, and HE4). The slight autofluorescence of capture beads and negligible non-specific adsorption fluorescence were observed, and no cross-reaction observed between antibodies. The positive control (ovarian cancer patient plasma exosomes) showed strong fluorescence signals after antibodies probing (CA-125, EpCAM, and CD24). However, we did not observe acceptable positive response from HE4 antibody probing, as HE4 is not expressed on exosome surface which demonstrates the negligible non-specific adsorption onto captured exosomes (Figure 2.6). In addition, Figure 2.5d shows low signal intensity for these three markers when their expression levels are low in healthy exosomes. This result also indicates negligible non-specific interference from non-specific antibody adsorption or cross-reactivity.

2.3.6. Western blotting

Tris-glycine pH 8.3, 4-12% precast polyacrylamide slab mini-gels with Blot Module (BioRad) was used for performing Western blottings, following standard protocol. Ultracentrifugation-purified exosomes were lyzed and prepared by adding protease inhibitors and running buffer (0.1% SDS), and heating at 65°C for 5 min. After electrophoresis at 125 V for 2 h, gels were electrotransferred to cellulose membranes (0.2 μm) at 25 V for 2.5 h in ice bucket. After twice washing (1×PBS, 0.5% Tween 20, pH 7.4), the membranes were blocked with 5% dry milk overnight at 4°C with shaking. The solution of primary biotinlylated antibody (1:1500) was added into blocking buffer for 2-h incubation with shaking at room temperature. After incubation, the membrane was washed 3 times for 10 min each. The secondary antibody streptavidin-HRP (Invitrogen, ELISA grade, 1.2 mg/mL) diluted 1:2500 in the blocking solution was added for 1-h incubation at room temperature with agitation. After that, the washing step was repeated three

times. The membrane was subsequently developed with chromogenic substrate reagent (BioRad) until the desired band intensity was achieved. Imaging was performed by using ChemiDoc imager (BioRad).

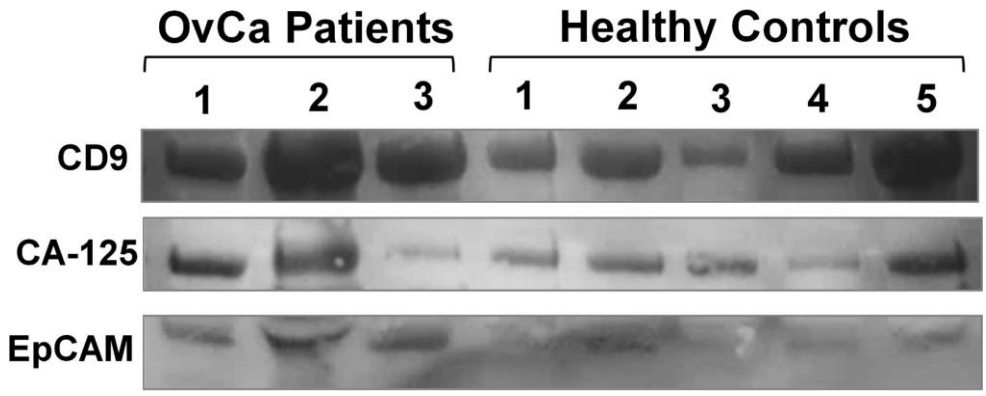

Figure 2.7. Western blotting analysis of expression levels of exosomal surface marker CD9, CA-125, and EpCAM. The plasma exosome samples were prepared from ovarian cancer patients and healthy controls using standard ultracentrifugation.

2.3.7. ExoSearch chip for blood-based ovarian cancer diagnosis

Currently, there is no single marker that can detect early-stage ovarian cancer with desired sensitivity and specificity (>98%).[49] A large number of combinations of biomarkers have been investigated to improve diagnostic sensitivity and specificity.[50] Circulating exosomes, enriched with a group of tumor antigens, provide a unique opportunity for cancer diagnosis using multi-marker combination. To this end, we employed the ExoSearch chip for blood-based diagnosis of ovarian cancer by simultaneously detecting three tumor antigens presented in the same exosome subpopulation. Standard Bradford assay of total protein levels in ultracentrifugation-purified exosomes from matched human subjects was performed for parallel comparison. Total of 20 human subjects (n_{OvCa}=15, $n_{healthy}$=5) were chosen for evaluating diagnostic accuracy, based on receiver operator characteristic analysis of adequate sample size (Table 2.2). Both ExoSearch and Bradford assay showed significantly increased level of exosome proteins from ovarian cancer

patients, compared to healthy controls (Figure 2.8a, Bradford assay p=0.001; ExoSearch chip p<0.001). Particularly, the ExoSearch chip gave individual exosomal protein expression level and the levels of CA-125 and EpCAM showed extremely significant differences between ovarian cancer patients and healthy controls (EpCAM, p=0.0009; CA-125, $p<10^{-4}$). The area under the receiver operator characteristic curve (a.u.c.) represents the overall accuracy of a test (Table 2.4). To determine the diagnostic accuracy of ExoSearch chip assay, we analyzed the true positives (sensitivity) and false positives (one-specificity) by receiver operating characteristic (ROC) curves. The areas under the curves (a.u.c.) obtained for CA-125, EpCAM, and CD24 were 1.0, 1.0 and 0.91, respectively, which were comparable with standard Bradford assay (a.u.c.=1.0, 95% CI) (Figure 2.8b & c). However, the diagnostic accuracy of using exosomal particle concentrations measured by NTA was relative poor with the a.u.c. of only 0.67 (Figure 2.8c, Figure 2.9, 95% CI). It could be attributed to the variation of NTA measurement which gives relative large uncertainty in size and concentration.[50, 51] In addition, the results were consistent with recent reports showing that counting exosomes along was insufficient for cancer diagnosis and targeting specific exosome phenotypes could markedly improve the diagnostic accuracy.[52] By ROC analysis (Table 2.1), the ExoSearch chip assay was highly accurate in discriminating plasma exosomes from ovarian cancer patients versus healthy individuals. The above results suggested the ExoSearch chip enables sensitive multiplexed exosomal marker detection for blood-based diagnosis of ovarian cancer with significant predictive power. The combination of plasma exosomal markers CA-125, EpCAM, and CD24 provided desirable diagnostic accuracy for non-invasive, early detection of ovarian cancer (Table 2.1).

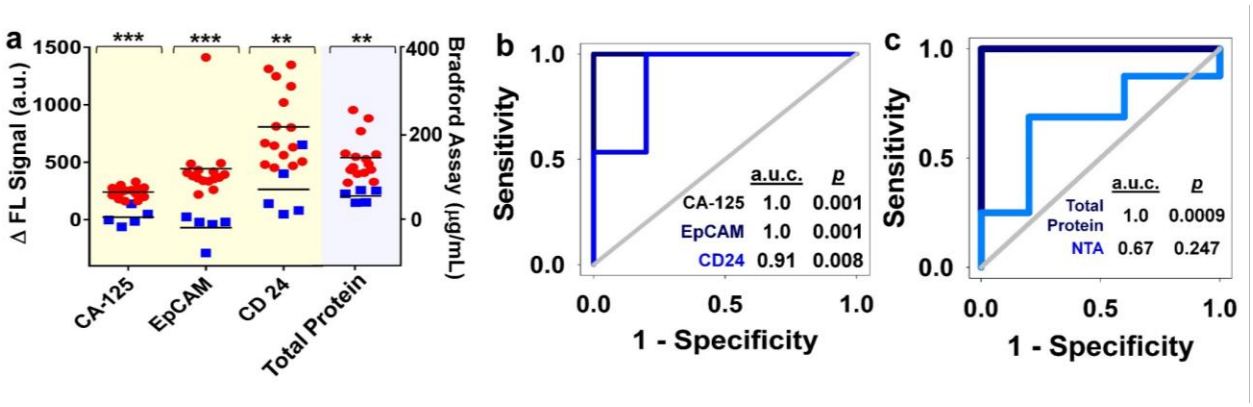

Figure 2.8. a) Scattering plots of expression levels of three tumor markers (CA-125, $p < 10^{-4}$; EpCAM, p = 0.0009; CD24, p = 0.003) from blood plasma derived exosomes (n_{OvCa}=15, $n_{healthy}$=5), compared to standard Bradford assay of total proteins (p = 0.0013) in ultracentrifugation-purified exosomes from matched human subjects. Black lines indicate average expression levels of each group. Ovarian cancer patients were represented by red dots, and healthy controls were represented by blue dots. **b)** ROC analysis of ExoSearch chip assay for in-situ, multiplexed detection of three ovarian tumor exosomal markers (CA-125 a.u.c.=1.0, p=0.001; EpCAM a.u.c.=1.0, p=0.001; CD24 a.u.c.=0.91, p=0.008). Confidence interval (CI) is 95%. **c)** ROC analysis of standard benchtop measurements (Bradford assay of total exosome protein, and NTA of exosome concentration) of blood plasma exosomes from matched patients in Fig 5b.

Table 2.1. Diagnostic accuracy analysis using the receiver operating characteristic curve

Test Variables	**ExoSearch chip**			**Bradford Assay/ Total Exosomal Protein**	**NTA/ Particle Concentration**
	CA125	EpCAM	CD24		
ROC Curve Area	1.000	1.000	0.9067	1.000	0.6750
Standard Error	0.000	0.000	0.0903	0.000	0.1332
95% Confidence Interval	1.000 To 1.000	1.000 To 1.000	0.729 To 1.084	1.000 To 1.000	0.413 To 0.936
P Value	0.0010	0.0010	0.0078	0.0009	0.2477

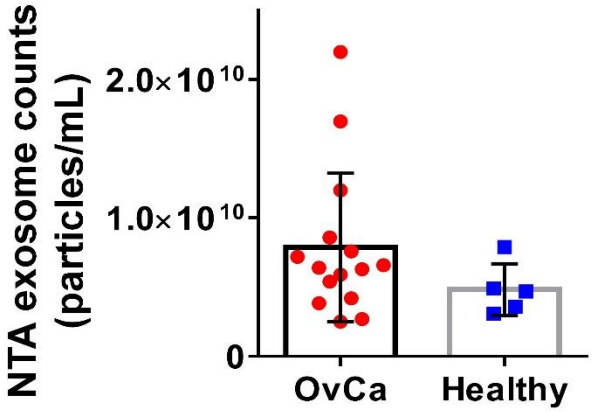

Figure 2.9. The plasma exosome particle concentrations from 20 human subjects measured by NTA (n_{OvCa}=15, $n_{healthy}$=5). Slightly higher average amount of plasma exosomes (1.5 fold) was observed from ovarian cancer patients, compared to healthy controls (p=0.25). The difference was not significant.

2.3.8. Reagents, antibodies and human samples.

The detection antibodies used in this study are CA-125 (B2626M, Meridian Life Science) conjugated with Alexfluor-488, EpCAM (323/A3, Thermo Scientific Pierce) conjugated with Alexfluor-550, CD24 (eBioSN3, eBioscience) conjugated with Alexfluor-633, HE4 (EPR4743, abcam) conjugated with Cyanine 5. The capture antibodies used in this study are CD9 biotin (C3-3A2, Ancell), CD81 biotin (1.3.3.22, Ancell), and CD63 biotin (H5C6, BioLegend). Exosome capture beads (Dynal beads M-270 Streptavidin, 2.8 μm in diameter) were obtained from Invitrogen and coupled with capture antibody through biotin-streptavidin linkage per the instruction, generating typical binding capacity of ~10 μg biotinylated antibody per 1 mg of beads. Antibodycoated beads (0.1 mg/mL) was introduced into microfluidic device for mixing with human blood plasma at varaible flow rates precisly controled by a programmable syringe pump. The human blood plasma were obtained from University of Kansas Cancer Center's Biospecimen Repository following consents and standard protocols.

Table 2.2. The list of human samples used in this study

OvCa Patients	**Age**	**Cancer stage***	**Treatment**	**Sample**
1.	72	T3N0M0	N	Blood Plasma
2.	67	T2NXM1	N	Blood Plasma
3.	70	T3N0M0	N	Blood Plasma
4.	80	T3N1M1	N	Blood Plasma
5.	65	T3N0M0	N	Blood Plasma
6.	61	T3N1MX	N	Blood Plasma
7.	76	T3N0M0	N	Blood Plasma
8.	74	T2N0M0	N	Blood Plasma
9.	64	T3N1MX	N	Blood Plasma
10.	78	T3N1MX	N	Blood Plasma
11.	66	T3N1MX	N	Blood Plasma
12.	75	T2N1MX	N	Blood Plasma
13.	67	T3N1MX	N	Blood Plasma
14.	55	T3N0M0	N	Blood Plasma
15.	53	T3N1M0	N	Blood Plasma
	Age	**Status**	**Treatment**	**Sample**
1.	51	Healthy	-	Blood Plasma
2.	53	Healthy	-	Blood Plasma
3.	50	Healthy	-	Blood Plasma
4.	52	Healthy	-	Blood Plasma
5.	53	Healthy	-	Blood Plasma

De-identified samples and matching information were obtained from University of Kansas Cancer Center's Biospecimen Repository following consents and standart protocols.

2.3.9. Sample size justification

Estimating the required sample size to adequately train developed diagnostic assay is of great practical importance.[53] We calculated the required sample size for evaluating diagnostic accuracy, by comparing the area under a ROC curve with a null hypothesis value of 0.5. The

sample size takes into account the required significance level of 0.05 and 80% power of the test. The statistical power 0.8 and sample ratio of 3 were chosen for statistical judgment with 0.2 probability of type I error α and 0.2 probability of type II error. Thus the sample size computational table was listed below in Table 2.3. The sample size of total 20 (15 ovarian cancer patients and 5 healthy controls) is adequate to evaluate diagnostic accuracy with acceptable diagnostic power.

Table 2.3. Sample size justification with desired errors

		Type I error- α	
		0.20	0.05
Type II error- β	0.20	**15+5**	27+9
	0.05	27+9	42+14

2.3.10. Diagnostic accuracy

Sensitivity and specificity are terms used to evaluate a clinical test. Receiver operator characteristic curve is a plot of (1−specificity) of a test on the x-axis against its sensitivity on the y-axis for all possible cut-off points. The area under this curve (a. u. c.) represents the overall accuracy of a test, with a value approaching 1.0 indicating a high sensitivity and specificity. The a.u.c. is a global measure of diagnostic accuracy. By comparison of areas under ROC curves, we can estimate which one of the tests is more suitable for distinguishing health from disease. The accuracy classification for a diagnostic test is listed below.[54, 55]

Table 2.4. Accuracy classification by a.u.c. for a diagnostic test

a.u.c. Range	**Classification**
0.9 < a.u.c. < 1.0	Excellent
0.8 < a.u.c. < 0.9	Good
0.7 < a.u.c. < 0.8	Worthless
0.6 < a.u.c. < 0.7	Not good

We statistically analyzed the specificity and sensitivity using receiver operator characteristic curves for on-chip measurements (expression levels of CA=125, EpCAM, and CD24), compared to conventional benchtop measurements (Bradford assay of total exosome protein, and NTA of exosome particle concentration), from 20 human subjects (n_{OvCa}=15, $n_{healthy}$=5). On-chip assay of multiple exosomal proteins showed excellent diagnostic accuracy (CA-125 a.u.c.=1.0; EpCAM a.u.c.=1.0; CD24 a.u.c.=0.91), which was comparable with conventional Bradford assay of total exosome proteins (a.u.c.=1.0). However, NTA assay of exosome concentration was unable to give acceptable accuracy using particles number as the diagnostic value (a.u.c.=0.67).

2.4. Conclusions

Because exosomes differ 5-fold in size and 10^4-fold in concentration in biological samples, and can contain other membrane derived subcellular structures,[7] accurate measurement of exosome concentration in biofluids is challenging. For conventional approaches, such as NTA and flow cytometry, exosome quantitation is limited primarily by minimum detectable vesicle sizes, resulting in relative large variation (CV = ~20%).[51, 56] The ExoSearch chip enables simultaneous, quantitative evaluation of multiple markers from the same exosome subpopulation with much improved measurement reproducibility (CV < 10%), indicating the good robustness of this method. Such robustness is essential for precision medicine and diagnostics involving exosomes. In addition, the continuous-flow design affords capability for obtaining distinct populations of exosomes from a wide range of preparation volumes (10 μL to 10 mL), which is useful for downstream comparative molecular profiling or therapeutic use.

As the surrogates of tumor cells, exosomes hold great promise for precise and personalized cancer diagnosis. Combinations of exosomal protein markers may constitute a "cancer signature" and provide improved detection as the first step in multimodal screening.[56] However, to our best knowledge, multiplexed assay of exosomes has not been well established yet. We demonstrated the feasibility of ExoSearch chip for non-invasive diagnosis of ovarian cancer using a combination of three exosomal tumor markers (CA-125, EpCAM, CD24), which showed comparable accuracy and diagnostic power (a.u.c. = 1.0, p = 0.001) with standard Bradford assay (a.u.c. = 1.0, p = 0.0009). However, the ExoSearch chip requires only 20 μL of human plasma for multiplexed detection of three tumor proteins within 40 mins, as compared to ~ 1 mL of plasma and ~ 12 hours required by Bradford assay.

To date, conventional tissue biopsy for pathological diagnosis of ovarian cancer is extremely invasive, as a difficult surgery. General imaging screenings, including tomography (CT) scans and magnetic resonance imaging (MRI) scans, are costly and unavailable in a majority of clinics. Therefore, blood-based assay for pre-screening is highly valuable and can dramatically decrease healthcare costs. The ExoSearch chip provides a cost-effective, accessible approach for specific, rapid isolation of blood diagnostic exosomes, paving the way for clinical utilization of exosomes. We will further validate diagnostic effectiveness of the ExoSearch chip in various sample cohorts and enhance disease discrimination power, including use of large-scale sample size and benign tumor group as a positive control. This work, as a preliminary proof-of-concept in discovery phase, is an essential step and could service as a basic platform for developing clinical tests in other diseases, as well as the fundamental laboratory research.

2.5. References

(1). Wendler, F.; Bota-Rabassedas, N.; Franch-Marro, X., Cancer becomes wasteful: emerging roles of exosomes(dagger) in cell-fate determination. *J Extracell Vesicles* **2013,** *2*.

(2). Melo, S. A.; Sugimoto, H.; O'Connell, J. T.; Kato, N.; Villanueva, A.; Vidal, A.; Qiu, L.; Vitkin, E.; Perelman, L. T.; Melo, C. A.; Lucci, A.; Ivan, C.; Calin, G. A.; Kalluri, R., Cancer Exosomes Perform Cell-Independent MicroRNA Biogenesis and Promote Tumorigenesis. *Cancer Cell* **2014,** *26* (5), 707-721.

(3). Alderton, G. K., Metastasis. Exosomes drive premetastatic niche formation. *Nat Rev Cancer* **2012,** *12* (7), 447.

(4). Camussi, G.; Deregibus, M. C.; Bruno, S.; Cantaluppi, V.; Biancone, L., Exosomes/microvesicles as a mechanism of cell-to-cell communication. *Kidney Int* **2010,** *78* (9), 838-848.

(5). Thery, C.; Zitvogel, L.; Amigorena, S., Exosomes: composition, biogenesis and function. *Nat Rev Immunol* **2002,** *2* (8), 569-79.

(6). Iero, M.; Valenti, R.; Huber, V.; Filipazzi, P.; Parmiani, G.; Fais, S.; Rivoltini, L., Tumour-released exosomes and their implications in cancer immunity. *Cell Death Differ* **2008,** *15* (1), 80-88.

(7). Raposo, G.; Stoorvogel, W., Extracellular vesicles: Exosomes, microvesicles, and friends. *J Cell Biol* **2013,** *200* (4), 373-383.

(8). Muller, L.; Hong, C. S.; Stolz, D. B.; Watkins, S. C.; Whiteside, T. L., Isolation of biologically-active exosomes from human plasma. *J Immunol Methods* **2014,** *411*, 55-65.

(9). Alikhani, V. S.; Malmer, A.; Ekstrom, K.; Bossios, A.; Sjostrand, M.; Lotvall, J., Exosomes detected in human blood plasma. *Allergy* **2007,** *62*, 452-452.

(10). Dejong, C. H.; Earnshaw, J. J., Surgical innovation. *Br J Surg* **2015,** *102* (2), e8-9.

(11). Alderton, G. K., DIAGNOSIS Fishing for exosomes. *Nature Reviews Cancer* **2015,** *15* (8), 453-453.

(12). Momen-Heravi, F.; Balaj, L.; Alian, S.; Mantel, P. Y.; Halleck, A. E.; Trachtenberg, A. J.; Soria, C. E.; Oquin, S.; Bonebreak, C. M.; Saracoglu, E.; Skog, J.; Kuo, W. P., Current methods for the isolation of extracellular vesicles. *Biol Chem* **2013,** *394* (10), 1253-1262.

(13). Greening, D. W.; Xu, R.; Ji, H.; Tauro, B. J.; Simpson, R. J., A protocol for exosome isolation and characterization: evaluation of ultracentrifugation, density-gradient separation, and immunoaffinity capture methods. *Methods Mol Biol* **2015,** *1295*, 179-209.

(14). Taylor, D. D.; Zacharias, W.; Gercel-Taylor, C., Exosome isolation for proteomic analyses and RNA profiling. *Methods Mol Biol* **2011,** *728*, 235-46.

(15). Jeppesen, D. K.; Hvam, M. L.; Primdahl-Bengtson, B.; Boysen, A. T.; Whitehead, B.; Dyrskjot, L.; Orntoft, T. F.; Howard, K. A.; Ostenfeld, M. S., Comparative analysis of discrete exosome fractions obtained by differential centrifugation. *J Extracell Vesicles* **2014,** *3*, 25011.

(16). Li, M.; Rai, A. J.; DeCastro, G. J.; Zeringer, E.; Barta, T.; Magdaleno, S.; Setterquist, R.; Vlassov, A. V., An optimized procedure for exosome isolation and analysis using serum samples: Application to cancer biomarker discovery. *Methods* **2015,** *87*, 26-30.

(17). Schageman, J.; Zeringer, E.; Li, M.; Barta, T.; Lea, K.; Gu, J.; Magdaleno, S.; Setterquist, R.; Vlassov, A. V., The complete exosome workflow solution: from isolation to characterization of RNA cargo. *Biomed Res Int* **2013,** *2013*, 253957.

(18). Rekker, K.; Saare, M.; Roost, A. M.; Kubo, A. L.; Zarovni, N.; Chiesi, A.; Salumets, A.; Peters, M., Comparison of serum exosome isolation methods for microRNA profiling. *Clin Biochem* **2014,** *47* (1-2), 135-8.

(19). Lobb, R. J.; Becker, M.; Wen, S. W.; Wong, C. S.; Wiegmans, A. P.; Leimgruber, A.; Moller, A., Optimized exosome isolation protocol for cell culture supernatant and human plasma. *J Extracell Vesicles* **2015,** *4*, 27031.

(20). Peng, P.; Yan, Y.; Keng, S., Exosomes in the ascites of ovarian cancer patients: origin and effects on anti-tumor immunity. *Oncol Rep* **2011,** *25* (3), 749-62.

(21). Beach, A.; Zhang, H. G.; Ratajczak, M. Z.; Kakar, S. S., Exosomes: an overview of biogenesis, composition and role in ovarian cancer. *J Ovarian Res* **2014,** *7*, 14.

(22). Fontana, S.; Saieva, L.; Taverna, S.; Alessandro, R., Contribution of proteomics to understanding the role of tumor-derived exosomes in cancer progression: state of the art and new perspectives. *Proteomics* **2013,** *13* (10-11), 1581-94.

(23). Aliotta, J. M., Tumor exosomes: a novel biomarker? *J Gastrointest Oncol* **2011,** *2* (4), 203-5.

(24). Kalra, H.; Adda, C. G.; Liem, M.; Ang, C. S.; Mechler, A.; Simpson, R. J.; Hulett, M. D.; Mathivanan, S., Comparative proteomics evaluation of plasma exosome isolation techniques and assessment of the stability of exosomes in normal human blood plasma. *Proteomics* **2013,** *13* (22), 3354-64.

(25). Koga, K.; Matsumoto, K.; Akiyoshi, T.; Kubo, M.; Yamanaka, N.; Tasaki, A.; Nakashima, H.; Nakamura, M.; Kuroki, S.; Tanaka, M.; Katano, M., Purification, characterization and biological significance of tumor-derived exosomes. *Anticancer Res* **2005,** *25* (6A), 3703-7.

(26). Liga, A.; Vliegenthart, A. D.; Oosthuyzen, W.; Dear, J. W.; Kersaudy-Kerhoas, M., Exosome isolation: a microfluidic road-map. *Lab Chip* **2015,** *15* (11), 2388-94.

(27). He, M.; Crow, J.; Roth, M.; Zeng, Y.; Godwin, A. K., Integrated immunoisolation and protein analysis of circulating exosomes using microfluidic technology. *Lab on a Chip* **2014,** *14* (19), 3773-3780.

(28). Davies, R. T.; Kim, J.; Jang, S. C.; Choi, E. J.; Gho, Y. S.; Park, J., Microfluidic filtration system to isolate extracellular vesicles from blood. *Lab Chip* **2012,** *12* (24), 5202-10.

(29). Santana, S. M.; Antonyak, M. A.; Cerione, R. A.; Kirby, B. J., Microfluidic isolation of cancer-cell-derived microvesicles from hetergeneous extracellular shed vesicle populations. *Biomed Microdevices* **2014,** *16* (6), 869-77.

(30). Kanwar, S. S.; Dunlay, C. J.; Simeone, D. M.; Nagrath, S., Microfluidic device (ExoChip) for on-chip isolation, quantification and characterization of circulating exosomes. *Lab Chip* **2014,** *14* (11), 1891-900.

(31). Zhu, L.; Wang, K.; Cui, J.; Liu, H.; Bu, X. L.; Ma, H. L.; Wang, W. Z.; Gong, H.; Lausted, C.; Hood, L.; Yang, G.; Hu, Z. Y., Label-Free Quantitative Detection of Tumor-Derived Exosomes through Surface Plasmon Resonance Imaging. *Anal Chem* **2014,** *86* (17), 8857-8864.

(32). Vaidyanathan, R.; Naghibosadat, M.; Rauf, S.; Korbie, D.; Carrascosa, L. G.; Shiddiky, M. J.; Trau, M., Detecting exosomes specifically: a multiplexed device based on alternating current electrohydrodynamic induced nanoshearing. *Anal Chem* **2014,** *86* (22), 11125-32.

(33). Im, H.; Shao, H.; Park, Y. I.; Peterson, V. M.; Castro, C. M.; Weissleder, R.; Lee, H., Label-free detection and molecular profiling of exosomes with a nano-plasmonic sensor. *Nat Biotechnol* **2014,** *32* (5), 490-5.

(34). Shao, H.; Chung, J.; Balaj, L.; Charest, A.; Bigner, D. D.; Carter, B. S.; Hochberg, F. H.; Breakefield, X. O.; Weissleder, R.; Lee, H., Protein typing of circulating microvesicles allows real-time monitoring of glioblastoma therapy. *Nat Med* **2012,** *18* (12), 1835-40.

(35). Thomas, S. N.; Liao, Z.; Clark, D.; Chen, Y.; Samadani, R.; Mao, L.; Ann, D. K.; Baulch, J. E.; Shapiro, P.; Yang, A. J., Exosomal Proteome Profiling: A Potential Multi-Marker Cellular Phenotyping Tool to Characterize Hypoxia-Induced Radiation Resistance in Breast Cancer. *Proteomes* **2013,** *1* (2), 87-108.

(36). Ji, H.; Greening, D. W.; Barnes, T. W.; Lim, J. W.; Tauro, B. J.; Rai, A.; Xu, R.; Adda, C.; Mathivanan, S.; Zhao, W.; Xue, Y.; Xu, T.; Zhu, H. J.; Simpson, R. J., Proteome profiling of exosomes derived from human primary and metastatic colorectal cancer cells reveal differential expression of key metastatic factors and signal transduction components. *Proteomics* **2013,** *13* (10-11), 1672-86.

(37). Crescitelli, R.; Lasser, C.; Szabo, T. G.; Kittel, A.; Eldh, M.; Dianzani, I.; Buzas, E. I.; Lotvall, J., Distinct RNA profiles in subpopulations of extracellular vesicles: apoptotic bodies, microvesicles and exosomes. *J Extracell Vesicles* **2013,** *2*.

(38). Tauro, B. J.; Greening, D. W.; Mathias, R. A.; Ji, H.; Mathivanan, S.; Scott, A. M.; Simpson, R. J., Comparison of ultracentrifugation, density gradient separation, and immunoaffinity capture methods for isolating human colon cancer cell line LIM1863-derived exosomes. *Methods* **2012,** *56* (2), 293-304.

(39). Bobrie, A.; Colombo, M.; Krumeich, S.; Raposo, G.; Thery, C., Diverse subpopulations of vesicles secreted by different intracellular mechanisms are present in exosome preparations obtained by differential ultracentrifugation. *J Extracell Vesicles* **2012,** *1*.

(40). Jiang, F.; Drese, K. S.; Hardt, S.; Kupper, M.; Schonfeld, F., Helical flows and chaotic mixing in curved micro channels. *Aiche J* **2004,** *50* (9), 2297-2305.

(41). Martel, J. M.; Toner, M., Inertial focusing in microfluidics. *Annu Rev Biomed Eng* **2014,** *16*, 371-96.

(42). Ng, A. H.; Uddayasankar, U.; Wheeler, A. R., Immunoassays in microfluidic systems. *Anal Bioanal Chem* **2010,** *397* (3), 991-1007.

(43). Lamparski, H. G.; Metha-Damani, A.; Yao, J. Y.; Patel, S.; Hsu, D. H.; Ruegg, C.; Le Pecq, J. B., Production and characterization of clinical grade exosomes derived from dendritic cells. *J Immunol Methods* **2002,** *270* (2), 211-26.

(44). Kharaziha, P.; Ceder, S.; Li, Q.; Panaretakis, T., Tumor cell-derived exosomes: a message in a bottle. *Biochim Biophys Acta* **2012,** *1826* (1), 103-11.

(45). Mahaweni, N. M.; Kaijen-Lambers, M. E.; Dekkers, J.; Aerts, J. G.; Hegmans, J. P., Tumour-derived exosomes as antigen delivery carriers in dendritic cell-based immunotherapy for malignant mesothelioma. *J Extracell Vesicles* **2013,** *2*.

(46). Runz, S.; Keller, S.; Rupp, C.; Stoeck, A.; Issa, Y.; Koensgen, D.; Mustea, A.; Sehouli, J.; Kristiansen, G.; Altevogt, P., Malignant ascites-derived exosomes of ovarian carcinoma patients contain CD24 and EpCAM. *Gynecol Oncol* **2007,** *107* (3), 563-71.

(47). Liang, B.; Peng, P.; Chen, S.; Li, L.; Zhang, M.; Cao, D.; Yang, J.; Li, H.; Gui, T.; Li, X.; Shen, K., Characterization and proteomic analysis of ovarian cancer-derived exosomes. *J Proteomics* **2013,** *80*, 171-82.

(48). Kristiansen, G.; Denkert, C.; Schluns, K.; Dahl, E.; Pilarsky, C.; Hauptmann, S., CD24 is expressed in ovarian cancer and is a new independent prognostic marker of patient survival. *Am J Pathol* **2002,** *161* (4), 1215-21.

(49). Nolen, B. M.; Lokshin, A. E., Biomarker testing for ovarian cancer: clinical utility of multiplex assays. *Mol Diagn Ther* **2013,** *17* (3), 139-46.

(50). Sokolova, V.; Ludwig, A. K.; Hornung, S.; Rotan, O.; Horn, P. A.; Epple, M.; Giebel, B., Characterisation of exosomes derived from human cells by nanoparticle tracking analysis and scanning electron microscopy. *Colloids Surf B Biointerfaces* **2011,** *87* (1), 146-50.

(51). van der Pol, E.; Coumans, F. A.; Grootemaat, A. E.; Gardiner, C.; Sargent, I. L.; Harrison, P.; Sturk, A.; van Leeuwen, T. G.; Nieuwland, R., Particle size distribution of exosomes and microvesicles determined by transmission electron microscopy, flow cytometry, nanoparticle tracking analysis, and resistive pulse sensing. *J Thromb Haemost* **2014,** *12* (7), 1182-92.

(52). Melo, S. A.; Luecke, L. B.; Kahlert, C.; Fernandez, A. F.; Gammon, S. T.; Kaye, J.; LeBleu, V. S.; Mittendorf, E. A.; Weitz, J.; Rahbari, N.; Reissfelder, C.; Pilarsky, C.; Fraga, M. F.; Piwnica-Worms, D.; Kalluri, R., Glypican-1 identifies cancer exosomes and detects early pancreatic cancer. *Nature* **2015,** *523* (7559), 177-82.

(53). Suresh, K.; Chandrashekara, S., Sample size estimation and power analysis for clinical research studies. *J Hum Reprod Sci* **2012,** *5* (1), 7-13.

(54). van Stralen, K. J.; Stel, V. S.; Reitsma, J. B.; Dekker, F. W.; Zoccali, C.; Jager, K. J., Diagnostic methods I: sensitivity, specificity, and other measures of accuracy. *Kidney Int* **2009,** *75* (12), 1257-1263.

(55). Zou, K. H.; O'Malley, A. J.; Mauri, L., Receiver-operating characteristic analysis for evaluating diagnostic tests and predictive models. *Circulation* **2007,** *115* (5), 654-7.

(56). Srivastava, A.; Filant, J.; Moxley, K. M.; Sood, A.; McMeekin, S.; Ramesh, R., Exosomes: a role for naturally occurring nanovesicles in cancer growth, diagnosis and treatment. *Curr Gene Ther* **2015,** *15* (2), 182-92.

Chapter 3: Microfluidic On-demand Engineering of Exosomes towards Cancer Immunotherapy

Extracellular Vesicles (EVs), particularly exosomes (30–150 nm), are an emerging delivery system in mediating cellular communications, which have been observed for priming immune responses by presenting parent cell signaling proteins or tumor antigens to immune cells. Therefore, preparation of antigenic exosomes that can play therapeutic roles, particularly in cancer immunotherapy, is emerging. However, standard benchtop methods (e.g., ultracentrifugation and filtration) lack the ability to purify antigenic exosomes specifically among other microvesicle subtypes, due to the non-selective and time-consuming (>10 h) isolation protocols. Exosome engineering approaches, such as the transfection of parent cells, also suffer from poor yield, low purity, and time-consuming operations. In this paper, we introduce a streamlined microfluidic cell culture platform for integration of harvesting, antigenic modification, and photo-release of surface engineered exosomes in one workflow, which enables the production of intact, MHC peptide surface engineered exosomes for cytolysis activation. The PDMS microfluidic cell culture chip is simply cast from a 3D-printed mold. The proof-of-concept study demonstrated the enhanced ability of harvested exosomes in antigen presentation and T cell activation, by decorating melanoma tumor peptides on the exosome surface (e.g., gp-100, MART-1, MAGE-A3). Such surface engineered antigenic exosomes were harvested in real-time from the on-chip culture of leukocytes isolated from human blood, leading to much faster cellular uptake. The activation of gp100-specific CD8 T cells which were purified from the spleen of 2 Pmel1 transgenic mice was evaluated using surface engineered exosomes prepared from murine antigen presenting cells. Antigen-specific CD8 T cell proliferation was significantly induced by the engineered exosomes compared to native, non-engineered exosomes. This microfluidic platform serves as an automated

and highly integrated cell culture device for rapid, and real-time production of therapeutic exosomes that could advance cancer immunotherapy.

3.1. Introduction

Extracellular Vesicles (EVs), especially exosomes in the nano-size range of 30 ~150 nm, have shown important roles in intercellular communications in recent decades.[1-4] Immune cell-derived exosomes have been well documented in the regulation of immune stimulation or suppression,[5, 6] driving inflammatory,[7] autoimmune[8] and infectious disease pathology.[9-11] Due to the formation of exosomes beginning with the creation of endosomes as the multivesicular bodies (MVBs), exosomes differ from other cellular membrane-derived microvesicles[12] in terms of molecular contents. Therefore, exosomes contain specific proteins and nucleic acids and represent their parent cell status and functions at the time of formation.[13, 14] Among many subtypes of exosomes, immunogenic exosomes with an intrinsic payload of MHC class I and II molecules and other co-stimulatory molecules are able to mediate immune responses,[15, 16] which opens up opportunities for the development of novel cancer vaccines and delivery in immunotherapy.[17-26]

Compared to other nano-sized delivery systems, such as lipid, polymers, gold, and silica material,[27-32] exosomes are living-cell derived, highly biocompatible nano-carriers with intrinsic payload, and exhibit much stronger flexibility in loading desired antigens for effective delivery.[33] Exosomes also eliminate allergenic responses without concerns of carrying virulent factors and avoid degradation or loss during delivery.[34, 35] However, the development of exosome-based vaccines is hindered by substantial technical difficulties in obtaining pure immunogenic exosomes.[36] The diverse subtypes of exosomes could confound the investigation on differentiating different cellular messages. On the other hand, molecular engineering of exosomes through either

membrane surface or internal loading could provide an untapped source for developing novel antigenic exosomes.[16] Bioengineered exosomes as emerging immunotherapeutics have gained substantial attention in developing a new generation of cancer vaccines, including recent phase-II trial using IFN-DC-derived exosomes loaded with MHC I/II restricted cancer antigens to promote T cell and natural killer (NK) cell-based immune responses in non-small cell lung cancer patients.[21, 37-41] Unfortunately, current exosome engineering approaches, such as the transfection or extrusion of parent cells and membrane permeabilization of secreted exosomes, suffer from poor yield, low purity, and time-consuming operations.[38, 42-45] Therefore, in this paper, we introduce a facile, 3D-printing molded PDMS microfluidic culture chip for solving this bottleneck problem. Due to the intrinsic features in automation and high-efficient mass transport, microfluidic systems overcome many of the drawbacks of benchtop systems and show superior performance in isolating,[46-51] detecting and molecular profiling exosomes.[52-56] However, the potential of the microfluidic platform for molecular engineering of exosomes has not been well-explored yet.[38] Herein, we developed the 3D molded PDMS microfluidic device which enables real-time harvesting, antigenic modification, and subsequent photo-release of intact, engineered antigenic exosomes on-demand. Specifically, we introduced a novel magnetic-nanoparticles functionalized with photo-cleavable, peptide affinity probe for capturing and on-demand releasing MHC-I positive exosomes via a light trigger. The photo-cleavable linker contains bi-functional groups of biotin and NHS chemistry for anchoring to the streptavidin immunomagnetic bead surface as well as keeping the other end of NHS group covalently bond with the MHC-I binding peptide via the primary amine. The MHC class I molecules are heterodimers and the two domains of α1 and α2 are folded to make up a groove for binding to 8–10 amino acid peptides (MHC-I binding peptide). Thus, the formed MHC-I/peptide binding complex can be displayed to cytotoxic T cells consequently for triggering

an immediate response from the immune system. The light release can restore the formed MHC-I/ peptide complex on the exosome membrane surface. The photo-release of modified exosomes in the microfluidic system can be well controlled spatially and temporally with ~95% release efficiency. Presently, the reported work on processing exosomes via microfluidic approaches are either in small quality or bound to solid surface/particles, and unable to release without extra capture probes/tags or stay intact for downstream therapeutic preparations.[57, 58] To the best of our knowledge, no comparable work has been reported for engineering cell-secreted antigenic exosomes in real time for advancing cancer immunotherapy. Such a functional-streamlined microfluidic cell culture system allows antigenic engineering of exosomes either through mediating their parent cell growth using stimulations, or direct molecular engineering on the surface of produced exosomes. The design of microfluidic continuous flow allows the accumulation and enrich of exosomes secreted from on-chip cultured cells in higher purity than benchtop ultracentrifugation. The inherent advantage of integration does not require using multiple instruments and significantly reduces the manual steps. Although the single culture chip device could be in-low production rate compared to benchtop batch processing, this platform can be amenable to scaling up in a multi-channel high-throughput format.

We studied several tumor antigenic peptides (e.g., gp-100, MAGE-A3, and MART-1) which are commonly used in developing cancer vaccines but difficult in delivery due to degradation. Our microfluidic system showed high-efficiency in engineering immunogenic exosomes (MHC I+), meanwhile, photo-releasing the intact functional exosomes downstream. We tested the cellular uptake of engineered exosomes by using antigen presentation cells, which displayed much-improved internalization ability compared to native, non-engineered exosomes. We also assessed the immunogenicity of engineered exosomes for activating transgenic mouse

isolated antigen-specific CD8 T cells, demonstrating their capacity to induce peptide-specific T cell proliferation and prove the viability and functionality of engineered exosomes towards application in cancer immunotherapy. This facile and low-cost microfluidic platform could serve as an investigation tool for understanding the roles of variable peptide-engineered exosomes in antitumor immune responses and cancer immunotherapy (See Figure 3.1).

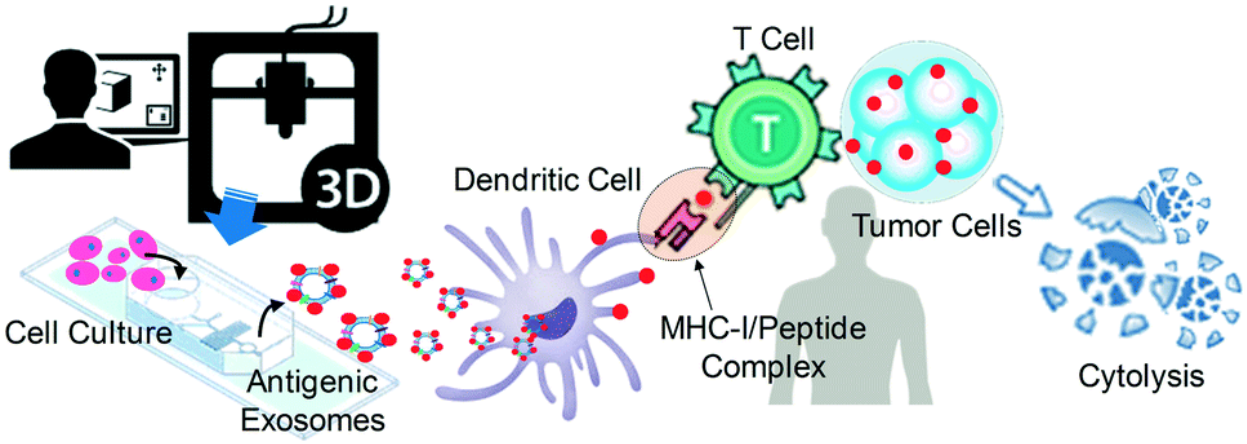

Figure 3.1. Illustration of 3D-printing molded PDMS microfluidic culture chip for streamlined engineering of antigenic exosomes employed in activating anti-tumor responses.

3.2. Experimental

3.2.1. 3D Printing and Fabrication of Microfluidic Culture Chip.

Three pieces of the molds were used for microfluidic PDMS chip fabrication, including a base, the side-wall molding, and top magnet holder. Molds were designed by using the SolidWorks® 2017 and printed out by the 3D printer (ProJet 1200 from 3D Systems). The finest structures printed by the 3D printer is in 30 μm. The height of the microfluidic channel is molded at 50 μm. The cylindrical cell culture chamber is molded in 1000-μm diameter and 500-μm height. All 3D-printed molds were sputtering coated with palladium in a thickness of 20 nm for easy release of molded-PDMS. Three pieces of molds were assembled to cast the PDMS microfluidic

cell culture device as shown in Figure 3.1, which was cast by a 10:1 ratio of Dow SYLGARD™ 184 silicone solution (Sigma-Aldrich) and incubated at the temperature of 40 °C for 6 hours. After a complete cure, the molded PDMS polymer can be peeled off easily. The molded cell culture chamber is open to the air and allows a PDMS-made plug to cap on the top. Chip inlets and outlets were formed by punching holes in 0.75 mm diameter. Piranha solution-cleaned glass slides and the PDMS layer were both treated with high-voltage plasma for at least 30 seconds, and then bond on the hot plate at the temperature of 40 °C for 5 mins. The formed microfluidic cell culture chip was cleaned by DI water, and then sterilized using autoclave at 121 °C for 30 mins.

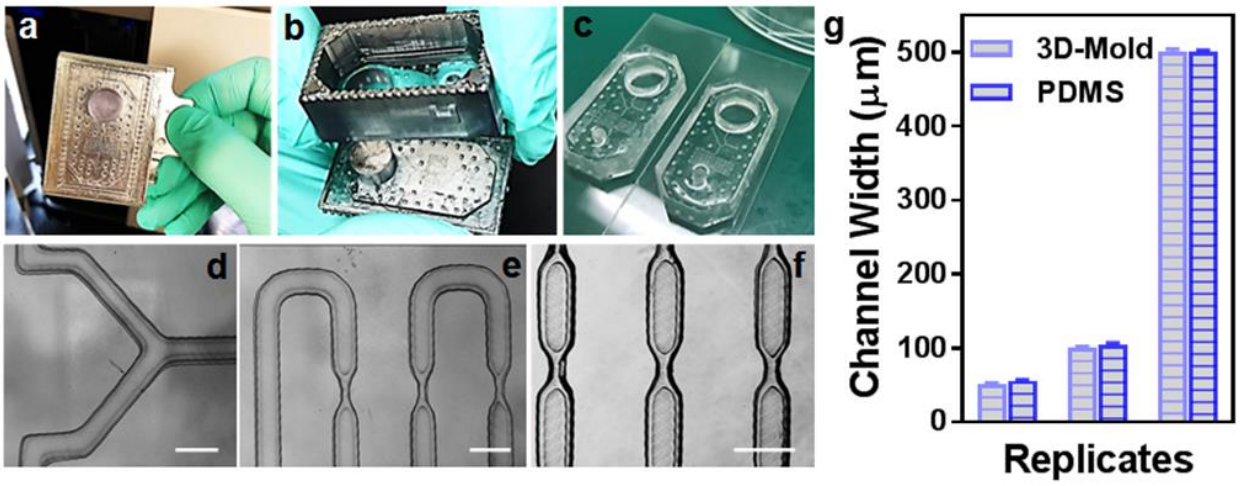

Figure 3.2. Illustration of 3D printing approach for one-step producing 3D mold and replicating PDMS microfluidic device integrated with cell culture and downstream exosome isolation, surface engineering, and on-demand photo release.

3.2.2. On-chip Cell Culture and Exosome Collection, Engineering, and Releasing.

The glass coverslip (8 mm) was autoclaved at 121 °C for 30 mins and treated with 500 uL of 0.1 mg/mL Poly-D-Lysine Hydrobromide (MP Biomedicals) before putting into the 24-well plate for cell seeding. Murine JAWSII cells (ATCC) or leukocytes isolated from human blood buffy coats (Innovative Research) were seeded in the 24-well plate which contains coverslips at

the bottom of wells in the biosafety cabinet. Thus, cell-seeded coverslip can be easily transferred to the microfluidic cell culture chamber which has the same diameter as the coverslip (8mm). The cell culture chamber is open to the air on the top for applying a PDMS-made, finger-push plug, which can produce pressure for flowing medium to downstream collection microchannel. The medium exchange can be performed via the open top using the pipette. The collection microchannel (B-Inlet) interconnects culture chamber at the bottom and an A-Inlet (200-μm wide and 200-μm high) for introducing immunomagnetic isolation beads to mix with eluted culture medium, as shown in Figure 3.3.

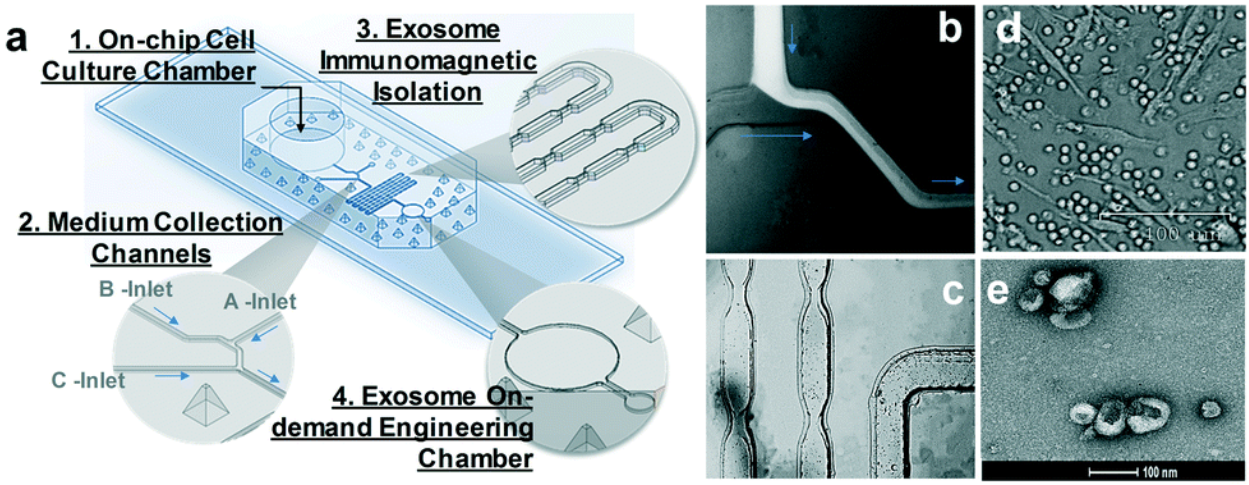

Figure 3.3. a) Illustration of 3D-printing molded microfluidic culture device for engineering immunogenic exosomes directly from on-chip cultured cells in real time. **b)** Fluorescence dye solution for showing the flow of immunomagnetic beads (A-Inlet) mixing with cell culture media (B-Inlet) eluted from the cell culture chamber. **c)** Bright-field microscopic image showing the immunomagnetic microbeads mixing process for isolating exosomes in the serpentine microchannel. **d)** Bright-field microscopic image showing the morphology of on-chip cultured leukocytes. **e)** SEM image showing the engineered exosomes released out of the chip.

For surface engineering of cell-secreted exosomes, a solution of β2-microglobulin at 20 μm/mL (Sigma-Aldrich, either human or murine) with synthesized tumor antigenic peptides at 100 μm/mL (MAGE-A3 from Genscript inc.; gp-100 and MART-1 were synthesized by KU Molecular

Probe Core) were prepared in the 1× PBS buffer as the antigenic loading buffer. The concentration of β2-microglobulin was experimentally optimized based on the reference.[16] As shown in Figure 3.3, by closing the B-inlet, antigenic loading buffer can be pumped through the A-inlet and the washing buffer can be pumped through the C-inlet into microfluidic channels at the volume flow rate of 1 μL/min or 0.1 μL/min for 10 mins. The washing step can be performed from both A-inlet and C-inlet at the volume flow rate of 1 μL/min for 15 mins. By taking off the magnet from the underneath of collection microchamber, the UV light via a UV objective can be projected to the magnetic beads aggregation area for photo-release of captured exosomes. The streptavidin magnetic beads (500 nm, Ocean Nanotech Inc) were conjugated with the Biotin-PC-NHS photo-cleavable linker (BroadPharm Inc.) and peptide probes per vendor's instruction. By applying another washing step from both A-inlet and C-inlet at the volume flow rate of 1 μL/min for 20 mins, the photo-released exosomes can be collected at the outlet of a microfluidic chip for subsequent in vitro or in vivo study.

3.2.3. Exosomes Staining and Cellular Uptake.

The microfluidically collected 20 μL exosomes were added to the ultracentrifuge tube and diluted to the final volume of 1 mL for centrifugation (Thermo Scientific™ Sorvall™ MTX) under 1,500 rcf for 30 mins. The supernatant was transferred to a fresh ultracentrifuge tube, and then centrifugated at the speed of 100,000 rcf for 1 hour. The cleaned exosomes were stained by using the PKH67 Green Fluorescent Cell Linker Midi Kit (Sigma-Aldrich) per vendor's instruction. For removing free dyes after exosome membrane dye labeling, 2 mL of FBS (exosome depleted) medium was added to quenching the free dye. The 1.5 mL of 0.971 M sucrose solution was prepared in complete media with total volume of 10 mL for density gradient centrifugation at

100,000 rcf for 1 hour. The supernatant was discarded after washing off the free dye. The 2 mL of 1× PBS was used to re-suspend the pellet. The 1 μL of Penicillin-Streptomycin (ATCC) was used to sterilize collected exosomes in solution. The collected final exosomes can be stored at 4°C for less than 1 week, and at −20°C for up to one month.

For cellular uptake experiments, the human THP-1 cell line (ATCC) was cultured using ATCC-formulated RPMI-1640 Medium plus 10 % exosome-depleted FBS. The cells used for uptaking exosomes were cultured at the density of 5×10^5/mL. The 20 μL native, non-engineered exosomes (NE) were added into 5 wells as the control group. The other 20 μL surface engineered exosomes (EE) were added into 5 wells separately as the experimental group. One extra well was set as a negative control. The incubation time intervals were set at 0 hour, 0.5 hour, 1 hour, 2 hours, 3 hours, and 4 hours. At each time point, cells were collected and suspended into 200 μL media for the cytocentrifugation at the speed of 400 rpm for 4 mins. The Fixative Solution (ThermoFisher) was used to cytospin cells and incubated at room temperature for 18 mins. The 100 μL of 1× PBS buffer was used to wash the fixed cells for three times. The slide was kept air-dry without any remaining water drops. The DAPI (ThermoFisher) was used to stain the cell nucleus per vendor's instructions. The ProLong™ Gold Antifade Mountant (ThermoFisher) was used and then covered with the coverslip without trapping any air bubbles. The prepared slides can be stored at room temperature for 24 hours before microscopic imaging.

For IFN-ɤ stimulation experiment, the gp-100 engineered exosomes and native, non-engineered exosomes were incubated with leukocytes in 96-well plate for monitoring stimulated cytokine secretion due to the antigen-specific immuno-responses. The red blood cell lysis, and human leukocytes culture and stabilization follow the standard protocols elsewhere (Innovative Research). The four different stimulation level of harvested exosomes were used (0 μL, 5 μL, 10

μL, 20 μL), and 20 μL was used as the best effective dose. The IFN-ɤ concentration from each condition (24 hr, 36 hr, and 48 hr) was measured using the IFN gamma ELISA Kit from Thermo Fisher with pokeweed mitogen protein as the positive stimulation control, per vendor's instruction. Three repeats were measured for calculating relative standard deviation (RSD).

3.2.4. In vitro CD8+ T Cell Activation and Flow Cytometry Analysis.

Female, CD8 T cell transgenic mice, aged 6–7 weeks, were purchased from Jackson Laboratories (B6.Cg-Thy1a/Cy Tg(TcraTcrb)8Rest/J). CD8 T cells from this strain express a transgenic T cell receptor that is specific for the gp-100 peptide of the premelanosome 17 protein. The murine monocyte JAWS-II cell line was purchased from ATCC. JAWS cells were cultured per ATCC recommendation and were maintained in alpha-MEM with ribonucleosides, deoxyribonucleosides, 4 mM L-glutamine, 1 mM sodium pyruvate, 5 ng/ml murine GM-CSF and 20% fetal bovine serum. For T cell co-culture studies, JAWS cells and T cells were maintained in complete RPMI composed of RPMI-1640 (Gibco, Carlsbad, CA) supplemented with 2 mm l-glutamine, 25 mm HEPES buffer, 1% antibiotic–antimycotic solution, 50 mg/mL gentamicin sulphate, 1% non-essential amino acids, 2% essential amino acids, 1% sodium pyruvate, 50 μm 2-mercaptoethanol and 10% (volume/volume) fetal bovine serum.

For T cell co-culture experiments, JAWS cells were activated 48 hours prior to the start of the experiment. JAWS cells were seeded at a concentration of 4×10^4 cells/well in cRPMI in a 96-well plate and were stimulated overnight at a concentration of 200 ng/mL Lipopolysaccharide (LPS). Parallel wells of JAWS cells remained unstimulated and were incubated overnight in media only. JAWSII cells were then washed twice with warm cRPMI.

Transgenic CD8 T cells were purified by magnetic cell separation per manufacturer's instructions (Miltenyi Biotech) and then labeled with Cell Trace Violet (Life Technologies). CD8 T cells were enumerated and plated at a concentration of 2×10^5 cells/well in cRPMI in wells alone (T cells only), with activated JAWSII cells or with normal JAWSII cells. Surface engineered exosomes were then added to the CD8 T cell cultures at increasing ratios of exosomes: dendritic cells (25, 50 and 100). Negative control wells did not receive exosomes. Positive control wells were stimulated with 5 ug/mL Conconavalin A. The cells and exosomes were co-cultured for 5 days. Cell cultures were then labeled with anti-mouse CD3 monoclonal antibody and anti-mouse CD8 monoclonal antibody (both from BD Biosciences) and CD8 T cells were analyzed by flow cytometry for Cell Trace Violet dilution. Cells were collected by a BD FACS Canto flow cytometer and the data were analyzed using FlowJo v10 (TreeStar).

3.3. Results and Discussions

3.3.1. 3D-printing Molded Microfluidic Cell Culture Device for Real-time Engineering and Harvesting Antigenic Exosomes.

In contrast to microfabrication conducted in a clean room, we introduce a facile and low-cost approach for making a PDMS microfluidic cell culture device via a 3D-printed mold (see Figure 3.1) with good molding reproducibility (RSD ~3%) and precision. This microfluidic culture device contains a cell culture chamber for on-chip growing cells and collecting exosomes in real time from eluted culture medium at downstream. The cell culture chamber is open to the air on the top for applying a PDMS-made, finger-push plug, which can produce pressure for flowing medium to downstream collection microchannel, as well as the medium exchange. The collection microchannel (B-Inlet) interconnects culture chamber at the bottom and an A-Inlet (200-μm wide

and 200-μm high) for introducing immunomagnetic isolation beads to mix with eluted culture medium, as shown in Figure 3.3. The consecutive narrow-neck microstructures (250 μm: 75μm ratio) in serpentine microchannel are shown in Figure 3.3 exploded isolation area for enhancing the mixing process. The C-Inlet is used to introduce the washing buffer driven by a syringe pump. Figure 3.3b demonstrated the mixing process through the A-Inlet and B-Inlet, and then exited to the exosome isolation serpentine channel by imaging a fluorescence dye solution using the fluorescence microscope. Figure 3.3c records the immunomagnetic beads mixing process within the serpentine channel. The microfluidic immunomagnetic beads mixing and capture of exosomes has been well studied previously by our group for achieving 100% mixing.[54] Human blood-derived leukocytes were cultured in the microfluidic culture chamber with the morphology shown in Figure 3.3d. Few red blood cells were observed as a cup shape, and the majority of cells were lymphocytes. The harvested exosomes from downstream of the microfluidic cell culture device were characterized by SEM imaging shown in Figure 3.3e, after on-chip immunomagnetic capture, isolation, and photo-release. The typical round cup shape in 100 nm was observed from harvested exosomes, which demonstrated the effective collection of cell secreted antigenic exosomes.

3.3.2. On-demand Photo-release of Surface Engineered Exosomes.

The current existing bead-based exosome isolation approach always delivers particles or solid surface-bound exosomes which inhibits further delivery of exosomes for cellular uptake or therapeutic applications. Therefore, we developed the conjugation of a photo-cleavable linker which contains bi-functional groups of biotin and NHS chemistry for anchoring to the streptavidin immunomagnetic bead surface, meanwhile, keeping the other end of NHS group covalently bond with the MHC-I binding peptide via the primary amine, as shown in Figure 3.4a. The MHC class

I molecules are heterodimers that consist of two polypeptide chain α, one noncovalent interaction domain of β2-microglobulin (β2m), and one α3 domain. The two domains of α1 and α2 are folded to make up a groove for binding to 8–10 amino acid peptides (MHC-I binding peptide). The formed MHC-I/peptide binding complex can be displayed to cytotoxic T cells consequently for triggering an immediate response from the immune system. Once the MHC-I positive exosomes are captured by tumor targeting antigenic (TTA) peptide and retained by immunomagnetic beads within the capture chamber under the magnetic field, the antigenic loading buffer with saturated TTA peptides can be introduced via C-Inlet to completely bind and replace the rest available MHC-I peptide binding sites. This antigenic surface engineering process can substantially enhance the loading amount of TTA peptides to the captured MHC-I positive exosomes and boost surface antigen presentation to activate T-cells.

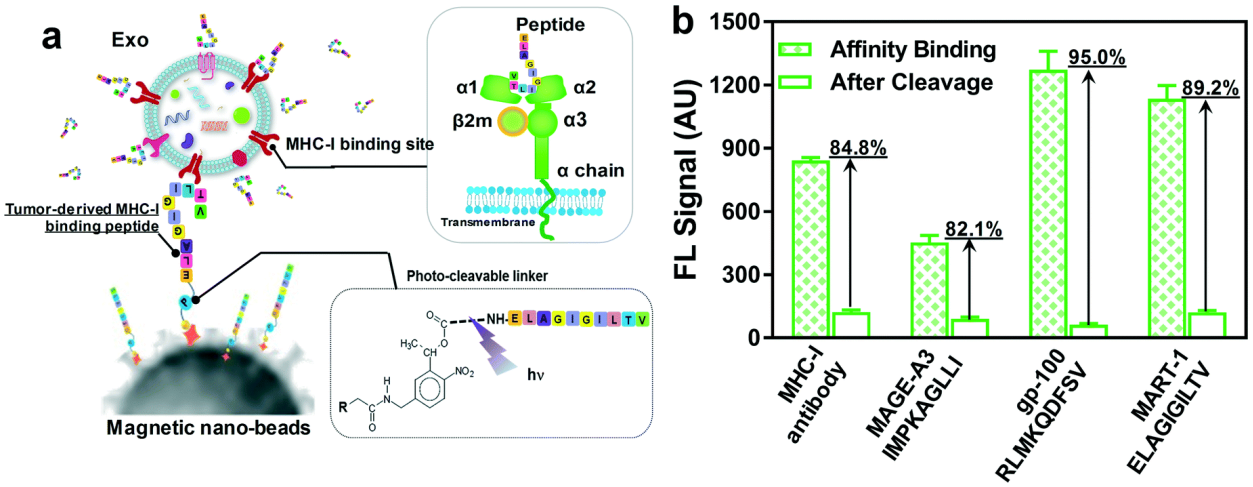

Figure 3.4. a) The illustration of immunomagnetic capture and on-demand photo-release of MHC-I positive, antigenic exosomes. **b)** Characterization of three tumor-targeting peptide antigens conjugated with photo-cleavable immunomagnetic beads for binding and photo-release of fluorescence-labeled immunogenic exosomes. The MHC-I antibody is used as the positive control. The error bar shows the three repeats with average measurement (RSD < ~5%).

For evaluating the binding strength between the MHC-I/peptide complex, several TTA MHC binding peptides were used as the affinity probe for capturing via photo-cleavable linker

conjugated immunomagnetic beads, as shown in Figure 3.4b. Herein, the MHC-I positive exosomes labeled with fluorescence can be captured via the MHC-peptide affinity binding. By comparing the fluorescence intensity of captured exosomes before and after photo-release, we can define the recovery rate for light-triggered harvesting. The MHC-I antibody serves as the positive control for capturing fluorescence-labeled exosomes and evaluating capacity that can form the MHC-I/peptide complex. As observed in Figure 3.4b, both gp-100 and MART-1 TTA peptides showed much higher fluorescence intensity compared to MHC antibody after affinity capture, which indicates the stronger binding complex formed between exo-MHC-I and gp-100 or MART-1 peptides. The gp-100 exhibits the highest recovery rate of 95% after photo-release. Due to the stronger binding capacity of MHC-I/peptide complex, the surface antigen presentation is more effective which can induce higher potency for activating T cell anti-tumor responses.[59, 60] We observed that gp-100 exhibited stronger ability to form MHC-I/peptide complex on exosome surface compared to other MART-1 and MAGE-A3 TTA peptides, and this MHC-I peptide binding capacity is even stronger than MHC-I antibody (95% vs 84.8%).

The performance of on-demand photo-release was characterized in Figure 3.5a. With the comparison between positive control and negative control, the evaluation of fluorescence-labeled exosomes on capture and photo-release was performed by measuring fluorescence intensity from beads aggregates under an invert fluorescence microscope. The SEM imaging approach was used to confirm the photo-release process as shown in Figure 3.5b & c. By comparing the SEM imaging of beads surface before and after photocleavage, there are no identifiable exosome particles presented on the surface of beads, indicating the good photo-release performance. The UV exposure time was characterized as well for reaching 98% photocleavage rate within 8-minute UV exposure (365 nm, ~ 2mW/cm^2). We evaluated the size distribution of photo-released, surface-

engineered exosomes for comparing with native exosomes, which showed an appropriate size range of exosomes between 50 nm – 200nm, confirming that surface-engineered exosomes are maintaining good integrity. The side-effect of UV exposure on exosome molecular contents was investigated in Figure 3.6, which showed non-detectable changes in terms of exosomal proteins, DNAs, and RNAs under 10-minute UV treatment. This result supports the photo-release of surface-engineered exosomes in good integrity and biological activity for subsequent cellular uptake and immune activation.

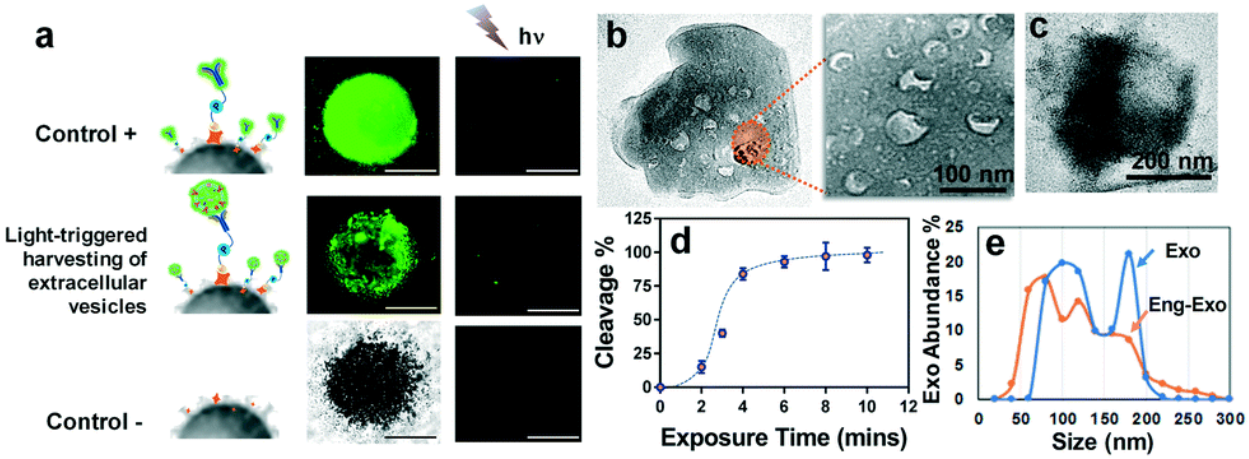

Figure 3.5. a) Characterization of the performance of on-demand photo-release of captured exosomes from immunomagnetic beads. The positive control is a fluorescence-labeled antibody captured by photo-release immunomagnetic beads. The negative control is the immunomagnetic beads without a photo-cleavable linker. **b)** The SEM image of the surface of photo-release immunomagnetic beads captured with exosomes. Exosome particles were seen as the cup shape due to the vacuum sample preparation. **c)** The SEM image of the surface of photo-release immunomagnetic beads after photocleavage. **d)** Characterization of UV exposure time influence on photo-cleavage efficiency. The error bar shows the three repeats with average measurement (RSD < ~5%). **e)** Nanoparticle tracking analysis of exosome size distribution between photo-released, surface engineered exosomes and native exosomes.

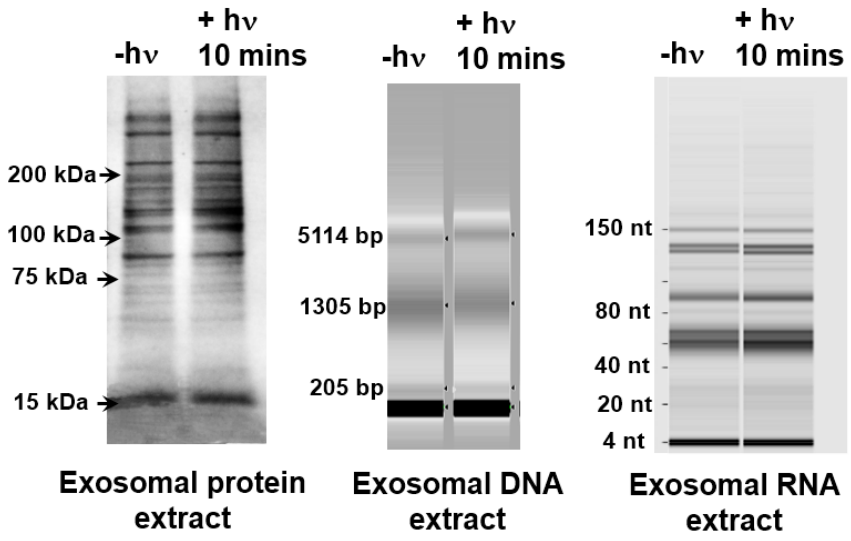

Figure 3.6. Investigation of the side-effect of UV exposure on exosome molecular contents in terms of proteins, DNAs and RNAs.

3.3.3. Immunogenic Potency of Surface Engineered Exosomes.

In order to evaluate the potency and integrity of surface-engineered exosomes which are photo-released from the microfluidic cell culture device, we labeled the harvested exosomes with green membrane dye PKH67, and then incubated both gp-100 engineered exosomes and native exosomes with the human monocytic THP1 cells, and monitored cellular uptake at one-hour intervals. After cell fixation and nucleus staining with DAPI, we observed abundantly distributed green dots as exosomes around the cell nucleus (Figure 3.8a), which is much more intense than uptake of native exosomes. The cellular uptake begins within one hour for both gp-100 engineered exosomes and native exosomes. However, the uptake capacity and speed is significantly greater for gp-100 engineered exosomes than native exosomes. After 4 hours, both gp-100 engineered exosomes and native exosomes were cleared by the lysosome pathway. This observation indicates that gp-100 engineered exosomes significantly enhanced the cellular uptake from dendritic monocytes by ~ 2 folds, compared to native exosomes (Figure 3.7).

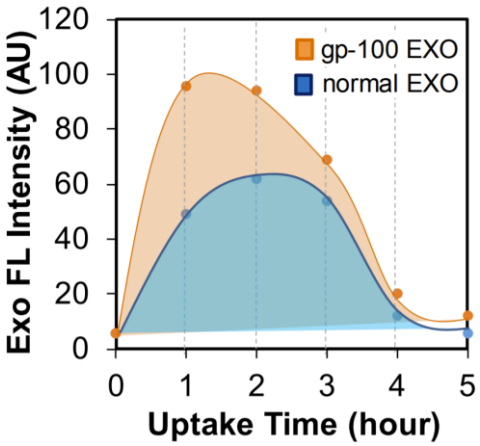

Figure 3.7. The fluorescence intensity analysis for showing the cellular uptake rate of gp-100 engineered exosomes and native exosomes.

We also monitored the expression of Cytokine IFN-ɤ from incubation of gp-100 engineered exosome with human leukocytes using ELISA. Compared with the stimulation from native exosomes, IFN-ɤ expression under gp-100 exosome stimulation is significantly higher by ~2-fold, with 48-hour continuous monitoring (Figure 3.8b). The gray dash line in the Figure 3.8b indicates the positive control using pokeweed mitogen protein as the stimulator. The leukocytes morphology upon stimulation was shown in Figure 3.9. Compared to the negative control without stimulation (yellow dash line), both pokeweed mitogen and gp-100 engineered exosomes significantly activated the immune lymphocytes and changed the morphology of leukocytes. The gp-100 engineered exosomes induced greater IFN-ɤ production than the control pokeweed mitogen. This result suggests that TTA peptide gp-100 engineered exosomes are rapidly internalized by antigen presenting cells and highly immunogenic for stimulating cytokine production.

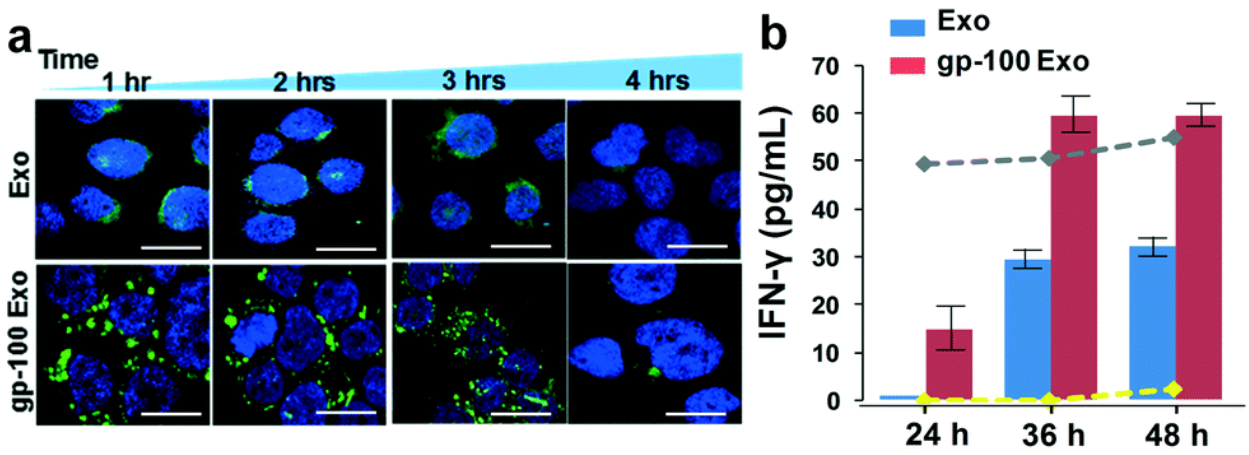

Figure 3.8. a) The confocal microscopic image of DC uptake of TTA peptide gp-100 surface engineered exosomes, compared with non-engineered native exosomes. The image was taken every one hour for tracking the green fluorescence labeled exosomes uptake by DCs (cell nucleus were stained with DAPI). The scale bar is about 5 μm. **b)** The release of Cytokine IFN-ɤ from DCs culture under stimulations between native exosomes and gp-100 engineered exosomes. The gray dash line indicates the positive control using pokeweed mitogen protein as the stimulator. The yellow dash line is the negative control without any stimulator. The error bar shows the three repeats with average measurement (RSD is ~5%).

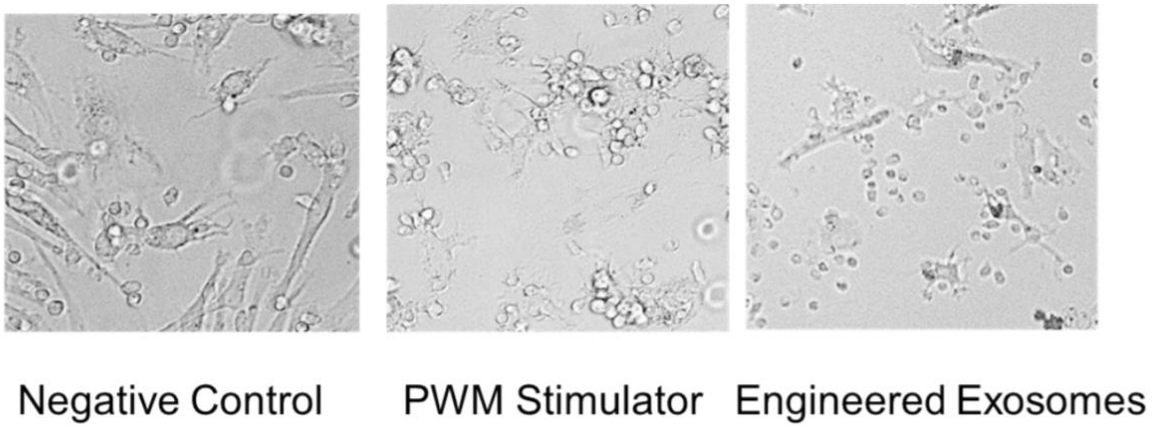

Figure 3.9. Human leukocytes culture under different stimulation conditions: 1) negative control is the leukocytes without any stimulation; 2) PWM protein stimulation as the positive control; 3) The gp-100 engineered exosome stimulation.

We further investigated the potency of gp-100 surface-engineered exosomes by testing their capacity to activate antigen-specific CD8+ T cells proliferation. Transgenic, gp100-specific

CD8 T cells were purified from the spleen of 2 Pmel1 transgenic mice by magnetic cell sorting and labeled with Cell Trace Violet proliferation dye. The purified T cells were cultured alone (T cells only), mixed at a 3:1 ratio with naïve JAWS cells (an immature dendritic cell line derived from a C57BL/6 mouse), T cells + JAWS cells, or JAWS cells that were activated for 48 hours with 200 ng/mL LPS (T cells + Activated JAWS cells). The surface-engineered exosomes bearing the gp100 peptide were added to the T cell cultures at increasing ratios of exosomes: dendritic cells (25, 50 and 100). The cells and exosomes were co-cultured for 5 days and then CD8 T cells were analyzed by flow cytometry for Cell Trace Violet dilution as a measure of T cell proliferation. As seen in Figure 3.10, surface-engineered exosomes alone had no capacity to induce antigen-specific T cell proliferation. However, in the presence of antigen presenting cells, gp100 surface-engineered exosomes stimulated significant CD8 T cell proliferation. The gp-100 exosomes induced the greatest proliferative response when cultured in the presence of LPS-activated JAWS cells, and this response was dose-dependent with ~30% proliferation rate of CD8+ T cells at the 100:1 ratio of exosomes:dendritic cells. These results have been further proved in Figure 3.11 with spiking 1 μM gp-100 peptide as the positive control which demonstrated that immuno celullar system we established here is highly responsive to gp-100. Note that our exosome loading amount of gp-100 is ~0.1 μM which is 10-fold lower than positive control. Three replicated measurements showed reproducible results with RSD < 5% in Figure 3.11. The gp-100 engineered exosomes used in the experiments were harvested from immature JAWS cells, and therefore may not carry the costimulatory molecules necessary to induce naïve T cell activation. It is still under the investigation that mature antigen presenting cells may secret exosomes with costimulatory moleucles,[61] which is the work beyond the proof-of-concept of the platform described here. Our results are consistent with prior studies showing the necessity of activated antigen presenting cells

in the optimal presentation of exosome-derived antigens in vitro.[19, 25, 62] Therefore, in addition to carrying antigen, exosomes promote the exchange of functional peptide-MHC complexes between DCs. Such a mechanism may increase the number of DCs bearing a particular peptide, thus amplifying the initiation of primary adaptive immune responses.[61] Thus, our developed microfluidic culture device with antigenic surface engineering and photo-release strategy could be a powerful tool for developing an effective exosome-based vaccine or delivery agents for priming immunity employed in Cancer Immunotherapy.

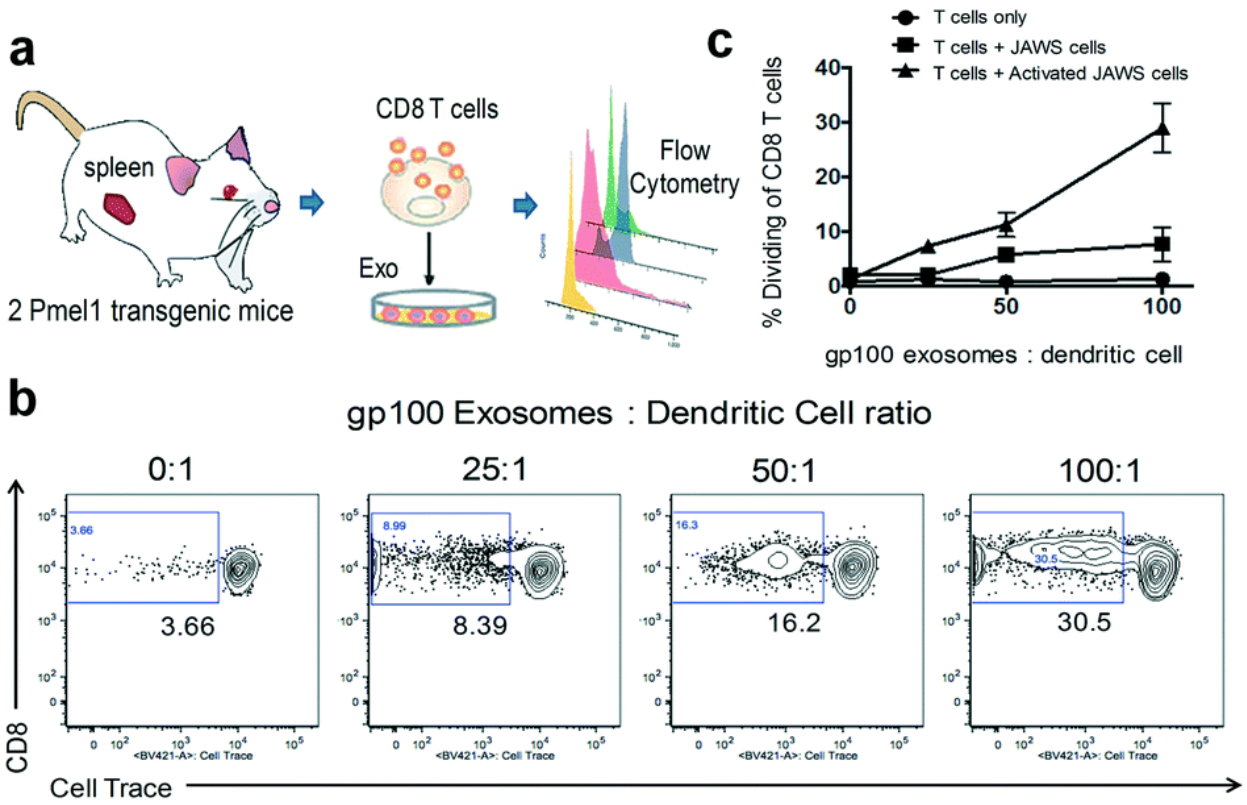

Figure 3.10. a) Illustration of ex vivo testing of surface-engineered exosomes for activating transgenic mice spleen-derived CD8+ T cells. **b)** depicts representative flow plots from wells containing T cells + Activated JAWS cells with increasing concentrations of the gp100-engineered exosomes. **c)** depicts the cumulative data from all three culture conditions showing the CD8+ T cell dividing rate under stimulation. The results are representative of 2 independent experiments with three duplicate wells for each culture condition (RSD < ~ 5%).

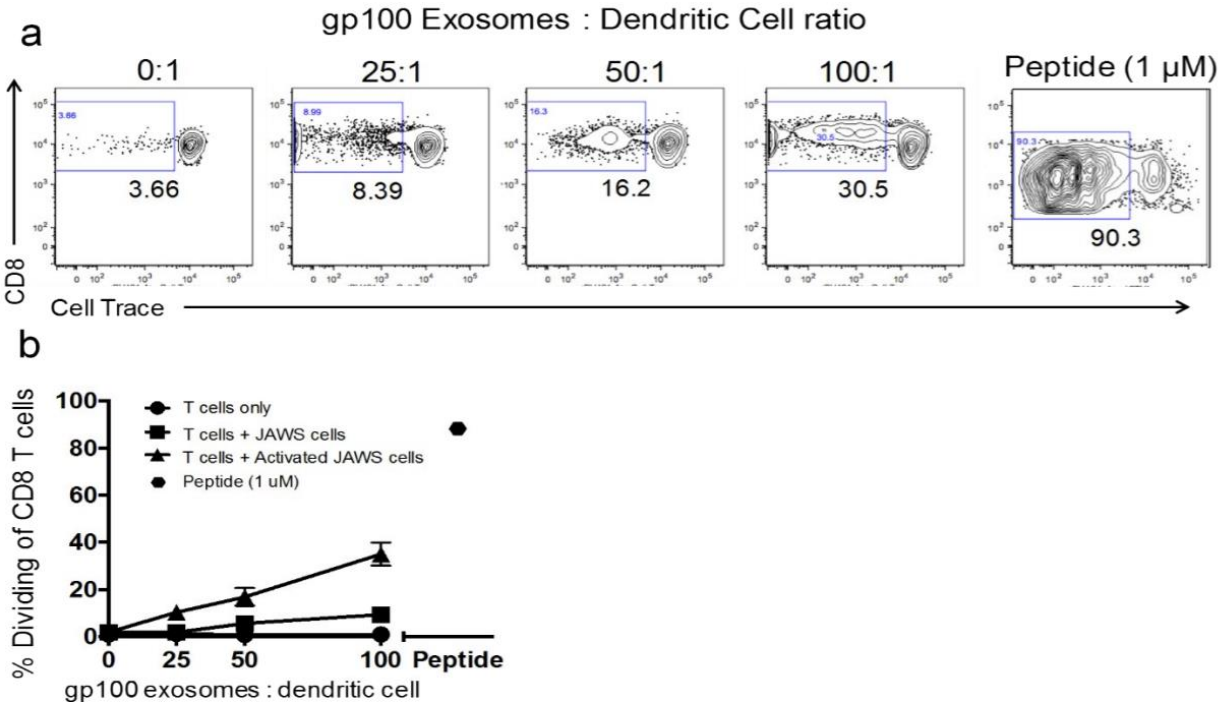

Figure 3.11. Ex vivo testing of surface-engineered exosomes for activating transgenic mice spleenderived CD8+ T cells. a) depicts representative flow plots from wells containing T cells + Activated JAWS cells with increasing concentrations of the gp100-engineered exosomes. The spiking gp-100 in μM serves as positive control. b) depicts the cumulative data from all four culture conditions showing the CD8+ T cell dividing rate under stimulation. The results are representative of 3 independent experiments with three duplicate wells for each culture condition (RSD < ~ 5%).

3.4. Conclusions

We demonstrated a simple microfluidic cell culture approach for real-time harvesting, antigenic modification, and photo-release of surface engineered exosomes within one workflow. The microfabrication of the device is straightforward by directly casting PDMS from a 3D printed mold using a consumer-grade 3D printer, without the needs of a clean room. The 3D-molded microstructures contain the z-dimension changes which are very challenging to be made by the conventional photolithographic approach using multi-layer bonding and alignment. The replication process is reproducible with RSD <3% and the variation between designed dimensions is ~5 μm with 30-μm printing precision (Figure 3.2).

The integrated antigenic modification and photo-release downstream of cell culture enable the real-time investigation of secreted exosomes in a dynamic process. Photo-release of exosomes with enhanced immunogenicity and biological activity has not been reported elsewhere. The recovery rate of released exosomes using our approach is ~95%. The entire operation duration using a microfluidic approach is about ~2 hrs for processing 4×10^4 cells seeded cells. This microfluidic approach is highly integrated compared to benchtop protocols which require multiple instruments for more than two days to complete the exosome isolation and peptide loading, such as using ultracentrifugation and incubation apparatus. Most importantly, our microfluidic immunomagnetic bead approach can specifically isolate MHC-I positive exosomes. In contrast, ultracentrifugation isolation approach only can get a mixture of EVs with lower yield (< 25%).[54] Our results demonstrated that 1) the engineered exosomes exhibit the strong capacity for uptake by antigen presenting cells; 2) the exosomes do carry the engineered peptides of interest (gp-100); and 3) they have the capacity to induce robust, antigen-specific CD8+ T cell proliferation compared to native exosomes. This developed microfluidic approach can serve as a powerful investigation tool for understanding the roles of variable peptide-engineered exosomes in antitumor immune responses and cancer immunotherapy. Although the current single culture chip design could be in-low production rate compared to benchtop batch processing, this platform can be amenable to scaling up in a multi-channel high-throughput format.

Current immunotherapy treatments can only benefit less than 15 % of patients, due to the poorly understood immunity modulation mechanism, and the lack of well-targeted delivery and clinical study designs that are optimized to determine maximum efficacy.[63-66] Immune cell-derived exosomes can be powerful vaccine templates for transferring stimulating factors, antigens, and drugs, which is highly promising by utilizing patient-derived exosomes for developing

personalized precision cancer vaccination.[40, 62, 67-70] Our developed microfluidic platform could serve as the powerful technology platform for facilitating this discovery in personalized cancer vaccines.

3.5. References

(1). Thery, C.; Zitvogel, L.; Amigorena, S., Exosomes: composition, biogenesis and function. *Nat Rev Immunol* **2002,** *2* (8), 569-79.

(2). Xu, R.; Rai, A.; Chen, M.; Suwakulsiri, W.; Greening, D. W.; Simpson, R. J., Extracellular vesicles in cancer - implications for future improvements in cancer care. *Nat Rev Clin Oncol* **2018,** *15* (10), 617-638.

(3). Pi, F.; Binzel, D. W.; Lee, T. J.; Li, Z.; Sun, M.; Rychahou, P.; Li, H.; Haque, F.; Wang, S.; Croce, C. M.; Guo, B.; Evers, B. M.; Guo, P., Nanoparticle orientation to control RNA loading and ligand display on extracellular vesicles for cancer regression. *Nat Nanotechnol* **2018,** *13* (1), 82-89.

(4). Thery, C., Cancer: Diagnosis by extracellular vesicles. *Nature* **2015,** *523* (7559), 161-2.

(5). Fujita, Y.; Kadota, T.; Araya, J.; Ochiya, T.; Kuwano, K., Extracellular Vesicles: New Players in Lung Immunity. *Am J Respir Cell Mol Biol* **2018,** *58* (5), 560-565.

(6). Hwang, I., Cell-cell communication via extracellular membrane vesicles and its role in the immune response. *Mol Cells* **2013,** *36* (2), 105-11.

(7). Buzas, E. I.; Gyorgy, B.; Nagy, G.; Falus, A.; Gay, S., Emerging role of extracellular vesicles in inflammatory diseases. *Nat Rev Rheumatol* **2014,** *10* (6), 356-64.

(8). Turpin, D.; Truchetet, M. E.; Faustin, B.; Augusto, J. F.; Contin-Bordes, C.; Brisson, A.; Blanco, P.; Duffau, P., Role of extracellular vesicles in autoimmune diseases. *Autoimmun Rev* **2016,** *15* (2), 174-83.

(9). Hosseini-Beheshti, E.; Grau, G. E. R., Extracellular vesicles as mediators of immunopathology in infectious diseases. *Immunol Cell Biol* **2018**.

(10). Fuhrmann, G.; Neuer, A. L.; Herrmann, I. K., Extracellular vesicles - A promising avenue for the detection and treatment of infectious diseases? *Eur J Pharm Biopharm* **2017,** *118*, 56-61.

(11). Schorey, J. S.; Harding, C. V., Extracellular vesicles and infectious diseases: new complexity to an old story. *J Clin Invest* **2016,** *126* (4), 1181-9.

(12). Raposo, G.; Stoorvogel, W., Extracellular vesicles: Exosomes, microvesicles, and friends. *J Cell Biol* **2013,** *200* (4), 373-383.

(13). Yu, X.; Odenthal, M.; Fries, J. W., Exosomes as miRNA Carriers: Formation-Function-Future. *Int J Mol Sci* **2016,** *17* (12).

(14). Brinton, L. T.; Sloane, H. S.; Kester, M.; Kelly, K. A., Formation and role of exosomes in cancer. *Cell Mol Life Sci* **2015,** *72* (4), 659-71.

(15). Andre, F.; Chaput, N.; Schartz, N. E.; Flament, C.; Aubert, N.; Bernard, J.; Lemonnier, F.; Raposo, G.; Escudier, B.; Hsu, D. H.; Tursz, T.; Amigorena, S.; Angevin, E.; Zitvogel, L., Exosomes as potent cell-free peptide-based vaccine. I. Dendritic cell-derived exosomes transfer functional MHC class I/peptide complexes to dendritic cells. *J Immunol* **2004,** *172* (4), 2126-36.

(16). Hsu, D. H.; Paz, P.; Villaflor, G.; Rivas, A.; Mehta-Damani, A.; Angevin, E.; Zitvogel, L.; Le Pecq, J. B., Exosomes as a tumor vaccine: enhancing potency through direct loading of antigenic peptides. *J Immunother* **2003,** *26* (5), 440-50.

(17). Jella, K. K.; Nasti, T. H.; Li, Z.; Malla, S. R.; Buchwald, Z. S.; Khan, M. K., Exosomes, Their Biogenesis and Role in Inter-Cellular Communication, Tumor Microenvironment and Cancer Immunotherapy. *Vaccines (Basel)* **2018,** *6* (4).

(18). Whiteside, T. L., The effect of tumor-derived exosomes on immune regulation and cancer immunotherapy. *Future Oncol* **2017,** *13* (28), 2583-2592.

(19). Tian, H.; Li, W., Dendritic cell-derived exosomes for cancer immunotherapy: hope and challenges. *Ann Transl Med* **2017,** *5* (10), 221.

(20). Syn, N. L.; Wang, L.; Chow, E. K.; Lim, C. T.; Goh, B. C., Exosomes in Cancer Nanomedicine and Immunotherapy: Prospects and Challenges. *Trends Biotechnol* **2017,** *35* (7), 665-676.

(21). Bell, B. M.; Kirk, I. D.; Hiltbrunner, S.; Gabrielsson, S.; Bultema, J. J., Designer exosomes as next-generation cancer immunotherapy. *Nanomedicine* **2016,** *12* (1), 163-9.

(22). Tran, T. H.; Mattheolabakis, G.; Aldawsari, H.; Amiji, M., Exosomes as nanocarriers for immunotherapy of cancer and inflammatory diseases. *Clin Immunol* **2015,** *160* (1), 46-58.

(23). Fatima, F.; Nawaz, M., Stem cell-derived exosomes: roles in stromal remodeling, tumor progression, and cancer immunotherapy. *Chin J Cancer* **2015,** *34* (12), 541-53.

(24). Romagnoli, G. G.; Zelante, B. B.; Toniolo, P. A.; Migliori, I. K.; Barbuto, J. A., Dendritic Cell-Derived Exosomes may be a Tool for Cancer Immunotherapy by Converting Tumor Cells into Immunogenic Targets. *Front Immunol* **2014,** *5*, 692.

(25). Viaud, S.; Thery, C.; Ploix, S.; Tursz, T.; Lapierre, V.; Lantz, O.; Zitvogel, L.; Chaput, N., Dendritic cell-derived exosomes for cancer immunotherapy: what's next? *Cancer Res* **2010,** *70* (4), 1281-5.

(26). Mignot, G.; Roux, S.; Thery, C.; Segura, E.; Zitvogel, L., Prospects for exosomes in immunotherapy of cancer. *J Cell Mol Med* **2006,** *10* (2), 376-88.

(27). Perez, S. E.; Carlucci, A. M., Lipid-based siRNA Nanodelivery Systems: A Learning Process for Improving Transfer from Concepts to Clinical Applications. *Curr Clin Pharmacol* **2018,** *13* (3), 142-163.

(28). Lu, M.; Xing, H.; Xun, Z.; Yang, T.; Zhao, X.; Cai, C.; Wang, D.; Ding, P., Functionalized extracellular vesicles as advanced therapeutic nanodelivery systems. *Eur J Pharm Sci* **2018,** *121*, 34-46.

(29). Irimie, A. I.; Sonea, L.; Jurj, A.; Mehterov, N.; Zimta, A. A.; Budisan, L.; Braicu, C.; Berindan-Neagoe, I., Future trends and emerging issues for nanodelivery systems in oral and oropharyngeal cancer. *Int J Nanomedicine* **2017,** *12*, 4593-4606.

(30). Aklakur, M.; Asharf Rather, M.; Kumar, N., Nanodelivery: An Emerging Avenue for Nutraceuticals and Drug Delivery. *Crit Rev Food Sci Nutr* **2016,** *56* (14), 2352-61.

(31). Ji, J.; Torrealba, D.; Ruyra, A.; Roher, N., Nanodelivery Systems as New Tools for Immunostimulant or Vaccine Administration: Targeting the Fish Immune System. *Biology (Basel)* **2015,** *4* (4), 664-96.

(32). Conniot, J.; Silva, J. M.; Fernandes, J. G.; Silva, L. C.; Gaspar, R.; Brocchini, S.; Florindo, H. F.; Barata, T. S., Cancer immunotherapy: nanodelivery approaches for immune cell targeting and tracking. *Front Chem* **2014,** *2*, 105.

(33). Aryani, A.; Denecke, B., Exosomes as a Nanodelivery System: a Key to the Future of Neuromedicine? *Mol Neurobiol* **2016,** *53* (2), 818-834.

(34). Bunggulawa, E. J.; Wang, W.; Yin, T.; Wang, N.; Durkan, C.; Wang, Y.; Wang, G., Recent advancements in the use of exosomes as drug delivery systems. *J Nanobiotechnology* **2018,** *16* (1), 81.

(35). Darband, S. G.; Mirza-Aghazadeh-Attari, M.; Kaviani, M.; Mihanfar, A.; Sadighparvar, S.; Yousefi, B.; Majidinia, M., Exosomes: natural nanoparticles as bio shuttles for RNAi delivery. *J Control Release* **2018,** *289*, 158-170.

(36). Tan, A.; De La Pena, H.; Seifalian, A. M., The application of exosomes as a nanoscale cancer vaccine. *Int J Nanomedicine* **2010,** *5*, 889-900.

(37). You, B.; Xu, W.; Zhang, B., Engineering exosomes: a new direction for anticancer treatment. *Am J Cancer Res* **2018,** *8* (8), 1332-1342.

(38). Zhu, Q.; Heon, M.; Zhao, Z.; He, M., Microfluidic engineering of exosomes: editing cellular messages for precision therapeutics. *Lab Chip* **2018,** *18* (12), 1690-1703.

(39). Li, Q.; Huang, Q.; Huyan, T.; Wang, Y.; Huang, Q.; Shi, J., Bifacial effects of engineering tumour cell-derived exosomes on human natural killer cells. *Exp Cell Res* **2018,** *363* (2), 141-150.

(40). Luan, X.; Sansanaphongpricha, K.; Myers, I.; Chen, H.; Yuan, H.; Sun, D., Engineering exosomes as refined biological nanoplatforms for drug delivery. *Acta Pharmacol Sin* **2017,** *38* (6), 754-763.

(41). Gilligan, K. E.; Dwyer, R. M., Engineering Exosomes for Cancer Therapy. *Int J Mol Sci* **2017,** *18* (6).

(42). Sato, Y. T.; Umezaki, K.; Sawada, S.; Mukai, S. A.; Sasaki, Y.; Harada, N.; Shiku, H.; Akiyoshi, K., Engineering hybrid exosomes by membrane fusion with liposomes. *Sci Rep* **2016,** *6*, 21933.

(43). García-Manrique, P.; Matos, M.; Gutiérrez, G.; Pazos, C.; Blanco-López, M. C., Therapeutic biomaterials based on extracellular vesicles: classification of bio-engineering and mimetic preparation routes. *J Extracell Vesicles* **2018,** *7* (1), 1422676.

(44). Kim, S. M.; Kim, H. S., Engineering of extracellular vesicles as drug delivery vehicles. *Stem Cell Investig* **2017,** *4*, 74.

(45). Lee, J.; Lee, H.; Goh, U.; Kim, J.; Jeong, M.; Lee, J.; Park, J. H., Cellular Engineering with Membrane Fusogenic Liposomes to Produce Functionalized Extracellular Vesicles. *ACS Appl Mater Interfaces* **2016,** *8* (11), 6790-5.

(46). Xu, H.; Liao, C.; Zuo, P.; Liu, Z.; Ye, B. C., Magnetic-Based Microfluidic Device for On-Chip Isolation and Detection of Tumor-Derived Exosomes. *Anal Chem* **2018,** *90* (22), 13451-13458.

(47). Hisey, C. L.; Dorayappan, K. D. P.; Cohn, D. E.; Selvendiran, K.; Hansford, D. J., Microfluidic affinity separation chip for selective capture and release of label-free ovarian cancer exosomes. *Lab Chip* **2018,** *18* (20), 3144-3153.

(48). Liu, C.; Guo, J.; Tian, F.; Yang, N.; Yan, F.; Ding, Y.; Wei, J.; Hu, G.; Nie, G.; Sun, J., Field-Free Isolation of Exosomes from Extracellular Vesicles by Microfluidic Viscoelastic Flows. *ACS Nano* **2017,** *11* (7), 6968-6976.

(49). Kanwar, S. S.; Dunlay, C. J.; Simeone, D. M.; Nagrath, S., Microfluidic device (ExoChip) for on-chip isolation, quantification and characterization of circulating exosomes. *Lab Chip* **2014,** *14* (11), 1891-900.

(50). Wang, Z.; Wu, H. J.; Fine, D.; Schmulen, J.; Hu, Y.; Godin, B.; Zhang, J. X.; Liu, X., Ciliated micropillars for the microfluidic-based isolation of nanoscale lipid vesicles. *Lab Chip* **2013,** *13* (15), 2879-82.

(51). Davies, R. T.; Kim, J.; Jang, S. C.; Choi, E. J.; Gho, Y. S.; Park, J., Microfluidic filtration system to isolate extracellular vesicles from blood. *Lab Chip* **2012,** *12* (24), 5202-10.

(52). Zhang, P.; He, M.; Zeng, Y., Ultrasensitive microfluidic analysis of circulating exosomes using a nanostructured graphene oxide/polydopamine coating. *Lab Chip* **2016,** *16* (16), 3033-42.

(53). He, M.; Crow, J.; Roth, M.; Zeng, Y.; Godwin, A. K., Integrated immunoisolation and protein analysis of circulating exosomes using microfluidic technology. *Lab on a Chip* **2014,** *14* (19), 3773-3780.

(54). Zhao, Z.; Yang, Y.; Zeng, Y.; He, M., A microfluidic ExoSearch chip for multiplexed exosome detection towards blood-based ovarian cancer diagnosis. *Lab Chip* **2016,** *16* (3), 489-96.

(55). Reátegui, E.; van der Vos, K. E.; Lai, C. P.; Zeinali, M.; Atai, N. A.; Aldikacti, B.; Floyd, F. P., Jr.; A, H. K.; Thapar, V.; Hochberg, F. H.; Sequist, L. V.; Nahed, B. V.; B, S. C.; Toner, M.; Balaj, L.; D, T. T.; Breakefield, X. O.; Stott, S. L., Engineered nanointerfaces for microfluidic isolation and molecular profiling of tumor-specific extracellular vesicles. *Nat Commun* **2018,** *9* (1), 175.

(56). Shao, H.; Im, H.; Castro, C. M.; Breakefield, X.; Weissleder, R.; Lee, H., New Technologies for Analysis of Extracellular Vesicles. *Chem Rev* **2018,** *118* (4), 1917-1950.

(57). Kang, Y. T.; Kim, Y. J.; Bu, J.; Cho, Y. H.; Han, S. W.; Moon, B. I., High-purity capture and release of circulating exosomes using an exosome-specific dual-patterned immunofiltration (ExoDIF) device. *Nanoscale* **2017,** *9* (36), 13495-13505.

(58). Li, P.; Kaslan, M.; Lee, S. H.; Yao, J.; Gao, Z., Progress in Exosome Isolation Techniques. *Theranostics* **2017,** *7* (3), 789-804.

(59). Koch, J.; Tampé, R., The macromolecular peptide-loading complex in MHC class I-dependent antigen presentation. *Cell Mol Life Sci* **2006,** *63* (6), 653-62.

(60). Jiang, J.; Natarajan, K.; Boyd, L. F.; Morozov, G. I.; Mage, M. G.; Margulies, D. H., Crystal structure of a TAPBPR-MHC I complex reveals the mechanism of peptide editing in antigen presentation. *Science* **2017,** *358* (6366), 1064-1068.

(61). Théry, C.; Duban, L.; Segura, E.; Véron, P.; Lantz, O.; Amigorena, S., Indirect activation of naïve CD4+ T cells by dendritic cell-derived exosomes. *Nat Immunol* **2002,** *3* (12), 1156-62.

(62). Delcayre, A.; Shu, H.; Le Pecq, J. B., Dendritic cell-derived exosomes in cancer immunotherapy: exploiting nature's antigen delivery pathway. *Expert Rev Anticancer Ther* **2005,** *5* (3), 537-47.

(63). Midgley, R.; Kerr, D., Immunotherapy for colorectal cancer: a challenge to clinical trial design. *Lancet Oncol* **2000,** *1*, 159-68.

(64). Makkouk, A.; Weiner, G. J., Cancer immunotherapy and breaking immune tolerance: new approaches to an old challenge. *Cancer Res* **2015,** *75* (1), 5-10.

(65). Abastado, J. P., The next challenge in cancer immunotherapy: controlling T-cell traffic to the tumor. *Cancer Res* **2012,** *72* (9), 2159-61.

(66). Vasievich, E. A.; Huang, L., The suppressive tumor microenvironment: a challenge in cancer immunotherapy. *Mol Pharm* **2011,** *8* (3), 635-41.

(67). Kibria, G.; Ramos, E. K.; Wan, Y.; Gius, D. R.; Liu, H., Exosomes as a Drug Delivery System in Cancer Therapy: Potential and Challenges. *Mol Pharm* **2018,** *15* (9), 3625-3633.

(68). Kim, S. M.; Yang, Y.; Oh, S. J.; Hong, Y.; Seo, M.; Jang, M., Cancer-derived exosomes as a delivery platform of CRISPR/Cas9 confer cancer cell tropism-dependent targeting. *J Control Release* **2017,** *266*, 8-16.

(69). Barile, L.; Vassalli, G., Exosomes: Therapy delivery tools and biomarkers of diseases. *Pharmacol Ther* **2017,** *174*, 63-78.

(70). Mahaweni, N. M.; Kaijen-Lambers, M. E.; Dekkers, J.; Aerts, J. G.; Hegmans, J. P., Tumour-derived exosomes as antigen delivery carriers in dendritic cell-based immunotherapy for malignant mesothelioma. *J Extracell Vesicles* **2013,** *2*.

Chapter 4: In-plane Nano-coulter Counter for Extracellular Vesicle Profiling

Extracellular vesicles (EVs) are evolving into an indispensable biomarker for liquid biopsies because of their unique biological and physical properties, which includes their molecular cargo, high abundance in body fluids, and prevalence even in early stage disease. There is clear evidence from previous studies that EVs can be used for cancer-related detection and screening. We have developed a platform for the isolation and enumeration of EVs with the combination of the EV-MAP (Micro-Affinity Purification) chip and the in-plane nano-Coulter counter (nCC) chip. With the platform, the quantity, concentration, and size distribution of enriched EVs can be rapidly profiled. Polystyrene beads with various sizes (46 nm and 100 nm) were used to calibrate the nCC chip and establish the analytical model. Furthermore, 16 ovarian cancer blood plasma samples were processed using anti-CD81 and anti-CA-125 immobilized EV-MAP chips and then released for downstream analysis by nCC chip. The results showed that the combination of the EV-MAP chip and nCC chips successfully characterized patients as to their ovarian cancer status and was able to provide tumor-related EV concentration of the samples. The combination platform has shown successful performance characteristics for EV isolation and enumeration from plasma samples, and the combination reduces the workflow and instrumentation requirements compared to conventional methods of enrichment, detection, and characterization of EVs.

4.1. Introduction

Extracellular vesicles (EVs) are lipid bilayer particles that are secreted by most living cells. Initially, EVs were described as a membrane fragment with cellular waste enclosed.[1] However, EVs have garnered widespread attention in recent years because both membrane markers and the intra-vesicle content have been verified with potential for disease diagnostic and therapeutic

purposes.[2-4] EVs can carry material belonging to the parental cells, including tetraspanins, lipids, RNAs, and cellular protein biomarkers. The cellular condition and phenotype can be understood by analyzing EV-associated components.[5-7]

There are three sub-types of EVs, including (1) apoptotic bodies (1 – 5 μm in size) released as blebbing of cells undergoing apoptosis; (2) microvesicles (100 nm – 1 μm) formed by regulated release of budding and blebbing of the plasma membrane; and (3) exosomes (30 – 150 nm) generated inside multivesicular bodies.[2, 8-10] The commonly used protocols for EV isolation are ultracentrifugation (UC), ultrafiltration, and precipitation methods. However, there are some limitations to the methods mentioned above, including pre-isolation requirements, long processing time, and expensive reagents.[11-14] Another critical limitation associated with the aforementioned isolation methods is the high levels of contamination. The major contaminants include large vesicles, unexpected sub-type of EV, proteins, and protein aggregates. The literature has reported that isolation methods based on the properties of size, lipid aggregation, or density can provide EV purity no more than 78.2% and can be as low as 11.4%.[15-17]

Many recent publications have ushered in the use of micro/nanofluidic technologies for EV isolation and quantification, which can significantly reduce the necessary reagents to microliter or even nanoliter scales, thus reducing assay cost.[18, 19] In addition, with the proper material and fabrication process, such as the use of thermoplastics for the microfluidic along with injection molding, the cost of each chip can be significantly reduced so that the platform can be supplied as a disposable, which is a requirement for *in vitro* diagnostic tests.[20-24] Our group has recently developed a microfluidic called EV-MAP, which was injection molded with the material of cyclic olefin copolymer (COC) serving as the substrate.[25] The EV-MAP chip can provide the ability to affinity-enrich EVs from various biological samples. In a previous publication, the EV-MAP was

used to affinity enrich EVs originating from T-cells to a concentration of ~10^{10} particles/mL to diagnose acute ischemic stroke (AIS) using mRNAs harvested from CD-7 expressing EVs. The assay and the associated microfluidic could potentially serve as a rapid point-of-care test (POCT) for rapid diagnosis of AIS to improve outcome for these patients. The recovery using the EV-MAP device was 96.6 ±1.3%. In addition, the EV-MAP could accommodate surface immobilization of different antibodies so that the chip is capable of collecting various EV types to make it applicable for other disease states. In summary, the EV-MAP shows strong performance for EV isolation and enrichment, and supports the ability to mass produce the microfluidic device for POCT.

Following the enrichment of EVs, they must be enumerated and analyzed to assure that EVs were indeed selected from the biological sample. For example, the International Society of Extracellular Vesicles (ISEV) recommends the following steps to confirm EV isolation: (i) TEM imaging; (ii) NTA analysis; (iii) positive for EV-related membrane protein markers, including the tetraspanins CD9, CD63, and CD81; and (iv) negative for certain cellular or extra-cellular markers, including apolipoproteins A1/2 and B (APOA1/2, APOB), and albumin (ALB).[26] From the ISEV list for confirming the presence of EVs, a number of instrumental techniques are necessary to fulfill these requirements, such as TEM,[27] NTA,[28, 29] and Western blotting to name a few.[30] Also, due to the small size of most EVs (exosomes' size range from 30 – 150 nm), the ability to use conventional flow cytometry as used for biological cells becomes intractable.[31, 32] In addition, the small size of most EVs also results in extremely small mass-loads of molecules and thus, requires high sensitivity techniques to analyze the molecular cargo of EVs.[33, 34]

Resistive-pulse sensing (RPS) has been engineered to analyze nanoparticles in recent years, which can be applied to determine the size and concentration of nanoparticles.[35] The RPS principle can be applied as an in-plane nano-coulter counter (nCC) to determine the size, concentration,

surface charge, and permeability of these particles.[36-39] Compared to NTA, nCC has higher resolution due to the electrical signal readout and smaller sample volume requirements.[37, 40-42] By collecting the electronic signal while particles are traveling through a nanopore, both size and concentration information can be acquired in a short time period. nCC has already been demonstrated for the analysis of virus,[42-45] bacteria,[46, 47] Au nanoparticles,[48, 49] cells,[41, 50, 51] proteins,[52, 53] and DNA.[54, 55] nCC has also been combined with microfluidic technology, which provides high-throughput sample processing capabilities, small device footprint, and simple electronics.[42] All of these advantages make RPS conjoined with microfluidics for enrichment and selection a valuable combination to enable POCT using EVs as the biomarker of choice.

We have developed an in-plane nano-coulter counter (nCC) device for EV sample profiling, including both size and concentration analysis. The sample was filled into the device and withdrawen through the nanochannel by hydrodynamic flow with a flow rate of approximately 10^{-7} μL/min. Whenever a nanoparticle translocates through the nanopore, a current amplitude change can be recorded and analyzed (Figure 4.1a & b). The nanopore was designed with a size of 200 nm × 200 nm × 100 nm (W × H × L) and could be fabricated by injection molding using poly(methylmethacrylate), PMMA, or any other plastic as the substrate material. The nCC chip has the capability to sense EVs <200 nm with a current amplifier to record the current signal trace to determine peak amplitude and width. A potential was clamped across the nanopore, and the resistance of the electrolyte in the device was considered as a series connection in the circuit. Whenever the EV traveled through the nanopore, the intra-vesicle content forms a parallel circuit with the nanopore, and Figure 4.1c shows the equivalent sensing circuit for the nCC chip, where R_{mc} is the resistance of the microchannel, R_{nc} is the resistance of the nanochannel, R_{np} is the resistance of the in-plane nanopore, and R_p is the resistance of the nanoparticle. Compared to other

technologies, our nCC chip has multiple advantages: (1) Due to the positioning of the nanopore sensing element with a fluidic network, the sample volume requirement is small (5 µL); (2) high-resolution electronic signal recordings can provide reliable and accurate information in terms of particle size (peak amplitude) and particle travel time (peak width); (3) dynamic range of 10^3 to 10^{16} particles/mL with a 100,000 Hz sampling frequency; (4) because of the sensing mechanism, the nCC is not only applicable to EVs but other nanoparticles such as viral particles; (5) because the device is made from a thermoplastic, it can be produced in a high production mode and at low cost to accommodate clinical applications. By combining the EV-MAP[25, 56] and nCC chips, we characterized 16 ovarian cancer patients and healthly control plasma samples and successfully characterized these samples as to their ovarian cancer status from CA-125 EV expression.

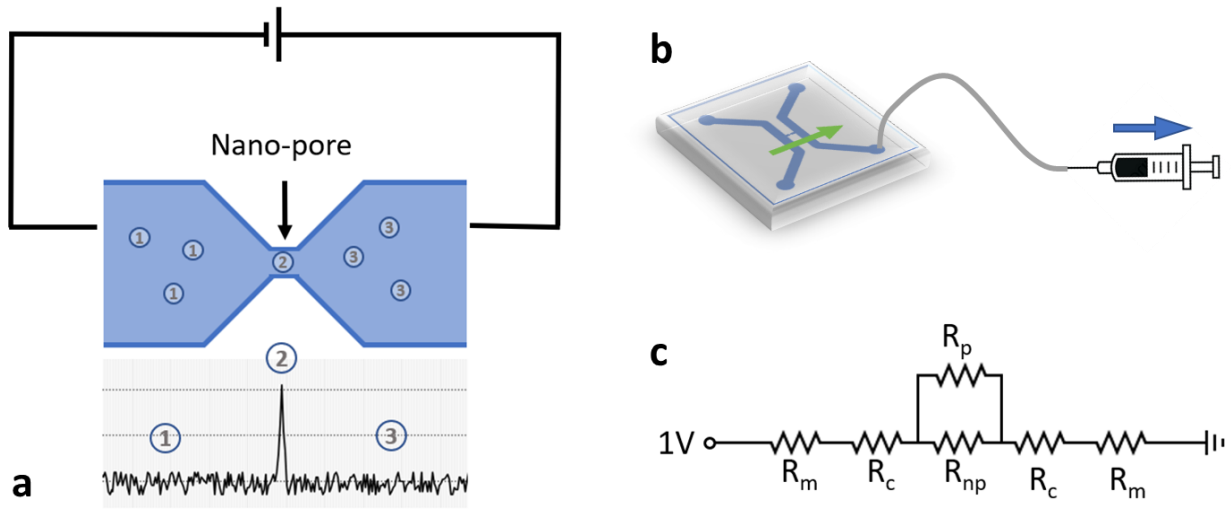

Figure 4.1. Operation of the nano-Coulter counter. **a)** Schematic showing the transport of an EV particle through the nano-coulter counter. Whenever an EV travels through the in-plane nanopore (position 2) with the hydrodynamic flow, from position 1 to position 3, an electrical signal is generated due to blockage (resistive pulse peak) of the pore by the EV. The EV size and concentration can be measured by analyzing the current amplitude and frequency of the resistive pulse peak. **b)** Hydrostatic pressure creates a flow through the nanopore, providing a flow rate as low as 10^{-7} µL/min. **c)** Equivalent sensing circuit for the nano-coulter counter, where R_{mc} is the resistance of the microchannel, R_{nc} is the resistance of nanochannel, R_{np} is the resistance of the in-plane nanopore, and R_{np} is the resistance of the nanoparticle. While a conductive nanoparticle traveling through the nanopore, the current streams through both particle and nanopore, thus the nanoparticle and nanopore can be considered as parallel configuration.

4.2. Experiments

4.2.1. Cyclic olefin copolymer (COC) EV-MAP chip fabrication and surface treatment.

Mold fabrication was accomplished using a commercial micromilling machine (KERN Micro- und Feinwerk Technik GmbH & Co.KG) as previously described and using brass as the material for the molding tool.[25, 57] Following machining, the brass mold was used for hot embossing. A 7.5 cm × 7.5 cm × 0.5 cm (L × W × H) COC plate (Topas Advanced Polymers) was used for hot embossing microchannels with a Precision Press model P3H-15-PLX (Wabash MPI). The Precision Press contained a heating module for real-time temperature control. The heating module was connected with both pressure and vacuum lines for heating and de-molding purposes. The hot embossing machine was located in a class 10,000 cleanroom to minimize particle contamination. Hot embossing consisted of the following stages: (i) The COC plate was set into the heating module with the temperature set at 162°C and vacuum on with a clamping force of 667 N for 60 s. (ii) The clamping force was then set with a linear ramp from 1779 to 4003 N over 30 s with a constant temperature set to 162°C. (iii) Both the temperature and clamping force conditions were kept constant for 300 s, and then the heating module was removed from the embossing machine. (iv) A cooling system was used to reduce the temperature from 162°C to 148°C, which is the glass transition temperature of the COC substrate. (v) A pressure airline was attached to the heating module once it reached 148°C and the brass mold was separated from the COC plate (*i.e.*, demolding). The channel features on the COC plate were checked under a microscope to determine replication fidelity.

Following embossing, the COC substrate and a COC cover plate were thermally fusion-bonded together to make a functional device. This was accomplished by cleaning the mating surfaces and then treated with UV/O_3 light for 13 min (254 /185 nm, 22 mV/cm^2). Finally, the

COC substrate and cover plate were clamped together with thermal fusion bonding at 134°C for 1 h. The performance of the EV-MAP chip were discussed in our previous published paper.[25]

4.2.2. EV capture and release using USER™ Enzyme.

To allow for enrichment of the CA-125 expressing EVs from a plasma sample followed by release for subsequent nCC counting, a heterobifunctional cleavable linker was used to covalently attach the anti-CA-125 monoclonal antibodies to the surface of the EV-MAP device. This bifunctional linker consisted of an oligonucleotide possessing a uracil (U) residue that could be subsequently cleaved enzymatically using an enzymatic mixture of Uracil DNA glycosylase (UDG) and DNA glycosylase-lyase Endonuclease VIII that can cleave the oligonucleotide at the U residue.[56] The UV/O_3 treated surfaces of the EV-MAP chip, which contained surface-confined carboxylic acid groups, were incubated with a solution containing 20 mg/mL EDC and 0.04 mM of the oligonucleotide bifunctional linker containing a primary amine group at its 5' end (Integrated DNA Technologies). The sequence of the bifunctional oligonucleotide linker used for the reaction was 5'/5AmMC 12/TTT TTT TTC CCT TCC TCC TCA CTT CCC TTT/ ideoxyU/TT TTT TTT T/3ThioMC3D/3' (MW = 12428.3 g/mol, and the melting temperature, T_m, = 61.2°C). The reaction solution was filled into the EV-MAP chip and the chip was kept at room temperature during the 2 h reaction. The anti-CA-125 (R & D Systems) and anti-CD81 (R & D Systems) monoclonal antibodies were dissolved separately into water with a succinimidyl 4-(N-maleimidomethyl) cyclohexane-1-carboxylate (SMCC) concentration of 0.06 mg/mL, and kept on a rocker at room temperature for 40 min to allow for coupling of the monoclonal antibodies to the 3' end of the bifunctional linker. The antibody-SMCC solution was also processed through Zebra™ Spin Desalting columns (Thermo Scientific) to remove excess SMCC. In a parallel step,

300 mM DTT in carbonate buffer (pH 10.8), which was filtered using a 0.45 µm filter, was injected into the chip at room temperature and kept for 30 min. The chip was quickly flushed with 1× PBS, and then filled with the conjugated antibody solution to allow the reaction with oligonucleotide biofunctional linker through a disulfide linkage. The chip was set at room temperature for 2 h. The DTT reduces the disulfide into a reactive sulfhydryl moiety (-S-H), which can react with the primary amine group of the antibody. Figure 4.2 shows the catch and release strategy to affinity select EVs from the sample and then release them for nCC enumeration.

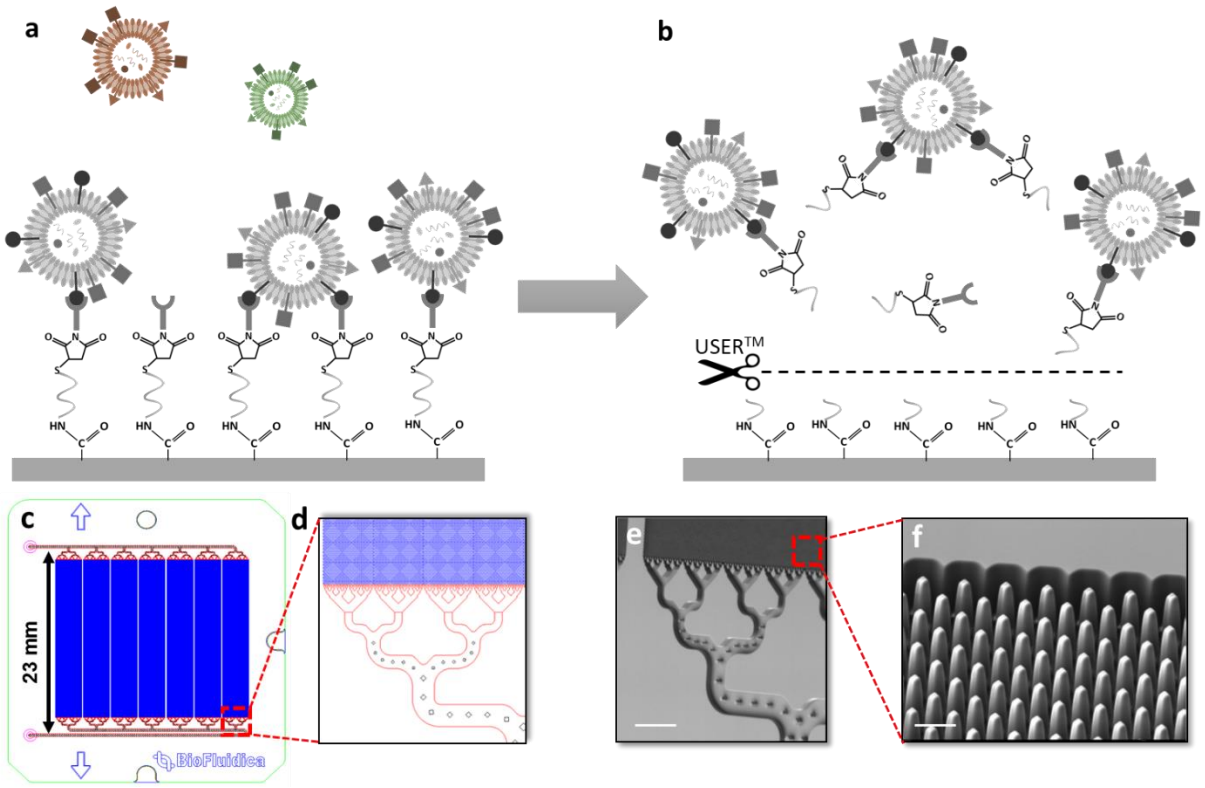

Figure 4.2. The schematic of the chip modification. **a)** With immobilized antibodies, the chip will gain the ability to capture the target proteins, leading to a specific sub-type of EV be captured on the chip. **b)** The USER™ enzyme was explicitly designed for the double-stranded DNA, and the captured EV will be released into the solution and can be collected for downstream analysis. **c)** 2D CAD drawing of EV-MAP chip at the top view. The bottom left and top left are the inlet/outlet. **d)** a zoomed-in view of the streaming channels to the pillar area. **e** & **g** The pillars under the scanning electron microscopy (SEM), scale bar = 300 µm and 25 µm, respectively.

Using the prepared EV-MAP chip, a 500 µL pre-wash buffer (0.5% BSA, 1% PVP, in 1X PBS) was passed through the chip at a flow rate of 10 µL/min for 30 min to reduce any non-specific binding. Then, a 200 µL plasma sample was sent through the chip using a robotic platform (Hamilton with software from Biofluidica) with a flow rate of 25 µL/min, and followed with a washing buffer (0.1% Tween-20, 1X PBS) at a flow rate of 10 µL/min. Fifteen µL of 0.2 U/µL USER^{TM} enzyme (New England Biolabs) was injected into the chip and kept at 37°C for 1 h to allow USER^{TM} to release the surface enriched EVs (Figure 4.2). Next, the washing buffer was sent through the chip at a flow rate of 10 µL/mL for 10 min, and the flow-through was collected for further experiments. CA-125 expressed EVs were enriched from 6 plasma samples using the anti-CA-125 monoclonal antibody modified EV-MAP chips. CA-125 expressed EVs were also enriched from 10 additional plasma samples using the EV-MAP chip, but included a pre-isolation using anti-CD81 monoclonal antibody modified EV-MAP chip, releasing these EVs and then the effluent sent to a second chip containing anti-CA-125 monoclonal antibodies. The eluted particles were then analyzed by the nCC chip as well as subjected to NTA.

4.2.3. Nano-Coulter counter chip fabrication.

An nCC master mold was made from a Cr coated silicon (Si) wafer, with the nCC chip containing both micro- and nano-dimensional features (Figure 4.3a). The micron-scale features were fabricated using positive photolithography followed by wet etching of the Si master to ensure appropriate pattern transfer. For positive photolithography, AZ1518 resist was spin-coated onto the Si wafer at a thickness of 5 µm and exposed to UV light (365 nm) for 4 s. The non-polymerized resist was developed using MIF 300, and wet etching was done using 40% KOH to the desired depth with the chromium layer as the mask for the wet etching process. The chromium layer was

removed using a Chromium etchant (Sigma-Aldrich). Finally, the nano-dimensional features of the nCC were fabricated by focused ion beam (FIB) milling using Ga ions.[58] Structures were milled with a beam current of 48 pA and a time of 1 µs. The final depths of the master mold were validated using metrology with a Keyence microscope (Keyence) and SEM (Figure 4.3b – d).

Poly-urethane acrylate (PUA resin; Minuta Technology) was used to replicate the nanostructures of the Si master mold into the desired plastic. The PUA resin was applied to the surface of the Si master mold and treated under a UV lamp with a power of 22 mW/cm^2 for 2.5 min. After UV curing, the stamp was transferred to PMMA using imprinting via nanoimprint lithography (NIL) at 135°C, 2.07 MPa for 5 min. The PMMA chip was then covered with a thin COC cover plate treated with O_2 plasma for 2 min and fusion bonded at 72°C, 0.83 MPa for 15 min. The fabricated nCC chips were used for particle enumeration.

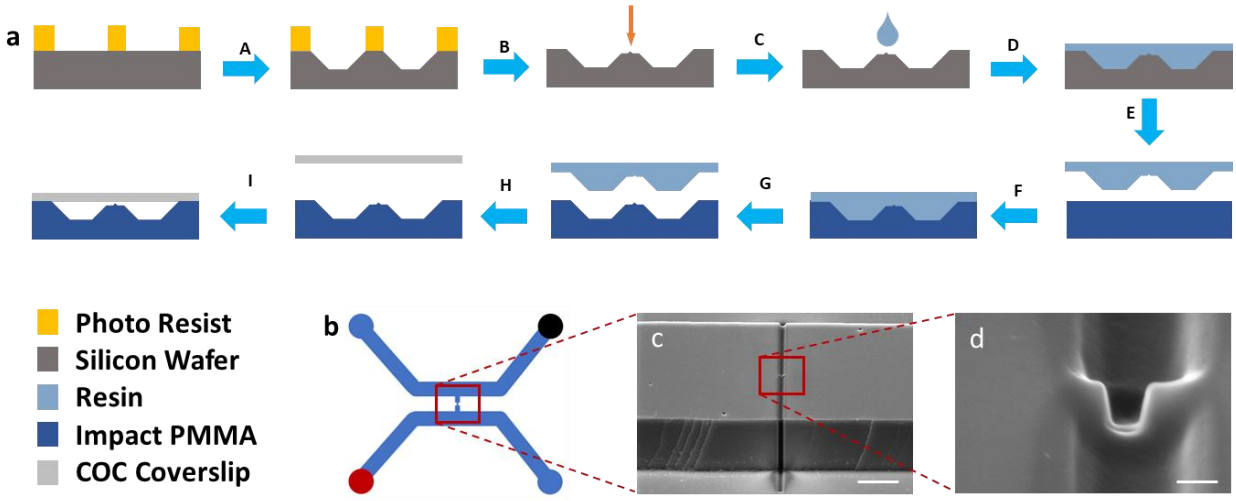

Figure 4.3. Fabrication of the fluidic circuit, including the in-plane nanopore. **a)** The processing steps for creating the nano-chip: A) Photolithography followed by wet etching of a silicon wafer; B) focused ion beam milling on producing the in-plane nanopore; C) PUA resin stamp fabrication by UV-NIL; D) 185 nm exposure for 2.5 mins to cross-link the resin; E), F), and G) pattern transfer of the resin stamp into PMMA using thermal NIL (conditions for the thermal NIL included 135°C and 2.07 MPa); H) and I) thermal fusion bonding between imprinted nano-chip with COC coverslip (76°C and 0.83 MPa). **b)** Schematic diagram of the nano-coulter counter chip (the colored reservoirs represent the applied voltage across the in-plane nanopore. **c)** SEM (scale bar 5 µm). The cross-bridge channel has 500 nm width, 500 nm depth, and 15 µm length. **d)** SEM of in-

plane nanopore (scale bar 200 nm). The nanopore has a 200 nm width, 200 nm depth, and 100 nm length.

4.2.4. In-plane nano-Coulter counter device setup and data analysis

The nCC chip filling and preparation steps are shown in Figure 4.4. The "low-pressure" side of the nCC chip was filled with running buffer first, and then the "high-pressure" side was filled with the sample. The syringe pump was then connected to "Outlet II," and "Outlet I" was sealed.

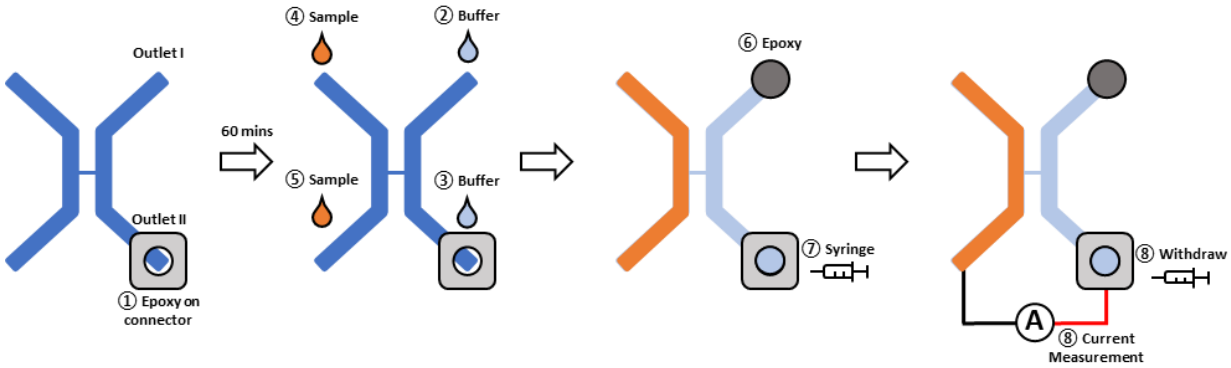

Figure 4.4. The syringe connecter was initially connected to the reservoir of the chip after fabrication. The buffer was filled through one side of the nCC chip, and the sample was filled through the other side. After solutions were successfully filled, one of the buffer side reservoirs was sealed by epoxy glue, and the syringe pump system was connected to the nCC chip. The chip will then be connected with the resistive pulse sensor and for electrical signal recording.

The withdrawal rate was set at 20 μL/min from "Outlet II" to create hydrodynamic flow, and the sample streamed from the high-pressure side to the low-pressure side. Once fluidic connections were made, the chip was transferred into a Faraday cage, and both of the electrodes were connected across the nCC using two Pt electrodes placed into reservoirs (see Figure 4.4). The Clampex (V10.1) was turned on for signal trace recording. The voltage across the nCC was -1 V, and based on simulationa, the majority of the voltage drop occurred across the nanochannels and

nanopore. In the 2D simulation, the nanopore had a sharper potential drop than other parts of the nanochannels, with about 10% of the potential drop occurring across the pore (Figure 4.5). The sampling frequency was 100,000 Hz, and a 10 kHz lowpass filter was applied. The signal trace was recorded for 10 min, and then the traces were analyzed by Clampfit. The trace background was zeroed, and a post 400 Hz highpass filter was applied to reduce the noise level resulting from external electrical sources and the intrinsic noise of the electronics. The standard deviation was calculated based on an open-pore current measurement, and a threshold condition was set at 5× the standard deviation in the signal. The signals with higher amplitude than the threshold and longer duration than 0.02 ms were scored as events.

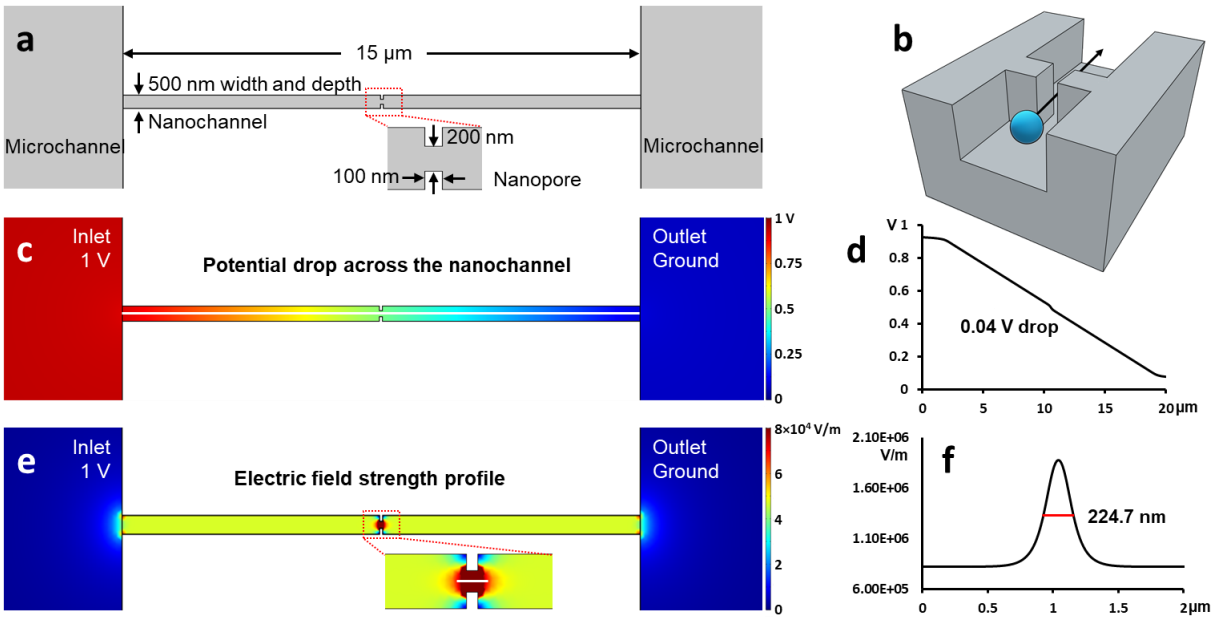

Figure 4.5. a) The 2D schematic diagram of the nanochannel with a length of 15 µm, 500 nm width, and 500 nm depth. The nanopore has a dimension of 200 nm width, 200 nm depth, and 100 nm length. **b)** The 3D schematic diagram of the nanochannel. **c)** The voltage potential drop across the nanochannel. **d)** The plot of potential drop vs. distance of nanochannel. The potential drop across the nanopore is only 4% in the 2D dimension. By involving the depth to the 3D factor, the nanopore only shares the potential by 10%. **e)** Electric field strength profile. **f)** The 50% of full strength was taken as the effective nanopore length, which is 224.7 nm.

4.2.5. Fluorescent beads for nCC characterization

A bead mixture was used to evaluate the performance of the nCC. The 46 and 100 nm diameter polystyrene beads with a fluorescent label (AF 565; excitation maximum = 565; emission maximum = 580; Thermo Scientific) were mixed and diluted in 1 M NaCl to concentrations of 4.7 x 10^{11} particles/mL and 1.8 x 10^{11} particles/mL, respectively. The bead mixture was filtered through a 0.22 μm filter to remove aggregates and applied to the nCC chip. The nCC chip was imaged using a fluorescence microscope with a 532 nm green laser (Diode-pumped solid-state - Coherent (DPSS) λ_{ex} = 532 nm; P = 2000 mW; 2 mm beam diameter), a 63× objective, and Cy3 color channel to visualize bead movement (Figure 4.6). The beads were analyzed optically using ImageJ. The events were collected from the electrical signal trace and analyzed for their size distribution as well using resistive pulse sensing. The relational cross-section areas of beads collected from the microscope were correlated with the electrical amplitude generated by the nCC used to calibrate the relationship between optical and electrical signals.

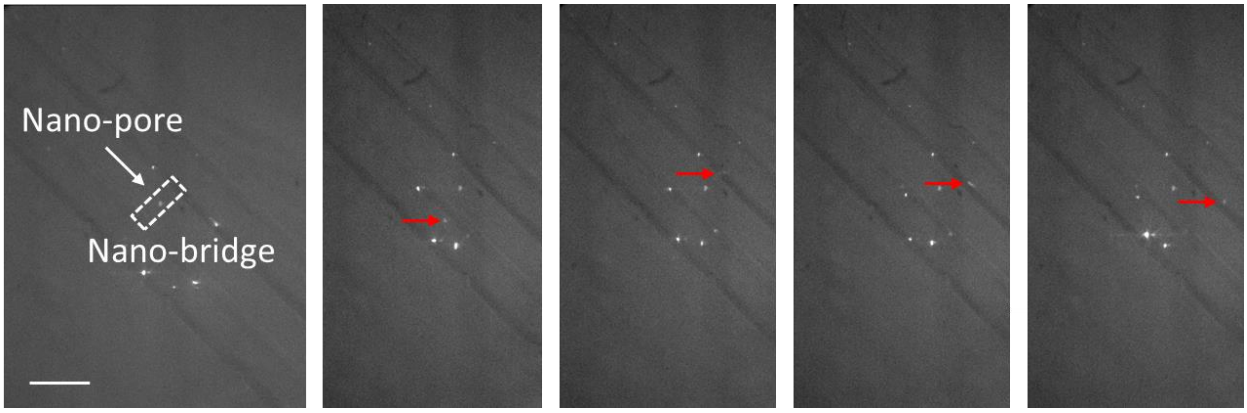

Figure 4.6. Beads were passing through nano-bridge and nanopore. 63× objective, 100 ms exposure time. Scale bar 20 μm. Red arrows are pointing a single bead location.

4.2.6. COMOSOL Simulation

A 2D model of the nCC was built-in AutoCAD and was imported into COMSOL (V. 5.5) to evaluate the potential drop and electric field strength across the nanochannel and the nanopore. The electrolyte used was 1X PBS, which is the same as the experimental conditions. The Physics used was Electrostatics under AC/DC flow. A DC bias of -1 V was applied at one end of the microchannel, and the other end of the nCC was ground. A no-slip boundary condition was given to all boundaries, and a stationary study was adopted to test the conditions.

4.3. Results and Discussion

4.3.1. nCC chip performance for artifacts beads and EV from cell culture media

For a single current transient trace of the fluorescent polystyrene beads of 46 and 100 nm diameter, the event signal amplitude ranged from 57 pA to 1203 pA, and the signal duration (formal width at half maximum) ranged from 0.15 to 0.95 ms (Figure 4.7a, b & d). The electrical signals were analyzed, and a histogram was built with a bin center of 100 pA. The histogram was fit to a normal distribution with two maxima (Figure 4.7e). The bead mixture was also imaged using fluorescence microscopy to make sure the resultant electrical signal was indeed due to transport of the beads through the in-plane pore. The bright fluorescent intensity areas within the image were collected as cross-sections and the intensity was found to be proportional to the beads' sizes and were correlated to the electrical signals generated by the nCC chip. The bead mixture fluorescence amplitude profile with respect to the electrical signals from the nCC chip showed high correlation ($R = 0.9988$, $p<0.001$) and confirmed that our electrical signals were originating from the bead translocation through the nanopore (Figure 4.7c). The relationship between bead diameter and electrical amplitude was established as noted in Equation 4.1, where D is the diameter

of the particle, A is the amplitude, Y_0 = 0.03408, and k = 3.648 × 10^{-5}. We estimated the particle's size with known amplitude and calculated the volumetric flow rate (Equation 4.2) and concentration (Equation 4.3) for the sample (Q is the volumetric flowrate, σ is the cross-section area of the nanopore, D_E is the distance of the effective electrical field, t is the time of particle traveling, C is the concentration, N is the total number of events, and T is the total recording duration).

Equation 4.1. $$D = 2\sqrt{\frac{\ln\frac{A}{Y_0}}{k\pi}}$$

Equation 4.2. $$Q = \frac{\sigma(D_E + D)}{t}$$

Equation 4.3. $$C = \frac{N}{QT}$$

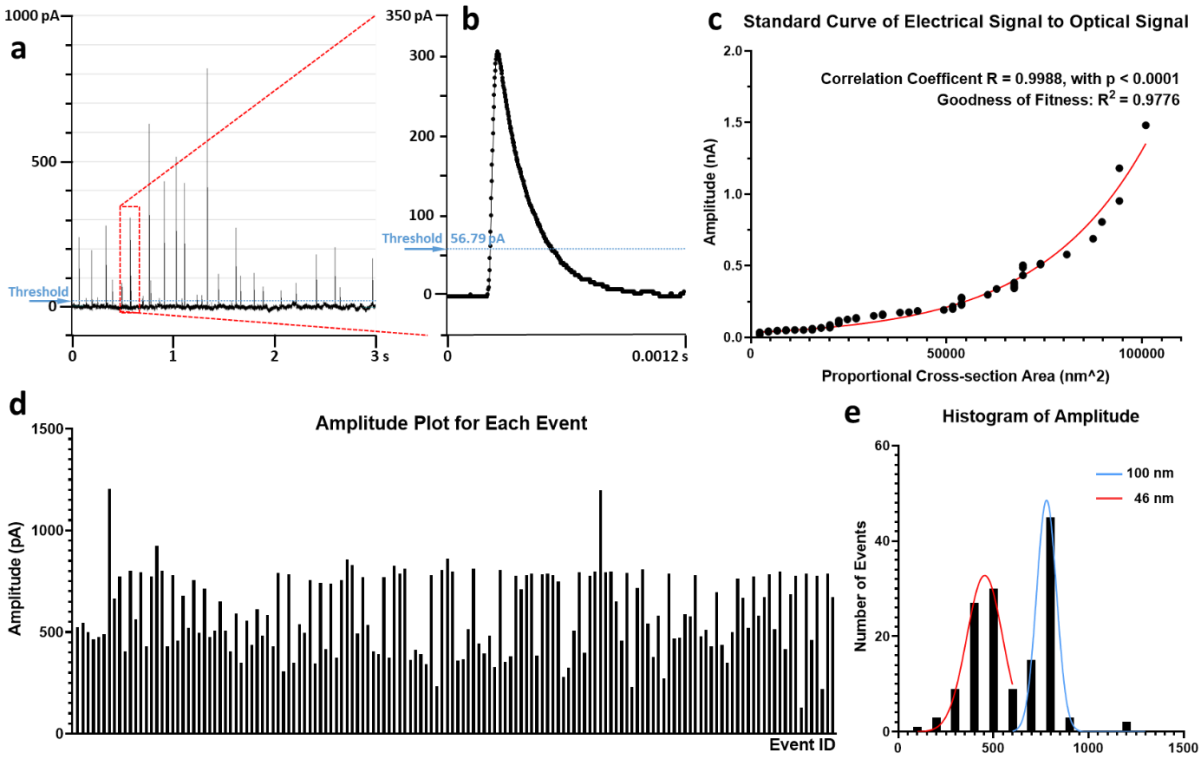

Figure 4.7. a) Electrical signal trace by the nano-coulter counter (nCC) from beads mixture (46 nm and 100 nm diameter). The threshold was calculated by 5 times the standard deviation of the whole trace. The trace was then analyzed by the suited software of pCLAMP. **b)** An example of an expanded view along the time axis of a single bead traveling through the nCC gives a standard width of 0.9 ms at an amplitude of 308 pA. **c)** The proportional optical signals of a mixture of 46

nm and 100 nm beads under 63× objective correlate to electrical signals, which showed a high correlation coefficient ($r^2 = 0.9991$, $p < 0.0001$). In addition, the plot was shown a fitness to the exponential relationship (Equation 4.1). **d)** Amplitude plot for a mixture of 46 nm and 100 nm beads. **e)** Histogram of the amplitude. The amplitude showed two normal distributions of signal peaks with two apparent ranges at the mean values of 454 pA and 779 pA, which could be referred to as 46 nm beads and 100 nm beads, respectively.

4.3.2. EV-MAP and nCC analysis of EVs from plasma samples.

In order to test the performance of the EV-MAP and nCC chips, 6 unknown high-grade serous carcinoma patient and healthy control samples (Table 4.1) were analyzed using the anti-CA-125 monoclonal antibody modified EV-MAP chip and following capture, the recovered particles were released by USER^{TM} enzyme into a volume of 100 µL with 1× PBS and 0.1% Tween-20. The nCC platform only needed 5 µL of the sample for profiling, and the signal trace could be obtained in as short as 1 min. The CA-125 expressing EV concentration information of the plasma sample is shown in Figure 4.8. As can be seen, a group of samples had a much higher EV concentration with a range from 7.46×10^{10} particles/mL to 9.56×10^{10} particles/mL, compared to another group, which was 1.77×10^{10} particles/mL. The samples were placed into one of two groups and labeled as ovarian cancer patients vs. healthy controls based on the EV concentration. The two groups showed a significant difference with a p-value of 0.0007.

With the first step of EV isolation using a CA-125 EV-MAP chip, tumor-related EVs with CA-125 surface expression were enriched, subsequently released, and counted using the nCC. From our previous work and literature, EVs with CA-125 surface expression could be used as a marker for distinguishing between high-grade serous carcinoma patients from healthy controls.[59, 60] However, literature has also shown that free CA-125 level in human plasma is also related to ovarian cancer stage.[61, 62] As a result, free CA-125 in the plasma could bind to the antibody

modified surface and thus, reduce the number of available sites for CA-125 EVs available for binding and thus, lower the dynamic range of the assay.

Table 4.1 List of plasma samples used in this study.

Sample ID	Age	Condition	Treatment	Isolation
003011	63	High grade serous carcinoma	No prior treatment	Singal (CA-125)
500007	20	Healthy	N/A	Singal (CA-125)
003457	63	High grade serous carcinoma	No prior treatment	Singal (CA-125)
023592	57	High grade serous carcinoma	No prior treatment	Singal (CA-125)
500012	38	Healthy	N/A	Singal (CA-125)
500160	28	Healthy	N/A	Singal (CA-125)
022598	53	High grade serous carcinoma	No prior treatment	Series (CD81 & CA-125)
026634	65	High grade serous carcinoma	No prior treatment	Series (CD81 & CA-125)
029948	60	High grade serous carcinoma	No prior treatment	Series (CD81 & CA-125)
035722	71	High grade serous carcinoma	No prior treatment	Series (CD81 & CA-125)
031065	66	High grade serous carcinoma	No prior treatment	Series (CD81 & CA-125)
005610	64	Healthy	N/A	Series (CD81 & CA-125)
500162	58	Healthy	N/A	Series (CD81 & CA-125)
019885	52	Healthy	N/A	Series (CD81 & CA-125)
024251	58	Healthy	N/A	Series (CD81 & CA-125)
027687	64	Healthy	N/A	Series (CD81 & CA-125)

In order to prevent free CA-125 protein in the plasma from interfering with the binding sites available for CA-125 expressing EVs, two sets of chips with different antibodies used in each chip was used, which included anti-CD81 antibodies in one chip and anti-CA-125 antibodies in a second chip. In this way, the total EV population could be collected in the first chip using the EV-map decorated with the antibody directed against the tetraspanin, CD-18, while free proteins could flow through the first chip. The collected EVs were then released from the first chip and then the CA-125 expressing EVs (i.e., ovarian cancer EVs) could be collected by the second chip. With this series of chips, interference from free CA-125 proteins could be minimized, and the target EV population could be collected and analyzed more efficiently.

Ten additional blood plasma samples from high-grade serous carcinoma patients and healthy controls were then analyzed (Table 4.1). For this analysis, 200 µl of blood plasma was processed through the chips with the series configuration. The eluted EV samples were analyzed in the nCC chip, and the concentration of each sample was calculated as shown in Figure 4.8c. Five of the samples showed relatively higher EV concentrations compared to the other 5 samples. Five patient samples were successfully identified from the sample with a p-value at 0.035. Thus, the combination of EV-MAP chip with EV enrichment and USER^{TM} enzyme releasing, and nCC chip with RPS strategies, has shown a high performance from EV isolation to the rapid characterization, therefore, showing excellent potential for tumor-related diagnostics and disease management for the clinical sites. However, the results showed the series EV-MAP configuration provided less difference compared to the single EV-MAP isolation. Two factors may affect the results: (i) The USER release will cleave the oligonucleotide with the antibody remaining on the surface of the EV. This may affect accessibility of the anti-CA-125 antibody binding on the subsequent enrichment step to the EV-antigen due to steric considerations. (ii) Additional steps of

isolation can result in additional material loss. We should note that following cleavage of the oligonucleotide bifunctional linker and the CA-125 antibody-bound proteins will also be released but not registered by the nCC due to size; the CA-125 proteins are smaller (<10 nm) than the CA-125 expressing EVs. By combining the EV-MAP chip and the nCC chip, target EVs were enriched and enumerated, and both of the clinical sensitivity and specificity is at 100%. The plasma samples used for series isolation configuration were also processed by UC for EV isolation, and analyzed by NTA. The mean and the mode of the particle size is from 121 – 197 nm and 48 – 163 nm, respectively, and the concentration range is from 2.05×10^9 to 1.04×10^{10} partciels/mL with no specific difference between the two gourps.

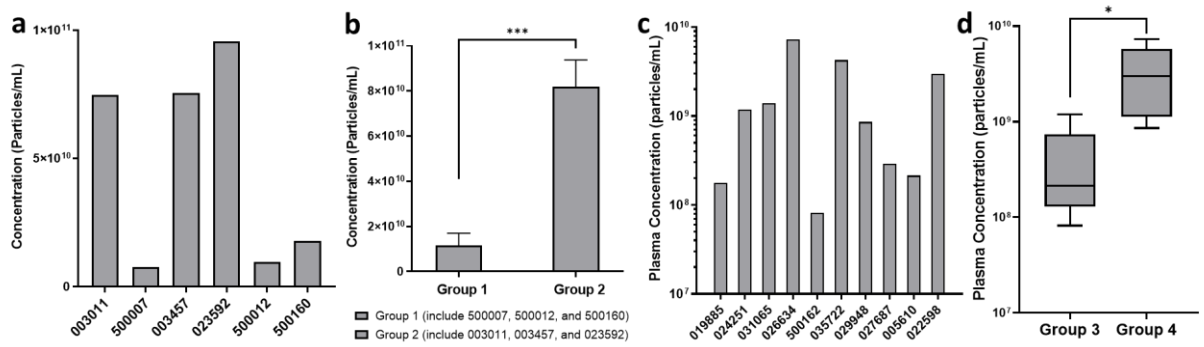

Figure 4.8. a) Captured and release EVs from the plasma, with 6 samples including 3 healthy control and 3 ovarian cancer patients. The isolated EVs from sample IDs of 003011, 003457, and 023592 showed much higher concentration than the sample ID of 500007, 500012, and 500160. **b)** Two groups were separated with tags of healthy control (500007, 500012, and 500160) and ovarian cancer patients (003011, 003457, and 023592) ($p = 0.0007$). **c)** Calculated CA-125 sub-type of EV concentration by nCC chip for 10 ovarian cancer patients. **d)** Two groups were separated with the tags of healthy control and ovarian cancer patients ($p = 0.035$)

4.3.3. Electronic signal polarity and analysis

The nCC chip generated positively oriented pulses in our electrical signals but not the negatively oriented pulses as most RPS data show.[36-39, 63] For RPS with a constant potential applied across the pore, non-conductive particles will increase the resistance while resident within the pore,

making negative polarity events. However, in the case of conductive particles, they can carry more ions than the surrounding electrolyte environment increasing the conductive when the particle is resident within the pore and thus, resulting in a positive polarity signal as we see here.[36] In our case we are using only 1× PBS as the carrier electrolyte without 1 M KCl spiked into the carrier electrolyte as is typically done in RPS experiments.

For the bead experiments, polystyrene was the bead material and literature has shown that polystyrene beads can provide positive polarity events in RPS because of the porous nature of the beads,[64-68] which creates significantly higher surface area than a solid bead. The porous beads will carry much more ions due to the larger surface area, making an increased charge/volume ratio. As a result, the ionic concentration in the bead is higher than the ionic concentration in the surrounding carrier electrolyte and thus results in positive-polarity events. The EVs when counted using the nCC chip with 1× PBS also showed positive polarity events. Due to the small size of the nanopore, the electrical field strength can be as high as 10 kV/cm, and the particles translocated through the pore in about 26 µs. With such a high electrical field strength and short translocation duration, the pore provides a sufficient electroporation condition for phospholipid bilayer for the EV membrane. The EV membrane can become permeable with the electroporation condition, and the vesicles with a permeable membrane would result in a higher conductivity than the vesicles with an intake membrane when the surrounding buffer condition was 1×PBS.[69, 70] As a result, with higher conductivity particles, the EV-related current transients would result in a higher conductivity and thus, higher current flow.

4.4. Conclusions

We demonstrated a combination chip platform consisting of chips for the enrichment of EVs (EV-MAP chip) followed by the label-free enumeration of the enriched EVs (nCC chip). Conventional methods for the analysis of EVs requires ultracentrifugation of all EV sub-types followed by the use of NTA and/or electron microscopy for enumeration, which show significant drawbacks such as large variability and sample selection bias,[71, 72] as well as complicated workflows that are require specialized operators and sophisticated equipment. The EV-MAP and nCC chip platform offers some unique advantages for the analysis of EVs including small sample consumption (5 μL), label-free detection using simple instrumentation, a large dynamic range (10^3 to 10^{16} particles/mL), and the potential of mass production of both chips via injection molding.

The EV-MAP chip was optimized to process plasma samples and release high purity of disease-associated EVs.[25] The nCC chip could analyze particles <200 nm in diameter and do so in a high-throughput fashion using simple instrumentation. A high correlation (correlation coefficient R=0.9988) was found between the electrical signal generated by the polystyrene beads and the optical signal deduced from a fluorescence microscope. Moreover, the correlation showed an exponential relationship between the intensity of the electrical signal and the cross-sectional area of the particle (Equation 4.1, R^2 = 0.9776). Also, the histogram of the beads' electrical signal showed two clear peaks that followed a normal distribution, which confirmed the two principal size distributions, which were 46 nm and 100 nm. When processing unknown samples, the combination of the EV-MAP chip and nCC chip successfully characterized ovarian cancer patients and healthy controls, which confirmed the performance of the EV-MAP chip and also the nCC chip is a proper tool for EV enumeration.

Thus, through a series of calibration and optimization experiments, the combined use of EV-MAP and nCC chip can successfully enrich, release, and analyze the target EVs from plasma samples. The platform has excellent potential and will be a powerful tool for EV sample analysis to achieve the demand for POCT for diagnostic purposes.

4.5. References

(1). Taylor, D. D.; Doellgast, G. J., Quantitation of peroxidase-antibody binding to membrane fragments using column chromatography. *Anal Biochem* **1979,** *98* (1), 53-9.

(2). Thery, C., Cancer: Diagnosis by extracellular vesicles. *Nature* **2015,** *523* (7559), 161-2.

(3). Li, X.; Corbett, A. L.; Taatizadeh, E.; Tasnim, N.; Little, J. P.; Garnis, C.; Daugaard, M.; Guns, E.; Hoorfar, M.; Li, I. T. S., Challenges and opportunities in exosome research-Perspectives from biology, engineering, and cancer therapy. *APL Bioeng* **2019,** *3* (1), 011503.

(4). Zhu, Q.; Heon, M.; Zhao, Z.; He, M., Microfluidic engineering of exosomes: editing cellular messages for precision therapeutics. *Lab Chip* **2018,** *18* (12), 1690-1703.

(5). Bebelman, M. P.; Smit, M. J.; Pegtel, D. M.; Baglio, S. R., Biogenesis and function of extracellular vesicles in cancer. *Pharmacol Ther* **2018,** *188*, 1-11.

(6). Martins, B.; Amorim, M.; Reis, F.; Ambrosio, A. F.; Fernandes, R., Extracellular Vesicles and MicroRNA: Putative Role in Diagnosis and Treatment of Diabetic Retinopathy. *Antioxidants (Basel)* **2020,** *9* (8).

(7). Lane, R. E.; Korbie, D.; Hill, M. M.; Trau, M., Extracellular vesicles as circulating cancer biomarkers: opportunities and challenges. *Clin Transl Med* **2018,** *7* (1), 14.

(8). Hessvik, N. P.; Llorente, A., Current knowledge on exosome biogenesis and release. *Cell Mol Life Sci* **2018,** *75* (2), 193-208.

(9). Vlassov, A. V.; Magdaleno, S.; Setterquist, R.; Conrad, R., Exosomes: current knowledge of their composition, biological functions, and diagnostic and therapeutic potentials. *Biochim Biophys Acta* **2012,** *1820* (7), 940-8.

(10). Gardiner, C.; Ferreira, Y. J.; Dragovic, R. A.; Redman, C. W.; Sargent, I. L., Extracellular vesicle sizing and enumeration by nanoparticle tracking analysis. *J Extracell Vesicles* **2013,** *2*.

(11). Jeppesen, D. K.; Hvam, M. L.; Primdahl-Bengtson, B.; Boysen, A. T.; Whitehead, B.; Dyrskjot, L.; Orntoft, T. F.; Howard, K. A.; Ostenfeld, M. S., Comparative analysis of discrete exosome fractions obtained by differential centrifugation. *J Extracell Vesicles* **2014,** *3*, 25011.

(12). Kalra, H.; Adda, C. G.; Liem, M.; Ang, C. S.; Mechler, A.; Simpson, R. J.; Hulett, M. D.; Mathivanan, S., Comparative proteomics evaluation of plasma exosome isolation techniques and assessment of the stability of exosomes in normal human blood plasma. *Proteomics* **2013,** *13* (22), 3354-64.

(13). Bobrie, A.; Colombo, M.; Krumeich, S.; Raposo, G.; Thery, C., Diverse subpopulations of vesicles secreted by different intracellular mechanisms are present in exosome preparations obtained by differential ultracentrifugation. *J Extracell Vesicles* **2012,** *1*.

(14). Cvjetkovic, A.; Lotvall, J.; Lasser, C., The influence of rotor type and centrifugation time on the yield and purity of extracellular vesicles. *J Extracell Vesicles* **2014,** *3*.

(15). Tian, Y.; Gong, M.; Hu, Y.; Liu, H.; Zhang, W.; Zhang, M.; Hu, X.; Aubert, D.; Zhu, S.; Wu, L.; Yan, X., Quality and efficiency assessment of six extracellular vesicle isolation methods by nano-flow cytometry. *J Extracell Vesicles* **2020,** *9* (1), 1697028.

(16). Zaborowski, M. P.; Balaj, L.; Breakefield, X. O.; Lai, C. P., Extracellular Vesicles: Composition, Biological Relevance, and Methods of Study. *Bioscience* **2015,** *65* (8), 783-797.

(17). Livshits, M. A.; Khomyakova, E.; Evtushenko, E. G.; Lazarev, V. N.; Kulemin, N. A.; Semina, S. E.; Generozov, E. V.; Govorun, V. M., Isolation of exosomes by differential centrifugation: Theoretical analysis of a commonly used protocol. *Sci Rep* **2015,** *5*, 17319.

(18). Momen-Heravi, F.; Balaj, L.; Alian, S.; Mantel, P. Y.; Halleck, A. E.; Trachtenberg, A. J.; Soria, C. E.; Oquin, S.; Bonebreak, C. M.; Saracoglu, E.; Skog, J.; Kuo, W. P., Current methods for the isolation of extracellular vesicles. *Biol Chem* **2013,** *394* (10), 1253-1262.

(19). Konoshenko, M. Y.; Lekchnov, E. A.; Vlassov, A. V.; Laktionov, P. P., Isolation of Extracellular Vesicles: General Methodologies and Latest Trends. *Biomed Res Int* **2018,** *2018*, 8545347.

(20). Shah, D.; Cronin, J.; Chacko, M.; Gillum, A., Impact of Formulation and Processing Parameters on Silicone Extraction from Cyclic Olefin Copolymer (COC) Syringes. *PDA J Pharm Sci Technol* **2011,** *65* (2), 109-15.

(21). Chen, P. C.; Zhang, R. H.; Aue, U. L. Y.; Chang, G. E., Micromachining Microchannels on Cyclic Olefin Copolymer (COC) Substrates with the Taguchi Method. *Micromachines (Basel)* **2017,** *8* (9).

(22). Pu, Q.; Oyesanya, O.; Thompson, B.; Liu, S.; Alvarez, J. C., On-chip micropatterning of plastic (cylic olefin copolymer, COC) microfluidic channels for the fabrication of biomolecule microarrays using photografting methods. *Langmuir* **2007,** *23* (3), 1577-83.

(23). Ogilvie, I. R.; Sieben, V. J.; Cortese, B.; Mowlem, M. C.; Morgan, H., Chemically resistant microfluidic valves from Viton(R) membranes bonded to COC and PMMA. *Lab Chip* **2011,** *11* (14), 2455-9.

(24). Battle, K. N.; Jackson, J. M.; Witek, M. A.; Hupert, M. L.; Hunsucker, S. A.; Armistead, P. M.; Soper, S. A., Solid-phase extraction and purification of membrane proteins using a UV-modified PMMA microfluidic bioaffinity mu SPE device. *Analyst* **2014,** *139* (6), 1355-1363.

(25). Wijerathne, H.; Witek, M. A.; Jackson, J. M.; Brown, V.; Hupert, M. L.; Herrera, K.; Kramer, C.; Davidow, A. E.; Li, Y.; Baird, A. E.; Murphy, M. C.; Soper, S. A., Affinity enrichment of extracellular vesicles from plasma reveals mRNA changes associated with acute ischemic stroke. *Commun Biol* **2020,** *3* (1), 613.

(26). Thery, C.; Witwer, K. W.; Aikawa, E.; Alcaraz, M. J.; Anderson, J. D.; Andriantsitohaina, R.; Antoniou, A.; Arab, T.; Archer, F.; Atkin-Smith, G. K.; Ayre, D. C.; Bach, J. M.; Bachurski, D.; Baharvand, H.; Balaj, L.; Baldacchino, S.; Bauer, N. N.; Baxter, A. A.; Bebawy, M.; Beckham, C.; Bedina Zavec, A.; Benmoussa, A.; Berardi, A. C.; Bergese, P.; Bielska, E.; Blenkiron, C.; Bobis-Wozowicz, S.; Boilard, E.; Boireau, W.; Bongiovanni, A.; Borras, F. E.; Bosch, S.; Boulanger, C. M.; Breakefield, X.; Breglio, A. M.; Brennan, M. A.; Brigstock, D. R.; Brisson, A.; Broekman, M. L.; Bromberg, J. F.; Bryl-Gorecka, P.; Buch, S.; Buck, A. H.; Burger, D.; Busatto, S.; Buschmann, D.; Bussolati, B.; Buzas, E. I.; Byrd, J. B.; Camussi, G.; Carter, D. R.; Caruso, S.; Chamley, L. W.; Chang, Y. T.; Chen, C.; Chen, S.; Cheng, L.; Chin, A. R.; Clayton, A.; Clerici, S. P.; Cocks, A.; Cocucci, E.; Coffey, R. J.; Cordeiro-da-Silva, A.; Couch, Y.; Coumans, F. A.; Coyle, B.; Crescitelli, R.; Criado, M. F.; D'Souza-Schorey, C.; Das, S.; Datta Chaudhuri, A.; de Candia, P.; De Santana, E. F.; De Wever, O.; Del Portillo, H.

A.; Demaret, T.; Deville, S.; Devitt, A.; Dhondt, B.; Di Vizio, D.; Dieterich, L. C.; Dolo, V.; Dominguez Rubio, A. P.; Dominici, M.; Dourado, M. R.; Driedonks, T. A.; Duarte, F. V.; Duncan, H. M.; Eichenberger, R. M.; Ekstrom, K.; El Andaloussi, S.; Elie-Caille, C.; Erdbrugger, U.; Falcon-Perez, J. M.; Fatima, F.; Fish, J. E.; Flores-Bellver, M.; Forsonits, A.; Frelet-Barrand, A.; Fricke, F.; Fuhrmann, G.; Gabrielsson, S.; Gamez-Valero, A.; Gardiner, C.; Gartner, K.; Gaudin, R.; Gho, Y. S.; Giebel, B.; Gilbert, C.; Gimona, M.; Giusti, I.; Goberdhan, D. C.; Gorgens, A.; Gorski, S. M.; Greening, D. W.; Gross, J. C.; Gualerzi, A.; Gupta, G. N.; Gustafson, D.; Handberg, A.; Haraszti, R. A.; Harrison, P.; Hegyesi, H.; Hendrix, A.; Hill, A. F.; Hochberg, F. H.; Hoffmann, K. F.; Holder, B.; Holthofer, H.; Hosseinkhani, B.; Hu, G.; Huang, Y.; Huber, V.; Hunt, S.; Ibrahim, A. G.; Ikezu, T.; Inal, J. M.; Isin, M.; Ivanova, A.; Jackson, H. K.; Jacobsen, S.; Jay, S. M.; Jayachandran, M.; Jenster, G.; Jiang, L.; Johnson, S. M.; Jones, J. C.; Jong, A.; Jovanovic-Talisman, T.; Jung, S.; Kalluri, R.; Kano, S. I.; Kaur, S.; Kawamura, Y.; Keller, E. T.; Khamari, D.; Khomyakova, E.; Khvorova, A.; Kierulf, P.; Kim, K. P.; Kislinger, T.; Klingeborn, M.; Klinke, D. J., 2nd; Kornek, M.; Kosanovic, M. M.; Kovacs, A. F.; Kramer-Albers, E. M.; Krasemann, S.; Krause, M.; Kurochkin, I. V.; Kusuma, G. D.; Kuypers, S.; Laitinen, S.; Langevin, S. M.; Languino, L. R.; Lannigan, J.; Lasser, C.; Laurent, L. C.; Lavieu, G.; Lazaro-Ibanez, E.; Le Lay, S.; Lee, M. S.; Lee, Y. X. F.; Lemos, D. S.; Lenassi, M.; Leszczynska, A.; Li, I. T.; Liao, K.; Libregts, S. F.; Ligeti, E.; Lim, R.; Lim, S. K.; Line, A.; Linnemannstons, K.; Llorente, A.; Lombard, C. A.; Lorenowicz, M. J.; Lorincz, A. M.; Lotvall, J.; Lovett, J.; Lowry, M. C.; Loyer, X.; Lu, Q.; Lukomska, B.; Lunavat, T. R.; Maas, S. L.; Malhi, H.; Marcilla, A.; Mariani, J.; Mariscal, J.; Martens-Uzunova, E. S.; Martin-Jaular, L.; Martinez, M. C.; Martins, V. R.; Mathieu, M.; Mathivanan, S.; Maugeri, M.; McGinnis, L. K.; McVey, M. J.; Meckes, D. G., Jr.; Meehan, K. L.; Mertens, I.; Minciacchi, V. R.; Moller, A.; Moller Jorgensen, M.; Morales-Kastresana, A.; Morhayim, J.; Mullier, F.; Muraca, M.; Musante, L.; Mussack, V.; Muth, D. C.; Myburgh, K. H.; Najrana, T.; Nawaz, M.; Nazarenko, I.; Nejsum, P.; Neri, C.; Neri, T.; Nieuwland, R.; Nimrichter, L.; Nolan, J. P.; Nolte-'t Hoen, E. N.; Noren Hooten, N.; O'Driscoll, L.; O'Grady, T.; O'Loghlen, A.; Ochiya, T.; Olivier, M.; Ortiz, A.; Ortiz, L. A.; Osteikoetxea, X.; Ostergaard, O.; Ostrowski, M.; Park, J.; Pegtel, D. M.; Peinado, H.; Perut, F.; Pfaffl, M. W.; Phinney, D. G.; Pieters, B. C.; Pink, R. C.; Pisetsky, D. S.; Pogge von Strandmann, E.; Polakovicova, I.; Poon, I. K.; Powell, B. H.; Prada, I.; Pulliam, L.; Quesenberry, P.; Radeghieri, A.; Raffai, R. L.; Raimondo, S.; Rak, J.; Ramirez, M. I.; Raposo, G.; Rayyan, M. S.; Regev-Rudzki, N.; Ricklefs, F. L.; Robbins, P. D.; Roberts, D. D.; Rodrigues, S. C.; Rohde, E.; Rome, S.; Rouschop, K. M.; Rughetti, A.; Russell, A. E.; Saa, P.; Sahoo, S.; Salas-Huenuleo, E.; Sanchez, C.; Saugstad, J. A.; Saul, M. J.; Schiffelers, R. M.; Schneider, R.; Schoyen, T. H.; Scott, A.; Shahaj, E.; Sharma, S.; Shatnyeva, O.; Shekari, F.; Shelke, G. V.; Shetty, A. K.; Shiba, K.; Siljander, P. R.; Silva, A. M.; Skowronek, A.; Snyder, O. L., 2nd; Soares, R. P.; Sodar, B. W.; Soekmadji, C.; Sotillo, J.; Stahl, P. D.; Stoorvogel, W.; Stott, S. L.; Strasser, E. F.; Swift, S.; Tahara, H.; Tewari, M.; Timms, K.; Tiwari, S.; Tixeira, R.; Tkach, M.; Toh, W. S.; Tomasini, R.; Torrecilhas, A. C.; Tosar, J. P.; Toxavidis, V.; Urbanelli, L.; Vader, P.; van Balkom, B. W.; van der Grein, S. G.; Van Deun, J.; van Herwijnen, M. J.; Van Keuren-Jensen, K.; van Niel, G.; van Royen, M. E.; van Wijnen, A. J.; Vasconcelos, M. H.; Vechetti, I. J., Jr.; Veit, T. D.; Vella, L. J.; Velot, E.; Verweij, F. J.; Vestad, B.; Vinas, J. L.; Visnovitz, T.; Vukman, K. V.; Wahlgren, J.; Watson, D. C.; Wauben, M. H.; Weaver, A.; Webber, J. P.; Weber, V.; Wehman, A. M.; Weiss, D. J.; Welsh, J. A.; Wendt, S.; Wheelock, A. M.; Wiener, Z.; Witte, L.; Wolfram, J.; Xagorari, A.; Xander, P.; Xu, J.; Yan, X.; Yanez-Mo, M.; Yin, H.; Yuana, Y.; Zappulli, V.; Zarubova, J.; Zekas, V.; Zhang, J. Y.; Zhao, Z.;

Zheng, L.; Zheutlin, A. R.; Zickler, A. M.; Zimmermann, P.; Zivkovic, A. M.; Zocco, D.; Zuba-Surma, E. K., Minimal information for studies of extracellular vesicles 2018 (MISEV2018): a position statement of the International Society for Extracellular Vesicles and update of the MISEV2014 guidelines. *J Extracell Vesicles* **2018,** *7* (1), 1535750.

(27). Chen, B. Y.; Sung, C. W.; Chen, C.; Cheng, C. M.; Lin, D. P.; Huang, C. T.; Hsu, M. Y., Advances in exosomes technology. *Clin Chim Acta* **2019,** *493*, 14-19.

(28). Soo, C. Y.; Song, Y.; Zheng, Y.; Campbell, E. C.; Riches, A. C.; Gunn-Moore, F.; Powis, S. J., Nanoparticle tracking analysis monitors microvesicle and exosome secretion from immune cells. *Immunology* **2012,** *136* (2), 192-7.

(29). Gross, J.; Sayle, S.; Karow, A. R.; Bakowsky, U.; Garidel, P., Nanoparticle tracking analysis of particle size and concentration detection in suspensions of polymer and protein samples: Influence of experimental and data evaluation parameters. *Eur J Pharm Biopharm* **2016,** *104*, 30-41.

(30). Coumans, F. A. W.; Gool, E. L.; Nieuwland, R., Bulk immunoassays for analysis of extracellular vesicles. *Platelets* **2017,** *28* (3), 242-248.

(31). Koritzinsky, E. H.; Street, J. M.; Star, R. A.; Yuen, P. S., Quantification of Exosomes. *J Cell Physiol* **2017,** *232* (7), 1587-1590.

(32). Nolan, J. P.; Jones, J. C., Detection of platelet vesicles by flow cytometry. *Platelets* **2017,** *28* (3), 256-262.

(33). Xu, R.; Greening, D. W.; Zhu, H. J.; Takahashi, N.; Simpson, R. J., Extracellular vesicle isolation and characterization: toward clinical application. *J Clin Invest* **2016,** *126* (4), 1152-62.

(34). Greening, D. W.; Simpson, R. J., Understanding extracellular vesicle diversity - current status. *Expert Rev Proteomics* **2018,** *15* (11), 887-910.

(35). DeBlois, R. W.; Uzgiris, E. E.; Cluxton, D. H.; Mazzone, H. M., Comparative measurements of size and polydispersity of several insect viruses. *Anal Biochem* **1978,** *90* (1), 273-88.

(36). Kozak, D.; Anderson, W.; Vogel, R.; Trau, M., Advances in Resistive Pulse Sensors: Devices bridging the void between molecular and microscopic detection. *Nano Today* **2011,** *6* (5), 531-545.

(37). Song, Y.; Zhang, J.; Li, D., Microfluidic and Nanofluidic Resistive Pulse Sensing: A Review. *Micromachines (Basel)* **2017,** *8* (7).

(38). Vaclavek, T.; Prikryl, J.; Foret, F., Resistive pulse sensing as particle counting and sizing method in microfluidic systems: Designs and applications review. *J Sep Sci* **2019,** *42* (1), 445-457.

(39). Willmott, G. R., Tunable Resistive Pulse Sensing: Better Size and Charge Measurements for Submicrometer Colloids. *Anal Chem* **2018,** *90* (5), 2987-2995.

(40). Choi, G.; Murphy, E.; Guan, W., Microfluidic Time-Division Multiplexing Accessing Resistive Pulse Sensor for Particle Analysis. *ACS Sens* **2019,** *4* (7), 1957-1963.

(41). Zhou, T.; Song, Y.; Yuan, Y.; Li, D., A novel microfluidic resistive pulse sensor with multiple voltage input channels and a side sensing gate for particle and cell detection. *Anal Chim Acta* **2019,** *1052*, 113-123.

(42). Fraikin, J. L.; Teesalu, T.; McKenney, C. M.; Ruoslahti, E.; Cleland, A. N., A high-throughput label-free nanoparticle analyser. *Nat Nanotechnol* **2011,** *6* (5), 308-13.

(43). Arima, A.; Tsutsui, M.; Harlisa, I. H.; Yoshida, T.; Tanaka, M.; Yokota, K.; Tonomura, W.; Taniguchi, M.; Okochi, M.; Washio, T.; Kawai, T., Selective detections of single-viruses using solid-state nanopores. *Sci Rep* **2018,** *8* (1), 16305.

(44). Heider, S.; Metzner, C., Quantitative real-time single particle analysis of virions. *Virology* **2014,** *462-463*, 199-206.

(45). Yang, L.; Yamamoto, T., Quantification of Virus Particles Using Nanopore-Based Resistive-Pulse Sensing Techniques. *Front Microbiol* **2016,** *7*, 1500.

(46). Song, Y.; Zhang, H.; Chon, C. H.; Chen, S.; Pan, X.; Li, D., Counting bacteria on a microfluidic chip. *Anal Chim Acta* **2010,** *681* (1-2), 82-6.

(47). Golichenari, B.; Nosrati, R.; Farokhi-Fard, A.; Faal Maleki, M.; Gheibi Hayat, S. M.; Ghazvini, K.; Vaziri, F.; Behravan, J., Electrochemical-based biosensors for detection of Mycobacterium tuberculosis and tuberculosis biomarkers. *Crit Rev Biotechnol* **2019,** *39* (8), 1056-1077.

(48). Wang, Y.; Kececi, K.; Mirkin, M. V.; Mani, V.; Sardesai, N.; Rusling, J. F., Resistive-pulse measurements with nanopipettes: detection of Au nanoparticles and nanoparticle-bound anti-peanut IgY. *Chem Sci* **2013,** *4* (2), 655-663.

(49). Chavis, A. E.; Brady, K. T.; Hatmaker, G. A.; Angevine, C. E.; Kothalawala, N.; Dass, A.; Robertson, J. W. F.; Reiner, J. E., Single Molecule Nanopore Spectrometry for Peptide Detection. *ACS Sens* **2017,** *2* (9), 1319-1328.

(50). Guo, J.; Huang, X.; Ai, Y., On-Demand Lensless Single Cell Imaging Activated by Differential Resistive Pulse Sensing. *Anal Chem* **2015,** *87* (13), 6516-9.

(51). Song, Y.; Li, M.; Pan, X.; Wang, Q.; Li, D., Size-based cell sorting with a resistive pulse sensor and an electromagnetic pump in a microfluidic chip. *Electrophoresis* **2015,** *36* (3), 398-404.

(52). Sexton, L. T.; Mukaibo, H.; Katira, P.; Hess, H.; Sherrill, S. A.; Horne, L. P.; Martin, C. R., An adsorption-based model for pulse duration in resistive-pulse protein sensing. *J Am Chem Soc* **2010,** *132* (19), 6755-63.

(53). Sexton, L. T.; Horne, L. P.; Sherrill, S. A.; Bishop, G. W.; Baker, L. A.; Martin, C. R., Resistive-pulse studies of proteins and protein/antibody complexes using a conical nanotube sensor. *J Am Chem Soc* **2007,** *129* (43), 13144-52.

(54). Blundell, E. L.; Vogel, R.; Platt, M., Particle-by-Particle Charge Analysis of DNA-Modified Nanoparticles Using Tunable Resistive Pulse Sensing. *Langmuir* **2016,** *32* (4), 1082-90.

(55). Booth, M. A.; Vogel, R.; Curran, J. M.; Harbison, S.; Travas-Sejdic, J., Detection of target-probe oligonucleotide hybridization using synthetic nanopore resistive pulse sensing. *Biosens Bioelectron* **2013,** *45*, 136-40.

(56). Nair, S. V.; Witek, M. A.; Jackson, J. M.; Lindell, M. A.; Hunsucker, S. A.; Sapp, T.; Perry, C. E.; Hupert, M. L.; Bae-Jump, V.; Gehrig, P. A.; Wysham, W. Z.; Armistead, P. M.; Voorhees, P.; Soper, S. A., Enzymatic cleavage of uracil-containing single-stranded DNA linkers

for the efficient release of affinity-selected circulating tumor cells. *Chem Commun (Camb)* **2015,** *51* (15), 3266-9.

(57). Hupert, M. L.; Jackson, J. M.; Wang, H.; Witek, M. A.; Kamande, J.; Milowsky, M. I.; Whang, Y. E.; Soper, S. A., Arrays of High-Aspect Ratio Microchannels for High-Throughput Isolation of Circulating Tumor Cells (CTCs). *Microsyst Technol* **2014,** *20* (10-11), 1815-1825.

(58). Menard, L. D.; Ramsey, J. M., Electrokinetically-driven transport of DNA through focused ion beam milled nanofluidic channels. *Anal Chem* **2013,** *85* (2), 1146-53.

(59). Zhao, Z.; Yang, Y.; Zeng, Y.; He, M., A microfluidic ExoSearch chip for multiplexed exosome detection towards blood-based ovarian cancer diagnosis. *Lab Chip* **2016,** *16* (3), 489-96.

(60). Nolen, B. M.; Lokshin, A. E., Biomarker testing for ovarian cancer: clinical utility of multiplex assays. *Mol Diagn Ther* **2013,** *17* (3), 139-46.

(61). Bonifacio, V. D. B., Ovarian Cancer Biomarkers: Moving Forward in Early Detection. *Adv Exp Med Biol* **2020,** *1219*, 355-363.

(62). Menon, U.; Karpinskyj, C.; Gentry-Maharaj, A., Ovarian Cancer Prevention and Screening. *Obstet Gynecol* **2018,** *131* (5), 909-927.

(63). Qiu, Y.; Siwy, Z., Probing charges on solid-liquid interfaces with the resistive-pulse technique. *Nanoscale* **2017,** *9* (36), 13527-13537.

(64). Wen-Jie Lan, C. K., Jie-Wen Xiong, Andreas Bund, and Henry S. White, Effect of Surface Charge on the Resistive Pulse Waveshape during Particle Translocation through Glass Nanopores. *The Journal of Physical Chemistry C* **2014,** *118* (5), 2726-2734.

(65). Justin Menestrina, C. Y., Matthew Schiel, Ivan Vlassiouk, and Zuzanna S. Siwy, Charged Particles Modulate Local Ionic Concentrations and Cause Formation of Positive Peaks in Resistive-Pulse-Based Detection. *The Journal of Physical Chemistry C* **2014,** *118* (5), 2391-2398.

(66). Cabello-Aguilar, S.; Abou Chaaya, A.; Picaud, F.; Bechelany, M.; Pochat-Bohatier, C.; Yesylevskyy, S.; Kraszewski, S.; Bechelany, M. C.; Rossignol, F.; Balanzat, E.; Janot, J. M.; Miele, P.; Dejardin, P.; Balme, S., Experimental and simulation studies of unusual current blockade induced by translocation of small oxidized PEG through a single nanopore. *Phys Chem Chem Phys* **2014,** *16* (33), 17883-92.

(67). Innes, L. M.; Chen, C. H.; Schiel, M.; Pevarnik, M.; Haurais, F.; Toimil-Molares, M. E.; Vlassiouk, I.; Theogarajan, L.; Siwy, Z. S., Velocity profiles in pores with undulating opening diameter and their importance for resistive-pulse experiments. *Anal Chem* **2014,** *86* (20), 10445-53.

(68). Goyal, G.; Freedman, K. J.; Kim, M. J., Gold nanoparticle translocation dynamics and electrical detection of single particle diffusion using solid-state nanopores. *Anal Chem* **2013,** *85* (17), 8180-7.

(69). Sweeney, D. C.; Douglas, T. A.; Davalos, R. V., Characterization of Cell Membrane Permeability In Vitro Part II: Computational Model of Electroporation-Mediated Membrane Transport. *Technol Cancer Res Treat* **2018,** *17*, 1533033818792490.

(70). Garcia-Sanchez, T.; Muscat, A.; Leray, I.; Mir, L. M., Pyroelectricity as a possible mechanism for cell membrane permeabilization. *Bioelectrochemistry* **2018,** *119*, 227-233.

(71). Srivastava, A.; Filant, J.; Moxley, K. M.; Sood, A.; McMeekin, S.; Ramesh, R., Exosomes: a role for naturally occurring nanovesicles in cancer growth, diagnosis and treatment. *Curr Gene Ther* **2015,** *15* (2), 182-92.

(72). van der Pol, E.; Coumans, F. A.; Grootemaat, A. E.; Gardiner, C.; Sargent, I. L.; Harrison, P.; Sturk, A.; van Leeuwen, T. G.; Nieuwland, R., Particle size distribution of exosomes and microvesicles determined by transmission electron microscopy, flow cytometry, nanoparticle tracking analysis, and resistive pulse sensing. *J Thromb Haemost* **2014,** *12* (7), 1182-92.

Chapter 5: Potential Applications of EV-MAP chip and Nano-coulter Counter Chip

In this chapter, applications of the EV-MAP and nCC chips were further explored in some unique applications, including the detection of radiation injury using EVs and the analysis of SARS-CoV-2 virus particles. The EV-MAP chip was used for the detection of radiation injury, which involved the analysis of three sets of mouse plasma samples, and used EV concentration as an indicator of physiological effects of radiation exposure. Both CD8 and CD81-associated EVs were affinity isolated and quantified using the BCA total protein expression assay. It was found that the level of CD81-associated EVs was unchanged, the CD8-associated EV subtype levels increased upon radiation exposure. This result was suspected to be due to the high cellular activity of CD8+ T cells upon radiation exposure. Cetain EV miRNAs associated with radiation injury, miR-92a-3p and miR-204-5p, were also confirmed to be upregulated following radiation exposure as determined via quantitative PCR (qPCR). Therefore, a strategy to diagnose and monitor radiation injury by analyzing CD8-related EV subtype is feasible. COVID-19 has become a global pandemic, and because of the nano-particle counting capability, the nCC chip was applied for SARS-CoV-2 virus particle counting. A known concentration of heat-inactivated SARS-CoV-2 particles were enumerated by the nCC chip to establish a calibration curve. In addition, with the application of EV-MAP chip charged with an aptamer directed against the ACE2 receptor binding domain of the spike protein was used to select SARS-CoV-2 particles from saliva samples and sent to the nCC chip for virus particle counting.

5.1. Introduction

As our previous studies have shown for high-grade serous ovarian cancer detection (see Chapter 4), the EV-MAP chip coupled with the nCC chip have sufficient performance for EV isolation and enumeration for cancer screening. However, both chips can also be applied to other disease states for screening as well. For example, in this chapter the EV-MAP/nCC combination chips were applied for EV isolation to determine radiation injury and diagnosis of COVID-19 using the EV-MAP chip for particle enrichment from followed by nCC enumeration of the enriched particles.

Accidental radiation exposure has been recognized as a disaster caused by humans, and more than 90 nuclear and radiation accidents have occurred in the past 60 years.[1, 2] Governments have spent >$20 billion for damage and recovery of accidental radiation exposure.[3-5] In addition, there are more than hundreds of thousands of deaths directly or indirectly resulting from ionizing radiation.[6-8] However, during triage to understand patient exposure levels and the effects physiologically, the attending physician can only estimate the radiation injury level by questioning the patient as to exposure details.[9]

Continuous DNA damage monitoring can be used to understand the long-term extent of radiation damage, this must proceed for years with frequent blood draws to understand long range effects of radiation exposure. Unfortunately, assessing radiation injury immediately following exposure can be underestimated because of mild symptoms. As a result, patients may miss the optimal treatment regimen in a timely manner, and the mortality can be dramatically increased without proper medications.[6, 10, 11] In addition, the diagnosis questionnaire usually takes a much longer time than other types of diagnoses. This means that medication will fail for a large group of patients who are potentially exposed to massive amounts of radiation, such as those involved in

the Fukushima nuclear power plant disaster. There were >170,000 residents in the radiation exposure zone, including about 10,000 residents who were diagnosed with various degrees of radiation injury.[2, 12] In such a disaster, it is clear that rapid and economical techniques would be beneficial to classify patients for providing timely and targeted medical assistance with favorable outcomes.

From recent studies, radiation injury-related proteins and miRNAs have been verified within EVs.[13, 14] In addition, both EV-related protein and miRNA have been evaluated and show a significant difference in expression after radiation exposure.[15, 16] As a summary, EV-related content, including protein and RNA, can be used as efficient biomarkers to diagnose the physiological status of radiation exposure. Unfortunately, EV studies are remaining on conventional isolation methods, including ultracentrifugation, ultrafiltration, or precipitation.[17-20] Challenges with assays using conventional EV isolation methods mentioned above all require different levels of sample pre-purification, which can extend the duration of the assay and complicate the workflow.[21]

Our target was to establish a platform with the advantages of less invasive, high throughput, rapid, and inexpensive EV isolation and analysis from plasma, which can help detect and monitor the status of radiation overexposed patients. A mouse model were provided and consisted of healthy, low dose (2 Gy), and high dose (12 Gy) mice with whole-body radiation and sacrificed within 24 h post-exposure. The EV-MAP chip was used for EV isolation from mouse plasma samples. Previous publications have shown that the cellular activity of CD8+ T cells can be induced by radiation, but the interference on EV activity is still unraveled.[22-24] The sub-type of EV with CD8 and CD81 expression were targets for isolation and subsequent analysis. The total protein content from isolated EVs was performed using the Bicinchoninic Acid (BCA) protein

assay, and RT-qPCR was used to analyze the intra-vesicle expression level of mmu-mir-92a-3p and mmu-mir-204-5p miRNAs to determined expression in post-radiation exposure units.[25]

The second application involved the use of our EV-MAP chip and nCC chip for the analysis of SARS-CoV-2 particles associated with COVID-19. Coronaviruses (CoVs) are a family of enveloped viruses with a size ~125 nm in diameter and consist of a single-stranded RNA genome.[26-30] In 2019, a new SARS-CoV-2 outbreak (originated in Wuhan, China) reached pandemic levels and remains uncontrolled with approximately 200,000 diagnosed patients globally per day.[31] By the end of October 2020, the pandemic had caused > 45 million confirmed cases and 1.1 million deaths worldwide.

As of this writing, there are no antiviral drugs or vaccines developed against SARS-CoV-2, and as such, detection of the virus is paramount for disease prevention and control of contagious spread among communities. RT-qPCR is the golden standard for the etiological detection of SARS-CoV-2 but requires highly trained operators with a 2-3 h of assay turnaround time.[32] The number of tests for COVID-19 is growing, especially in the U.S., even though more than 120 million tests have been carried out in the U.S. as of October 14, 2020. However, the positivity rate is 8.6%, which is much higher than the recommended 5%.[33] More tests are urgent to fulfill the tremendous expansion of disease spreading.

The Food and Drug Administration (FDA) has approved five PCR-based diagnostic tests that can give results in ~1 hour: (i) the Acula SARS-CoV-2 test (30 min);[34] (ii) the BioFire COVID-19 test (50 min); (iii) BioFire Respiratory Panel 2.1 (45 min);[35] (iv) QIAstat-Dx Respiratory SARS-CoV-2 multiplex PCR assay (1 h);[36] and (v) NeuMoDx SARS-CoV-2 Assay (1 h).[37] Cepheid has developed Xpert® Xpress, a rapid molecular diagnostic tool that uses RT-qPCR and can be performed in a doctor's office with a turnaround time <1 h. The high-temperature

step in PCR can be replaced by loop-mediated isothermal amplification (LAMP) by using a strand displacement DNA polymerase.[38] Abbott has rolled out a small footprint instrument called the ID NOW, which uses LAMP technology to amplify viral RNA as a point-of-care test (POCT), and returns results in ~13 min.[31] The CRISPR/Cas system has recently been transformed into virus detection,[39] and the combination of CRISPR/Cas13a with isothermal amplification was recently reported for the detection of SARS-CoV-2 by earning FDA approval through an emergency use authorization (EUA).[40] Rapid antigen detection kits have also been developed to detect active infections.[41-43] However, they have limited sensitivity compared to RT-qPCR and increased false-negative results.[44, 45]

In this study, the EV-MAP chip was used to selectively isolate SARS-CoV-2 viral particles from a clinical sample (saliva or nasal swab) and enumerate them using the nCC chip and building a calibration plot for viral load determinations. Collectively, this system could be used as a simple and rapid screening tool to determine SARS-CoV-2 infection in a patient's sample in <15 min.

5.2. Experiments

5.2.1. EV isolation from mouse plasma samples

The EV isolation chip fabrication and surface treatment have been described in previous publications.[46-48] Direct antibody immobilization was used here instead of a cleavable oligonucleotide biofunctional linker. After chip surface treatment using UV/O_3 irradiation, 2 mg/mL NHS and 20 mg/mL EDC in MES buffer (pH 5.0) was infused into the chip and left at room temperature for 25 min. Then, an antibody solution with a concentration of 0.625 mg/mL was infused into the chip and allowed to react at room temperature for 2 h. A wash buffer (0.5% BSA and 1% PVP in 1 × PBS) was pumped through the chip at a flow rate of 10 µL/min for 30

min to eliminate non-specifically bound antibody. Then, a 100 µL plasma sample was flowed through the chip at a flow rate of 5 µL/min, followed by a second washing buffer (0.1% Tween-20 in 1X PBS) that was flowed through the chip at 5 µL/min for 20 min. Mouse plasma sample information is listed in Table 5.1. In one set of experiments, mouse plasma samples were analyzed using an anti-CD81 antibody (431301, R&D Systems) EV-MAP chip, and the EVs were released by injecting 1 mg/mL proteinase K (Thermo Scientific) into the chip. The chip was incubated at 37°C for 30 min and then rinsed using a washing buffer at a flow rate of 10 µL/min for 20 min. The effluent was stored at –80°C and/or sent for NTA analysis.

For some mouse samples, both anti-CD81 and anti-CD8 (53-6.7, R&D Systems) antibody chips were used for EV isolation and in this case, the total protein content was analyzed by the BCA total protein assay. After the EVs were isolated and washed on the EV chip, 10 µL of RIPA buffer was injected into the chip to lyse the EVs. The chip was placed in a sonicator for 10 min. Finally, the washing buffer was pumped through the chip at a flow rate of 10 µL/min for 20 min. The effluent was either stored at -80°C for further experiments or directly used for the BCA total protein assay and RNA extraction for RT-qPCR.

Table 5.1. Mouse models of ionized radiation treatment chart.

	Radiation Doses (Gy)	Post-exposure Time (h)	Sample Number
1st round – CD81	0	0	4
	12	0	5
2nd round – CD81	0	0	5
	12	6	4
	12	24	4
3rd round – CD81 & CD8	0	0	12
	2	24	10
	12	24	10

5.2.2. BCA total protein assay

BCA total protein assay, which was used to correlate with EV number, was carried out using the Micro BCA Protein Assay Kit (Thermo Fisher Scientific). For this assay, 50 µL of the effluent from the EV-MAP chip following proteinase K treatment was used for the BCA assay, and the "Microplate Procedure" was used to determine the total protein from each sample. A BSA (bovine serum albumin) protein standard was prepared with serial dilution to establish the calibration curve. The samples and standards were separately mixed with the working reagent at a 1:1 ratio and placed into a heating chamber at 37°C for 2 h. The plate was then cooled to room temperature and set into a plate reader with 562 nm absorbance readout.

5.2.3. miRNA extraction and RT-qPCR

From the EV-MAP chip effluent (50 µL of lysate) was used for RNA extraction and RT-qPCR experiments. The Direct-zol^{TM} RNA MiniPrep (Zymo Research) was used to extract total RNA from the lysed EV samples. From this extraction step, 30 µL of the eluent was collected. The extracted RNA was stored on ice and immediately used for PT-qPCR. The RNA samples were reverse transcripted by a miScript II RT kit (Qiagen), and consisted of 13 µL of eluted RNA sample mixed with 4 µL of 5× miScript HiSpec Buffer, 2 µL of 10× miScript Nucleics Mix, 2 µL of miScript Reverse Transcriptase Mix and made up to a total reaction volume of 20 µL. The reverse transcription solution was incubated at 37°C for 60 min and then incubated at 95°C for 60 min to inactivate the miScript Reverse Transcriptase. The cDNA templates were transferred to a new 96-well plate for qPCR and used the miScript SYBR Green PCR Kit (Qiagen) and miScript Primer Kit (Qiagen). A total of 7.5 µL of template cDNA was mixed with 12.5 µL of 2× QuantiTect SYBR Green PCR Master Mix, 2.5 µL of 10× miScript Universal Primer, and 2.5 µL of 10×

miScript Primer (Qiagen, mm_miR-92_1, 5'UAUUGCACUUGUCCCGGCCUG or mm_miR-204_2 5'UUCCCUUUGUCAUCCUAUGCCU), which targeted a mature miRNA mmu-miR-92a-3p and mmu-miR-204-5p, respectively. The 96-well plate with 25 µL reaction solution in each well was centrifuged at 1000 g for 1 min and then placed into a real-time PCR system (BioRed). The cycling conditions were setup based on the recommendation of the miScript SYBR Green PCR Kit, and the cycle number was 45.

5.2.4. Calibration curve for viral particle counting

Pre-heat inactivated SARS-CoV-2 viral particles (ATCC) in cell culture media were in the stock concentration and consisted of 3×10^8 particles/mL. The stock solution was diluted with serially in 1× PBS to establish the calibration curve (Table 5.2). A total of 5 µL of sample was filled into the nCC chip described in Chapter 4 (see Section 2.4 and Figure 4.4). The sample was withdrawn at a rate of 20 µL/min while the electrodes were connected across the nanopore. The entire setup was placed in a Faraday cage and -1 V potential was applied. The electrical signals were recorded using an Axoptach 200B and analyzed using Clampfit 10.1 software. Each point of the standard curve was collected in duplicate.

Table 5.2. SARS-CoV-2 stock solution with serial dilution factors and relevant concentrations.

Sample ID	Dilution Factors	Concentration (particles/mL)
Stock	1	3×10^8
A	5	6×10^7
B	25	12×10^6
C	125	2.4×10^6
D	250	1.2×10^6

5.2.5. Sample recognition by nCC

Four samples were used to evaluate the performance of the nCC chip for SARS-CoV-2 enumeration. All saliva samples from donors tested negative for SARS-CoV-2 RNA by RT-qPCR and 2 samples were spiked with the heat-inactivated SARS-CoV-2 viral particles (ATCC) to simulate positive samples. The saliva samples were processed through the EV-MAP chip for SARS-CoV-2 particle selection with the affinity agent consisting of a DNA aptamer targeting the spike protein (S protein) of the SARS-CoV-2 viral envelop.[49] Following photochemical release of the selected viral particles, the eluted samples were then analyzed by the nCC chip.

5.3. Results and discussion

5.3.1. Isolated EV with concentration and total protein content analysis

The 1st round of mouse plasma samples were analyzed using the anti-CD81 EV-MAP selection chip, which would collect the entire population of small EVs irrespective of their cell-of-origin. However, neither EV quantity nor size distribution showed significant differences between healthy controls and radiation exposed mice (Figure 5.1.a&b). According to the experimental design, the plasma of the radiation exposed group was sacrificed after exposure. However, based on the literature, the prodromal stage of ionizing radiation is from 4 to 24 h, and the level of circulating EV production may peak after 6 h.[15, 25, 50, 51] Therefore, we performed a second set of experiments that included analysis of plasma samples in mice 6 h and 24 h post-radiation exposure. However, there was still no significant difference in EV quantity or size distribution for both groups compared to the healthy control group (Figure 5.1.c&d) when using anti-CD81 antibodies for EV selection from plasma. For the EVs isolated using anti-CD81, the entire population of small EVs was expected to be selected by the chip.[52-54] The concentrations of

total EVs in the plasma can be adjusted to a consistent levels due to the higher uptake rate with post-radiation exposure.[55]

On the other hand, literature precedence has shown that radiation exposure will induce total cellular activity of CD8+ T cells.[22, 24, 56-59] As summarizing our previous results and information from the literature, a hypothesis was stated that more CD8+ T cell-related EVs may be expected because of this increased cellular activity, while the total small EV subtype can be adjusted to a consistent level. As a result, the CD8+ T cell-related EVs can have a higher ratio in the total small EV, and makes CD8 expressed EV a better target for post-radiation detection. Therefore, we performed a third round of experiments that analyzed the total small EV subtype, and also the CD8 expressed subtype. In this assay, 32 plasma samples, including 12 healthy controls, 10 low dose mice, and 10 high dose exposed mice (Table 5.1) were analyzed using anti-CD81 and anti-CD8 EV-MAP chips. The total protein amount from the isolated EVs was analyzed to validate our hypothesis.

The expression of EV-associated proteins is considered to be a good indicator of EV level,[25, 60-62] and thus was used to determine EV amount in the EV-MAP chip isolate. As shown in Figure 5.2a&b, the total protein content of CD8-related EVs for the low dose group and high dose group exhibited significantly higher amounts of protein compared to the control group ($p = 0.0001$, and $p = 0.0076$, respectively). These results showed that CD8-related EV expression level was upregulated in both of the low-dose and high-dose groups compared to those mice receiving no radiation. In the case of CD81-related EV samples, there was no significant difference in all groups (Figure 5.2). The 3rd round sample set showed a consistent statement to our previous observation and hypothesis that the overall quantity of small EVs isolated via CD-81 would not have a significant difference, whereas CD8-related small EV subtype expression level was significantly

upregulated upon radiation exposure. Thus, our strategy of diagnosing populations exposed to ionizing radiation can be detected using the CD8-related small EV subtype.

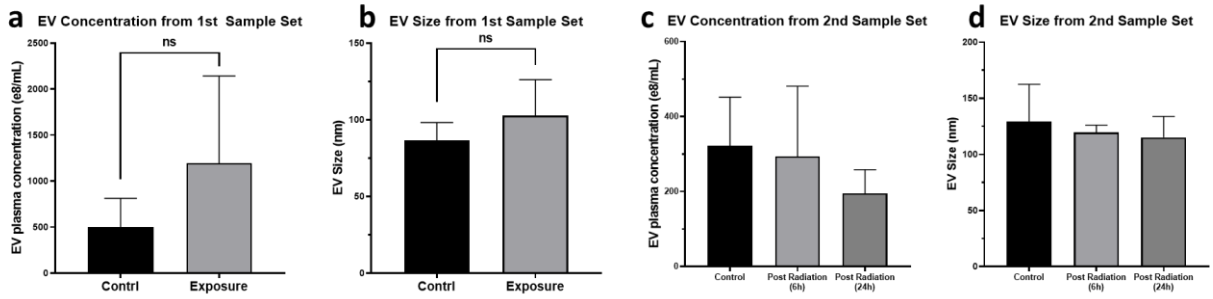

Figure 5.1. 1st and 2nd round of mice plasma sample sets. Two different groups of mice including 4 healthy controls, 5 radiation exposure (12 Gy) from 1st sample set; and three different groups of mice including 5 healthy controls, 4 radiation exposure (6 hours after 12 Gy), 4 radiation exposure (24 hours after 12 Gy). EVs were isolated by anti-CD81 immobilized EV-MAP chip for both sample sets, and analyzed by nanoparticle tracking analysis. **a&b)** EV plasma concentration and size shows no significant difference between the two groups.**c&d)** EV plasma concentration and size shows no significant difference among the three groups.

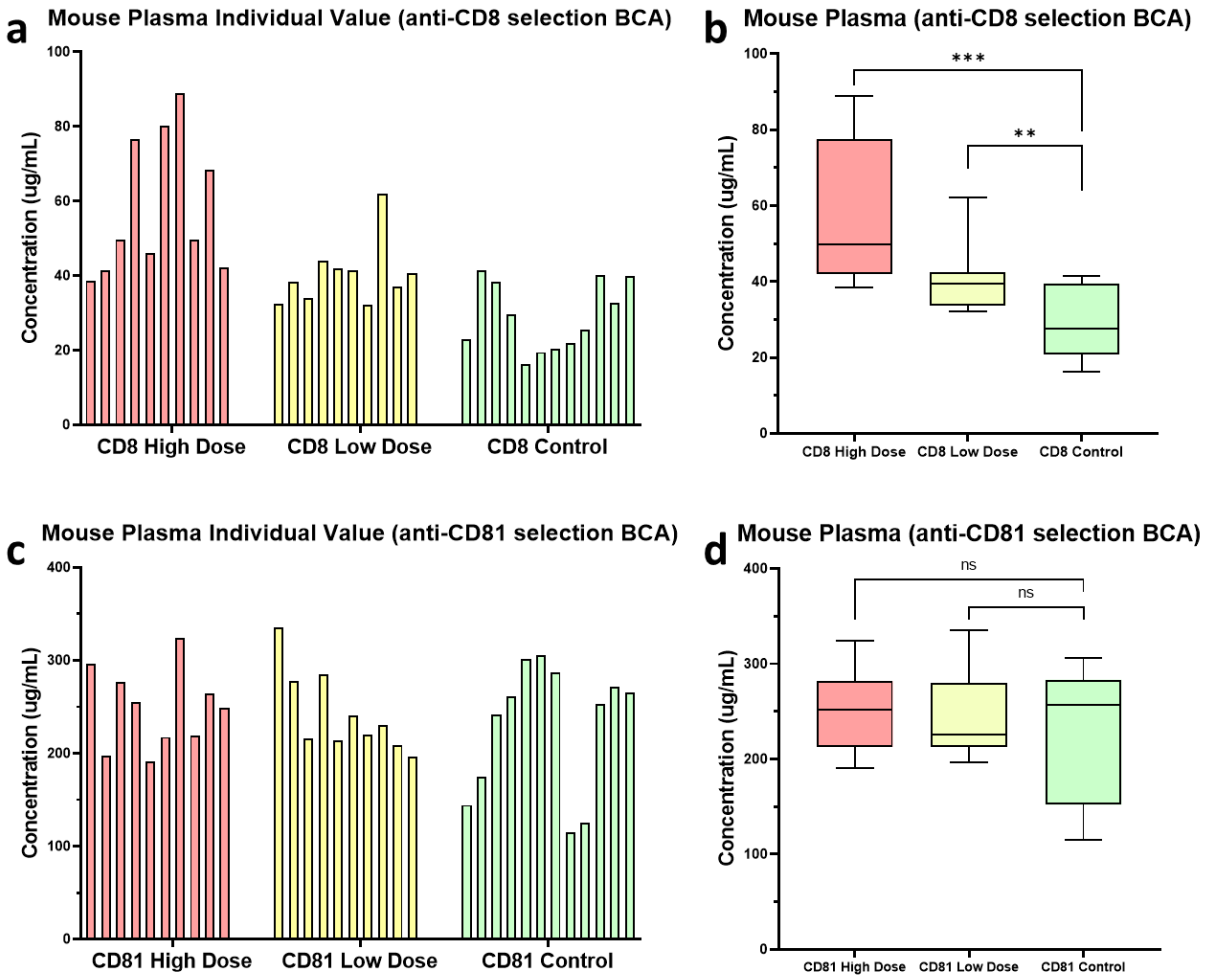

Figure 5.2. 3rd round of mice plasma sample set. Three different groups of mice, including 12 healthy controls, 10 low dose radiation units (2 Gy), and 10 high dose radiation units (12 Gy). **a)** EVs were isolated by anti-CD8 immobilized EV-MAP chip, lysed, and analyzed by BCA total protein assay. **b)** Among the three groups, the protein expression was much higher in the high dose group ($p = 0.0001$) and low dose group ($p = 0.0076$), comparing to the healthy control group. **c)** EVs were isolated by anti-CD81 immobilized EV-MAP chip, lysed, and analyzed by BCA total protein assay. **d)** Among the three groups, the protein expression had no significant difference between the high dose or the low dose to the control.

5.3.2. RT-qPCR results

In the 3rd round of mouse plasma samples, two mature miRNAs were also analyzed, which included miR-92a-3p and miR-204-5p. These two miRNAs have been verified in EVs in several previous studies, and both miRNAs are upregulated after radiation exposure.[25, 63, 64] Therefore, a

strategy was established to analyze the expression level of miR-92a-3p and miR-204-5p in EVs to determine the radiation injury level. The total small EVs isolated by the anti-CD81 and the subtype isolated by the anti-CD8 EV-MAP chips were used as sample sources for the RT-PCR assay. Total RNA was extracted and subjected to reverse transcription and amplified for quantitative analysis targeting the miR-92a-3p and miR-204-5p for EV-related miRNA expression levels. As Figure 5.3 shows, the amplification targeting miR-92a-3p for CD-81 isolated EVs, there were significant differences in C_q values at low and high dose samples compared to the control (Low Dose to Control $p = 0.0171$, High Dose to Control $p = 0.0001$). For the CD-8 subtype, C_q values were significantly different only at the high dose level compared to the control ($p = 0.0001$). In the amplification targeting miR-204-5p, there were significant differences between the low dose, high dose and control groups for both CD-81 small EVs and the CD8-subtype (CD81 Low Dose to Control $p = 0.0008$, CD81 High Dose to Control $p = 0.0003$, CD8 Low Dose to Control $p = 0.0188$, CD81 High Dose to Control $p = 0.0015$). Since there was no reference gene or standard curve introduced in the experiment, the actual miRNA copy number could not be calculated. From the data, there was an obvious trend towards upregulation of both target miRNAs in the CD-18 population of small EVs after the mouse samples were exposed to either low or high doses of radiation. However, the significant difference in the CD-8 subtype was only prevalent with the high dose versus the control. With the consideration of previous protein expression results (Figure 5.2), the high secretion level of EVs in the CD-8 subtype did not additionally lead to significant overexpression of the miR-92a-3p and miR-204-5p in the isolated EV's cargo. As a hypothesis, the major expression of the miR-92a-3p and miR-204-5p were not in the cargo of CD-8 subtype EVs but possibly in other subtype of EVs. Therefore, the results only showed that the target miRNA expression of the CD-81 population EVs had a better difference compared to the CD-8

subtype EV. Thus far, our strategy of targeting up-regulation of miRNA expression in EV to diagnose and predict target radiation injury is feasible. At the same time, further studies on the miRNA variability in specific EV subtypes are necessary.

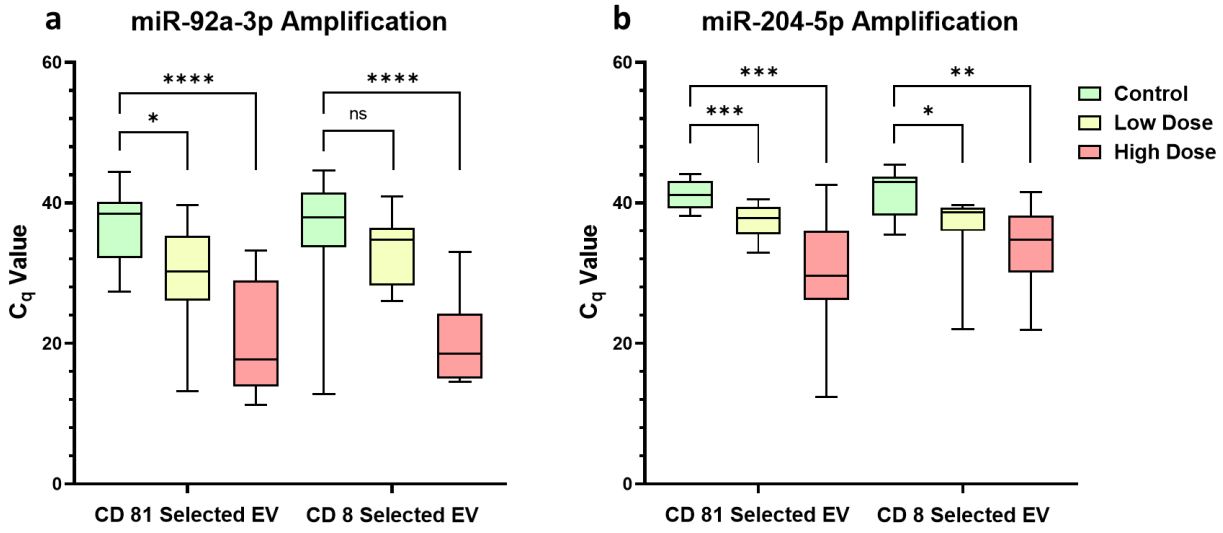

Figure 5.3. 3rd round of mice plasma sample set. Three different groups of mice, including 12 healthy controls, 10 low dose radiation units (2 Gy), and 10 high dose radiation units (12 Gy). Total RNA was extracted, reverse transcript, and quantified by real-time PCR from both EVs isolated by anti-CD81 immobilized EV-MAP chip and the subpopulation isolated by anti-CD8 immobilized EV-MAP chip. The Cq values were used to characterize the expression levels. **a)** miR-92a-3p was the targeting miRNA for RT-qPCR. The miRNA input levels were showing significant difference, that CD81 Low Dose to Control p = 0.0171, CD81 High Dose to Control p = 0.0001. CD8 Low Dose to Control has no significant differences, CD8 High Dose to Control p = 0.0001. **b)** miR-204-5p was the targeting miRNA for RT-qPCR. The miRNA input levels were showing significant difference, that CD81 Low Dose to Control p = 0.0008, CD81 High Dose to Control p = 0.0003, CD8 Low Dose to Control p = 0.0188, CD81 High Dose to Control p = 0.0015.

5.3.3. SARS-CoV-2 particle counting by nCC chip

Because of the structure of the nCC chip, including its 200 nm × 200 nm pore size, the nCC chip was also used to perform SARS-CoV-2 viral particle counting, which has an average particle size similar to small EVs. Before counting the samples, a standard curve was established to evaluate the nCC chip's performance for the SARS-CoV-2 viral particles by serial dilution of a

stock solution (Figure 5.4a). Each dilution factor had duplicate data points, and the standard curve had a favorable correlation coefficient (R^2 = 0.9714). We also tested the nCC to enumerate viral particle spiked in clinical saliva samples (Figure 5.4b). In these samples, the concentration of samples 1 and 2 were 5.54 × 10^8 particles/mL and 2.12 × 10^8 particles/mL, respectively, while samples 3 and 4 had no particle detected. The results showed that the nCC chip is capable of enumerating SARS-CoV-2 viral particles. However, further optimization are necessary to quantify the viral particles for COVID-19 screening purposes, especially at lower viral loads.

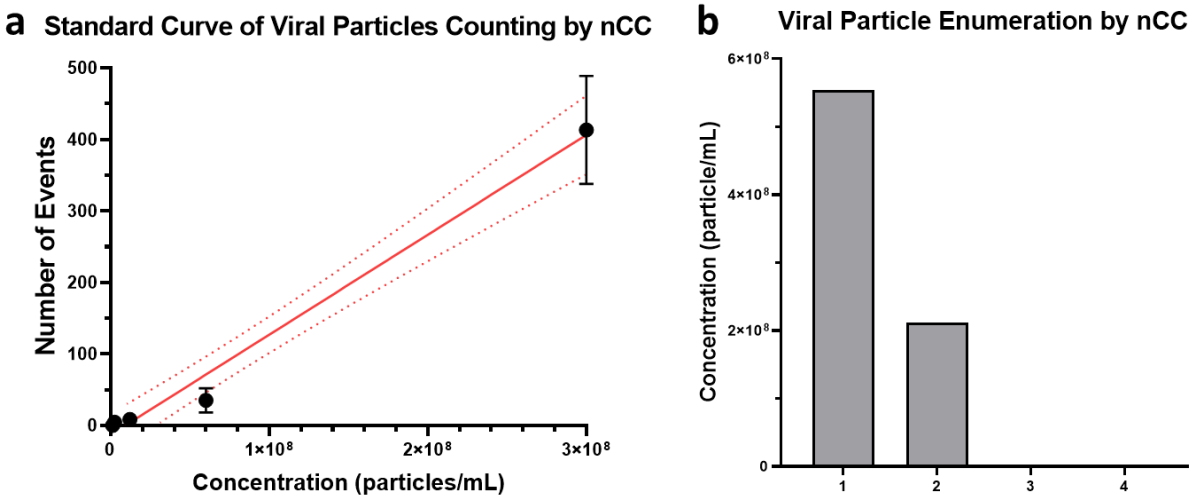

Figure 5.4. a) A standard curve of the SARS-CoV-2 viral particle enumerating by nCC chip (R^2 = 0.9714). The stock concentration was 3 × 10^8 particles/mL. **b)** The concentration profiles of the 4 samples enriched by the EV-MAP chip and enumerated by nCC chips.

5.4. Conclusions

In this chapter, additional applications were established using a combination of the EV-MAP and nCC chips, including identifying radiation injury and the enumeration of SRAS-CoV-2 viral particles. The results and data from three sets of mice indicated that the subtype of CD8-associate EV showed upregulated expression without significant changes in protein expression in the overall small EV population. In this condition, CD8+ T cells may increase in cellular activity

in the presence of radiation injury, which includes serving as a repair mechanism of damaged or mutated cells. The high level of cellular activity increased the secretion of EVs, which are also used for cell-to-cell communication.[65, 66] On the other hand, EVs isolated by the EV-MAP chip can also be used for miRNA studies. In experiments with miR-92a-3p and miR-204-5p, the difference in miRNA expression was more significant in the entire small EV population isolated by anti-CD81 antibody EV-MAP chip than in the subtype of EVs isolated by the anti-CD8 antibody EV-MAP chip. From this data, it can be inferred that the CD8 subtype may not be a major expression site for miR-92a-3p or miR-204-5p, and further studies are necessary to unravel more information concerning the selective packaging of miRNAs into small EVs. In addition, results were observed that the expression level of EV-related miR-92a-3p and miR-204-5p in plasma were up-regulated after ionizing radiation injury.

The nCC is widely used for particle counting, and our nCC chip was established and calibrated for EV enumeration. There are a number of published papers supporting the usage of nCC for virus particle counting.[67, 68] Our nCC chip also has the capability to count viruses smaller than 200 nm, and was adapted for SRAR-CoV-2 viral particle counting because of the emerging need for rapid screening for the COVID-19 pandemic. The concentration of viral particles in a sample can be measured from the frequency and number of electrical signals collected through an established concentration standard curve. In the four samples tested so far, the nCC chip was able to characterize the samples and estimate the concentration of viral particles from the upstream enrichment. However, the current performance of the nCC chip for SARS-CoV-2 enumeration may still require further optimization and calibration.

5.5. References

(1). Rojavin, Y.; Seamon, M. J.; Tripathi, R. S.; Papadimos, T. J.; Galwankar, S.; Kman, N.; Cipolla, J.; Grossman, M. D.; Marchigiani, R.; Stawicki, S. P., Civilian nuclear incidents: An overview of historical, medical, and scientific aspects. *J Emerg Trauma Shock* **2011,** *4* (2), 260-72.

(2). Clement, C. H., Experiences of Fukushima. *Ann ICRP* **2016,** *45* (2_suppl), 4-6.

(3). Matzo, M.; Wilkinson, A.; Lynn, J.; Gatto, M.; Phillips, S., Palliative care considerations in mass casualty events with scarce resources. *Biosecur Bioterror* **2009,** *7* (2), 199-210.

(4). Mettler, F. A., Jr.; Voelz, G. L., Major radiation exposure--what to expect and how to respond. *N Engl J Med* **2002,** *346* (20), 1554-61.

(5). Gerber, T. C.; Carr, J. J.; Arai, A. E.; Dixon, R. L.; Ferrari, V. A.; Gomes, A. S.; Heller, G. V.; McCollough, C. H.; McNitt-Gray, M. F.; Mettler, F. A.; Mieres, J. H.; Morin, R. L.; Yester, M. V., Ionizing radiation in cardiac imaging: a science advisory from the American Heart Association Committee on Cardiac Imaging of the Council on Clinical Cardiology and Committee on Cardiovascular Imaging and Intervention of the Council on Cardiovascular Radiology and Intervention. *Circulation* **2009,** *119* (7), 1056-65.

(6). Burgio, E.; Piscitelli, P.; Migliore, L., Ionizing Radiation and Human Health: Reviewing Models of Exposure and Mechanisms of Cellular Damage. An Epigenetic Perspective. *Int J Environ Res Public Health* **2018,** *15* (9).

(7). DiCarlo, A. L.; Maher, C.; Hick, J. L.; Hanfling, D.; Dainiak, N.; Chao, N.; Bader, J. L.; Coleman, C. N.; Weinstock, D. M., Radiation injury after a nuclear detonation: medical consequences and the need for scarce resources allocation. *Disaster Med Public Health Prep* **2011,** *5 Suppl 1*, S32-44.

(8). Koenig, K. L.; Goans, R. E.; Hatchett, R. J.; Mettler, F. A., Jr.; Schumacher, T. A.; Noji, E. K.; Jarrett, D. G., Medical treatment of radiological casualties: current concepts. *Ann Emerg Med* **2005,** *45* (6), 643-52.

(9). Kunkler, J.; Adams, T. G.; Manger, M.; Casagrande, R., Review of Cases of Occult Radiation Exposure and an Analysis of Time to Diagnosis. *Health Phys* **2018,** *115* (2), 308-312.

(10). Shi, L.; Tashiro, S., Estimation of the effects of medical diagnostic radiation exposure based on DNA damage. *J Radiat Res* **2018,** *59* (suppl_2), ii121-ii129.

(11). Rothkamm, K.; Barnard, S.; Moquet, J.; Ellender, M.; Rana, Z.; Burdak-Rothkamm, S., DNA damage foci: Meaning and significance. *Environ Mol Mutagen* **2015,** *56* (6), 491-504.

(12). Loh, S. L.; Amir, S., Healing Fukushima: Radiation hazards and disaster medicine in post-3.11 Japan. *Soc Stud Sci* **2019,** *49* (3), 333-354.

(13). Szatmari, T.; Hargitai, R.; Safrany, G.; Lumniczky, K., Extracellular Vesicles in Modifying the Effects of Ionizing Radiation. *Int J Mol Sci* **2019,** *20* (22).

(14). Flamant, S.; Tamarat, R., Extracellular Vesicles and Vascular Injury: New Insights for Radiation Exposure. *Radiat Res* **2016,** *186* (2), 203-18.

(15). Kulkarni, S.; Koller, A.; Mani, K. M.; Wen, R.; Alfieri, A.; Saha, S.; Wang, J.; Patel, P.; Bandeira, N.; Guha, C.; Chen, E. I., Identifying Urinary and Serum Exosome Biomarkers for Radiation Exposure Using a Data Dependent Acquisition and SWATH-MS Combined Workflow. *Int J Radiat Oncol Biol Phys* **2016,** *96* (3), 566-77.

(16). Acharya, S. S.; Fendler, W.; Watson, J.; Hamilton, A.; Pan, Y.; Gaudiano, E.; Moskwa, P.; Bhanja, P.; Saha, S.; Guha, C.; Parmar, K.; Chowdhury, D., Serum microRNAs are early indicators of survival after radiation-induced hematopoietic injury. *Sci Transl Med* **2015,** *7* (287), 287ra69.

(17). Alvaro, D., The challenge of cholangiocarcinoma diagnosis: The turning point is in extracellular vesicles? *Hepatology* **2017,** *66* (4), 1029-1031.

(18). Gardiner, C.; Ferreira, Y. J.; Dragovic, R. A.; Redman, C. W.; Sargent, I. L., Extracellular vesicle sizing and enumeration by nanoparticle tracking analysis. *J Extracell Vesicles* **2013,** *2*.

(19). Heinemann, M. L.; Ilmer, M.; Silva, L. P.; Hawke, D. H.; Recio, A.; Vorontsova, M. A.; Alt, E.; Vykoukal, J., Benchtop isolation and characterization of functional exosomes by sequential filtration. *J Chromatogr A* **2014,** *1371*, 125-35.

(20). Sunkara, V.; Woo, H. K.; Cho, Y. K., Emerging techniques in the isolation and characterization of extracellular vesicles and their roles in cancer diagnostics and prognostics. *Analyst* **2016,** *141* (2), 371-81.

(21). Li, P.; Kaslan, M.; Lee, S. H.; Yao, J.; Gao, Z., Progress in Exosome Isolation Techniques. *Theranostics* **2017,** *7* (3), 789-804.

(22). Filatenkov, A.; Baker, J.; Mueller, A. M.; Kenkel, J.; Ahn, G. O.; Dutt, S.; Zhang, N.; Kohrt, H.; Jensen, K.; Dejbakhsh-Jones, S.; Shizuru, J. A.; Negrin, R. N.; Engleman, E. G.; Strober, S., Ablative Tumor Radiation Can Change the Tumor Immune Cell Microenvironment to Induce Durable Complete Remissions. *Clin Cancer Res* **2015,** *21* (16), 3727-39.

(23). Bristol, J. A.; Schlom, J.; Abrams, S. I., Development of a murine mutant Ras CD8+ CTL peptide epitope variant that possesses enhanced MHC class I binding and immunogenic properties. *J Immunol* **1998,** *160* (5), 2433-41.

(24). Lee, Y.; Auh, S. L.; Wang, Y.; Burnette, B.; Wang, Y.; Meng, Y.; Beckett, M.; Sharma, R.; Chin, R.; Tu, T.; Weichselbaum, R. R.; Fu, Y. X., Therapeutic effects of ablative radiation on local tumor require CD8+ T cells: changing strategies for cancer treatment. *Blood* **2009,** *114* (3), 589-95.

(25). Yentrapalli, R.; Merl-Pham, J.; Azimzadeh, O.; Mutschelknaus, L.; Peters, C.; Hauck, S. M.; Atkinson, M. J.; Tapio, S.; Moertl, S., Quantitative changes in the protein and miRNA cargo of plasma exosome-like vesicles after exposure to ionizing radiation. *Int J Radiat Biol* **2017,** *93* (6), 569-580.

(26). Cui, J.; Li, F.; Shi, Z. L., Origin and evolution of pathogenic coronaviruses. *Nat Rev Microbiol* **2019,** *17* (3), 181-192.

(27). Bárcena, M.; Oostergetel, G. T.; Bartelink, W.; Faas, F. G.; Verkleij, A.; Rottier, P. J.; Koster, A. J.; Bosch, B. J., Cryo-electron tomography of mouse hepatitis virus: insights into the structure of the coronavirion. *Proceedings of the National Academy of Sciences* **2009,** *106* (2), 582-587.

(28). Neuman, B. W.; Adair, B. D.; Yoshioka, C.; Quispe, J. D.; Orca, G.; Kuhn, P.; Milligan, R. A.; Yeager, M.; Buchmeier, M. J., Supramolecular architecture of severe acute respiratory syndrome coronavirus revealed by electron cryomicroscopy. *Journal of virology* **2006,** *80* (16), 7918-7928.

(29). Wang, Y.; Sun, J.; Zhu, A.; Zhao, J.; Zhao, J., Current understanding of middle east respiratory syndrome coronavirus infection in human and animal models. *Journal of thoracic disease* **2018,** *10* (Suppl 19), S2260.

(30). Chen, B.; Tian, E. K.; He, B.; Tian, L.; Han, R.; Wang, S.; Xiang, Q.; Zhang, S.; El Arnaout, T.; Cheng, W., Overview of lethal human coronaviruses. *Signal Transduct Target Ther* **2020,** *5* (1), 89.

(31). Yuan, X.; Yang, C.; He, Q.; Chen, J.; Yu, D.; Li, J.; Zhai, S.; Qin, Z.; Du, K.; Chu, Z., Current and Perspective Diagnostic Techniques for COVID-19. *ACS infectious diseases* **2020,** *6* (8), 1998-2016.

(32). Jin, Y.-H.; Cai, L.; Cheng, Z.-S.; Cheng, H.; Deng, T.; Fan, Y.-P.; Fang, C.; Huang, D.; Huang, L.-Q.; Huang, Q., A rapid advice guideline for the diagnosis and treatment of 2019 novel coronavirus (2019-nCoV) infected pneumonia (standard version). *Military Medical Research* **2020,** *7* (1), 4.

(33). University, J. H. DAILY STATE-BY-STATE TESTING TRENDS. https://coronavirus.jhu.edu/testing/individual-states (accessed Nov 18, 2020).

(34). Hogan, C. A.; Garamani, N.; Lee, A. S.; Tung, J. K.; Sahoo, M. K.; Huang, C.; Stevens, B.; Zehnder, J.; Pinsky, B. A., Comparison of the Accula SARS-CoV-2 test with a laboratory-developed assay for detection of SARS-CoV-2 RNA in clinical nasopharyngeal specimens. *Journal of Clinical Microbiology* **2020**.

(35). Creager, H. M.; Cabrera, B.; Schnaubelt, A.; Cox, J. L.; Cushman-Vokoun, A. M.; Shakir, S. M.; Tardif, K. D.; Huang, M.-L.; Jerome, K. R.; Greninger, A. L., Clinical evaluation of the BioFire® Respiratory Panel 2.1 and detection of SARS-CoV-2. *Journal of Clinical Virology* **2020,** *129*, 104538.

(36). Visseaux, B.; Le Hingrat, Q.; Collin, G.; Bouzid, D.; Lebourgeois, S.; Le Pluart, D.; Deconinck, L.; Lescure, F.-X.; Lucet, J.-C.; Bouadma, L., Evaluation of the QIAstat-Dx Respiratory SARS-CoV-2 Panel, the first rapid multiplex PCR commercial assay for SARS-CoV-2 detection. *Journal of clinical microbiology* **2020**.

(37). Noerz, D.; Fischer, N.; Schultze, A.; Kluge, S.; Mayer-Runge, U.; Aepfelbacher, M.; Pfefferle, S.; Luetgehetmann, M., Clinical evaluation of a SARS-CoV-2 RT-PCR assay on a fully automated system for rapid on-demand testing in the hospital setting. *Journal of Clinical Virology* **2020**, 104390.

(38). Zanoli, L. M.; Spoto, G., Isothermal amplification methods for the detection of nucleic acids in microfluidic devices. *Biosensors* **2013,** *3* (1), 18-43.

(39). Broughton, J. P.; Deng, X.; Yu, G.; Fasching, C. L.; Servellita, V.; Singh, J.; Miao, X.; Streithorst, J. A.; Granados, A.; Sotomayor-Gonzalez, A., CRISPR–Cas12-based detection of SARS-CoV-2. *Nature Biotechnology* **2020**, 1-5.

(40). Zhang, F.; Abudayyeh, O. O.; Gootenberg, J. S., A protocol for detection of COVID-19 using CRISPR diagnostics. *A protocol for detection of COVID-19 using CRISPR diagnostics* **2020,** *8*.

(41). Lambert-Niclot, S.; Cuffel, A.; Le Pape, S.; Vauloup-Fellous, C.; Morand-Joubert, L.; Roque-Afonso, A.-M.; Le Goff, J.; Delaugerre, C., Evaluation of a rapid diagnostic assay for detection of SARS CoV-2 antigen in nasopharyngeal swab. *Journal of clinical microbiology* **2020**.

(42). Nagura-Ikeda, M.; Imai, K.; Tabata, S.; Miyoshi, K.; Murahara, N.; Mizuno, T.; Horiuchi, M.; Kato, K.; Imoto, Y.; Iwata, M., Clinical evaluation of self-collected saliva by RT-qPCR, direct RT-qPCR, RT-LAMP, and a rapid antigen test to diagnose COVID-19. *Journal of Clinical Microbiology* **2020**.

(43). Grant, B. D.; Anderson, C. E.; Williford, J. R.; Alonzo, L. F.; Glukhova, V. A.; Boyle, D. S.; Weigl, B. H.; Nichols, K. P., SARS-CoV-2 coronavirus nucleocapsid antigen-detecting half-strip lateral flow assay toward the development of point of care tests using commercially available reagents. *Analytical chemistry* **2020,** *92* (16), 11305-11309.

(44). Mertens, P.; De Vos, N.; Martiny, D.; Jassoy, C.; Mirazimi, A.; Cuypers, L.; Van den Wijngaert, S.; Monteil, V.; Melin, P.; Stoffels, K., Development and potential usefulness of the COVID-19 Ag Respi-Strip diagnostic assay in a pandemic context. *Frontiers in Medicine* **2020,** *7*, 225.

(45). Mak, G. C.; Cheng, P. K.; Lau, S. S.; Wong, K. K.; Lau, C.; Lam, E. T.; Chan, R. C.; Tsang, D. N., Evaluation of rapid antigen test for detection of SARS-CoV-2 virus. *Journal of Clinical Virology* **2020**, 104500.

(46). Wijerathne, H.; Witek, M. A.; Jackson, J. M.; Brown, V.; Hupert, M. L.; Herrera, K.; Kramer, C.; Davidow, A. E.; Li, Y.; Baird, A. E.; Murphy, M. C.; Soper, S. A., Affinity enrichment of extracellular vesicles from plasma reveals mRNA changes associated with acute ischemic stroke. *Commun Biol* **2020,** *3* (1), 613.

(47). Hupert, M. L.; Jackson, J. M.; Wang, H.; Witek, M. A.; Kamande, J.; Milowsky, M. I.; Whang, Y. E.; Soper, S. A., Arrays of High-Aspect Ratio Microchannels for High-Throughput Isolation of Circulating Tumor Cells (CTCs). *Microsyst Technol* **2014,** *20* (10-11), 1815-1825.

(48). Harshani Wijerathne, M. A. W., Mateusz L. Hupert, Joshua M. Jackson, Steven A. Soper, Microfluidic Device for EV and T-cell Isolation. **2019**.

(49). Pahattuge, T. N.; Jackson, J. M.; Digamber, R.; Wijerathne, H.; Brown, V.; Witek, M. A.; Perera, C.; Givens, R. S.; Peterson, B. R.; Soper, S. A., Visible photorelease of liquid biopsy markers following microfluidic affinity-enrichment. *Chem Commun (Camb)* **2020,** *56* (29), 4098-4101.

(50). Webb, R. L.; Kaiser, E. E.; Jurgielewicz, B. J.; Spellicy, S.; Scoville, S. L.; Thompson, T. A.; Swetenburg, R. L.; Hess, D. C.; West, F. D.; Stice, S. L., Human Neural Stem Cell Extracellular Vesicles Improve Recovery in a Porcine Model of Ischemic Stroke. *Stroke* **2018,** *49* (5), 1248-1256.

(51). Jelonek, K.; Widlak, P.; Pietrowska, M., The Influence of Ionizing Radiation on Exosome Composition, Secretion and Intercellular Communication. *Protein Pept Lett* **2016,** *23* (7), 656-63.

(52). Tian, Y.; Ma, L.; Gong, M.; Su, G.; Zhu, S.; Zhang, W.; Wang, S.; Li, Z.; Chen, C.; Li, L.; Wu, L.; Yan, X., Protein Profiling and Sizing of Extracellular Vesicles from Colorectal Cancer Patients via Flow Cytometry. *ACS Nano* **2018,** *12* (1), 671-680.

(53). Tauro, B. J.; Greening, D. W.; Mathias, R. A.; Ji, H.; Mathivanan, S.; Scott, A. M.; Simpson, R. J., Comparison of ultracentrifugation, density gradient separation, and immunoaffinity capture methods for isolating human colon cancer cell line LIM1863-derived exosomes. *Methods* **2012,** *56* (2), 293-304.

(54). Jeppesen, D. K.; Hvam, M. L.; Primdahl-Bengtson, B.; Boysen, A. T.; Whitehead, B.; Dyrskjot, L.; Orntoft, T. F.; Howard, K. A.; Ostenfeld, M. S., Comparative analysis of discrete exosome fractions obtained by differential centrifugation. *J Extracell Vesicles* **2014,** *3*, 25011.

(55). Hazawa, M.; Tomiyama, K.; Saotome-Nakamura, A.; Obara, C.; Yasuda, T.; Gotoh, T.; Tanaka, I.; Yakumaru, H.; Ishihara, H.; Tajima, K., Radiation increases the cellular uptake of exosomes through CD29/CD81 complex formation. *Biochem Biophys Res Commun* **2014,** *446* (4), 1165-71.

(56). Garnett, C. T.; Palena, C.; Chakraborty, M.; Tsang, K. Y.; Schlom, J.; Hodge, J. W., Sublethal irradiation of human tumor cells modulates phenotype resulting in enhanced killing by cytotoxic T lymphocytes. *Cancer Res* **2004,** *64* (21), 7985-94.

(57). Chakraborty, M.; Abrams, S. I.; Camphausen, K.; Liu, K.; Scott, T.; Coleman, C. N.; Hodge, J. W., Irradiation of tumor cells up-regulates Fas and enhances CTL lytic activity and CTL adoptive immunotherapy. *J Immunol* **2003,** *170* (12), 6338-47.

(58). Zheng, L.; Li, Z.; Ling, W.; Zhu, D.; Feng, Z.; Kong, L., Exosomes Derived from Dendritic Cells Attenuate Liver Injury by Modulating the Balance of Treg and Th17 Cells After Ischemia Reperfusion. *Cell Physiol Biochem* **2018,** *46* (2), 740-756.

(59). McKelvey, K. J.; Hudson, A. L.; Back, M.; Eade, T.; Diakos, C. I., Radiation, inflammation and the immune response in cancer. *Mamm Genome* **2018,** *29* (11-12), 843-865.

(60). Zhang, Q.; Bansal, A., Role of Extracellular Vesicles in the Diagnosis and Pathogenesis of Barrett's Esophagus: A Mini-Review. *Dig Dis Sci* **2020**.

(61). Jabalee, J.; Towle, R.; Garnis, C., The Role of Extracellular Vesicles in Cancer: Cargo, Function, and Therapeutic Implications. *Cells* **2018,** *7* (8).

(62). Thery, C.; Zitvogel, L.; Amigorena, S., Exosomes: composition, biogenesis and function. *Nat Rev Immunol* **2002,** *2* (8), 569-79.

(63). Fu, F.; Jiang, W.; Zhou, L.; Chen, Z., Circulating Exosomal miR-17-5p and miR-92a-3p Predict Pathologic Stage and Grade of Colorectal Cancer. *Transl Oncol* **2018,** *11* (2), 221-232.

(64). Yao, S.; Yin, Y.; Jin, G.; Li, D.; Li, M.; Hu, Y.; Feng, Y.; Liu, Y.; Bian, Z.; Wang, X.; Mao, Y.; Zhang, J.; Wu, Z.; Huang, Z., Exosome-mediated delivery of miR-204-5p inhibits tumor growth and chemoresistance. *Cancer Med* **2020**.

(65). Barile, L.; Vassalli, G., Exosomes: Therapy delivery tools and biomarkers of diseases. *Pharmacol Ther* **2017,** *174*, 63-78.

(66). Raposo, G.; Stoorvogel, W., Extracellular vesicles: Exosomes, microvesicles, and friends. *J Cell Biol* **2013,** *200* (4), 373-383.

(67). Harms, Z. D.; Mogensen, K. B.; Nunes, P. S.; Zhou, K. M.; Hildenbrand, B. W.; Mitra, I.; Tan, Z. N.; Zlotnick, A.; Kutter, J. P.; Jacobson, S. C., Nanofluidic Devices with Two Pores in Series for Resistive-Pulse Sensing of Single Virus Capsids. *Anal Chem* **2011,** *83* (24), 9573-9578.

(68). Yang, L.; Yamamoto, T., Quantification of Virus Particles Using Nanopore-Based Resistive-Pulse Sensing Techniques. *Front Microbiol* **2016,** *7*, 1500.

Chapter 6: Conclusion and Future Direction

6.1. Conclusions

Extracellular vesicle (EV) has been recognized as a relatively effective target biomarker in clinical liquid biopsy testing.[1, 2] The novel studies include not only techniques for the isolation and detection of EVs,[3, 4] but also techniques for tissue engineering of EVs as drug vector.[5] Simultaneously, microfluidic and nanofluidic technologies offer many advantages, such as minimized sample requirements, reduce device cost for clinical consumption, high throughput of sample processing, and higher downstream yield.[4, 6] With the advantages, our research is focused on the isolation, enrichment, and detection of EVs using microfluidics or nanofluidics devices. In addition, we are continually improving our chips for various purposes, including early detection of ovarian cancer by analyzing EV surface proteins; isolation, modify and releasing EVs for immunotherapy; radiation injury detection by EV proteins and miRNAs; and detection of ovarian cancer samples by measuring the size, and concentration of specific population of EVs.

Our Exosearch chip can isolate the EVs in plasma by immunoaffinity. The captured EVs by magnetic beads were labeled with different antibodies-fluorescence conjugations (anti-CA-125-Alexfluor-488, anti-EpCAM-Alexfluor-550, anti-CD24-Alexfluor-633). By analyzing the intensity of fluorescence from each sample, the expression level of the relevant proteins on the EV surface was understood, in order to characterize the plasma samples into the healthy unit or ovarian cancer patient.[7] Based on the Exosearch chip, we optimized the microfluidic chip fabrication by 3D printed mold, a faster chip fabrication process that facilitates prototype improvement. The most delicate structure of the mold produced by the 3D printing abrasive was 50 μm. With this chip, 500 nm magnetic beads were used to enrich, modify, and release the target subpopulations of EVs for cancer immunotherapy. By modifying the specific peptide (gp-100), the engineered EVs had

the ability to activate the immune system. The strategy of immunotherapy was: the engineered EVs were uptaken by the monocyte, and the peptide was expressed on the monocyte surface to proliferate as antigen-presenting cells (APCs). Then, the CD8 + T cell contacted the APC, and was stimulated and convented into cytotoxic T cell (CTL). The CTL would target the specific peptide that the monocytes uptaken, which was originally from the tumor cells.[8]

Next, the EV-MAP chip was furtherly improved to meet the need for greater EV isolation capacity and faster microfluidic chip fabrication. So we used a thermoplastic material, cyclic olefinic copolymer (COC), to fabricate the chip. Compared to the traditional microfluidic material polydimethylsiloxane (PDMS), COC has 100× more available antibody binding sites but only 50% of sampling processing time.[9-15] Furthermore, the EV-MAP chip was injection molded with a much faster production rate at 30 s/chip, which has lifted the feasibility of microfluidic chip mass production.[14] In a series of experiments, we realized that nanoparticle tracking analysis (NTA) might not be the ideal method for EV size and concentration analysis due to its detection variation and the large volume of sample requirement.[16, 17] The resistive pulse sensing (RPS) was first developed for viral particle characterization and well studied through the last few decays.[18] The RPS principle was also used as a coulter counter to enumerate the virus,[19-22] bacteria,[23, 24] Au nanoparticles,[25, 26] cells,[27-29] proteins,[30, 31] and DNA.[32, 33] In addition, the research field has started to use RPS principle for EV enumeration in recent years.[34, 35] We developed an in-plane (nCC) chip with the principle of RPS for EV sample size and concentration analysis to fulfill the drawback of current EV quantifications methods.[35, 36] nCC mold was fabricated using a focused ion beam (FIB) milling and the chip was fabricated using a nanoimprint for precise temperature and pressure control. The nCC chip includes advantages: (1) small sample volume consumption (5 μL); (2) high-resolution electronic signal; (3) High dynamic range of 10^6 to 10^{16} particles/mL

based on 100,000 Hz sampling frequency with 600 s recording; (4) capable of different type of sample processing, such as EV and viral particles; (5) thermoplastic material has lifted the potential of mass production. The combination of EV-MAP chip and nCC chip was used to isolate and enumerate tumor-related EV from high-grade serous carcinoma patients/healthy. Specific CA-125 expressed sub-type of EV were isolated and eluted by EV-MAP chips with the strategy of USER™ Enzymetic releasing. The eluted EV samples were introduced into the nCC chip for enumeration. Totally 16 of the patient plasma samples were processed and successfully characterized as their disease status from tumor-related EV number.

Finally, the combination of EV-MAP chip and nCC chip was also used in various applications, including detecting radiation injury level and enumeration of SARS-CoV-2 viral particles. The total population of small EVs was isolated from the plasma by CD-81 immobilized EV-MAP chip, and the CD8-associated sub-type of EVs was isolated from the plasma by anti-CD8 immobilized EV-MAP chip. The EV protein content was analyzed to verify the expression level for post-radiation exposure. The results indicated that, with 24 hours post-exposure units, the quantity of small EV population remained unaffected, but because of the increased activity of CD8+ T cell induced by radiation, the CD8 expressed EV secretion was upregulated. In addition, the intra-vesicle miRNA content, including miR-92a-3p and miR-204-5p, were upregulated with post-radiation exposure.

By combining these chips together, we are able to perform many EV-related experiments and analysis, including 1) Isolate and enrich the specific population of EVs from plasma samples at a higher purity, 2) Engineer and modify the isolated EVs, 3) Analyze EV-associated proteins and miRNAs, 4) Analyze the size and concentration of EVs in the samples.

6.2. Future direction

6.2.1. New parallel nanochannels design for nCC chip

The current nCC chip can enumerate particles, analyze the size and concentration of the target particles. However, there are several limitations that can be improved for the nCC chip, including the total sampling efficiency, electrical setup, and device fabrication.

For our current nCC chip operation, 5 uL of sample is required to perform the analysis. Most of the samples are used to fill the micro-channel outside of the nanochannel. Which makes the overall sampling size is about 15 pL, and sampling efficiency is only 1.5×10^{-4} %. From the previous publications, the shape and structure of nanochannel entrance can significantly affect the sampling efficacy, such as the funnel structure can increase the λDNA sampling efficiency ~8-fold (Figure 6.1a). For the current nCC chip, we have the blunt entrance (Figure 4.3c) that can be optimized to the funnel structure to enhance our sampling efficiency. The sampling efficiency can also be optimized by reducing the size of the micro-channel and increasing the number of nanochannels. By combining the factors of funnel entrance structure, reduced size of the microchannel, and parallel nanochannels, the sampling efficiency of the nCC chip can be significantly increased (Figure 6.1).

The electrical signal input and detection can be optimized as well. Currently, we are using AxoPatch, which allows for potential output and record electrical signal trace. However, AxoPatch has some limitations, such as the format of the output data is only compatible with the pCLAMP suit-software. The output data has to be analyzed by the pCLAMP. However, the AxoPatch is designed to characterize individual signals from the axons, but not for continuous event counting. As a result, the AxoPatch shows disadvantages for particle enumeration, such as miss identification for low amplitude, sizeable random access memory (RAM) consumption with multiple events, and

maximum output potential at 1V. Our collaborator, Dr. Collin McKenny (University of North Carolina), has developed a portable Trans-Impedance Amplifier (TIA) in a box measuring only 15 cm × 10 cm × 5 cm in size. The box can output potential up to 10 V and can generate data in binary and text format. They are also developing a MatLab-based software package to replace the AxoPatch software suite to meet the requirements of enumeration data analysis. Last but not least is the manufacturing of the nCC chip. Currently, nCC chips are manufactured via nanoimprint, which is limited by the speed of controlling temperature and pressure. The injection molding has shown high performance and suitable for both microsize and nanosize chip fabrication.[37] Therefore, an adaptation of the nCC chip design and injection molding will be the next goal of our nano-device research.

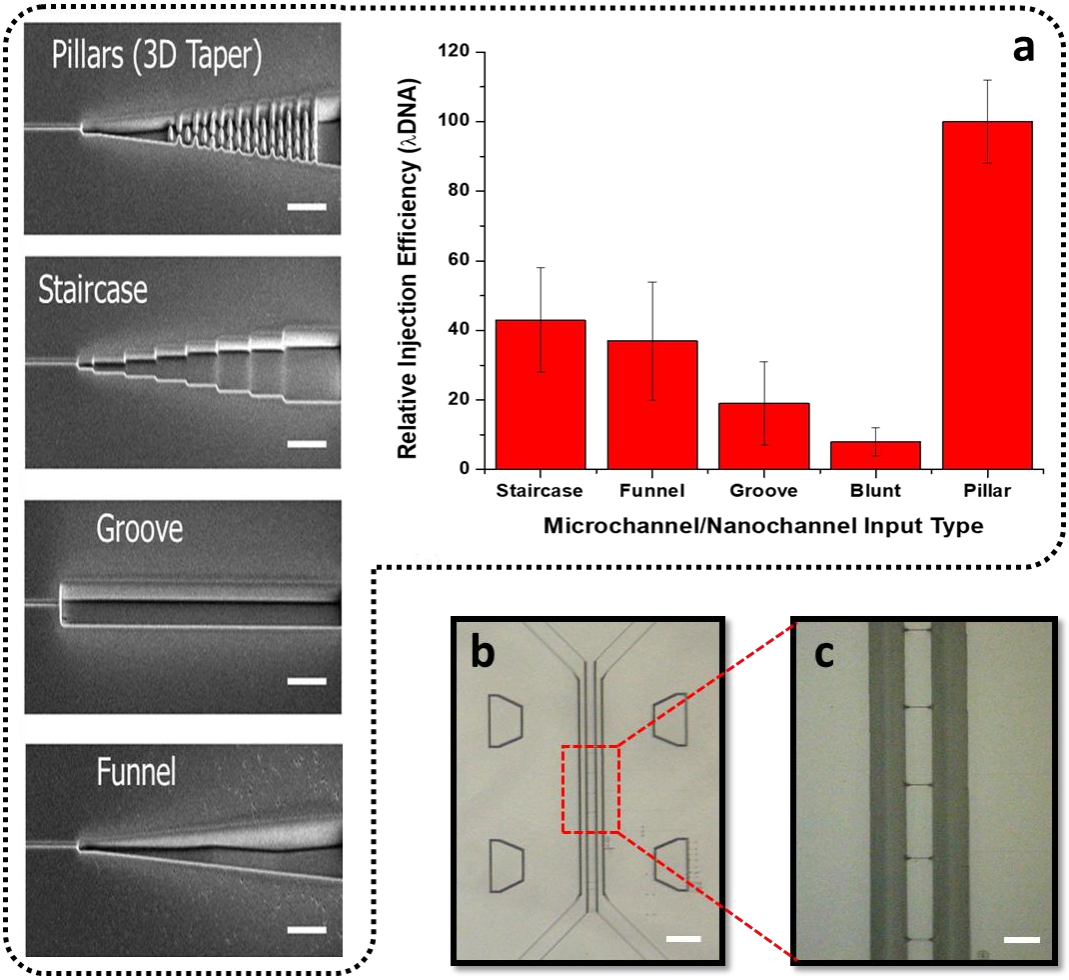

Figure 6.1. a) Relative injection efficiency of λDNA by the different structures of nanochannel entrance. The funnel structure shows a ~8-fold increased efficiency, and the pillars with 3D tapers structure show a ~20-fold increased efficiency. **b)** An optimized nCC chip with parallel nanochannels (scale bar = 50 μm). **c)** An zoomed-in snap of 5 parallel nanochannels, which can increase the sampling efficiency for at least 5-fold (scale bar = 20 μm).

6.2.2. New nCC chip optimization and COVID-19 Turnaround Screening

Our COVID-19 turnaround screening team has set golds for rapid and convenient COVID-19 screening with the technology on our hands. The EV-MAP chips allow us to enrich SARS-CoV-2 viral particles from the saliva sample, and the nCC chip will contribute to enumerate the eluted viral particles from the EV-MAP chip. However, since both of the devices were initially calibrated for EV enumeration, so, the EV-MAP chip will need further optimization to increase the viral particle recovery rate, and the new nCC chip will need calibrations for the increased sampling efficiency.

Because the new design of the nCC chip has 5 parallel nanochannels, that 5 times of the baseline current should be expected. Optimize the bandwidth to maintain the peak to peak noise level should be considered primarily. For previous experiments, a 100 kHz lowpass filter and 400 Hz highpass filter was set for signal nanochannel nCC chips. With a 5 times higher current, the theoretical peak to peak noise level can be up to 5 times. A smaller frequency of lowpass filter may be necessary to reduce the unexpected noise. However, the bandwidth will be reduced if a smaller lowpass filter is applied, and the signal amplitude will be furtherly reduced or completely covered by the noise. In this case, a fine adjustment and calibration for the bandwidth should proceed for the new nCC chip. The test can be processed with a known concentration of non-conductive beads as a similar property and translocation event shape to the viral particle. With the known event shapes and frequency belongs to the beads, the bandwidth can be adjusted to the

optimal conditions with minimal amplitude reduction and maximum noise level inhibition. In addition, the non-conductive beads should have a size of between 50 to 150 nm, which can completely cover the size range of the viral particles. The beads should be diluted with different dilution factors, and a calibration curve can be established. With the optimized bandwidth and calibration curve, the feeding viral particle concentration can be collected and analyzed rapidly.

With the well-calibrated platform, 100 COVID-19/healthy clinical samples will be received from the clinical site by Dr. Godwin (University of Kansas Medical Center). All the samples will be processed through the EV-MAP chip for SARS-CoV-2 particle isolation and enrichment. Furthermore, the viral particle will be eluted by photocleavage, and the eluted particles will be fed into the new nCC chip.[38]

The COVID-19 turnaround screening team is also trying to engineer and miniaturize the EV-MAP chip and the nCC chip into a handheld instrument (Figure 6.2a). The device will include a sample input module, insertable chip holder, electrical contacts, and a screen for displaying results. The inserted chip will combine a newly designed EV-MAP chip and nCC chip (Figure 6.2b). The sandwich-like micro/nanofluidic device can be fabricated by injection molding with the material of cyclic olefin copolymer (COC). The top layer of the device will be the cover and also includes the connectors for the sample and buffer inlets and also waste outlet. The electrodes are also deposited on the top layer, that used to apply the potential, and meanwhile, sensing the viral particles flow through the nanopore. The middle layer will be the nCC chip layer used for viral particle enumeration. The bottom layer will be the EV-MAP chip layer, which can enrich viral particles from the saliva and release those particles to the middle nCC layer. Each of the chips can be consumable for each test, and the injection-molded device can guarantee the supplement for a large number of test needs. The handheld instrument is designed for a rapid COVID-19 infectious

condition screening to provide the preliminary information for the clinical site, and trend to benefit the management and control for the COVID-19 pandemic.

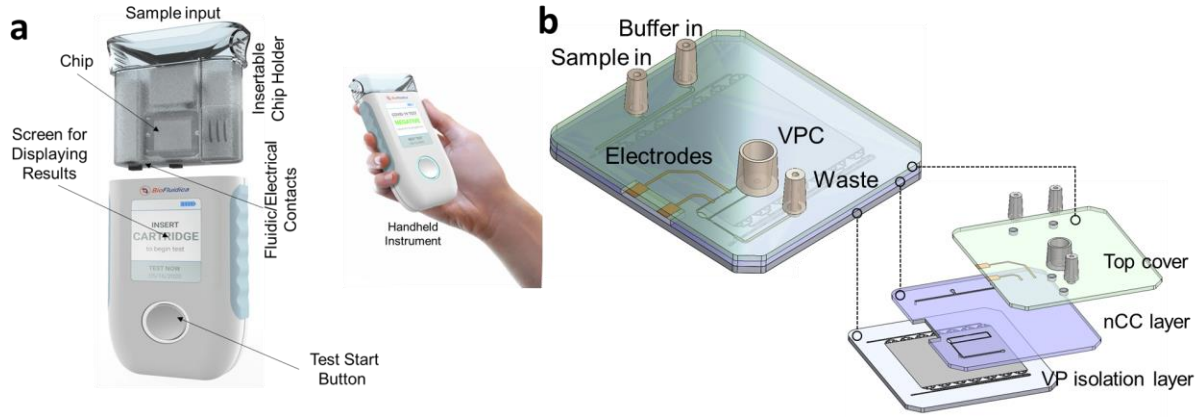

Figure 6.2. a) The demonstration of the handheld instrument for rapid COVID-19 infectious condition screening. The instrument includes a sample input module, an insertable chip holder, fluidic electrical contacts, and a screen for displaying results. **b)** The re-designed sandwich chip that includes the EV-MAP and nCC is used to insert into the handheld instrument.

6.3. References

(1). Pang, B.; Zhu, Y.; Ni, J.; Thompson, J.; Malouf, D.; Bucci, J.; Graham, P.; Li, Y., Extracellular vesicles: the next generation of biomarkers for liquid biopsy-based prostate cancer diagnosis. *Theranostics* **2020,** *10* (5), 2309-2326.

(2). Yoshioka, Y.; Katsuda, T.; Ochiya, T., Extracellular vesicles and encapusulated miRNAs as emerging cancer biomarkers for novel liquid biopsy. *Jpn J Clin Oncol* **2018,** *48* (10), 869-876.

(3). Brenner, A. W.; Su, G. H.; Momen-Heravi, F., Isolation of Extracellular Vesicles for Cancer Diagnosis and Functional Studies. *Methods Mol Biol* **2019,** *1882*, 229-237.

(4). Konoshenko, M. Y.; Lekchnov, E. A.; Vlassov, A. V.; Laktionov, P. P., Isolation of Extracellular Vesicles: General Methodologies and Latest Trends. *Biomed Res Int* **2018,** *2018*, 8545347.

(5). Gilligan, K. E.; Dwyer, R. M., Engineering Exosomes for Cancer Therapy. *Int J Mol Sci* **2017,** *18* (6).

(6). Chen, B. Y.; Sung, C. W.; Chen, C.; Cheng, C. M.; Lin, D. P.; Huang, C. T.; Hsu, M. Y., Advances in exosomes technology. *Clin Chim Acta* **2019,** *493*, 14-19.

(7). Zhao, Z.; Yang, Y.; Zeng, Y.; He, M., A microfluidic ExoSearch chip for multiplexed exosome detection towards blood-based ovarian cancer diagnosis. *Lab Chip* **2016,** *16* (3), 489-96.

(8). Zhao, Z.; McGill, J.; Gamero-Kubota, P.; He, M., Microfluidic on-demand engineering of exosomes towards cancer immunotherapy. *Lab Chip* **2019,** *19* (10), 1877-1886.

(9). Chen, P. C.; Zhang, R. H.; Aue, U. L. Y.; Chang, G. E., Micromachining Microchannels on Cyclic Olefin Copolymer (COC) Substrates with the Taguchi Method. *Micromachines (Basel)* **2017,** *8* (9).

(10). Currivan, S.; Connolly, D.; Paull, B., Production of novel polymer monolithic columns, with stationary phase gradients, using cyclic olefin co-polymer (COC) optical filters. *Analyst* **2012,** *137* (11), 2559-66.

(11). Keller, N.; Nargang, T. M.; Runck, M.; Kotz, F.; Striegel, A.; Sachsenheimer, K.; Klemm, D.; Lange, K.; Worgull, M.; Richter, C.; Helmer, D.; Rapp, B. E., Tacky cyclic olefin copolymer: a biocompatible bonding technique for the fabrication of microfluidic channels in COC. *Lab Chip* **2016,** *16* (9), 1561-4.

(12). Ladner, Y.; Bruchet, A.; Cretier, G.; Dugas, V.; Randon, J.; Faure, K., New "one-step" method for the simultaneous synthesis and anchoring of organic monolith inside COC microchip channels. *Lab Chip* **2012,** *12* (9), 1680-5.

(13). Pu, Q.; Oyesanya, O.; Thompson, B.; Liu, S.; Alvarez, J. C., On-chip micropatterning of plastic (cylic olefin copolymer, COC) microfluidic channels for the fabrication of biomolecule microarrays using photografting methods. *Langmuir* **2007,** *23* (3), 1577-83.

(14). Hupert, M. L.; Jackson, J. M.; Wang, H.; Witek, M. A.; Kamande, J.; Milowsky, M. I.; Whang, Y. E.; Soper, S. A., Arrays of High-Aspect Ratio Microchannels for High-Throughput Isolation of Circulating Tumor Cells (CTCs). *Microsyst Technol* **2014,** *20* (10-11), 1815-1825.

(15). Jackson, J. M.; Witek, M. A.; Hupert, M. L.; Brady, C.; Pullagurla, S.; Kamande, J.; Aufforth, R. D.; Tignanelli, C. J.; Torphy, R. J.; Yeh, J. J.; Soper, S. A., UV activation of polymeric high aspect ratio microstructures: ramifications in antibody surface loading for circulating tumor cell selection. *Lab on a Chip* **2014,** *14* (1), 106-117.

(16). Szatanek, R.; Baj-Krzyworzeka, M.; Zimoch, J.; Lekka, M.; Siedlar, M.; Baran, J., The Methods of Choice for Extracellular Vesicles (EVs) Characterization. *Int J Mol Sci* **2017,** *18* (6).

(17). Vestad, B.; Llorente, A.; Neurauter, A.; Phuyal, S.; Kierulf, B.; Kierulf, P.; Skotland, T.; Sandvig, K.; Haug, K. B. F.; Ovstebo, R., Size and concentration analyses of extracellular vesicles by nanoparticle tracking analysis: a variation study. *J Extracell Vesicles* **2017,** *6* (1), 1344087.

(18). DeBlois, R. W.; Wesley, R. K., Sizes and concentrations of several type C oncornaviruses and bacteriophage T2 by the resistive-pulse technique. *J Virol* **1977,** *23* (2), 227-33.

(19). Arima, A.; Tsutsui, M.; Harlisa, I. H.; Yoshida, T.; Tanaka, M.; Yokota, K.; Tonomura, W.; Taniguchi, M.; Okochi, M.; Washio, T.; Kawai, T., Selective detections of single-viruses using solid-state nanopores. *Sci Rep* **2018,** *8* (1), 16305.

(20). Heider, S.; Metzner, C., Quantitative real-time single particle analysis of virions. *Virology* **2014,** *462-463*, 199-206.

(21). Fraikin, J. L.; Teesalu, T.; McKenney, C. M.; Ruoslahti, E.; Cleland, A. N., A high-throughput label-free nanoparticle analyser. *Nat Nanotechnol* **2011,** *6* (5), 308-13.

(22). Yang, L.; Yamamoto, T., Quantification of Virus Particles Using Nanopore-Based Resistive-Pulse Sensing Techniques. *Front Microbiol* **2016,** *7*, 1500.

(23). Song, Y.; Zhang, H.; Chon, C. H.; Chen, S.; Pan, X.; Li, D., Counting bacteria on a microfluidic chip. *Anal Chim Acta* **2010,** *681* (1-2), 82-6.

(24). Golichenari, B.; Nosrati, R.; Farokhi-Fard, A.; Faal Maleki, M.; Gheibi Hayat, S. M.; Ghazvini, K.; Vaziri, F.; Behravan, J., Electrochemical-based biosensors for detection of Mycobacterium tuberculosis and tuberculosis biomarkers. *Crit Rev Biotechnol* **2019,** *39* (8), 1056-1077.

(25). Wang, Y.; Kececi, K.; Mirkin, M. V.; Mani, V.; Sardesai, N.; Rusling, J. F., Resistive-pulse measurements with nanopipettes: detection of Au nanoparticles and nanoparticle-bound anti-peanut IgY. *Chem Sci* **2013,** *4* (2), 655-663.

(26). Chavis, A. E.; Brady, K. T.; Hatmaker, G. A.; Angevine, C. E.; Kothalawala, N.; Dass, A.; Robertson, J. W. F.; Reiner, J. E., Single Molecule Nanopore Spectrometry for Peptide Detection. *ACS Sens* **2017,** *2* (9), 1319-1328.

(27). Zhou, T.; Song, Y.; Yuan, Y.; Li, D., A novel microfluidic resistive pulse sensor with multiple voltage input channels and a side sensing gate for particle and cell detection. *Anal Chim Acta* **2019,** *1052*, 113-123.

(28). Guo, J.; Huang, X.; Ai, Y., On-Demand Lensless Single Cell Imaging Activated by Differential Resistive Pulse Sensing. *Anal Chem* **2015,** *87* (13), 6516-9.

(29). Song, Y.; Li, M.; Pan, X.; Wang, Q.; Li, D., Size-based cell sorting with a resistive pulse sensor and an electromagnetic pump in a microfluidic chip. *Electrophoresis* **2015,** *36* (3), 398-404.

(30). Sexton, L. T.; Mukaibo, H.; Katira, P.; Hess, H.; Sherrill, S. A.; Horne, L. P.; Martin, C. R., An adsorption-based model for pulse duration in resistive-pulse protein sensing. *J Am Chem Soc* **2010,** *132* (19), 6755-63.

(31). Sexton, L. T.; Horne, L. P.; Sherrill, S. A.; Bishop, G. W.; Baker, L. A.; Martin, C. R., Resistive-pulse studies of proteins and protein/antibody complexes using a conical nanotube sensor. *J Am Chem Soc* **2007,** *129* (43), 13144-52.

(32). Blundell, E. L.; Vogel, R.; Platt, M., Particle-by-Particle Charge Analysis of DNA-Modified Nanoparticles Using Tunable Resistive Pulse Sensing. *Langmuir* **2016,** *32* (4), 1082-90.

(33). Booth, M. A.; Vogel, R.; Curran, J. M.; Harbison, S.; Travas-Sejdic, J., Detection of target-probe oligonucleotide hybridization using synthetic nanopore resistive pulse sensing. *Biosens Bioelectron* **2013,** *45*, 136-40.

(34). Lobb, R. J.; Becker, M.; Wen, S. W.; Wong, C. S.; Wiegmans, A. P.; Leimgruber, A.; Moller, A., Optimized exosome isolation protocol for cell culture supernatant and human plasma. *J Extracell Vesicles* **2015,** *4*, 27031.

(35). Maas, S. L.; de Vrij, J.; van der Vlist, E. J.; Geragousian, B.; van Bloois, L.; Mastrobattista, E.; Schiffelers, R. M.; Wauben, M. H.; Broekman, M. L.; Nolte-'t Hoen, E. N., Possibilities and limitations of current technologies for quantification of biological extracellular vesicles and synthetic mimics. *J Control Release* **2015,** *200*, 87-96.

(36). Song, Y.; Zhang, J.; Li, D., Microfluidic and Nanofluidic Resistive Pulse Sensing: A Review. *Micromachines (Basel)* **2017,** *8* (7).

(37). Utko, P.; Persson, F.; Kristensen, A.; Larsen, N. B., Injection molded nanofluidic chips: fabrication method and functional tests using single-molecule DNA experiments. *Lab Chip* **2011,** *11* (2), 303-8.

(38). Pahattuge, T. N.; Jackson, J. M.; Digamber, R.; Wijerathne, H.; Brown, V.; Witek, M. A.; Perera, C.; Givens, R. S.; Peterson, B. R.; Soper, S. A., Visible photorelease of liquid biopsy markers following microfluidic affinity-enrichment. *Chem Commun (Camb)* **2020,** *56* (29), 4098-4101.

Appendix 1: Macro order of ImageJ for 1000 random points selection

```
// START OF MACRO
// This macro assumes you have a binary image.

// Number of points to generate
n_points = 1000;



name = getTitle(); // Name of the image
getDimensions(x,y,z,c,t); // Size of the image

// Initialize arrays that will contain point coordinates
xcoords = newArray(n_points);
ycoords = newArray(n_points);

// Seed the random number generator
random('seed', getTime());

// Create n_points points in XY
for (i=0; i<n_points; i++) {
	xcoords[i] = round(random()*x);
	ycoords[i] = round(random()*y);
}
```

```
// Overlay them on the image
makeSelection("point", xcoords, ycoords);

// Count points that have a value of 255
prevRes = nResults;
run("Measure");
count = 0;

for (i=0; i<n_points;i++) {
	val = getResult("Mean",i+prevRes);
	if (val == 255) {
		count++;
	}
}

// Output to log window.
print("Image "+name+": "+count+" points out of "+n_points+" inside objects of interest");

// END OF MACRO
```